

**Computational Modeling of Progressive Failure in FRP
Composite Laminates Subjected to Static and Impact
Transverse Loading**

**Computational Modeling of Progressive Failure in FRP
Composite Laminates Subjected to Static and Impact
Transverse Loading**

Proefschrift

ter verkrijging van de graad van doctor
aan de Technische Universiteit Delft,
op gezag van de Rector Magnificus Prof.ir. K.C.A.M. Luyben,
voorzitter van het College voor Promoties,
in het openbaar te verdedigen op dinsdag 9 september 2014 om 10.00 uur

door

Awais AHMED
Master of Science in Earthquake Engineering
IUSS - Institute for Advanced Study
and
Università Degli Studi di Pavia
geboren te Peshawar, Pakistan

Dit proefschrift is goedgekeurd door de promotor:

Prof.dr.ir. L.J. Sluys

Samenstelling promotiecommissie:

Rector Magnificus

Prof.dr.ir. L.J. Sluys

Prof. S. Hallet

Prof.dr. W. Van Paepegem

Prof.dr.ir. A.S.J. Suiker

Prof. P.M.P.R. de Camanho

Prof.dr.ir. R. Marissen

Dr. J.J.C. Remmers

Voorzitter

Technische Universiteit Delft, promotor

University of Bristol

Universiteit Ghent

Technische Universiteit Eindhoven

Universidade do Porto

Technische Universiteit Delft

Technische Universiteit Eindhoven

This research has been supported by the N-W.F.P University of Engineering & Technology Peshawar, Pakistan, under the HEC approved project titled “Strengthening of existing earthquake engineering center” and Delft University of Technology, The Netherlands.

Keywords: composite laminates, finite element method, solid-like shell element, progressive failure

Published by Ipskamp Drukkers, Enschede, The Netherlands

Copyright © 2014 by A. Ahmed

ISBN 978-94-6186-351-5

Summary

Computational Modeling of Progressive Failure in FRP Composite Laminates Subjected to Static and Impact Transverse loading

In order to arrive at safe and reliable design of composite structures, understanding of the mechanisms and mechanics of damage growth in these materials is of paramount significance. Numerical models, if designed, implemented and used carefully, can be helpful not only to understand the mechanisms and mechanics of damage growth but also to predict the susceptibility of a structure to failure. This information can later be used for the design and optimization of materials and structures. The rise in computer power and recent advances in computational methods have intensified the need for using state of the art numerical models for virtual testing of composites more than ever. However, the presence of different damage mechanisms and their mutual interaction, in fiber-reinforced laminated composites, makes the development of robust and reliable computational model a challenge.

In this thesis, advanced finite elements and numerical methods are explored to develop a computationally efficient and reliable numerical framework for the analysis of damage growth in laminated composite plates subjected to quasi-static and dynamic transverse loads. A solid-like shell element is used to obtain a three-dimensional stress state in fiber-reinforced laminated composites. The element is further extended to model mesh-independent matrix cracking by incorporating a discontinuity in the shell mid-surface, shell director and thickness stretching field. A progressive failure model is developed which is able to simulate impact induced damage in laminated composites. The discontinuous shell model is combined with a shell interface element to describe progressive failure in laminate analyses. Care is taken to accurately describe the interaction between matrix cracks and delamination damage which is crucial for accurate predictions of fracture phenomena and laminate strength. Furthermore, a time- dependent progressive failure model is developed to simulate crack growth in laminated composites under dynamic loading conditions. The proposed mass discretization schemes for the solid-like shell element ensure efficient performance of the element in implicit as well as explicit elasto-fracture analysis of composite laminates. Additionally, an efficient mass scaling technique is presented to increase the critical timestep in explicit dynamic simulations. The presented numerical framework also discusses computational modeling of coupled thermo-mechanics

of laminated composites in the presence of cracks. A unified computational model is presented which is able to simulate coupled adiabatic-isothermal cracks propagating arbitrarily through the finite element mesh.

The reliability and accuracy of the numerical framework and each individual model has been tested against analytical, numerical and experimental results. Numerical results reveal that the introduced numerical framework allows for a robust and reliable progressive failure analysis of composite laminated plates under quasi-static and dynamic loading conditions which can be used for detailed numerical investigation of laminated composite materials and structures under a variety of mechanical and thermal loading conditions.

Samenvatting

Numerieke Modelling van Progressief Bezijken in FRP Composietlaminaten Blootgesteld aan Statische en Impact Dwarsbelasting

Begrip van de mechanismen en de mechanica van schadeontwikkeling in composieten is van uiterst belang voor een veilig en betrouwbaar ontwerp van constructies van deze materialen. Computermodellen kunnen, indien ze met zorg ontworpen, geïmplementeerd en gebruikt worden, van nut zijn voor zowel het begrijpen van de mechanismen en de mechanica van schadeontwikkeling als het voorspellen van de bezwijkgevoeligheid van een constructie. Deze informatie kan vervolgens gebruikt worden voor ontwerp en optimalisatie van materialen en constructies. Door de toegenomen rekenkracht en nieuwe ontwikkelingen in computermethodes is de behoefte om computermodellen te gebruiken voor het virtueel testen van composieten toegenomen. Door de aanwezigheid van en interactie tussen verschillende schade-mechanismen blijft het ontwikkelen van robuuste en betrouwbare computermodellen echter een uitdaging.

In dit proefschrift worden geavanceerde eindige-elementen- en computermethodes onderzocht met het oog op ontwikkeling van een efficiënt en betrouwbaar numeriek raamwerk voor de analyse van schadeontwikkeling in gelamineerde composieten platen onder quasi-statische en dynamische dwarsbelasting. Een ‘solid-like shell’ element wordt toegepast voor het verkrijgen van een driedimensionale spanningstoestand in vezelversterkte composietlaminaten. Het element wordt voor het mesh-onafhankelijk modelleren van matrixscheuren verrijkt met een discontinuïteit in zowel het middelvlak, de ‘director’ als de dikte- ϵ van de schaal. Een model voor progressief bezijken is ontwikkeld waarmee schadeontwikkeling in composietlaminaten als gevolg van impactbelasting gesimuleerd kan worden. Het discontinue schaalmodel wordt gecombineerd met een speciaal interface-element voor schalen zodat het progressief bezijken in laminaten gesimuleerd kan worden. Hierbij wordt zorg besteed aan nauwkeurige beschrijving van de interactie tussen matrixscheuren en delaminatie, hetgeen cruciaal is voor nauwkeurige voorspellingen van breukverschijnselen en de sterkte van laminaten. Bovendien wordt een tijdsafhankelijk model voor progressief bezijken ontwikkeld voor het simuleren van scheurgroei in composietlaminaten onder dynamische belasting. Een massa-discretisatieschema wordt voorgesteld voor de ‘solid-like shell’ elementen waarmee de efficiëntie van het ele-

ment in zowel impliciete als expliciete analyse van composietlaminaten gewaarborgd wordt. Verder wordt een methode gepresenteerd voor het schalen van massa waarmee de kritische tijdstap in expliciete dynamische simulaties vergroot wordt. Het gepresenteerde numerieke raamwerk omvat ook computermodellering van gekoppelde thermo-mechanica van composietlaminaten in de aanwezigheid van scheuren. Een enkelvoudig computermodel wordt gepresenteerd waarin gekoppelde adiabatische-isothermische scheuren arbitrair door het eindige-elementenmesh kunnen lopen.

De betrouwbaarheid en de nauwkeurigheid van het numerieke raamwerk en van de afzonderlijke modellen is getest ten opzichte van analytische, numerieke en experimentele resultaten. De numerieke resultaten tonen dat het voorgestelde numerieke raamwerk robuuste en betrouwbare analyse van het progressief bezwijken van composietlaminaten onder quasi-statische en dynamische belasting mogelijk maakt, waardoor het raamwerk gebruikt kan worden voor gedetailleerde computeranalyses van gelamineerde composietmaterialen en -constructies onder verschillende mechanische en thermische belastingen.

Acknowledgments

All praise and thanks to Almighty ALLAH for the knowledge and wisdom that HE bestowed on me in all my endeavors.

My heartiest thanks to two most important peoples in my life- my parents. It would not have been possible without their support and encouragement to come along this far and achieve what I have today.

I am sincerely grateful to Prof. L.J. Sluys for his valuable time, guidance and allowing me to work with complete freedom and independence. Working with him was indeed a fruitful and an unforgettable experience of my life. Thanks are also due to Erik J. Lingen for providing help and support in programming with JemJive C++ numerical toolkit. I would also like to thank all my colleagues and administrative staff at the structural mechanics section for providing me a pleasant and motivating working environment. Special thanks to Adrian sillem and F.P van der Meer for helping me with the dutch translation of the thesis summary.

Awais Ahmed,
July 2014

Contents

Summary	v
Samenvatting	vii
Acknowledgments	ix
1 Introduction	1
1.1 Objective and novelty of the work	2
1.2 Thesis Outline	4
2 Discontinuous solid-like shell element (DSLS)	7
2.1 Introduction	7
2.2 Mathematical preliminaries	10
2.3 Kinematics of solid-like shell element (SLS)	12
2.4 Kinematics of discontinuous solid-like shell element (DSLS)	13
2.5 Equilibrium of DSLS	20
2.6 Linearization of the equilibrium equations	22
2.7 Finite element discretization	24
2.8 Assumed natural strains	29
2.9 Numerical examples	30
2.10 Conclusions	40
3 Three-dimensional progressive failure model	43
3.1 Introduction	43
3.2 Discontinuous shell model for matrix cracking	47
3.3 Shell interface model for delamination cracking	49
3.4 Interaction of matrix cracking and delamination	50
3.5 Constitutive laws	55
3.6 Implementation details	58
3.7 Numerical examples	60
3.8 Conclusions	77
4 Solid-like shell element for dynamic analysis of plates and shells	81
4.1 Introduction	81
4.2 Dynamic Solid-Like Shell Element (SLS) formulation	83
4.3 Mass discretization schemes	88
4.4 Numerical examples	94
4.5 Concluding remarks	106

5	Dynamic fracture in laminated composite plates	107
5.1	Introduction	107
5.2	Meso-level progressive failure model	110
5.3	Implementation aspects	113
5.4	Numerical examples	117
5.5	Conclusions	139
6	Discontinuous thermo-mechanical computational model	141
6.1	Introduction	141
6.2	Thermo-mechanical discrete damage model	143
6.3	Constitutive relations	148
6.4	Finite element formulation	151
6.5	Numerical examples	152
6.6	Concluding remarks	169
7	Conclusions	173
A	Anomalous behavior of bi- and tri-linear elements in XFEM	175
A.1	Extended finite element method (XFEM) basics	175
A.2	Model problem	179
A.3	Explanation of analysis results	183
A.4	Interface element analysis	189
A.5	Mesh refinement study	191
A.6	Conclusions	196
B	Implementation aspects of DSLS	203
B.1	Transformation matrix	203
B.2	Computation of strains and B matrix	203
B.3	Stiffness matrices	205
C	Mass matrix for solid-like shell element	209
C.1	Discretized inertial virtual work	209
D	Properties of dirac-delta function	211
	References	213
	Publications	225
	Propositions	227
	Stellingen	229
	Curriculum vitae	231

Chapter 1

Introduction

There is an increasing use of fiber-reinforced composite laminates, in myriad fields of engineering, such as civil engineering, mechanical engineering and aerospace engineering. In many applications, they are subjected to extreme loading conditions such as impact, thermal shock, thermal and mechanical cycles etc. Safe and reliable design of composite structures heavily relies on accurate predictions of strength and stiffness. Virtual testing of composite laminates plays a vital role in understanding the mechanisms and mechanics of damage growth in composite laminates and for assessing its susceptibility to failure under variety of boundary conditions. This knowledge can be used for the design and optimization of composite materials and structures. Moreover, numerical simulations also help in interpreting experimental results. However, the presence of different failure processes and their mutual interaction makes the development of computational models a challenge.

Damage in fiber-reinforced composite laminated plates usually appears as cracking in the matrix material, fiber-matrix debonding, fiber breakage, local and global buckling, delamination and total perforation in case of high velocity impact. Delamination damage, which is the debonding of plies, is considered to be one of the dominant damage modes and can significantly reduce the strength of the laminate. On the other hand, matrix cracking/splitting is observed to be the initial failure mode of impact damage. Matrix cracks act as stress enhancers which initiate delamination damage at the ply interfaces. Even though matrix cracking/splitting in a laminate alone, may not significantly reduce the strength and stiffness of the laminate but may become a key failure mode e.g. in case of pressure vessels, in which gas leakage is considered to be the failure of the structure. Therefore, accurate predictions of initiation and propagation of both matrix cracking and delamination damage is crucial in assessing the susceptibility of a laminate to failure.

To achieve the goal of developing efficient and accurate numerical models, the importance of mechanism based failure models was soon recognized [120]. Significant work has been done to model progressive failure in laminated composites subjected to in-plane loads with different failure models such as plasticity, continuum damage and failure based models. A detailed survey of the numerical models for failure analysis of laminated composites can be found in [114]. However, discrete fracture models such as cohesive zone models using interface elements are often preferred.

It was further shown by [161], that good predictions of progressive damage in laminated composites can be made if individual damage modes are modeled accurately. As opposed to the interface element model, partition-of-unity based methods such as the extended finite element method (XFEM) [107, 159] and phantom node method [58, 106] allows for the modeling of crack propagation independent of the underlying mesh structure. These advanced numerical methods have been used to model the in-plane response of composite laminates [74, 153] but not for out-of-plane loaded composites. Computational modeling of progressive failure in laminated composite plates and shells, subjected to transverse static and dynamic loads, presents additional challenges and requires the development of improved finite elements and numerical procedures. The work presented in this thesis aims at addressing these issues and explores the potential of advanced finite elements and numerical methods to model progressive mechanical and thermo-mechanical damage in laminated composite plates/shells, subjected to quasi-static and dynamic transverse loads.

1.1 Objective and novelty of the work

In this thesis a meso-scopic, progressive failure model to simulate interacting damage mechanisms in fiber-reinforced laminated composite plates subjected to quasi-static and dynamic transverse loading is presented. The objective here is to develop an efficient computational framework for numerical analysis of out-of-plane loaded composite laminates. The work presented in this thesis exploits the use of advanced numerical methods, i.e. the phantom node method, which allows for the mesh-independent crack propagation through a finite element mesh. A cohesive zone approach is used to simulate non-linear material behavior in front of the crack-tip. It is however, essential to use a fine mesh in the regions where prospective cracks may initiate and propagate, in order to resolve the cohesive zone. Mesh refinement is also needed for an accurate predictions of stresses and strains in the vicinity of the cohesive crack-tip [5].

Another key ingredient of the present formulation is the use of solid-like shell element for laminate analysis. In principle, the out-of-plane response of laminated composites can be modeled using two-dimensional (2-D) plate and shell elements, however, accurate predictions of delamination damage requires determination of a three-dimensional (3-D) stress field. This motivated the use of 3-D solid/brick elements in many computational models for laminate analysis. However, solid elements perform poorly in thin shell applications. On the other hand, solid-like shell elements possess the necessary properties of both 2-D shell and 3-D solid elements. Solid-like shell elements use the kinematics from the classical shell theory and thus can be used in thin shell applications and the three-dimensional nature of the element allows for the computation of a three-dimensional stress field.

The new developments and/or improvements made to the existing computational approaches for modeling progressive damage in out-of-plane loaded composite laminates in this thesis are:

1. A geometrically non-linear, discontinuous solid-like shell element (DSLS) is developed, which is able to simulate mesh-independent cracking in thin shells and plates. The element incorporates a discontinuity in the shell mid-surface, shell director and thickness stretching field.
2. The nonlinear solid-like shell theory of [116] is improved to include strain terms corresponding to the higher-order thickness coordinate. These strain terms become important in the presence of large strains with bending deformations and shells with large bending curvatures [108].
3. The DSLS is adapted to model cohesive matrix cracking/splitting, oriented along the fiber direction of the ply in a laminate analysis.
4. A partition-of-unity based shell interface element for efficient numerical simulation of delamination damage is introduced.
5. The effect of matrix cracking on delamination damage is carefully taken into account and an enhanced shell interface model is developed.
6. Mass discretization strategies for solid-like shell elements in implicit and explicit dynamic analysis are proposed.
7. Mass scaling procedures for solid-like shell elements in explicit dynamic simulations are developed.
8. A time-dependent progressive failure model is introduced for the simulation of fast crack growth (matrix cracking and delamination cracks) in composite laminates.
9. The issue of time-continuity and numerically induced oscillations in the velocity and stress/strain profiles in dynamic simulations is discussed and a possible remedy is proposed.
10. A mixed-mode, exponentially decaying cohesive law for laminate analysis is introduced for an efficient numerical simulation.
11. A partition-of-unity based thermo-mechanical model for coupled adiabatic-isothermal cracking in laminated composites is presented.

12. The notion of thermo-fracture heating, as theoretically introduced by [28], is incorporated in the numerical framework and is enhanced to simulate heat generation due to craze formation and breakdown and frictional sliding between crack flanks.
13. The issue of approximation inconsistencies in highly celebrated partition-of-unity based methods e.g. XFEM,GFEM and phantom node methods are discussed and possible remedies are proposed [3]. See also appendix A.

1.2 Thesis Outline

One of the key ingredients of the computational strategy proposed in this thesis is the solid-like shell element for laminate analysis. In order to simulate cohesive cracks propagating arbitrarily through a finite element mesh of solid-like shell elements, a discontinuous solid-like shell element is developed. This is achieved through the phantom node method. Chapter 2 of the thesis discusses in detail the kinematics, variational and finite element formulation for the discontinuous solid-like shell element.

In chapter 3, the discontinuous shell model is combined with a shell interface element to model progressive failure in composite laminated plates subjected to quasi-static transverse loads. Mesh-independent matrix cracking/splitting is modeled with the discontinuous solid-like shell element (DSLSE). In order to model delamination damage, a partition-of-unity based shell interface model for large deformation problems is developed. Moreover, modeling the interaction between matrix cracking and delamination damage is discussed. The chapter discusses in detail the numerical framework, algorithmic and implementation details of the progressive failure model. The chapter concludes with illustrative numerical examples in simulating quasi-impact damage in laminated composite plates.

The remaining part of the thesis concerns with the numerical modeling of composite laminates subjected to rapidly applied loads. Chapter 4 describes the formulation and finite element details of the solid-like shell element for dynamic analysis of isotropic/orthotropic plates and shells. Mass discretization strategies for implicit as well as explicit dynamic analysis using solid-like shell elements are presented. Moreover, mass scaling to increase the critical time step in explicit dynamic simulation, without affecting the solution's accuracy, is also discussed. Numerical examples are presented in order to show the performance and salient features of the dynamic solid-like shell element.

Chapter 5 presents a computational model for progressive failure in laminated plates subjected to rapidly applied loads. The quasi-static model developed in chapter 3 is extended for dynamic applications. Numerical results on fast crack growth,

with crack-tip speed approaching to the longitudinal wave speed, in laminated composite plates are presented. Damage initiation, growth and their interaction under different loading rates is discussed. Numerical issues related to modeling dynamic crack propagation are discussed. A solution strategy to remove numerical oscillations due to imbalance of forces at the crack interface, at the time of insertion of new crack segments, is presented.

Dynamic fracture in laminated composites may generate heat which may influence the response of the laminate. Chapter 6 presents a numerical model to simulate mesh-objective, coupled adiabatic-isothermal cracking in a composite laminate. The model simulates heat transfer through an interface and heat generation at the interface during fracture. A phantom node method is exploited to simulate arbitrary propagating cracks through a finite element mesh. A thermo-fracture heating term is introduced to take the heat generation due to craze formation and breakdown and friction into account.

Chapter 2

Discontinuous solid-like shell element (DSL_S)*

This chapter presents a novel geometrically nonlinear, discontinuous solid-like shell finite element for the simulation of cracking phenomena in thin shell structures. The discontinuous shell element is based on the solid-like shell element, having a layout similar to brick elements but better performance in bending. The phantom node method is employed to achieve a fully discontinuous shell finite element, which incorporates a discontinuity in the shell mid-surface, director and in thickness stretching field. This allows the element to model arbitrary propagating cracks in thin shell structures in combination with geometrical non-linearities. The kinematics of the discontinuous shell element as well as the detailed finite element formulation and implementation are described. Several numerical examples are presented to demonstrate the performance of the element.

2.1 Introduction

2.1.1 Motivation

Shell structures are frequently used in many fields of engineering due to their structural efficiency and light weight. However, shell structures like others are also endowed with material and/or geometrical non-linearities such as initiation and propagation of cracks, global and local buckling etc. which may impair structural soundness. Correct predictions of failure in such structures is fundamental. There has been growing interest in the industrial and defense community in developing reliable and computationally efficient numerical tools, able to represent different failure mechanisms. These tools are necessary for the design and analysis of new or existing structures and materials.

When it comes to modeling thin shell structures, classical shell elements based on the Mindlin-Reissner theory [109] offer means for modeling thin structures. Over the years these elements were modified and more robust and efficient shell elements were developed for general linear and nonlinear applications, see for example [14, 34, 50, 68, 71, 82, 135]. However, these models are based on plane-stress constitutive relations therefore thickness change was not taken into account in these

* This chapter is extracted from [10]

formulations. Hence, these elements do not allow for a damage analysis at lower levels of observation e.g. meso-scopic level and may give un-realistic results in bending dominated problems. Apart from this, coupling of rotational degrees of freedom with the purely displacement based interface elements is also not straightforward for problems involving crack growth or delamination in laminated structures. [167] used two dimensional shell elements based on the Mindlin-Reissner theory and proposed a cohesive constitutive law which included a bending moment-rotation relation to avoid problems with the rotational degrees of freedom.

To model damage in shell structures, continuum damage or plasticity type approaches have been used. For example [20] used a continuum damage approach based on Gurson's damage model [56] to simulate ductile crack growth in thin-walled shell structures. A finite element analysis was performed using a 5-parameter shell element, which consisted of a 4-node iso-parametric element with three translational and two rotational degrees of freedom at each node.

Inspired by the idea of discrete fracture modeling and a cohesive zone approach, several contributions were made in which cohesive interface elements were embedded on predefined locations along element edges of shell elements, see for example [39, 95, 129]. [138] used modified line spring elements on predefined locations to simulate cracking in shell structures.

Acknowledging the importance of full three dimensional analysis to investigate local failure mechanisms, 3D continuum elements were explored in [21] using continuum damage analysis for shell structures. A modified Gurson's damage model based on Tvergaard's [149] cohesive constitutive law was utilized to take into account the ductile degradation process caused by void nucleation, growth and coalescence. Several other researchers favored discrete fracture modeling with a cohesive zone approach using volume elements for thin shell structures. [55] and [127] used a discrete cohesive cracking approach with volume elements to simulate ductile fracture in thin shells. However, it has been observed [27], that volume elements, when employed with large aspect ratios, tend to lock. This phenomenon is known as Poisson-thickness locking and causes serious numerical problems.

In order to allow arbitrarily propagating cracks through a finite element mesh, partition of unity based methods like the extended finite element method (XFEM) are to be preferred. [16] used an alternative approach to XFEM, based on the methodology of [58], for mesh independent discrete fracture modeling in thin shell structures using shell elements based on Kirchoff-Love conditions [17]. However, these shell elements do not account for possible shear deformations. [141] proposed a discontinuous shell element based on a degeneration concept [1], for dynamic fracture problems. The method utilizes a shell element [25] based on Mindlin-Reissner theory. Unfortunately these shell models do not include thickness stretching. Recently [94] proposed a discontinuous shell model based on shell element proposed by [27],

where the XFEM methodology is explored to incorporate discontinuities in the shell mid-surface and director field. However, the proposed model does not address the issues regarding inhomogeneous stretching of cracked shell elements, which may result from non-uniform bending on opposite crack faces.

In this chapter, a new geometrically nonlinear continuum based shell element for the simulation of through-the-thickness cracking in thin shell structures is presented. The shell element is based on a solid-like shell theory [116], which on one hand incorporates the kinematics of shells directly by linear interpolation of three dimensional kinematic relations and removes contradictory assumptions originated from the dimensional reduction from 3D to 2D in conventional shell elements. On the other hand, it removes the Poisson thickness locking effect commonly found for volume elements, when employed in thin shell applications. To model matrix cracks, an alternative approach to XFEM, based on the method of [58], where an element crossed by a discontinuity is replaced by overlapping elements, is exploited. This results in a simpler implementation than the traditional XFEM [107], as the overlapped elements are similar to standard finite elements. In order to incorporate inelastic material behavior near the crack tip zone, we follow the work by [159] for cohesive fracture, where such nonlinearities are captured by a cohesive constitutive law which relates the interface tractions to the jump in the displacement field.

2.1.2 Scope of study

A failure model for shell and plate structures is presented, where a shell layer is modeled with an eight-noded solid-like shell element. The discontinuous solid-like shell element has only displacement degrees of freedom and provides a complete three-dimensional state of stress. The key features of the discontinuous shell element are:

- The element is capable of simulating mesh independent, arbitrarily moving cohesive cracking in shell/plate structures subjected to static or dynamic out-of-plane loading conditions.
- The model presents a fully discontinuous shell formulation, where in addition to a discontinuity in the shell mid-surface and the shell director field, a discontinuity is included in the thickness stretching, see section 2.4.3 for details.
- The model is able to capture simultaneously the effects of geometrical instabilities and material non-linearity.
- The model is able to simulate through the thickness inclined cracks, which need not to be normal to the mid-surface, e.g compression cracks.

- Due to the three dimensional nature of the shell element, the discontinuous model can be used in combination with higher dimensional elements in a finite element mesh and hence, methods like displacement compatibility [131], the use of transition elements [81] can be avoided, which are commonly used for connecting shell elements to 3D elements.

This chapter is ordered as follows: In the next section, we summarize the mathematical preliminaries of the proposed model. In section 2.3, a brief overview of the kinematics of the solid-like shell element is presented followed by a detailed derivation of the kinematics of the discontinuous solid-like shell element in sections 2.4. Equilibrium of the discontinuous solid-like shell element and its consistent linearization is presented in sections 2.5 and 2.6. Finite element discretization of the equilibrium equations is discussed in section 2.7. Section 2.8 briefly discusses the method of assumed natural strains (ANS) for the removal of shear locking in eight noded solid-like shell element. The performance of the discontinuous solid-like shell element is demonstrated by means of several numerical examples in section 2.9. Finally section 10 summarizes the main conclusions drawn from the article.

2.2 Mathematical preliminaries

To describe shell kinematics, we consider two states of a continuum body, an undeformed state represented by \mathbb{B}_o with domain Ω_o and a deformed state represented with \mathbb{B} and domain Ω . Following standard conventions we shall use, capital characters to denote quantities referring to the undeformed configuration and lower-case characters for quantities referring to the deformed configuration.

In order to formulate the discontinuous shell theory in a consistent way, we introduce a curvilinear coordinate system $\boldsymbol{\xi}(\xi, \eta, \zeta)$, which automatically preserves objectivity. ξ and η are defined as in-plane coordinates and ζ represents the thickness coordinate. In addition to this we also define a global Cartesian coordinate system $\mathbf{i}(i_1, i_2, i_3)$, see figure 2.1.

The position vectors in the reference and current configurations are denoted by \mathbf{X} and \mathbf{x} , respectively. The covariant base vectors are obtained as the partial derivative of the position vectors with respect to the curvilinear coordinates as

$$\mathbf{G}_\alpha = \frac{\partial \mathbf{X}}{\partial \xi^\alpha} \quad (2.1)$$

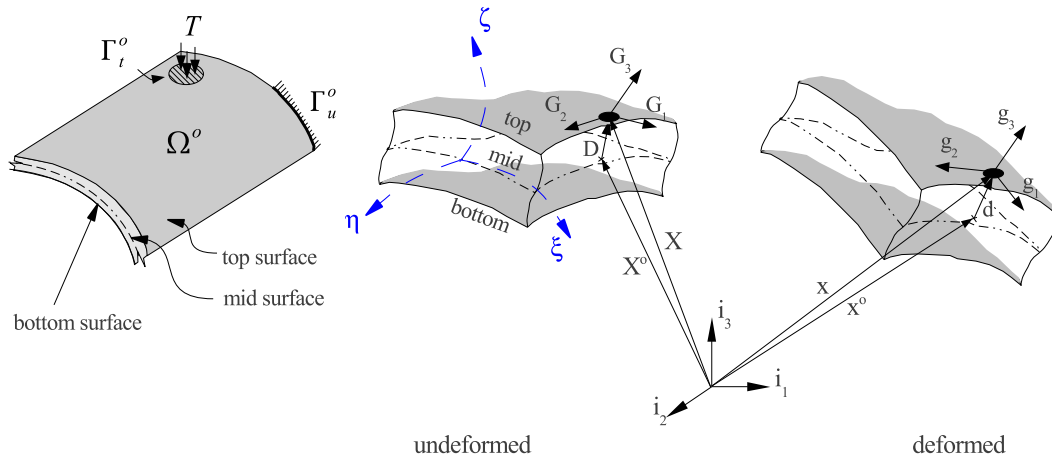
$$\mathbf{G}_3 = \frac{\partial \mathbf{X}}{\partial \xi^3}, \quad \alpha = 1, 2 \quad \boldsymbol{\xi} = \{\xi, \eta, \zeta\} \quad (2.2)$$

The covariant base vectors in the deformed configuration may be written as

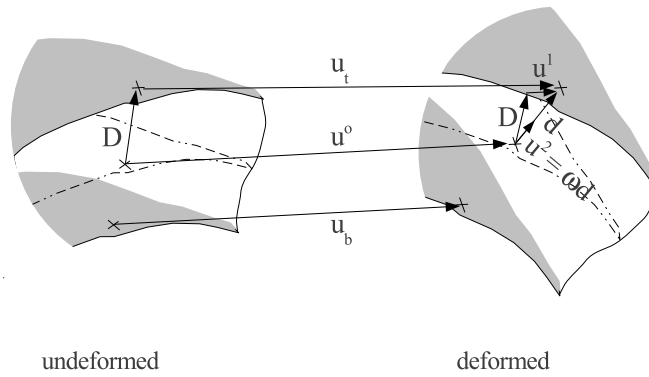
$$\mathbf{g}_\alpha = \frac{\partial \mathbf{x}}{\partial \xi^\alpha} = \mathbf{G}_\alpha + \boldsymbol{\vartheta}_{,\alpha} \quad (2.3)$$

$$\mathbf{g}_3 = \frac{\partial \mathbf{x}}{\partial \xi^3} = \mathbf{G}_3 + \boldsymbol{\vartheta}_{,3} \quad (2.4)$$

where $\boldsymbol{\vartheta}$ represents the displacement field of a solid-like shell element. Note that we defined the in-plane and out-of-plane components independently, in order to clearly define strain components in thickness and transverse directions.



(a) Geometry and kinematics of solid-like shell



(b) Different components of displacement field

Figure 2.1 Geometry and kinematics of thin shell in undeformed and deformed configurations

The metric tensors are defined as

$$G_{ij} = \mathbf{G}_i \cdot \mathbf{G}_j \quad , \quad g_{ij} = \mathbf{g}_i \cdot \mathbf{g}_j \quad i, j = 1, 2, 3 \quad (2.5)$$

Accordingly the contravariant base vectors are defined as

$$\mathbf{G}^j = G_{ij}^{-1} \mathbf{G}_i \quad , \quad \mathbf{g}^j = g_{ij}^{-1} \mathbf{g}_i \quad i, j = 1, 2, 3 \quad (2.6)$$

2.3 Kinematics of solid-like shell element (SLS)

In this section, we review the kinematics of a solid-like shell element [116]. The shell body is defined with a top surface, bottom surface and a degenerated mid-surface. When \mathbf{X} denotes the position of a particle in the reference configuration, the geometry of the shell element in the curvilinear coordinate system $\boldsymbol{\xi}(\xi, \eta, \zeta)$, is given as

$$\mathbf{X}(\xi, \eta, \zeta) = \mathbf{X}^o(\xi, \eta) + \zeta \mathbf{X}^1(\xi, \eta) \quad (2.7)$$

where \mathbf{X}^o represents the position vector of the midsurface and \mathbf{X}^1 represents the shell's director. Mathematically they are expressed as,

$$\mathbf{X}^o(\xi, \eta) = [\mathbf{X}_t(\xi, \eta) + \mathbf{X}_b(\xi, \eta)] / 2 \quad (2.8)$$

$$\mathbf{X}^1(\xi, \eta) = [\mathbf{X}_t(\xi, \eta) - \mathbf{X}_b(\xi, \eta)] / 2 \quad (2.9)$$

The subscripts $(\cdot)_b$ and $(\cdot)_t$ define the quantities projected on top and bottom surfaces of the shell. Any material point \mathbf{x} in the current configuration can be described by introducing the displacement field, $\boldsymbol{\vartheta}$ as

$$\mathbf{x}(\xi, \eta, \zeta) = \mathbf{X}(\xi, \eta, \zeta) + \boldsymbol{\vartheta}(\xi, \eta, \zeta) \quad (2.10)$$

The displacement field of a solid-like shell element is defined as a function of the displacement field of top surface \mathbf{u}_t , bottom surface \mathbf{u}_b and an internal stretch parameter ω and is given as

$$\boldsymbol{\vartheta}(\xi, \eta, \zeta) = \mathbf{u}^o(\xi, \eta) + \zeta \mathbf{u}^1(\xi, \eta) + (1 - \zeta^2) \mathbf{u}^2(\xi, \eta) \quad (2.11)$$

where \mathbf{u}^o is the displacement of the shell mid-surface

$$\mathbf{u}^o(\xi, \eta) = [\mathbf{u}_t(\xi, \eta) + \mathbf{u}_b(\xi, \eta)] / 2 \quad (2.12)$$

\mathbf{u}^1 is the displacement of the shell director, \mathbf{D}

$$\mathbf{u}^1(\xi, \eta) = [\mathbf{u}_t(\xi, \eta) - \mathbf{u}_b(\xi, \eta)] / 2 \quad (2.13)$$

and \mathbf{u}^2 denotes internal stretching of an element, which is collinear with the deformed shell director, \mathbf{d} , and a function of thickness stretch parameter, ω

$$\mathbf{u}^2(\xi, \eta) = \omega(\xi, \eta) \mathbf{d}(\xi, \eta) \quad (2.14)$$

The covariant base vectors in the reference configuration for a solid-like shell element can now be defined as,

$$\mathbf{G}_\alpha = \mathbf{X}_{,\alpha}^o + \zeta \mathbf{X}_{,\alpha}^1 \quad (2.15)$$

$$\mathbf{G}_3 = \mathbf{X}^1 = \mathbf{D} \quad (2.16)$$

The covariant base vectors in the deformed configuration can be written as

$$\mathbf{g}_\alpha = \mathbf{G}_\alpha + \mathbf{u}_{,\alpha}^o + \zeta \mathbf{u}_{,\alpha}^1 \quad (2.17)$$

$$\mathbf{g}_3 = \mathbf{G}_3 + \mathbf{u}^1 - 2\zeta \mathbf{u}^2 \quad (2.18)$$

where \mathbf{u}^2 is considered to be very small as compared to other degrees of freedom, hence its spatial derivatives (i.e $\mathbf{u}_{,\alpha}^2$) are ignored.

2.4 Kinematics of discontinuous solid-like shell element (DSL_S)

2.4.1 Representation of the displacement field

The discontinuous shell formulation is based on an eight node solid-like shell element. Figure 2.2 shows a solid-like shell element with domain $\Omega^{o,elem}$ in the reference configuration. The element is crossed by a crack surface Γ_c^o , which divides the whole domain into two sub-domains $\Omega_A^{o,elem}$ and $\Omega_B^{o,elem}$ such that $\Omega^{o,elem} = \Omega_A^{o,elem} \cup \Omega_B^{o,elem}$. The superscript *elem* represents a particular element in a finite element mesh crossed by a discontinuity.

Following the method proposed by [58], we replace the cracked element with a pair of elements which are only partially active (figure 2.2) and with the addition of phantom nodes on top of the real nodes. Both elements now contain real nodes (n_i) inherited from the uncracked element as well as phantom nodes (\tilde{n}_i). The real nodes are present in the active domains of the pair of elements, while phantom nodes are present in the non-active domains. The displacement field is continuous over the active domains of each element and discontinuous over Γ_c^o .

Since the two elements do not share any of their nodes, the displacement fields of the two elements are independent of each other and thus incorporates the desired discontinuity in the element.

$$\boldsymbol{\vartheta}(\mathbf{X}) = \begin{cases} \boldsymbol{\vartheta}_A(X) & \forall \mathbf{X} \in \Omega_A^o \\ \boldsymbol{\vartheta}_B(X) & \forall \mathbf{X} \in \Omega_B^o \end{cases} \quad (2.19)$$

Note that the displacement fields of the two elements will only interact through a cohesive law which relates the tractions across the interface to the displacement jump. As the two newly added elements are similar to uncracked shell elements

except from the fact that they will only be integrated over their active domains, we can readily write the displacement field for the pair of elements as:

$$\boldsymbol{\vartheta}_e = \mathbf{u}_e^o + \zeta \mathbf{u}_e^1 + (1 - \zeta^2) \mathbf{u}_e^2 \quad e = A, B \quad (2.20)$$

where the definition of displacement components \mathbf{u}^o , \mathbf{u}^1 and \mathbf{u}^2 as well as the shell's geometry is the same as defined in section 2.3. From the finite element implementation point of view, this results in a simplification, since no special algorithm is required to be written for the computation of strains and other mechanical quantities in the cracked elements. Following the same analogy, the deformation mapping function φ can also be defined independently on both sides of the discontinuity Γ_c^o as φ_A and φ_B , which maps the particles $\mathbf{X} \in \Omega^o$ from reference configuration to current configuration $\mathbf{x} \in \Omega$ and they are continuous in their respective domains.

$$\varphi(\mathbf{X}) = \begin{cases} \varphi_A(\mathbf{X}) & \forall \mathbf{X} \in \Omega_A^o \\ \varphi_B(\mathbf{X}) & \forall \mathbf{X} \in \Omega_B^o \end{cases} \quad (2.21)$$

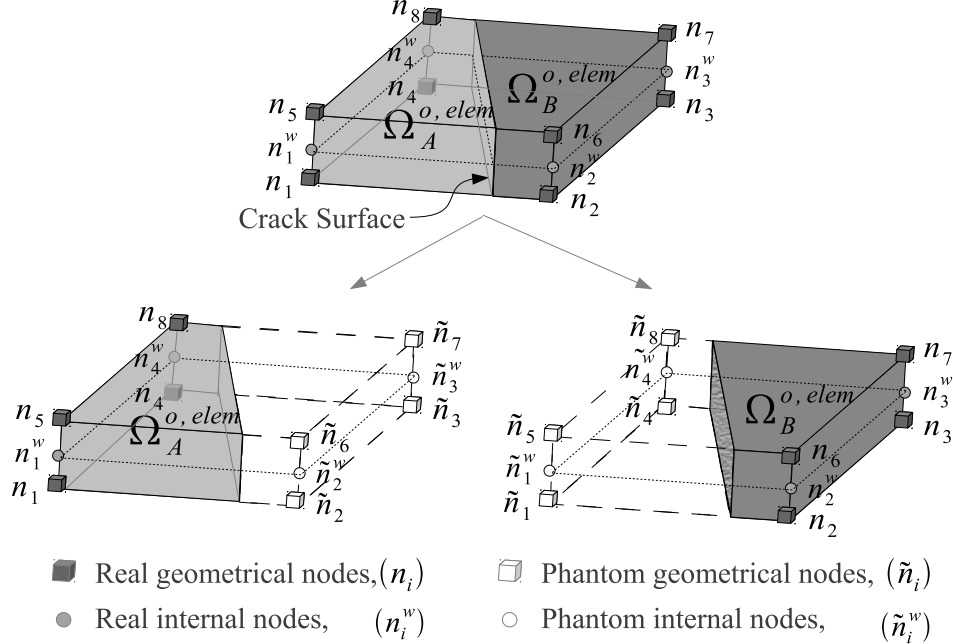


Figure 2.2 An element with domain $\Omega^o = \Omega_A^o \cup \Omega_B^o$ crossed by a discontinuity surface Γ_c^o is replaced with a pair of partially active elements, having real nodes (n_i, n_i^w) and phantom nodes ($\tilde{n}_i, \tilde{n}_i^w$)

Accordingly, the deformation gradient \mathbf{F} can be defined as

$$\mathbf{F} = \begin{cases} \mathbf{F}_A = \nabla_X \varphi_A = g_{i,A} \otimes G^i & \forall \mathbf{X} \in \Omega_A^o \\ \mathbf{F}_B = \nabla_X \varphi_B = g_{i,B} \otimes G^i & \forall \mathbf{X} \in \Omega_B^o \end{cases} \quad (2.22)$$

where the symbol \otimes represents the dyadic product defined as $(\circ \otimes \bullet)_{ij} = (\circ)_i (\bullet)_j$

Alternative representation of displacement field in cracked elements

It is interesting to note that the displacement field in a cracked element can also be written as a summation of the displacement fields of a pair of partially active elements in combination with equation (2.19)

$$\boldsymbol{\vartheta}(\mathbf{X}) = \boldsymbol{\vartheta}_A(\mathbf{X}) + \boldsymbol{\vartheta}_B(\mathbf{X}) \quad (2.23)$$

Since the displacement field of a solid-like shell element is a function of \mathbf{u}_t , \mathbf{u}_b and ω , we can readily write for the cracked element

$$\mathbf{u}_b = \mathbf{u}_{bA} + \mathbf{u}_{bB} \quad (2.24a)$$

$$\mathbf{u}_t = \mathbf{u}_{tA} + \mathbf{u}_{tB} \quad (2.24b)$$

$$\omega = \omega_A + \omega_B \quad (2.24c)$$

This leads to the definitions of the displacement field for the cracked shell element as:

$$\boldsymbol{\vartheta} = \mathbf{u}^o + \zeta \mathbf{u}^1 + (1 - \zeta^2) \mathbf{u}^2 \quad (2.25)$$

where

$$\mathbf{u}^o = \mathbf{u}_A^o + \mathbf{u}_B^o \quad (2.26)$$

$$\mathbf{u}^1 = \mathbf{u}_A^1 + \mathbf{u}_B^1 \quad (2.27)$$

and

$$\mathbf{u}_e^o = \left(\frac{\mathbf{u}_t + \mathbf{u}_b}{2} \right)_e \quad (2.28a)$$

$$\mathbf{u}_e^1 = \left(\frac{\mathbf{u}_t - \mathbf{u}_b}{2} \right)_e \quad e = A, B \quad (2.28b)$$

The internal stretch parameter \mathbf{u}^2 for the cracked element is then defined as:

$$\mathbf{u}^2 = \omega \mathbf{d} \quad (2.29a)$$

$$= (\omega_A + \omega_B)(\mathbf{D} + \mathbf{u}_A^1 + \mathbf{u}_B^1) \quad (2.29b)$$

$$= \omega_A(\mathbf{D} + \mathbf{u}_A^1) + \omega_B(\mathbf{D} + \mathbf{u}_B^1) + \omega_A \mathbf{u}_B^1 + \omega_B \mathbf{u}_A^1 \quad (2.29c)$$

$$= \omega_A \mathbf{d}_A + \omega_B \mathbf{d}_B + \omega_A \mathbf{u}_B^1 + \omega_B \mathbf{u}_A^1 \quad (2.29d)$$

where $\mathbf{d}_e = \mathbf{D} + \mathbf{u}_e^1$. Noting the fact that $\omega_A \mathbf{u}_B^1 = \omega_B \mathbf{u}_A^1 = 0$, the above expression simplifies to

$$\mathbf{u}^2 = \omega_A \mathbf{d}_A + \omega_B \mathbf{d}_B \quad (2.30)$$

It can be observed that the thickness stretch parameter \mathbf{u}^2 can also be expressed as the sum of two independent fields.

$$\mathbf{u}^2 = \mathbf{u}_A^2 + \mathbf{u}_B^2 \quad (2.31)$$

Incorporating equations (2.26), (2.27) and (2.31) in equation (2.25), two independent equations for the displacement fields in a pair of partially active solid-like shell elements are obtained

$$\boldsymbol{\vartheta}_e = \mathbf{u}_e^0 + \zeta \mathbf{u}_e^1 + (1 - \zeta^2) \mathbf{u}_e^2 \quad \forall \mathbf{X} \in \Omega_e^o, \quad e = A, B \quad (2.32)$$

which is similar to the result presented earlier (equation (2.20)).

2.4.2 Strain measure

We use the Green Lagrange strain tensor \mathbf{E} as a suitable strain measure for large deformation problems.

$$\mathbf{E} = \frac{1}{2} (\mathbf{F}^T \mathbf{F} - \mathbf{I}) \quad (2.33)$$

where \mathbf{I} is the second order identity tensor. Since the deformation gradient can also be represented in terms of a covariant base vector in deformed configuration \mathbf{g}_i and a contravariant base vector in reference configuration \mathbf{G}^i , equation (2.22), we can also express the Green Lagrange strain tensor in terms of a contravariant basis \mathbf{G}^i as

$$\mathbf{E}_e = (E_{ij} \mathbf{G}^i \otimes \mathbf{G}^j)_e \quad (2.34)$$

with

$$E_{ij|_e} = \frac{1}{2} (\mathbf{G}_i \cdot \boldsymbol{\vartheta}_{,j} + \mathbf{G}_j \cdot \boldsymbol{\vartheta}_{,i} + \boldsymbol{\vartheta}_{,i} \cdot \boldsymbol{\vartheta}_{,j})_e \quad (2.35)$$

where \mathbf{G}^i is a contravariant base vector in the reference configuration. Note that due to the independent definitions of displacement fields in the pair of elements, the strain fields can also be defined independently in each element. Thus, the model allows for different strain conditions on both sides of the discontinuity, which is essential for modeling phenomena like local buckling, which may occur on only one side of the crack.

Equation (2.35) also requires the gradients of the displacement field for the computation of strains, which are given as:

$$\boldsymbol{\vartheta}_{,\alpha} = \mathbf{u}_{,\alpha}^o + \zeta \mathbf{u}_{,\alpha}^1 \quad \alpha = 1, 2 \quad (2.36a)$$

$$\boldsymbol{\vartheta}_{,3} = \mathbf{u}^1 - 2\zeta \mathbf{u}^2 \quad (2.36b)$$

where \mathbf{u}^2 is considered to be very small as compared to other degrees of freedom, hence its spatial derivatives (i.e $\mathbf{u}_{,\alpha}^2$) are ignored.

It is worth to note that E_{33} is no longer constant along the thickness direction

$$E_{33} = \mathbf{D} \cdot (\mathbf{u}^1 - 2\zeta \mathbf{u}^2) + \frac{1}{2} (\mathbf{u}^1 - 2\zeta \mathbf{u}^2) \cdot (\mathbf{u}^1 - 2\zeta \mathbf{u}^2) \quad (2.37)$$

Furthermore, it is also evident from equation (2.35) that in contrast to [15, 27, 116], higher order terms in ζ are not ignored in our formulation . This includes higher order strain terms in the bending part of the strain tensor. Of course in the limit of thin shells, ($\zeta \ll 1$), the formulation approaches to the element proposed by [116].

As usual in shell theory the strains are referred to the mid-surface of the shell. This is accomplished by the following relationship

$$E_{ab}^o = (\mathbf{G}_a^o \cdot \mathbf{G}^i)(\mathbf{G}_b^o \cdot \mathbf{G}^j)E_{ij} \quad (2.38)$$

In a similar way the strains can then be transferred to the global frame of reference $\mathbf{i}(i_1, i_2, i_3)$ or any local frame of reference, e.g element's local orthonormal coordinate system $\mathbf{l}(l_1, l_2, l_3)$ by

$$E_{ab}^g = (\mathbf{l}_a \cdot \mathbf{G}^{oi})(\mathbf{l}_b \cdot \mathbf{G}^{oj})E_{ij}^o \quad (2.39)$$

Where \mathbf{G}_i^o and \mathbf{G}^{oi} are the covariant and contravariant base vectors computed at the shell mid-surface ,

\mathbf{G}_i and \mathbf{G}^i are the covariant and contravariant base vectors computed at any material point (ξ, η) and

\mathbf{l}_i represents the base vectors of a Cartesian coordinate system, in the element's local coordinate system.

The above equations can be written in compact form as:

$$\mathbf{E}^o = \mathbf{T}^o \mathbf{E} \mathbf{T}^{oT} \quad (2.40a)$$

$$\mathbf{E}^g = \mathbf{T}^g \mathbf{E}^o \mathbf{T}^{gT} \quad (2.40b)$$

where

$$\mathbf{T}^o = \mathbf{G}_i^o \cdot \mathbf{G}^j \quad , \quad \mathbf{T}^g = \mathbf{l}_i \cdot \mathbf{G}^{oj} \quad (2.41)$$

From the finite element point of view, the strain tensor is often represented in Voigt notation, hence equations (2.40a) and (2.40b) are written as

$$\mathbf{E}^o = \mathbb{T}^o \mathbf{E} \quad (2.42a)$$

$$\mathbf{E}^g = \mathbb{T}^g \mathbf{E}^o \quad (2.42b)$$

or simply

$$\mathbf{E}^g = \mathbb{T}^{og} \mathbf{E} \quad (2.43)$$

The corresponding transformation matrices \mathbb{T}^o , \mathbb{T}^g and \mathbb{T}^{og} in Voigt notation are given in B.1.

2.4.3 Representation of a discontinuity

The displacement jump across the discontinuity in the cracked element is given as

$$\begin{aligned} \llbracket \boldsymbol{\vartheta}(\mathbf{X}) \rrbracket &= \boldsymbol{\vartheta}(\mathbf{X}_{\Gamma_c^o} + \boldsymbol{\epsilon}) - \boldsymbol{\vartheta}(\mathbf{X}_{\Gamma_c^o} - \boldsymbol{\epsilon}) \\ &= \boldsymbol{\vartheta}_B(\mathbf{X}) - \boldsymbol{\vartheta}_A(\mathbf{X}) \quad \forall \mathbf{X} \in \Gamma_c^o \end{aligned} \quad (2.44)$$

It is evident from the above equation that the displacement jump across a discontinuity can be obtained by taking simple difference of the displacement fields of the two elements. The displacement jump can also be expressed in terms of a jump in the deformation mapping functions φ as

$$\begin{aligned} \llbracket \boldsymbol{\vartheta}(\mathbf{X}) \rrbracket &= \varphi^B(\mathbf{X}) - \mathbf{X} - \varphi^A(\mathbf{X}) + \mathbf{X} \\ &= \llbracket \varphi \rrbracket \quad \forall \mathbf{X} \in \Gamma_c^o \end{aligned} \quad (2.45)$$

Since the displacement field of a solid-like shell element is a function of \mathbf{u}_t , \mathbf{u}_b and ω , after some manipulations, we can express displacement jump across a discontinuity as

$$\llbracket \boldsymbol{\vartheta} \rrbracket = \llbracket \mathbf{u}^o \rrbracket + \zeta \llbracket \mathbf{u}^1 \rrbracket + (1 - \zeta^2) \llbracket \mathbf{u}^2 \rrbracket \quad (2.46)$$

Note that in the above equation

- The first term, $\llbracket \mathbf{u}^o \rrbracket$, describes the discontinuity in the shell mid-surface,
- The second term, $\llbracket \mathbf{u}^1 \rrbracket$, describes the discontinuity in the rotation vector and gives rise to a discontinuous shell's director defined as $(\mathbf{D} + \llbracket \mathbf{u}^1 \rrbracket)$.
- The third term, $\llbracket \mathbf{u}^2 \rrbracket$, incorporates discontinuity in the stretch parameter

$$\llbracket \mathbf{u}^2 \rrbracket = \llbracket \omega \rrbracket \mathbf{D} + \omega_B \mathbf{u}_B^1 - \omega_A \mathbf{u}_A^1 \quad (2.47)$$

This feature equips the discontinuous shell element to have different thickness stretching on both sides of the crack due to different bending moments.

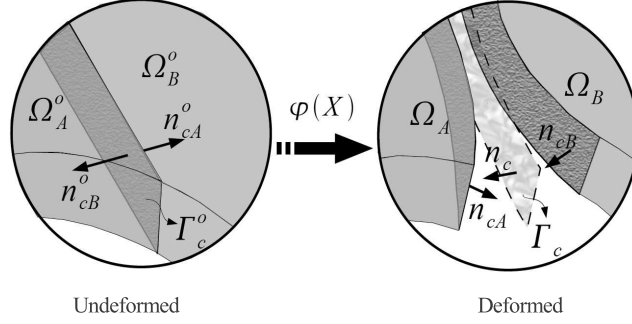


Figure 2.3 Normals to the real crack surface and average crack surface

2.4.4 Average kinematics at the deformed crack surface

As identified by [158], in case of large deformations at the interface, the triads defined on each side of the discontinuity are different, hence no unique normal can be defined in the current configuration (figure 2.3). The normals $(\mathbf{n}_{cA}, \mathbf{n}_{cB})$ on both sides of the discontinuity in the deformed configuration using Nanson's formula are given by

$$\mathbf{n}_{cA} = J_A(\mathbf{F}_A)^{-T} \mathbf{n}_c^o \frac{dA}{da_A} \quad (2.48a)$$

$$\mathbf{n}_{cB} = J_B(\mathbf{F}_B)^{-T} \mathbf{n}_c^o \frac{dA}{da_B} \quad (2.48b)$$

where $\mathbf{n}_{cB}^o = -\mathbf{n}_{cA}^o = \mathbf{n}_c^o$ is an outward normal of Ω_B^o . J_A and J_B are the Jacobians, defined as $J_A = \det(\mathbf{F}_A)$ and $J_B = \det(\mathbf{F}_B)$. dA represents a differential area in the reference configuration while da_A and da_B represent differential areas in the deformed configuration for the crack faces related to domain Ω_A and Ω_B , respectively. Using a heuristic approach, we define an average crack surface Γ_c^o in the current configuration. The average deformation gradient is then defined as

$$\bar{\mathbf{F}} = \frac{1}{2} [\mathbf{F}_A + \mathbf{F}_B] \quad (2.49a)$$

$$= \frac{1}{2} [g_{iA} \otimes G^i + g_{iB} \otimes G^i] \quad (2.49b)$$

$$= \bar{g}_i \otimes G^i \quad (2.49c)$$

in which

$$\bar{g}_i = \frac{1}{2} [g_{iA} + g_{iB}] \quad i = [\xi, \eta, \zeta] \quad (2.50)$$

The normal to an average crack surface can now be defined as:

$$\mathbf{n}_c = \bar{J}(\bar{\mathbf{F}})^{-T} \mathbf{n}_c^o \frac{dA}{\bar{d}a} \quad (2.51)$$

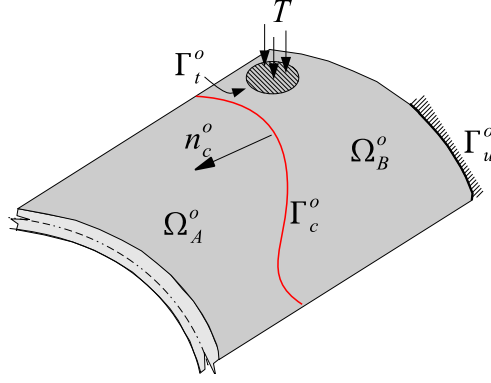


Figure 2.4 Shell body with a crack in reference configuration

where $\bar{J} = \det(\bar{\mathbf{F}})$ and $\bar{d}a = \bar{J} \|\bar{\mathbf{F}}^{-T} \mathbf{n}_c^o\| dA$

2.5 Equilibrium of DSLS

Consider a shell body with domain Ω^o containing an internal surface Γ_c^o , such that it divides the domain into two sub-domains Ω_A^o and Ω_B^o , see figure 2.4.

We start with the strong form of the momentum balance equation in the reference configuration. The static equilibrium of the body in the reference configuration is given as

$$\text{DIV} \mathbf{P} + \hat{\mathbf{b}} = \mathbf{0} \quad \text{in } \Omega^o \setminus \Gamma_c^o \quad (2.52)$$

where \mathbf{P} is the first Piola-Kirchoff stress tensor. $\hat{\mathbf{b}}$ is the body force in the current configuration with respect to reference volume and defined as

$$\hat{\mathbf{b}} = J \mathbf{b} \quad (2.53)$$

where J is Jacobian, $J = \det(\mathbf{F})$ and \mathbf{b} is the body force in the current configuration with respect current volume.

The corresponding boundary conditions of the problem are

$$\mathbf{u} = \bar{\mathbf{u}} \quad \text{at } \Gamma_u^o \quad (2.54)$$

$$\mathbf{P} \cdot \mathbf{n}_t^o = \mathbf{T} \quad \text{at } \Gamma_t^o \quad (2.55)$$

$$\mathbf{P}_B \cdot \mathbf{n}_{cB}^o = \mathbf{T}_{cB} \quad \text{at } \Gamma_c^o \quad (2.56)$$

$$\mathbf{P}_A \cdot \mathbf{n}_{cA}^o = \mathbf{T}_{cA} \quad \text{at } \Gamma_c^o \quad (2.57)$$

Note that equation (2.56) and (2.57) enforce traction continuity across the discontinuity surface Γ_c^o in the reference configuration, where $\mathbf{T}_{cB} = -\mathbf{T}_{cA} = \mathbf{T}_c$ are the

first Piola cohesive tractions acting on the crack surface Γ_c^o and $\mathbf{n}_{cB}^o = -\mathbf{n}_{cA}^o = \mathbf{n}_c^o$, an outward normal of Ω_B^o .

By defining $\delta\boldsymbol{\vartheta}$ as the compatible variation of the displacement field and ignoring the integrands for brevity, the weak form of equilibrium is obtained as

$$\int_{\Omega^o \setminus \Gamma_c^o} \nabla^o \delta\boldsymbol{\vartheta} : \mathbf{P} + \int_{\Gamma_c^o} [[\delta\boldsymbol{\vartheta}]] \cdot \mathbf{T}_c - \int_{\Gamma_c^o} \delta\boldsymbol{\vartheta} \cdot \mathbf{T} - \int_{\Omega^o \setminus \Gamma_c^o} \delta\boldsymbol{\vartheta} \cdot \hat{\mathbf{b}} = \mathbf{0} \quad (2.58)$$

Since the term $\nabla^o \delta\boldsymbol{\vartheta} : \mathbf{P}$ is energetically equivalent to the work-conjugate term $\delta\mathbf{E} : \boldsymbol{\Sigma}$, the above equilibrium equation can be written as

$$\int_{\Omega^o \setminus \Gamma_c^o} \delta\mathbf{E} : \boldsymbol{\Sigma} + \int_{\Gamma_c^o} [[\delta\boldsymbol{\vartheta}]] \cdot \mathbf{T}_c - \int_{\Gamma_c^o} \delta\boldsymbol{\vartheta} \cdot \mathbf{T} - \int_{\Omega^o \setminus \Gamma_c^o} \delta\boldsymbol{\vartheta} \cdot \hat{\mathbf{b}} = \mathbf{0} \quad (2.59)$$

in which $\boldsymbol{\Sigma}$ is the Second Piola-Kirchoff stress tensor. $\delta\mathbf{E}$ is defined as

$$\delta E_{ij} = \frac{1}{2} (\mathbf{G}_i \cdot \delta\boldsymbol{\vartheta}_{,j} + \mathbf{G}_j \cdot \delta\boldsymbol{\vartheta}_{,i} + \delta\boldsymbol{\vartheta}_{,i} \cdot \boldsymbol{\vartheta}_{,j} + \boldsymbol{\vartheta}_{,i} \cdot \delta\boldsymbol{\vartheta}_{,j}) \quad (2.60)$$

in which the higher order term $(\delta\boldsymbol{\vartheta}_{,i} \cdot \delta\boldsymbol{\vartheta}_{,j})$ is considered to be very small and may be neglected, [60, 61, 116]. The variation of the displacement field is given as:

$$\delta\boldsymbol{\vartheta} = \delta\mathbf{u}^o + \zeta\delta\mathbf{u}^1 + (1 - \zeta^2)\delta\mathbf{u}^2 \quad (2.61)$$

The variation of the gradients of the displacement field is given as:

$$\delta\boldsymbol{\vartheta}_{,\alpha} = \delta\mathbf{u}_{,\alpha}^o + \zeta\delta\mathbf{u}_{,\alpha}^1 \quad \alpha = 1, 2 \quad (2.62a)$$

$$\delta\boldsymbol{\vartheta}_{,3} = \delta\mathbf{u}^1 - 2\zeta\delta\mathbf{u}^2 \quad (2.62b)$$

in which the variation of \mathbf{u}^2 yields

$$\delta\mathbf{u}^2 = \delta\omega\mathbf{d} + \omega\delta\mathbf{u}^1 \quad (2.63)$$

The equation (2.59) defines the principle of virtual work. It can also be written in a more compact form as

$$\mathcal{L} = \mathcal{L}^{int} + \mathcal{L}^{coh} - \mathcal{L}^{ext} = \mathbf{0} \quad (2.64)$$

where \mathcal{L}^{int} is the internal virtual work, \mathcal{L}^{ext} is the external virtual work performed by applied loads and \mathcal{L}^{coh} is the virtual work performed by the cohesive tractions on the crack surface Γ_c^o . They are defined as

$$\mathcal{L}^{int} = \int_{\Omega^o \setminus \Gamma_c^o} \delta\mathbf{E} : \boldsymbol{\Sigma} \quad (2.65a)$$

$$\mathcal{L}^{ext} = \int_{\Gamma_c^o} \delta\boldsymbol{\vartheta} \cdot \mathbf{T} + \int_{\Omega^o \setminus \Gamma_c^o} \delta\boldsymbol{\vartheta} \cdot \hat{\mathbf{b}} \quad (2.65b)$$

$$\mathcal{L}^{coh} = \int_{\Gamma_c^o} [[\delta\boldsymbol{\vartheta}]] \cdot \mathbf{T}_c \quad (2.65c)$$

Using the additive property of integrals in combination with equation (2.19) and taking one of the admissible variations $\delta\boldsymbol{\vartheta}_A$ and $\delta\boldsymbol{\vartheta}_B$ at the time, the following two variational statements are obtained

$$\int_{\Omega_A^o} \delta\mathbf{E}_A : \boldsymbol{\Sigma} + \int_{\Gamma_c^o} -\delta\boldsymbol{\vartheta}_A \cdot \mathbf{T}_c - \int_{\Gamma_{t,A}^o} \delta\boldsymbol{\vartheta}_A \cdot \mathbf{T} - \int_{\Omega_A^o} \delta\boldsymbol{\vartheta}_A \cdot \hat{\mathbf{b}} = \mathbf{0} \quad (2.66a)$$

$$\int_{\Omega_B^o} \delta\mathbf{E}_B : \boldsymbol{\Sigma} + \int_{\Gamma_c^o} \delta\boldsymbol{\vartheta}_B \cdot \mathbf{T}_c - \int_{\Gamma_{t,B}^o} \delta\boldsymbol{\vartheta}_B \cdot \mathbf{T} - \int_{\Omega_B^o} \delta\boldsymbol{\vartheta}_B \cdot \hat{\mathbf{b}} = \mathbf{0} \quad (2.66b)$$

Note that in the absence of internal surface Γ_c^o , the two variational statements are similar to the standard variational form for the uncracked domains. Furthermore, in case of traction free cracks, the two equations act independently i.e. there is no interaction between the two domains separated by the crack and hence the equations can be solved independently from each other. The fields of the two domains will only interact when cohesive tractions are active on the cracked surface.

2.6 Linearization of the equilibrium equations

Consistent linearization of a nonlinear system of equations is imperative for a robust and efficient numerical simulation. The nonlinear system of equation is solved using an incremental/iterative procedure according to the Newton Raphson method, which requires computation of a consistent tangent operator. This is obtained by differentiating the equilibrium equation as

$$d\mathcal{L} = d\mathcal{L}^{int} + d\mathcal{L}^{coh} = \mathbf{0} \quad (2.67)$$

where d is a standard symbol for total differentials.

2.6.1 Evaluation of $d\mathcal{L}^{int}$

Using equation (2.65a), we get

$$\begin{aligned} d\mathcal{L}^{int} &= d \int_{\Omega^o \setminus \Gamma_c^o} \delta\mathbf{E} : \boldsymbol{\Sigma} \\ &= \int_{\Omega^o \setminus \Gamma_c^o} (d\boldsymbol{\Sigma} : \delta\mathbf{E} + \boldsymbol{\Sigma} : d(\delta\mathbf{E})) \end{aligned} \quad (2.68)$$

where $\delta \mathbf{E}$ is defined by equation (2.60). The derivative of the variational strain field, $d(\delta \mathbf{E})$, is given as

$$\begin{aligned}
2d(\delta E_{\alpha\beta}) &= [\delta \boldsymbol{\vartheta}_{,\alpha} \cdot d\boldsymbol{\vartheta}_{,\beta} + d\boldsymbol{\vartheta}_{,\alpha} \cdot \delta \boldsymbol{\vartheta}_{,\beta}] \\
&= \partial \mathbf{u}_{,\alpha}^o \cdot d\mathbf{u}_{,\beta}^o + \partial \mathbf{u}_{,\beta}^o \cdot d\mathbf{u}_{,\alpha}^o \\
&+ \zeta (\partial \mathbf{u}_{,\alpha}^o \cdot d\mathbf{u}_{,\beta}^1 + \partial \mathbf{u}_{,\beta}^1 \cdot d\mathbf{u}_{,\alpha}^o + \partial \mathbf{u}_{,\alpha}^1 \cdot d\mathbf{u}_{,\beta}^o + \partial \mathbf{u}_{,\beta}^o \cdot d\mathbf{u}_{,\alpha}^1) \\
&+ \zeta^2 (\partial \mathbf{u}_{,\alpha}^1 \cdot d\mathbf{u}_{,\beta}^1 + \partial \mathbf{u}_{,\beta}^1 \cdot d\mathbf{u}_{,\alpha}^1) \tag{2.69a}
\end{aligned}$$

$$\begin{aligned}
2d(\delta E_{\alpha 3}) &= [\mathbf{G}_\alpha \cdot d(\delta \boldsymbol{\vartheta}_{,3}) + \delta \boldsymbol{\vartheta}_{,\alpha} \cdot d\boldsymbol{\vartheta}_{,3} + d\boldsymbol{\vartheta}_{,\alpha} \cdot \delta \boldsymbol{\vartheta}_{,3} + \boldsymbol{\vartheta}_{,\alpha} \cdot d(\delta \boldsymbol{\vartheta}_{,3})] \\
&= \partial \mathbf{u}^1 \cdot d\mathbf{u}_{,\alpha}^o + \partial \mathbf{u}_{,\alpha}^o \cdot d\mathbf{u}^1 + \zeta (\partial \mathbf{u}_{,\alpha}^1 \cdot d\mathbf{u}^1 + \partial \mathbf{u}^1 \cdot d\mathbf{u}_{,\alpha}^1) \\
&- 2\zeta \mathbf{d} \cdot (\partial \mathbf{u}_{,\alpha}^o d\omega + \partial \omega d\mathbf{u}_{,\alpha}^o) - 2\zeta \omega (\partial \mathbf{u}_{,\alpha}^o \cdot d\mathbf{u}^1 + \partial \mathbf{u}^1 \cdot d\mathbf{u}_{,\alpha}^o) \\
&- 2\zeta^2 \mathbf{d} \cdot (\partial \mathbf{u}_{,\alpha}^1 d\omega + \partial \omega d\mathbf{u}_{,\alpha}^1) - 2\zeta^2 \omega (\partial \mathbf{u}_{,\alpha}^1 \cdot d\mathbf{u}^1 + \partial \mathbf{u}^1 \cdot d\mathbf{u}_{,\alpha}^1) \\
&- 2\zeta \partial \omega (\mathbf{G}_\alpha + \mathbf{u}_{,\alpha}^o + \zeta \mathbf{u}_{,\alpha}^1) \cdot d\mathbf{u}^1 \\
&- 2\zeta \partial \mathbf{u}^1 \cdot (\mathbf{G}_\alpha + \mathbf{u}_{,\alpha}^o + \zeta \mathbf{u}_{,\alpha}^1) d\omega \tag{2.69b}
\end{aligned}$$

$$\begin{aligned}
2d(\delta E_{33}) &= [\mathbf{G}_3 \cdot d(\delta \boldsymbol{\vartheta}_{,3}) + \mathbf{G}_3 \cdot d(\delta \boldsymbol{\vartheta}_{,3}) + d(\delta \boldsymbol{\vartheta}_{,3}) \cdot \boldsymbol{\vartheta}_{,3} \\
&+ \boldsymbol{\vartheta}_{,3} \cdot d(\delta \boldsymbol{\vartheta}_{,3}) + \delta \boldsymbol{\vartheta}_{,3} \cdot d\boldsymbol{\vartheta}_{,3} + d\boldsymbol{\vartheta}_{,3} \cdot \delta \boldsymbol{\vartheta}_{,3}] \\
&= \partial \mathbf{u}^1 \cdot d\mathbf{u}^1 - 4\zeta \mathbf{d} \cdot (\partial \omega d\mathbf{u}^1 + \partial \mathbf{u}^1 d\omega) - 4\zeta \omega \partial \mathbf{u}^1 \cdot d\mathbf{u}^1 \\
&+ 8\zeta^2 \mathbf{u}^2 \cdot (\partial \omega d\mathbf{u}^1 + \partial \mathbf{u}^1 d\omega) + 4\zeta^2 (\mathbf{d} \cdot \mathbf{d}) \partial \omega d\omega \\
&+ 4\zeta^2 \omega^2 \partial \mathbf{u}^1 \cdot d\mathbf{u}^1 \tag{2.69c}
\end{aligned}$$

where $d(\delta \boldsymbol{\vartheta}_{,3})$ is computed by making use of equations (2.62b) and (2.63) as

$$d(\delta \boldsymbol{\vartheta}_{,3}) = -2\zeta [\delta \omega d\mathbf{u}^1 + d\omega \delta \mathbf{u}^1]$$

Next we assume that small changes in $\boldsymbol{\Sigma}$ can be related to small changes in \mathbf{E} through a tangent \mathbb{C}^4 , i.e

$$d\boldsymbol{\Sigma} = \mathbb{C}^4 : d\mathbf{E} \tag{2.70}$$

Incorporating equation (2.70) into (2.68) results in

$$d\mathcal{L}^{int} = \int_{\Omega^o \setminus \Gamma_e^o} (\delta \mathbf{E} : \mathbb{C}^4 : d\mathbf{E} + \boldsymbol{\Sigma} : d(\delta \mathbf{E})) \tag{2.71}$$

We can express the same for an overlapped pair of elements as:

$$d\mathcal{L}_e^{int} = \int_{\Omega_e^o} (\delta \mathbf{E}_e : \mathbb{C}^4 : d\mathbf{E}_e + \boldsymbol{\Sigma}_e : d(\delta \mathbf{E}_e)) \tag{2.72}$$

2.6.2 Evaluation of $d\mathcal{L}^{coh}$

For the linearization of the cohesive part, we strictly follow [54]. Using equation (2.65c), we obtain

$$d\mathcal{L}^{coh} = \int \llbracket \delta \vartheta \rrbracket \cdot d\mathbf{T}_c \quad (2.73)$$

Interface cohesive laws are often given in terms of Cauchy tractions, \mathbf{t}_c . They are related to first Piola tractions \mathbf{T}_c as

$$\mathbf{T}_c = \mathbf{t}_c \lambda_a \quad (2.74)$$

Where λ_a defines the area ratio, $\lambda_a = \bar{d}a/dA$. The incremental change in \mathbf{T}_c is given as

$$d\mathbf{T}_c = d\mathbf{t}_c \lambda_a + \mathbf{t}_c d\lambda_a \quad (2.75)$$

For large deformations at the crack surfaces, the cohesive tractions are function of the displacement jump, $\llbracket \vartheta \rrbracket$ across the interface, Γ_c and a unit normal, \mathbf{n}_c to the average crack surface. Hence, the linearized Cauchy tractions are obtained as

$$d\mathbf{t}_c = \mathbb{C}_{\llbracket u \rrbracket} d\llbracket u \rrbracket + \mathbb{C}_n d\mathbf{n}_c \quad (2.76)$$

where $\mathbb{C}_{\llbracket u \rrbracket}$ and \mathbb{C}_n are the tangent operators defined as $\partial \mathbf{t}_c / \partial \llbracket \vartheta \rrbracket$ and $\partial \mathbf{t}_c / \partial \mathbf{n}_c$, respectively.

The incremental change in deformed average normal is given as, [54]

$$d\mathbf{n}_c = \mathbf{n}_c \otimes \mathbf{n}_c \otimes \mathbf{n}_c \bar{\mathbf{F}}^{-T} - \mathbf{n}_c (\mathbf{I} \boxtimes \bar{\mathbf{F}}^{-T}) : d\bar{\mathbf{F}} \quad (2.77)$$

where the symbol \boxtimes represents the square tensor product defined as $(\circ \boxtimes \bullet)_{ijkl} = (\circ)_{ik} (\bullet)_{jl}$

The change in area ratio is given as, [54]

$$d\lambda_a = \lambda_a (\bar{\mathbf{F}}^{-T} - (\mathbf{n}_c \otimes \mathbf{n}_c) \bar{\mathbf{F}}^{-T}) : d\bar{\mathbf{F}} \quad (2.78)$$

2.7 Finite element discretization

The solid-like shell element considered in this work is an eight-noded solid element. In addition to these geometrical nodes, the element contains four independent internal nodes at the corners of the element mid-surface. The node numbering and geometry of the element are shown in figure 2.2. Each geometrical node i is associated with three degrees of freedom $\mathbf{u}(u_x, u_y, u_z)_i$ and each internal node is associated with one degree of freedom ω_i . Consequently, in total the element has 28 degrees of freedom. For an element e , the displacement vector is arranged as:

$$\hat{\boldsymbol{\vartheta}} = [\hat{\mathbf{u}}_1, \hat{\mathbf{u}}_2, \dots, \hat{\mathbf{u}}_8, \hat{\omega}_1, \dots, \hat{\omega}_4]^T = [\hat{\mathbf{U}}, \hat{\mathbf{W}}]^T \quad (2.79)$$

The nodal quantities are represented with a hat over the quantity. Since the displacement fields \mathbf{u}_t and \mathbf{u}_b are functions of surface coordinates and are constructed only through top or bottom nodes, 2D isoparametric shape functions, $\phi(\xi, \eta)$ are used for the interpolation of the displacement field. Hence, the displacement field at top and bottom surface of an element is given by:

$$\mathbf{u}_{t,e} = \sum_{i=1}^4 \Phi_{i,e} \hat{\mathbf{u}}_{i+4} = \mathbf{\Phi}_e \hat{\mathbf{U}}_{t,e} \quad (2.80a)$$

$$\mathbf{u}_{b,e} = \sum_{i=1}^4 \Phi_{i,e} \hat{\mathbf{u}}_i = \mathbf{\Phi}_e \hat{\mathbf{U}}_{b,e} \quad (2.80b)$$

where $\Phi_i = \phi_i \mathbf{I}$ is the standard shape function matrix for a node i in three directions x,y,z. The element shape functions matrix, $\mathbf{\Phi}_e$ is arranged as:

$$\mathbf{\Phi}_e = [\Phi_1, \Phi_2, \Phi_3, \Phi_4]_e \quad (2.81)$$

The discretized displacement field of a shell mid-surface (\mathbf{u}^o), shell director (\mathbf{u}^1) and internal stretching (\mathbf{u}^2) is then given as as:

$$\mathbf{u}^o = \mathbf{N}^o \hat{\mathbf{U}} = [\mathbf{N}^o]_{3 \times 24} [\hat{\mathbf{U}}]_{24 \times 1} \quad (2.82a)$$

$$\mathbf{u}^1 = \mathbf{N}^1 \hat{\mathbf{U}} = [\mathbf{N}^1]_{3 \times 24} [\hat{\mathbf{U}}]_{24 \times 1} \quad (2.82b)$$

$$\mathbf{u}^2 = \mathbf{d} \mathbf{N}^\omega \hat{\mathbf{W}} = [\mathbf{d}]_{3 \times 1} [\mathbf{N}^\omega]_{1 \times 4} [\hat{\mathbf{W}}]_{4 \times 1} \quad (2.82c)$$

with the interpolation matrices given as

$$\mathbf{N}^o = \frac{1}{2} [\mathbf{\Phi}, \mathbf{\Phi}] \quad (2.83a)$$

$$\mathbf{N}^1 = \frac{1}{2} [-\mathbf{\Phi}, \mathbf{\Phi}] \quad (2.83b)$$

$$\mathbf{N}^\omega = [\phi_1, \phi_2, \phi_3, \phi_4] \quad (2.83c)$$

Further, the spatial derivatives of the displacement fields and their variations are obtained as:

$$\mathbf{u}_{,\alpha}^o = \mathbf{N}_{,\alpha}^o \hat{\mathbf{U}} \quad , \quad \delta \mathbf{u}_{,\alpha}^o = \mathbf{N}_{,\alpha}^o \delta \hat{\mathbf{U}} \quad (2.84a)$$

$$\mathbf{u}_{,\alpha}^1 = \mathbf{N}_{,\alpha}^1 \hat{\mathbf{U}} \quad , \quad \delta \mathbf{u}_{,\alpha}^1 = \mathbf{N}_{,\alpha}^1 \delta \hat{\mathbf{U}} \quad (2.84b)$$

2.7.1 Discretization of variational fields

To discretize the variational equilibrium, equation (2.66), we are also required to evaluate the discretized variational fields, $\delta \mathbf{E}$ and $\delta \vartheta$.

We begin with defining the vector of virtual strain components as

$$[\delta \mathbf{E}]_{6 \times 1} = \{\delta E_{11}, \delta E_{22}, \delta E_{33}, 2\delta E_{12}, 2\delta E_{23}, 2\delta E_{13}\} \quad (2.85)$$

The vector of virtual strains is related to nodal displacement vector through a gradient operator matrix \mathbf{B}

$$[\delta \mathbf{E}]_{6 \times 1} = [\mathbf{B}_L + \mathbf{B}_{NL}]_{6 \times 28} [\delta \hat{\boldsymbol{\vartheta}}]_{28 \times 1} = [\mathbf{B}]_{6 \times 28} [\delta \hat{\boldsymbol{\vartheta}}]_{28 \times 1} \quad (2.86)$$

with \mathbf{B}_L and \mathbf{B}_{NL} are defined in B.2. The matrix \mathbf{B} refers to the quantities in the covariant coordinate description. A matrix \mathbb{T}^{og} must be used to transform it to the element's local coordinate system \mathbf{l} , equation (2.43).

The discrete form of the variation of the compatible displacement field for the solid-like shell element is given as

$$\delta \boldsymbol{\vartheta}_A(\mathbf{X}) = \mathbf{N}_A^I(\mathbf{X}) \delta \hat{\boldsymbol{\vartheta}}_A^I = [\mathbf{N}_A]_{3 \times 28} [\delta \hat{\boldsymbol{\vartheta}}_A]_{28 \times 1} \quad \forall \mathbf{X} \in \Omega_A^o \quad (2.87a)$$

$$\delta \boldsymbol{\vartheta}_B(\mathbf{X}) = \mathbf{N}_B^I(\mathbf{X}) \delta \hat{\boldsymbol{\vartheta}}_B^I = [\mathbf{N}_B]_{3 \times 28} [\delta \hat{\boldsymbol{\vartheta}}_B]_{28 \times 1} \quad \forall \mathbf{X} \in \Omega_B^o \quad (2.87b)$$

The matrix \mathbf{N}_e is given as

$$[\mathbf{N}_e] = [\mathbf{N}_e^o + \zeta \mathbf{N}_e^1 + (1 - \zeta^2) \omega_e \mathbf{N}_e^1 \quad (1 - \zeta^2) \mathbf{d}_e \mathbf{N}_e^\omega] \quad (2.88)$$

where higher order terms in ζ are also included.

Moreover, since the load can only be applied on the geometrical nodes [116], we define a modified variational field $\delta \boldsymbol{\vartheta}^*$, which will replace the variational terms corresponding to external load parts of the variational equilibrium equation. The modified variational field is defined as

$$\delta \boldsymbol{\vartheta}^* = \mathbf{u}^o + \zeta \mathbf{u}^1 \quad (2.89)$$

The corresponding discretized form of the modified variational field is given as

$$\delta \boldsymbol{\vartheta}_A^*(\mathbf{X}) = \mathbf{N}_A^{*I}(\mathbf{X}) \delta \hat{\mathbf{u}}_A^I = [\mathbf{N}_A^*]_{3 \times 24} [\delta \hat{\mathbf{U}}_A]_{24 \times 1} \quad \forall \mathbf{X} \in \Omega_A^o \quad (2.90a)$$

$$\delta \boldsymbol{\vartheta}_B^*(\mathbf{X}) = \mathbf{N}_B^{*I}(\mathbf{X}) \delta \hat{\mathbf{u}}_B^I = [\mathbf{N}_B^*]_{3 \times 24} [\delta \hat{\mathbf{U}}_B]_{24 \times 1} \quad \forall \mathbf{X} \in \Omega_B^o \quad (2.90b)$$

where the matrix \mathbf{N}_e^* is defined as

$$\mathbf{N}_e^* = \mathbf{N}_e^o + \zeta \mathbf{N}_e^1 \quad (2.91)$$

Note that, in this work it is assumed that phantom nodes do not carry external loads.

Incorporating the variations in the variational equations (2.66), we obtain

$$\int_{\Omega_A^o} (B_A)^T \boldsymbol{\Sigma} + \int_{\Gamma_c^o} (-N_A)^T \mathbf{T}_c - \int_{\Gamma_{t,A}^o} (N_A^*)^T \mathbf{T} - \int_{\Omega_A^o} (N_A^*)^T \hat{\mathbf{b}} = \mathbf{0} \quad (2.92a)$$

$$\int_{\Omega_B^o} (B_B)^T \boldsymbol{\Sigma} + \int_{\Gamma_c^o} (N_B)^T \mathbf{T}_c - \int_{\Gamma_{t,B}^o} (N_B^*)^T \mathbf{T} - \int_{\Omega_B^o} (N_B^*)^T \hat{\mathbf{b}} = \mathbf{0} \quad (2.92b)$$

or in more compact form

$$f_{int_e} + f_{coh_e} - f_{ext_e} = 0 \quad (2.93)$$

where

$$f_{int_e} = \int_{\Omega_e^o} (B_e)^T \boldsymbol{\Sigma} \quad (2.94a)$$

$$f_{ext_e} = \int_{\Gamma_{t,e}^o} (N_e^*)^T \mathbf{T} + \int_{\Omega_e^o} (N_e^*)^T \mathbf{b} \quad (2.94b)$$

$$f_{coh_e} = \beta_e \int_{\Gamma_c^o} (N_e)^T \mathbf{T}_c \quad (2.94c)$$

in which

$$\beta_e = \begin{cases} -1 & \text{for } e = A \\ 1 & \text{for } e = B \end{cases} \quad (2.95)$$

2.7.2 Linearization of the discretized equations

Using standard notions, we note that the linearized equilibrium equation (2.67) for an element e can also be expressed as

$$d\mathcal{L}_e = \delta \boldsymbol{\vartheta}_e^T \frac{\partial \boldsymbol{\mathfrak{R}}_e}{\partial \boldsymbol{\vartheta}_e} d\boldsymbol{\vartheta}_e = \delta \boldsymbol{\vartheta}_e^T \mathbf{K}_{t_e} d\boldsymbol{\vartheta}_e \quad (2.96)$$

where $\boldsymbol{\mathfrak{R}}_e$ is the residual force vector defined as:

$$\boldsymbol{\mathfrak{R}}_e = \mathbf{f}_{int_e} + \mathbf{f}_{coh_e} - \mathbf{f}_{ext_e} \quad (2.97)$$

It follows from equations (2.96) and (2.97) that

$$d\mathcal{L}_e = \delta \boldsymbol{\vartheta}_e^T \left(\frac{\partial \mathbf{f}_{int_e}}{\partial \boldsymbol{\vartheta}_e} + \frac{\partial \mathbf{f}_{coh_e}}{\partial \boldsymbol{\vartheta}_e} \right) d\boldsymbol{\vartheta}_e = \delta \boldsymbol{\vartheta}_e^T (\mathbf{K}_{t,int_e} + \mathbf{K}_{t,coh_e}) d\boldsymbol{\vartheta}_e \quad (2.98)$$

For problems involving large deformations/large strains, both the stresses and geometric matrix B depend on displacements, hence the tangent stiffness matrix will have two contributions, the so-called material stiffness and geometric stiffness. In addition to this, for cohesive laws that depend on a displacement jump and a normal to the discontinuity, the stiffness contribution from both, will also consist of two parts, the material part which comes from the relation between tractions and jump, and the geometric part which comes from changes in normal and surface area of the discontinuity surface. Therefore we can now write

$$\mathbf{K}_{t_e} = (\mathbf{K}_{mat,int_e} + \mathbf{K}_{mat,coh_e}) + (\mathbf{K}_{geo,int_e} + \mathbf{K}_{geo,coh_e}) \quad (2.99)$$

$$\delta \boldsymbol{\vartheta}_e^T \left(\int_{\Omega_e^o} (B_e)^T \mathbb{C} B_e \right) d\boldsymbol{\vartheta}_e = \delta \boldsymbol{\vartheta}_e^T (\mathbf{K}_{mat,int_e}) d\boldsymbol{\vartheta}_e \quad (2.100)$$

$$\int_{\Omega_e^o} (\boldsymbol{\Sigma}_e : d(\delta \mathbf{E}_e)) = \delta \boldsymbol{\vartheta}_e^T (\mathbf{K}_{geo,int_e}) d\boldsymbol{\vartheta}_e \quad (2.101)$$

As said earlier, the displacement field of the pair of elements (A and B) will interact in the presence of tractions on the crack surfaces due to the coupling of \mathbf{f}_{coh_A} with $\boldsymbol{\vartheta}_A$ and vice versa, via tractions $\mathbf{t}_c([\![\vartheta]\!] , \mathbf{n}_c)$. The cohesive tangent matrix will also involve coupling terms and the total contribution to the global stiffness matrix is given as

$$\delta \boldsymbol{\vartheta}_{A \cup B}^T \int_{\Gamma_c^o} (N_B - N_A)^T d\mathbf{T}_c = \delta \boldsymbol{\vartheta}_{A \cup B}^T (\mathbf{K}_{coh}) d\boldsymbol{\vartheta}_{A \cup B} \quad (2.102)$$

where the matrix $\mathbf{K}_{coh} = \mathbf{K}_{mat,coh} + \mathbf{K}_{geo,coh}$, is defined as

$$\mathbf{K}_c = \begin{bmatrix} \mathbf{K}_{coh_{AA}} & \mathbf{K}_{coh_{AB}} \\ \mathbf{K}_{coh_{BA}} & \mathbf{K}_{coh_{BB}} \end{bmatrix} \quad (2.103)$$

Further details of matrix \mathbf{K}_{coh} and \mathbf{K}_{geo,int_e} are given in B.3. The discretized system of equilibrium equations can be written in a matrix form as

$$\begin{bmatrix} \mathbf{K}_{t_e} \end{bmatrix} \begin{bmatrix} \Delta(\delta \hat{\boldsymbol{\vartheta}}_e) \end{bmatrix} = \begin{bmatrix} \boldsymbol{\mathfrak{R}}_e \end{bmatrix} \quad (2.104)$$

$$\begin{bmatrix} \mathbf{K}_{t_e}^{uu} & \mathbf{K}_{t_e}^{u\omega} \\ \mathbf{K}_{t_e}^{\omega u} & \mathbf{K}_{t_e}^{\omega\omega} \end{bmatrix} \begin{bmatrix} \Delta(\delta \hat{\mathbf{U}}_e) \\ \Delta(\delta \hat{\boldsymbol{\omega}}_e) \end{bmatrix} = \begin{bmatrix} \boldsymbol{\mathfrak{R}}_e^u \\ \boldsymbol{\mathfrak{R}}_e^\omega \end{bmatrix} \quad (2.105)$$

Remark 1. Since internal degrees of freedom ($\hat{\boldsymbol{\omega}}_e$) are not supporting external loads, they can be eliminated at element level using the static condensation method, similar to [116, 125]. The reduced system of equations, with standard degrees of freedom ($\hat{\mathbf{U}}_e$) as primary unknowns, can be written as

$$\tilde{\mathbf{K}}_{t_e}^{uu} \Delta(\delta \hat{\mathbf{U}}_e) = \tilde{\boldsymbol{\mathfrak{R}}}_e^u \quad (2.106)$$

The condensed stiffness matrix ($\tilde{\mathbf{K}}_{t_e}^{uu}$) and residual vector ($\tilde{\boldsymbol{\mathfrak{R}}}_e^u$) are given as

$$\tilde{\mathbf{K}}_{t_e}^{uu} = \mathbf{K}_{t_e}^{uu} - \mathbf{K}_{t_e}^{u\omega} (\mathbf{K}_{t_e}^{\omega\omega})^{-1} \mathbf{K}_{t_e}^{\omega u} \quad (2.107)$$

$$\tilde{\boldsymbol{\mathfrak{R}}}_e^u = \boldsymbol{\mathfrak{R}}_e^u + \mathbf{K}_{t_e}^{u\omega} (\mathbf{K}_{t_e}^{\omega\omega})^{-1} \boldsymbol{\mathfrak{R}}_e^\omega \quad (2.108)$$

However, such a condensed stiffness matrix becomes ill-conditioned for the case in which the crack cuts the two adjacent edges of an element, figure 2.5. Therefore, internal degrees of freedom are not condensed out at element level and the full system of equations (equation 2.105) is used in this work.

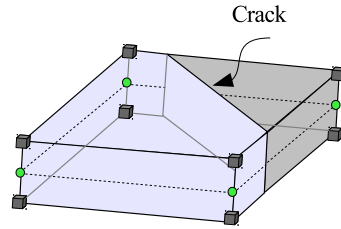


Figure 2.5 Two adjacent edges of an element cut by a crack

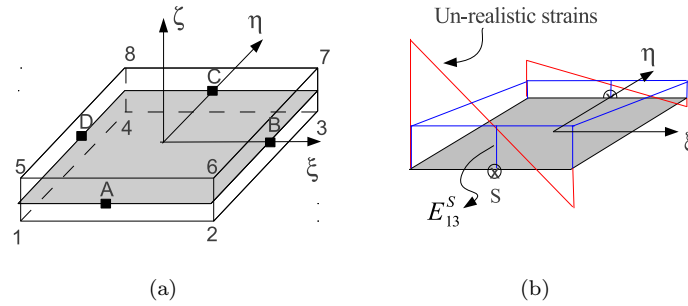


Figure 2.6 Un-realistic transverse shear strains due to bending deformations

2.8 Assumed natural strains

To avoid transverse shear locking in the eight noded solid-like shell element, an assumed natural strain (ANS) method proposed by [50] is used. Since the strain field of the solid-like shell element has contribution from standard degrees of freedom (dofs) as well as from internal degrees of freedom, the implementation of ANS to solid-like shell element demands care. Locking occurs, if only strain terms corresponding to standard dofs are modified with ANS method. This is demonstrated in detail through example 2.9.1.

Using the method proposed by [50], the transverse shearing strains computed at sampling points, $S = \{A, B, C, D\}$, are linearly interpolated over the domain of the shell element, see figure 2.6.

For simplicity of implementation, we assume a constant shear strain distribution along the thickness for this contribution, which is a reasonable assumption for a thin shell structure [83].

The interpolated strains are given as

$$E_{13} = \chi_A E_{13}^A + \chi_C E_{13}^C \quad (2.109)$$

$$E_{23} = \chi_B E_{23}^B + \chi_D E_{23}^D \quad (2.110)$$

where $E_{\alpha 3}^S$ represents the strain component at node S and $\chi_A, \chi_B, \chi_C, \chi_D$ are interpolation functions defined as

$$\begin{aligned} \chi_A &= \frac{1}{2}(1 - \eta), & \chi_C &= \frac{1}{2}(1 + \eta) \\ \chi_B &= \frac{1}{2}(1 - \xi), & \chi_D &= \frac{1}{2}(1 + \xi) \end{aligned} \quad (2.111)$$

The virtual shear strain at the node S is then computed as

$$\delta E_{13} = (\chi_A B_{13}^A + \chi_C B_{13}^C) \delta \hat{\boldsymbol{\nu}} \quad (2.112)$$

$$\delta E_{23} = (\chi_B B_{23}^B + \chi_D B_{23}^D) \delta \hat{\boldsymbol{\nu}} \quad (2.113)$$

or simplifying it, we may write

$$\delta E_{\alpha 3} = B^{ANS} \delta \hat{\boldsymbol{\nu}} \quad (2.114)$$

where

$$[B^{ANS}] = \begin{bmatrix} \chi_A B_{13}^A + \chi_C B_{13}^C \\ \chi_B B_{23}^B + \chi_D B_{23}^D \end{bmatrix} \quad (2.115)$$

in which the row vector $B_{\alpha 3}^S$ is computed using equation (B.11) with local coordinates of sampling points S . Note that for the matrices H and A (equations (B.9), (B.10)), only the rows that corresponds to the strain components $E_{\alpha 3}$, need to be evaluated. The matrix B^{ANS} thus obtained will replace the rows corresponding to strain components E_{13} and E_{23} in the original B matrix (equation (2.86)). It should be noted that in order to have a completely locking free element, the terms of the B matrix corresponding to internal degrees of freedom are also be modified with ANS. As a consequence, the complete row of the B matrix corresponding to shear strain terms $E_{\alpha 3}$, including contributions from the standard and internal degrees of freedom is replaced with B^{ANS} .

2.9 Numerical examples

Several numerical simulations are performed to demonstrate the performance of the element. The first example demonstrates the necessity of applying ANS correction to shear strain terms coming from internal dofs. The second example demonstrates several features of cracked body mechanics under large deformations. Next, a series

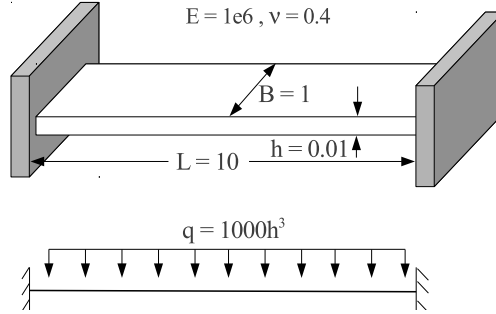


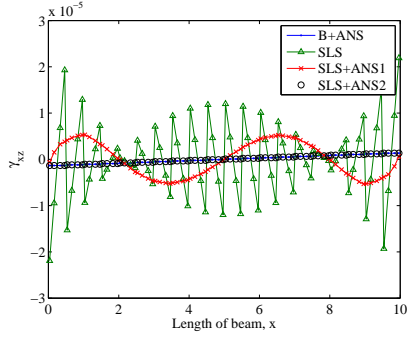
Figure 2.7 Fixed Beam: Model geometry and material properties

of examples are presented, where in addition to simultaneous modeling of physical and geometrical nonlinearities, attention is focused on the role and significance of the discontinuous mid-surface, director and thickness stretch field of the newly developed element. The significance of each term appearing in the displacement jump field (equation (2.46)) is illustrated separately in each example. Finally, a cohesive crack growth analysis of a semi-cylinder subjected to large displacements and rotations is presented.

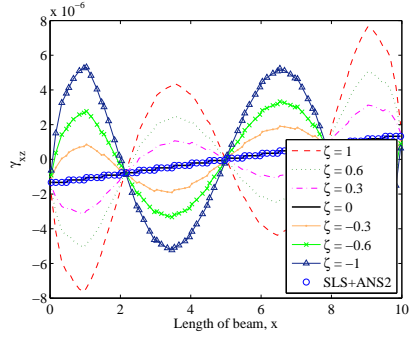
2.9.1 Uniformly loaded fixed beam – Coupling between normal strains and shear strains

In this numerical example, it is demonstrated that locking occurs, if only strain terms corresponding to standard dofs are replaced with ANS methodology. The geometry and material properties of the model problem are shown in figure 2.7. A finite element mesh of $20 \times 1 \times 1$ solid-like shell elements is used for analysis.

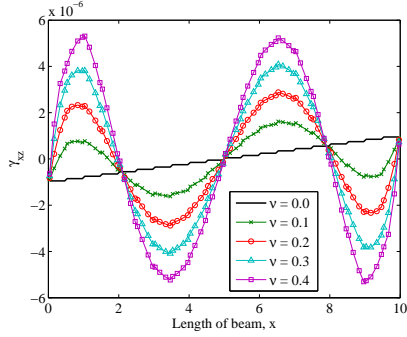
Figure 2.8a shows the variation of transverse shear strains along the length of a fixed beam subjected to uniform loading, in the outermost fibers. The beam is analyzed using four different elements, namely the standard volume element with ANS improvement denoted as B+ANS, the solid-like shell element without ANS improvement, denoted as SLS, the solid-like shell element with ANS improvement to the strain terms corresponding to the dofs of geometrical nodes denoted as SLS+ANS1 and the solid-like shell element with ANS improvement to all dofs denoted as SLS+ANS2. It can be seen from figure 2.8a, that only improving the strain terms corresponding to the standard dofs did not remove the unrealistic oscillations. Figure 2.8b shows the strain variation along the length of the beam for element SLS+ANS1 in comparison with element SLS+ANS2 at different depths. It can be observed that for element SLS+ANS1 the oscillations increase with increasing ζ



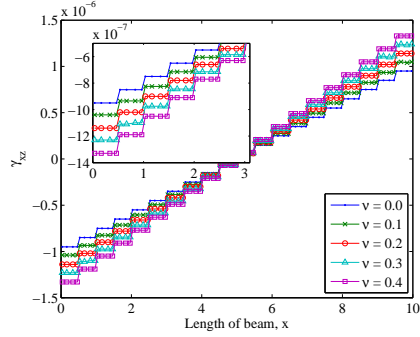
(a) Comparison of strain profiles of different elements



(b) Strain profiles with element SLS+ANS1



(c) Strain profiles with element SLS+ANS1



(d) Strain profiles with element SLS+ANS2

Figure 2.8 Un-realistic transverse shear strains due to internal stretch field

while element SLS+ANS2 shows the same strain profile at all depths without oscillations. The oscillations in the strain profile for element SLS+ANS1 are due to the coupling between transverse shear strains and normal strains and more specifically the components of normal strain due to internal stretch. At $\zeta = 0$ the internal stretch variable vanishes in equation (2.37), and no oscillations are observed. These oscillations also increase with increasing Poisson ratio, figure 2.8c. These evidences clearly suggest that locking is not completely removed by only modifying the strain terms coming from the standard dofs. A locking free element will be obtained when strain terms coming from both the standard as well internal dofs will be modified using ANS methodology. This requires simply the replacement of the whole row of B matrix corresponding to strain terms E_{13} and E_{23} with the B^{ANS} matrix. Figure 2.8d shows the strain profiles using element SLS+ANS2 which is obtained by modifying the strain terms coming from the standard as well as the internal dofs using ANS for different Poisson ratio. It is concluded from figures 2.8a,b,d that the

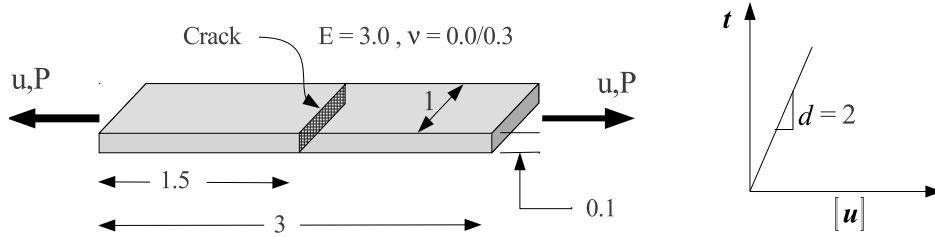


Figure 2.9 One dimensional cracked strip geometry and material model

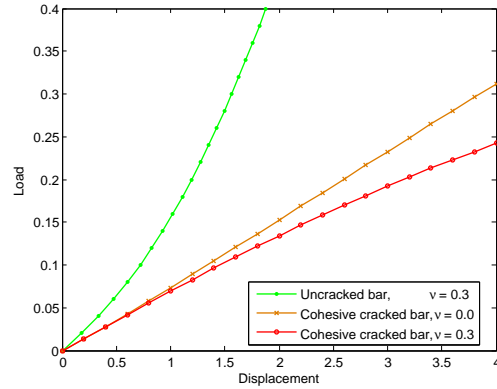


Figure 2.10 Comparison of load displacement curves of cohesively cracked strip with different Poisson ratio

element SLS+ANS2 is optimal.

2.9.2 Uni-axial cohesive cracked bar under large deformations

The process of cracking may involve large displacements at the interface. For example, the process of fibrillation in polymers involves large displacements at the interface as well as large deformation in the bulk material. In order to understand the mechanics and behaviors of cracked bodies under large deformations, we simulate a simple academic example of a uni-axial tension bar with an elastic discontinuity at its mid length. The geometry and material properties of the bar and crack are given in figure 2.9. A finite element mesh of 3 solid-like shell elements is used. The problem is analyzed with two different Poisson ratios, i.e $\nu = 0.0$ and $\nu = 0.3$.

Figure 2.10 compares the global load displacement curves for an uncracked strip and cohesively cracked strip with $\nu = 0.0$ and $\nu = 0.3$. The first observation is, that

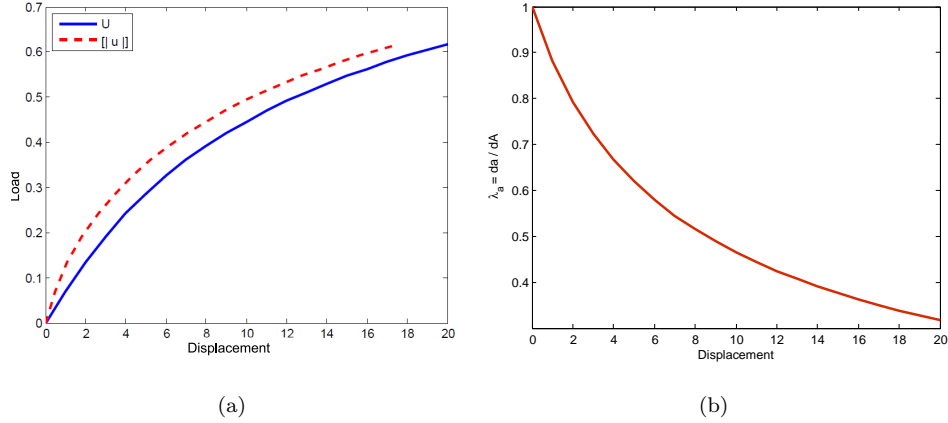


Figure 2.11 Geometrically non-linear analysis results of cohesively cracked strip with $\nu = 0.3$, (a) Global load-displacement curves (b) Evolution of area ratio λ_a with increasing deformations

the inclusion of a crack resulted in stress relaxation of the bulk material for both the cases ($\nu = 0.0$ and $\nu = 0.3$). This can be explained from figure 2.11a, which shows variation of global displacement (u) and displacement jump ($[[u]]$) with the applied load. It is observed that with increasing load level, the contribution to the global displacement from the cohesive zone is dominant, while the contribution from the bulk is nearly constant and not so significant. This is due to the fact that, at large deformations the bulk material experiences a stress stiffening effect. In such cases, the work done by the external loads over a body will be utilized in the crack opening. Thus, with increasing load level the bulk material will become stiffer and in contrast, the crack widens more, such that the contribution from the cohesive interface to the total displacement of the body dominates the solution. In other words, the rate of crack opening increases with increasing load in large deformation problems. Consequently, this will result in a more significant softening response of the structure.

Next, if we look at the response of cracked strips, it can be observed that, at smaller deformations the response of both cracked strips (with $\nu = 0.0$ and $\nu = 0.3$) is approximately the same and the load displacement curve for the cracked strip with non zero Poisson ratio shows a double curvature. The slope of the curve initially increases with the increase in load level in a concave up shape. After a certain stage, the increasing slope of the curve starts gradually to decrease. The graph shows a concave down shape and the load displacement response shows much softer behavior compared to the cracked strip with zero Poisson ratio. This increased rate of crack opening is due to the changes in crack surface area and results in a much faster unloading of the bulk material.

At smaller deformations, since the deformed area is approximately equal to the undeformed area, ($da \geq 0.95dA$, figure 2.11b), the response is similar to the response of a strip with zero Poisson ratio and does not cause a significant reduction of the stiffness of the material. As the deformation increases, the deformed area of the crack surface becomes smaller and smaller compared to the crack surface area in undeformed configuration. Consequently, the elemental force vector, $\mathbf{df} = \mathbf{t}_n da$, acting on the differential crack surface area da , which is keeping the two surfaces intact, also decreases. This decrease in the differential force on that area means a reduced cohesive stiffness and more crack opening displacement, which consequently results in a faster decrease in load carrying capacity of the structure compared to the case with zero Poisson ratio, figure 2.10.

It is worth to note, that using partition of unity method for modeling crack propagation problems, where such interfaces are defined within the continuum element as their integral parts, automatically takes into account the thickness changes in the crack surfaces due to changes in the element's volume as a consequence of Poisson effect. Thus, avoids the need of continuous and complicated thickness update of the crack surfaces which otherwise is required to be performed when using interface elements, see for example [95].

2.9.3 Symmetric and anti-symmetric buckling of a cracked strip

In this section we present a series of numerical tests of academic nature to demonstrate the performance of the newly developed discontinuous solid-like shell element and the significance of different jump terms appearing in equation (2.46). A thin strip with a pre-crack, running throughout its length, and subjected to a compressive load is considered. The strip is clamped at one of the ends while its other end is hinged. The material properties used for the analysis are: Young's modulus, $E = 100\text{N/mm}^2$ and Poisson ratio, $\nu = 0.0$. The model geometry and boundary conditions are shown in figure 2.12. All dimensions are in mm.

The performance of the element is investigated for the case of combined cracking and geometrical stability. For this purpose two different buckling modes are simulated: Case I, symmetric buckling and Case II, anti-symmetric buckling. Case I, is simulated to see the effect of interaction between two different features of nonlinearities, i.e. physical and geometrical nonlinearities. Since the buckling mode is symmetric, it is anticipated that the response of such a strip even in the presence of a crack should be similar to a response of uncracked strip of the same geometry and material properties and the crack should not influence the response of the strip. Case II simulates the anti-symmetric mode. This will result in a discontinuous mid-surface and a director field of the shell and hence will trigger the terms $\llbracket \mathbf{u}^o \rrbracket$ and $\llbracket \mathbf{u}^1 \rrbracket$ of equation (2.46).

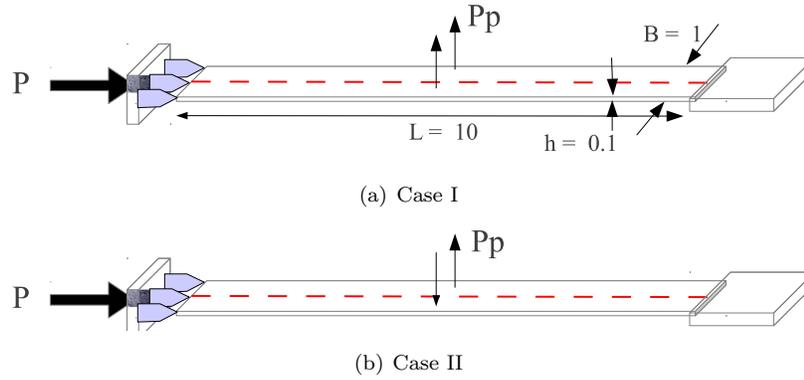


Figure 2.12 Buckling strip models (All dimensions are in mm)

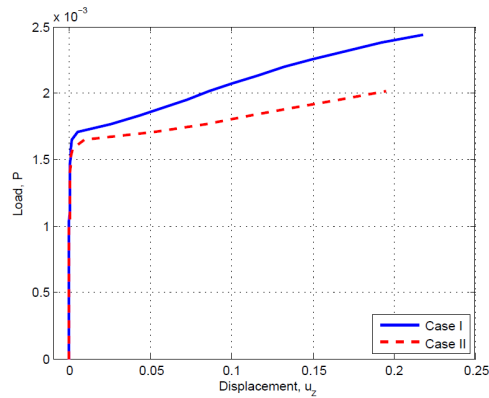


Figure 2.13 Load deformation curves

In order to trigger the desired buckling mode a perturbation force, $P_p = 1.7e-7N$ is applied at the mid-length of the strip. The critical Euler buckling load for this problem is, $P_{cr} = 0.0016835N$. Figure 2.13 shows the load vs mid-span deflection curve of the strip for the two cases. Figure 2.14 shows the corresponding deformed shapes of the buckled strip for the two cases. Note that the deformations are not scaled in the figure.

It is evident from figure 2.13, that in both cases the Euler critical buckling load is predicted very well and the presence of a crack in Case I, did not influence the response of the strip. For case II, it can be observed (figure 2.14b) that the shell surface on one side of the crack, near the crack tip is rotated approximately 90° compared with the shell surface on the other side of the crack, or in other words the

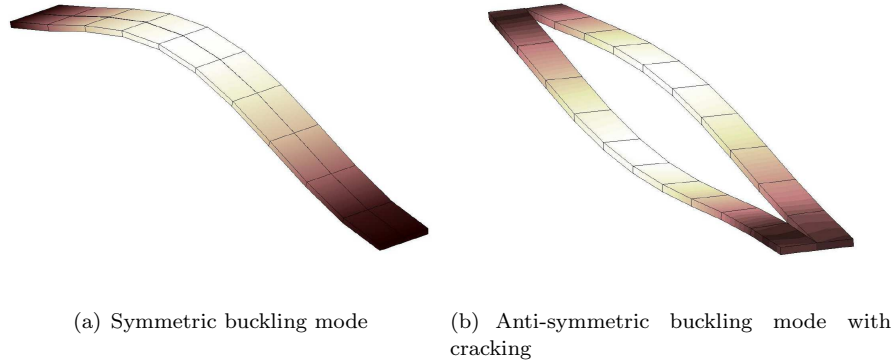


Figure 2.14 Buckling strip deformed shapes

shell director on one side of the crack is rotated approximately 90° compared with the shell director on the other side of the crack. This resulted in a strong discontinuity in the shell director field and has been modeled accurately by the element.

2.9.4 Cracked rectangular plate

Thin shell structures are often prone to local buckling near geometrical defects such as cracks. This situation may result in inhomogeneous bending on both sides of the crack, where one side may experience significantly more bending than the other side. From the computational modeling point of view, such conditions result in a discontinuous mid-surface and director field of a shell finite element. In addition to this, since the shell domains on both sides of the crack are experiencing different bending deformations, the two sides will experience different stretching in the shell thickness direction with non-zero Poisson ratio. This thickness change is captured in solid-like shell element through the internal stretch parameter, ω . The inhomogeneous bending on both sides of the crack will result in a discontinuous stretch. In our formulation this is taken care of by the jump term $[[\omega]]$ in equation (2.46), which incorporates the desired discontinuity in the stretch field over the domain and gives locking free (Poisson thickness locking) behavior for inhomogeneous stretching on both sides of the crack.

To demonstrate the ability of the developed discontinuous shell element for modeling inhomogeneous stretching, a clamped plate strip with a central traction free crack is analyzed. The crack extends over the whole length of the plate strip. The model geometry and boundary conditions are shown in figure 2.15. The plate is subjected to an axial compressive loading on one side of the crack. In order to simulate a buckling response, we also applied a small perturbation load, $P_p = 1.75e-3$ on

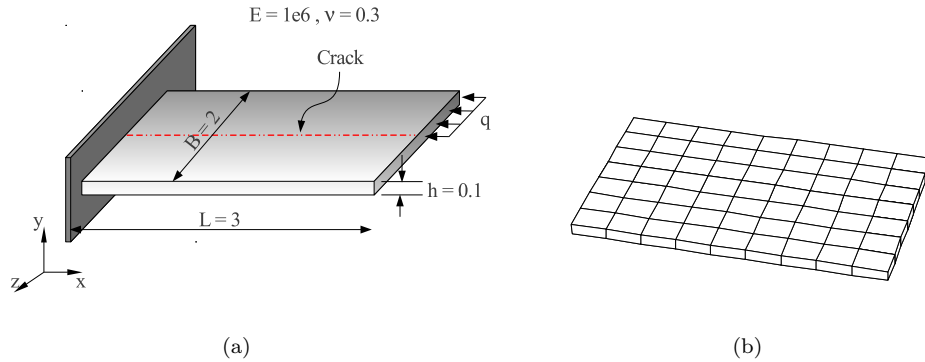
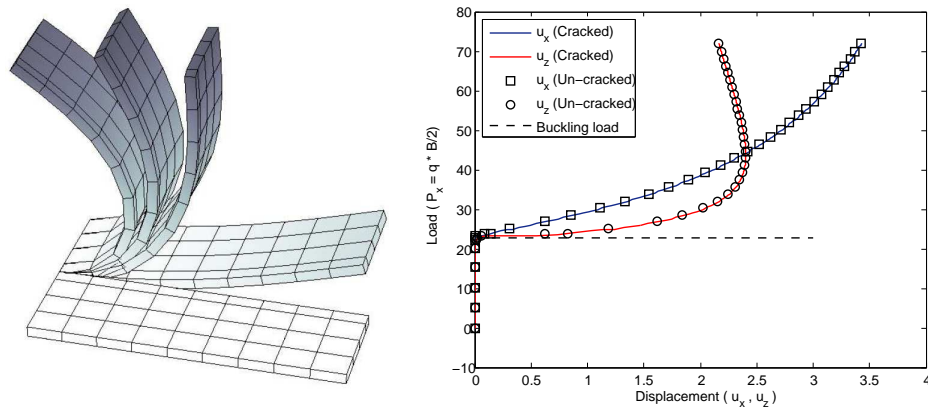


Figure 2.15 Cracked plate model and finite element mesh



(a) Deformed shapes at $P_x = 23.5, 36, 48$ (b) Load vs Deformation curves of cracked plate compared with uncracked plate of width, $B/2$, 72

Figure 2.16 Cracked plate analysis results

the loaded edge in y direction. The critical Euler buckling load for this problem is, $P_{cr} = 22.8456$.

Figure 2.16a shows various deformed configurations under axial compression. It can be observed, that on reaching the critical buckling load level, one side of the plate buckles and shows large bending deformation, while the other half of the plate shows no deformation. The un-deformed side of the plate will not experience internal stretching while the deformed side of the plate will show internal stretching due to bending with $\nu \neq 0$, i.e the bending deformation with $\nu \neq 0$ will cause the mid-surface

of the loaded side of the plate to move down, relative to top and bottom surface. This induces a discontinuity in the internal stretching field ω . Omission of term $[[\omega]]$ will lead to mild artificial stiffening of the loaded side of the plate and unrealistic bending of the un-loaded side of the plate. Figure 2.16b shows the loaded edge displacements of the cracked plate in comparison with an uncracked plate strip, with the same geometrical and material properties but a width of $B/2$. The displacement axis shows absolute values of displacement. The response of both analyses shows excellent agreement which suggest that the discontinuity in the internal stretch field is modeled properly. As a consequence Poisson thickness locking on the loaded part is completely removed and unrealistic bending is not observed on the unloaded part of the plate.

2.9.5 Pinched semi-cylinder with crack growth

A cohesive crack growth analysis is performed in combination with large displacement/rotation analysis of a shell structure. Figure 2.17a shows the semi-cylindrical shell with an initial crack of length, $a = 0.5675$. Several other researchers have performed an uncracked analysis of the corresponding example, see for example [15, 83, 143]. The cylinder is subjected to an end pinching force at the middle of the free-hanging circumferential periphery. The length of the cylinder is $L = 3.048$, inner radius, $R = 1.016$ and thickness, $t = 0.03$. The material parameters used for the analysis are: Young's modulus, $E = 2.0685e7$ and Poisson ration, $\nu = 0.3$. For the cohesive constitutive part, we use an exponential mode-I decohesion law, defined as:

$$\mathbf{t}_n = \alpha e^{-\beta [[u]]_n} \mathbf{n} \quad (2.116)$$

where α and β are material parameters and given as $\alpha = f_t$ and $\beta = f_t/G_c$. f_t is material tensile strength, $f_t = 6e4$ and G_c is mode-I fracture toughness of the material, $G_c = 3e3$. The crack is extended when the principle stresses ahead of the crack tip exceed the tensile strength of the material.

Two mesh discretizations, mesh I and mesh II are used for the analysis. mesh I consist of 33 elements in circumferential and 32 elements in axial direction, while mesh II consists of 65 elements in circumferential and 64 elements in axial direction.

Figure 2.17b shows the load displacement response of the cracked cylinder in comparison with the uncracked cylinder. The uncracked pinched cylinder results form [143] are also plotted for reference. It can be observed that mesh objective results are obtained once the mesh is refined enough to resolve the field. The inclusion of a crack resulted in a ductile response of the cylinder compared to an uncracked cylinder. Moreover, the process of crack growth and large rotations and displacements are simultaneously captured very well. Note that the downward displacement of the

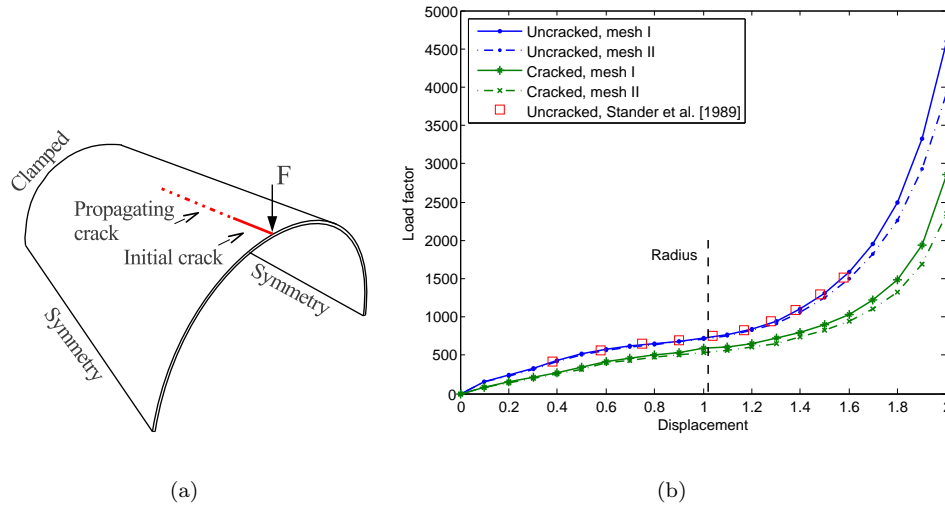


Figure 2.17 Pinched semi-cylinder model and load-deflection curves

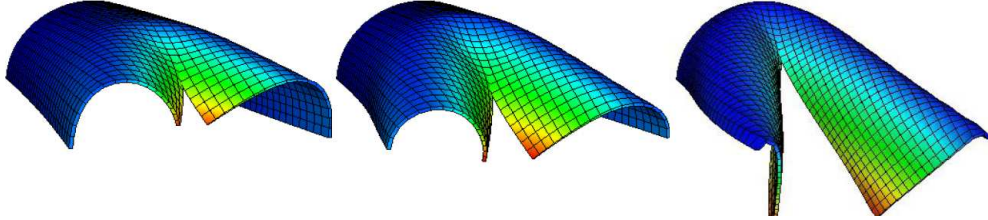


Figure 2.18 Deformed shapes at $\vartheta_z = 0.8, 1.2, 2.0$

loaded point is twice the radius of the specimen. Figure 2.18 shows the deformed shapes of the specimen at different load steps with mesh I.

2.10 Conclusions

In this chapter, a new geometrically nonlinear, fully discontinuous shell finite element is presented for arbitrary propagating cracks in thin shell structures. The proposed model avoids the need for predefining crack locations and adaptive mesh refinement in finite element simulations as the crack grows. The discontinuous behavior is achieved by incorporating discontinuities in the shell mid-surface, director and more importantly thickness stretching field, which becomes important for in-

homogeneous bending on both sides of the crack. This is achieved using a variant of XFEM, the phantom node method, where a cracked element is replaced by overlapping elements. This results in a simpler implementation and requires small modifications to the standard finite element code, due to the fact that the overlapped pair of elements are similar to uncracked elements. The discontinuous solid-like shell element has only displacement degrees of freedom and provides a complete three-dimensional state of stress. Additionally, the proposed model addresses the issue of simultaneously capturing the effects of geometrical instabilities in combination with material non-linearity. Numerical examples presented show excellent performance of the element in combined physically and geometrically non-linear analysis.

Chapter 3

Three-dimensional progressive failure model*

A novel, three-dimensional computational model is presented for the simulation of progressive failure in laminated composites subjected to out-of-plane loading conditions. Solid-like shell elements are used to model the thin plies of the laminate. In order to model mesh independent matrix cracking, a discontinuous solid-like shell element (DSLS) is utilized. A partition of unity approach is exploited to incorporate the discontinuity in the shell mid-surface, shell director and internal stretching field. A shell interface model is presented for the modeling of delamination damage. The model allows for the computationally efficient simulation of delamination and the evaluation of a consistently linearized tangent stiffness matrix for large deformation problems, which is essential for convergence. To model the coupled response of matrix cracking and delamination under large deformations, a computational framework is developed. The combined modeling of matrix cracking and delamination is achieved without incorporation of additional degrees of freedom. Numerical results are presented to show the performance and several distinct features of the model to simulate progressive failure in laminated composite shell structures. The numerical model is validated against experimental results.

3.1 Introduction

Fiber-reinforced composites are used in variety of fields of engineering including aircraft, marine and defense industry. These composite structures are susceptible to impact by foreign objects. Impact loading on laminated composites may cause significant damage in terms of matrix cracking and delamination. It has been experimentally observed, e.g. [36, 37, 43, 76, 92] that these two damage mechanisms also appear concurrently and there is a strong interaction between them. The aim of this manuscript is to present an integrated computational framework to take the coupled response of matrix cracking and delamination efficiently and accurately into account for out-of-plane loaded composite laminates. This is achieved in geometrical nonlinear finite element framework.

One of the prominent features of the proposed progressive failure model is the use of discontinuous shell element for the simulation of mesh independent matrix

* This chapter is extracted from [5]

cracking, for out-of-plane loaded composite laminates. One of the major difficulties in failure analysis is the process of localization of deformation, which refers to intense straining of a material within thin bands. Localization of deformation may occur due to microcracking, macrocracking, shear banding, delamination and local and global buckling of structural elements. Several investigators proposed failure based models, see for example [36, 67, 101, 168], others presented continuum damage models, for example [48, 73], for the prediction of impact damage in laminated composites. However, these models do not perform well in localization problems [151] and give mesh dependent results.

In an alternative approach, the use of discrete fracture/cohesive zone models automatically introduces a characteristic length scale into the formulation, which solves the problem of mesh dependency. Based on this concept, many hybrid models were developed which modeled delamination cracking using discrete fracture models, while matrix cracking/splitting is modeled using continuum damage or plasticity models, such as by [42, 60, 61]. A drawback of this approach was, that even though delamination damage was modeled using a discrete fracture approach, the use of a plasticity model for intra-ply damage can still create problems due to strain localization, resulting in ill-posedness of the governing equations and mesh dependency.

Inspired by the idea of discrete fracture approach for localization problems, several formulations were presented which modeled both matrix and delamination cracking using discrete fracture mechanics approach, see for instance [88, 99, 156]. A similar approach based on cohesive zone models in combination with interface elements was used by [161, 164] to model the in-plane response and by [30, 47] to model the out-of-plane response of laminated composites. However, a restriction of the computational strategy presented was, that the use of interface elements required the finite element mesh to be aligned with the crack geometry and cracks can only grow along predefined locations. As a result of this, the methodology could only be used for limited types of laminate configurations. Moreover, it was required to generate different finite element meshes for different ply orientations, e.g. a ± 45 laminate requires a finite element mesh of diamond shape elements citeBouvet2009.

The restriction of predefined crack paths associated with the use of interface elements can be circumvented by exploiting partition-of-unity based approaches [107, 159], which allow for a simulation of arbitrary propagating cracks through a finite element mesh. These methods have been used for modeling the in-plane response of composite laminates e.g. [74, 152] using plane-stress elements. However, mesh independent modeling of discrete matrix cracking/splitting in shell and plate composite structures subjected to out-of-plane loading have never been exploited. This may be partially due to the shear complexity involved in discrete modeling of damage with nonlinear shell theories, where in addition to other problems, a complicated update of rotations is necessary, even for undamaged material in geometrically

nonlinear situations.

The presented progressive failure model is based on solid-like shell elements, which give a complete three-dimensional stress state. This is important for delamination onset and propagation [36–38]. Moreover, the use of solid-like shell elements removes Poisson thickness locking effect [27], commonly found for solid (volume) elements. The proposed progressive failure model provides an integrated computational framework to simulate mesh independent matrix cracking through a finite element mesh of solid-like-shell elements using phantom node method [58] and delamination cracking using the shell interface model. The combined model is able to take into account the coupled response of matrix and delamination cracking.

3.1.1 Failure mechanisms

The energy absorption mechanism of laminated composites subjected to impact loading consists of the creation of (1) a large cracked area at the weaker interfaces between the composite layers, the so-called delamination damage, (2) matrix-matrix debonding, matrix-fiber debonding or matrix cracking/splitting, (3) fiber breakage and (4) total perforations in case of high velocity impact. It has been observed that the shape of the delaminated area due to impact consists of two lobes, commonly called as peanut-shape, oriented along the fiber direction of one of the plies connected to an interface [36].

One of the reasons for this damage pattern is the difference in flexural rigidity of the plies between fiber and transverse direction [98]. As a result of this, a simple orthotropic plate subjected to a concentrated load tends to show large negative bending curvatures in transversal direction as compared to bending in fiber direction. Moreover, this behavior is more pronounced with an increase in material anisotropy, figure 3.1a. When these orthotropic plates are stacked together to form a laminate, the difference in bending of the two plates will result in a potential peanut-shaped zone of delamination, figure 3.1b.

Another reason for onset of delamination damage is the presence of matrix cracks in one of the plies connected to an interface which increases the interfacial stresses and hence triggers premature onset of delamination damage [38]. This is one of the computationally challenging failure mechanisms, as explained earlier, and requires careful numerical treatment. These matrix cracks are formed due to in-plane bending stresses (therefore called bending cracks) or due to in-plane shear stresses or a combination of in-plane bending and shear stresses (therefore called shear cracks) [36].

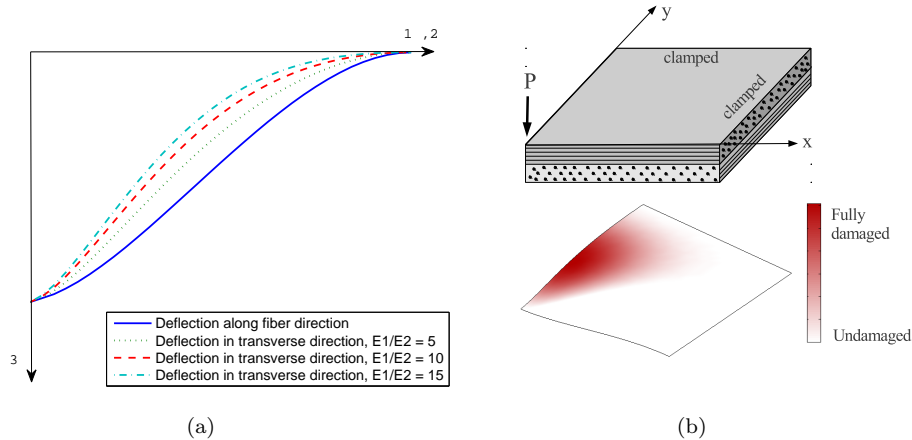


Figure 3.1 Damage due to material anisotropy of laminates, (a) Bending along fiber and transverse direction of an orthotropic plate, the 1-axis is aligned with the fiber orientation, the 2-axis is the in-plane and the 3-axis is the out-of-plane transversal axis, respectively, (b) Schematic delamination zone of cross-ply laminate ($E1/E2 = 15$)

3.1.2 Scope of study

In this chapter a novel mesoscopic failure model for laminated composite plates and shells is presented. Each ply of the laminate is modeled with a single layer of solid-like shell elements in thickness direction. Two damage mechanisms are considered, namely matrix cracking and delamination damage. Fiber failure or shear nonlinearity is not considered in this contribution. However, this is to remark that, inclusion of continuum damage and/or plasticity based models for shear nonlinearity and fibre failure is straightforward [88, 92, 161], unless rigorous homogenization technique is employed.

A discontinuous solid-like shell element (DSLS) [10] is used to model matrix cracking. Fracture is modeled as a gradual process using a cohesive zone model. The model allows for arbitrary propagation of matrix cracking/splitting through the finite element mesh of solid-like shell elements, without a restriction to the laminate configuration and finite element shape. The crack surfaces are assumed to be normal to the shell mid-surface, however, this is not a limitation of the methodology. Moreover, it is envisioned that since individual plies are thin compared to the thickness of the laminate, the error introduced by modeling through-the-thickness inclined cracks such as shear cracks with the above assumption, will not be significant.

Delamination cracking is modeled using the shell interface model. In contrast to traditional interface elements, the shell interface model allows efficient simulation of delamination damage and its coupling with matrix cracking/splitting. The numerical

framework is able to capture the interaction between matrix cracking and delamination in laminated composites subjected to transverse loading. The discontinuity introduced by matrix cracking in one or both planes of the delamination interface is properly modeled. If this is not the case, it may result in over-prediction of the load capacity.

This chapter is organized as follows: In section 3.2 and 3.3, a brief introduction of matrix cracking/splitting and the shell interface model is presented, respectively. Section 3.4 describes in detail the progressive failure model, which takes into account the interaction between matrix cracking and delamination. Several computational aspects of the model are explained. In section 3.5, a mixed-mode exponentially decaying cohesive constitutive law for delamination and matrix cracking interface is presented. Section 3.6 deals with the implementational aspects of the novel progressive failure model. The performance of the progressive failure model is demonstrated by means of several numerical examples in Section 3.7.

3.2 Discontinuous shell model for matrix cracking

To model matrix cracking, a discontinuous solid-like shell element (DSLS) [10] is used, where a partition-of-unity approach is exploited to incorporate the discontinuity in the shell mid-surface, shell director and in the internal stretching field, figure 3.2. This enables the element to model arbitrary propagating cracks through a finite element mesh. The model is also able to predict the buckling response of laminated composites, which is crucial, as this can substantially reduce the strength of the laminate and may trigger other failure mechanisms such as buckling-induced cracking and/or delamination.

The solid-like shell element resembles an eight-noded solid element. In addition to geometrical nodes, the element contains four independent internal nodes at the corners of the element mid-surface. To model the discontinuity, a finite element approach proposed by [58] is used. The cracked element is replaced by two overlapping partially active elements with domains Ω_A^o and Ω_B^o , respectively. The nodes in the active part of the element are the real nodes, while the nodes in the in-active domains are the phantom nodes. The displacement field $\boldsymbol{\vartheta}(\mathbf{X})$ of a cracked shell element is given by

$$\boldsymbol{\vartheta}(\mathbf{X}) = \begin{cases} \boldsymbol{\vartheta}_A(\mathbf{X}) & \forall \mathbf{X} \in \Omega_A^o \\ \boldsymbol{\vartheta}_B(\mathbf{X}) & \forall \mathbf{X} \in \Omega_B^o \end{cases} \quad (3.1)$$

where $\boldsymbol{\vartheta}_e$ is defined as

$$\boldsymbol{\vartheta}_e = \mathbf{u}_e^o + \zeta \mathbf{u}_e^1 + (1 - \zeta^2) \mathbf{u}_e^2 \quad e = A, B \quad (3.2)$$

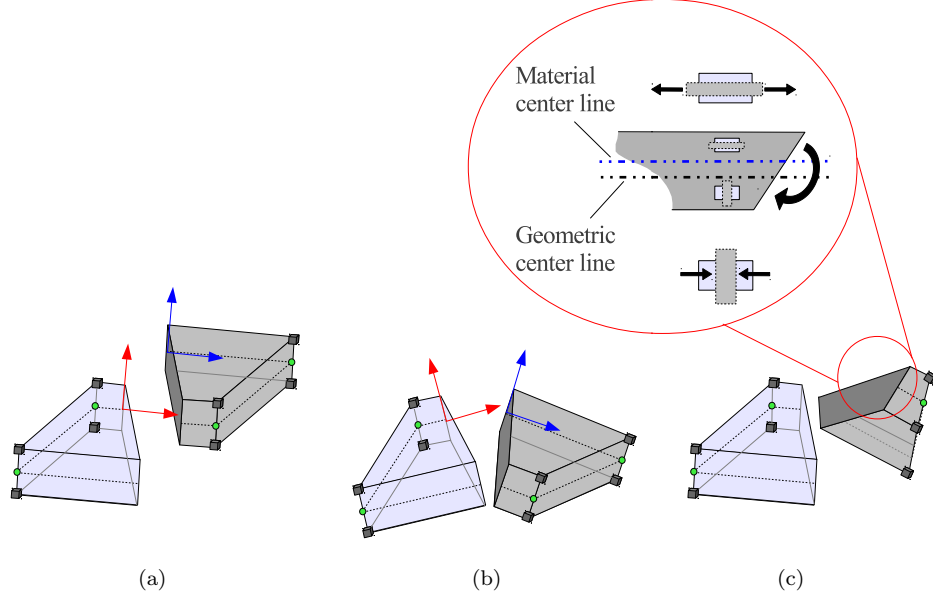


Figure 3.2 Discontinuous solid-like shell element, (a) discontinuity in the shell mid-surface, (b) discontinuity in the shell director, (c) discontinuity in the internal stretching field due to unsymmetric bending on both sides of crack. Zoom-in shows shift of material center line (initially coincident with geometric center line) to the side which is stretched.

The discretized displacement field of a shell mid-surface (\mathbf{u}^o), shell director (\mathbf{u}^1) and internal stretching (\mathbf{u}^2) is then given as:

$$\mathbf{u}_e^o = \mathbf{N}^o \hat{\mathbf{U}}_e \quad (3.3a)$$

$$\mathbf{u}_e^1 = \mathbf{N}^1 \hat{\mathbf{U}}_e \quad (3.3b)$$

$$\mathbf{u}_e^2 = \mathbf{d}_e \mathbf{N}^\omega \hat{\mathbf{W}}_e \quad (3.3c)$$

in which \mathbf{N}^o , \mathbf{N}^1 and \mathbf{N}^ω are the shape function matrices of solid-like shell element, $\hat{\mathbf{U}}$ and $\hat{\mathbf{W}}$ are the nodal displacements of surface and mid-surface nodes of shell elements, respectively (see [10]). The displacement jump across the discontinuity in the cracked element is given as

$$\llbracket \boldsymbol{\vartheta}(\mathbf{X}) \rrbracket = \boldsymbol{\vartheta}_B(\mathbf{X}) - \boldsymbol{\vartheta}_A(\mathbf{X}) \quad \forall X \in \Gamma_c^o \quad (3.4)$$

More details on element formulation and finite element implementation can be found in [10].

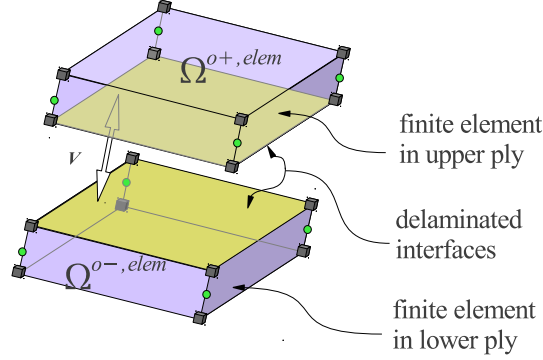


Figure 3.3 Discontinuous solid-like shell element

3.3 Shell interface model for delamination cracking

To simulate delamination cracking, an alternative approach to traditional interface elements based on the kinematics presented in [93] is used. As a result of modified kinematics, the interfaces of the two connecting plies can be defined within the continuum shell elements. This avoids the need for a separate model for interfacial phenomena e.g interface elements. The method also allows for a complete kinematic description of the interfaces as opposed to interface elements.

The total displacement field, $\bar{\boldsymbol{\vartheta}}$, of a shell body containing an interface for potential delamination is considered to consist of a continuous regular displacement field, $\boldsymbol{\vartheta}$, and an additional displacement field \mathbf{v} which determines the magnitude of the displacement jump at the interface, figure 3.3. Mathematically the displacement field is defined as

$$\bar{\boldsymbol{\vartheta}}(\xi, \eta, \zeta) = \boldsymbol{\vartheta}(\xi, \eta, \zeta) + \widetilde{\mathcal{H}}\mathbf{v}(\xi, \eta, \zeta) \quad (3.5)$$

in which $\widetilde{\mathcal{H}} = \mathcal{H} - \mathcal{H}_i$, where \mathcal{H} represents the step function, defined as

$$\mathcal{H}(\mathbf{X}) = \begin{cases} 1 & \mathbf{X} \in \Omega^{o+} \\ 0 & \mathbf{X} \in \Omega^{o-} \end{cases} \quad (3.6)$$

and \mathcal{H}_i is a value of the step function at the i th node (\mathbf{X}_i). In the present contribution, it is assumed that the location of the interfaces are known in advance, which is usual for delamination surfaces. In this case the definition of the displacement jump field \mathbf{v} is straight forward, and is given as

$$\mathbf{v} = \boldsymbol{\vartheta}_b^+ - \boldsymbol{\vartheta}_t^- \quad (3.7)$$

where $\boldsymbol{\vartheta}_b^+$ defines the displacement field at the bottom surface of the shell layer with domain Ω^{o+} and $\boldsymbol{\vartheta}_t^-$ defines the displacement field at the top surface of the shell layer with domain Ω^{o-} . Mathematically they are expressed as

$$\boldsymbol{\vartheta}_b^+ = \boldsymbol{\vartheta}_{\zeta=-1}^+ \quad (3.8)$$

$$\boldsymbol{\vartheta}_t^- = \boldsymbol{\vartheta}_{\zeta=1}^- \quad (3.9)$$

The discretized displacement jump at the interface is computed as

$$\mathbf{v} = \mathbf{N}_i^+ \hat{\boldsymbol{\vartheta}}_{ib}^+ - \mathbf{N}_i^- \hat{\boldsymbol{\vartheta}}_{it}^- \quad (3.10)$$

$$\mathbf{v} = \bar{\mathbf{N}}_i \hat{\boldsymbol{\vartheta}}_i^{Intf} \quad (3.11)$$

in which $[\bar{\mathbf{N}}] = [\mathbf{N}^+, -\mathbf{N}^-]$. The matrices \mathbf{N}^+ and \mathbf{N}^- are the shape function matrices computed in the domains Γ_c^+ and Γ_c^- , respectively. The shape function matrix for an element e according to [10], is defined as $\mathbf{N} = [\mathbf{N}^o + \zeta \mathbf{N}^1, (1 - \zeta^2) \mathbf{N}_w \mathbf{d}]$.

The vector $\boldsymbol{\vartheta}^{intf}$ is defined as $[\boldsymbol{\vartheta}^{intf}] = [\boldsymbol{\vartheta}_b^+, -\boldsymbol{\vartheta}_t^-]$. The displacement fields of the top and bottom interfaces are given as

$$\boldsymbol{\vartheta}_b^+ = \mathbf{N}_i^+ \hat{\boldsymbol{\vartheta}}_{ib}^+ \quad (3.12)$$

$$\boldsymbol{\vartheta}_t^- = \mathbf{N}_i^- \hat{\boldsymbol{\vartheta}}_{it}^- \quad (3.13)$$

It is important to note that the above discretized equations are similar to the traditional interface elements. However, since interfaces are defined within the continuum elements, a complete kinematic description of the interface is included. It is also possible to obtain a consistently linearized tangent stiffness matrix for the interface contribution in large deformation problems [158]. This is important for quadratic convergence of the Newton-Raphson scheme. Moreover, the computation of the deformation gradient and other geometric quantities such as the computation of the normal to the interface is straightforward, as will be discussed in section 3.4.4.

3.4 Interaction of matrix cracking and delamination

The appearance of a matrix crack in one ply or both plies connected to each other results in an interface which is also discontinuous, figure 3.4. In a finite element computation, it is pivotal to take the coupling between matrix cracking and delamination into account for an accurate representation of crack path interaction and energy dissipation, as will be discussed in section 3.4.2 and demonstrated in section 3.7.1. The issue and significance of interaction between matrix cracking and delamination has also been addressed in [87] in which it was shown that the constitutive law of the delamination interface is dependent upon the matrix cracking of the adjacent plies.

Modeling interfaces with interface elements will require one or both interfaces of the interface element to be adapted accordingly to take the coupling between

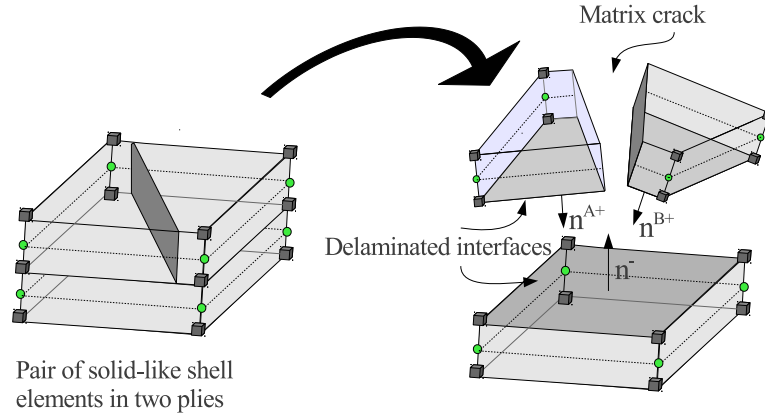


Figure 3.4 Progressive failure model

matrix cracking and delamination, figure 3.4. An XFEM-type enrichment to the displacement field of interface element can be applied to take the discontinuity in the interface element into account. This will require a modification of the connectivity and integration scheme of the interface element. Alternatively, defining the interfaces as integral parts of the continuum elements, as is done in the present work, the connectivity and the integration scheme is automatically updated. Consequently, no finite element modification or additional degrees of freedom are necessary to incorporate the discontinuity in the two planes of the interfaces.

3.4.1 Integration of cohesive interfaces

The formulation of the progressive failure model allows the use of any type of integration scheme for the integration of the shell interface model. However, it is known that spurious oscillations occur in the tractions when Gauss integration is used [130]. Therefore a nodal integration scheme is preferred to avoid numerical difficulties. It is worth to note that a nodal integration scheme inherently assumes that there is a delaminated area already present, whose size is equal to the element size. However, the error induced by such under-integration (see [130, 136]) of the shell interfaces lies at sub-element level and vanishes upon mesh refinement.

When one or both planes of the shell interface are cracked, the shell interface is required to be adapted as described above and in figure 3.4. This will also require adapting the integration scheme for the cracked interface. However, in such cases even using low-order Newton-Cotes or Gauss-Lobatto integration schemes will result in integration points within the domain of the shell interfaces. This will give rise to the coupling terms in the stiffness matrix of shell interfaces [136]. As a conse-

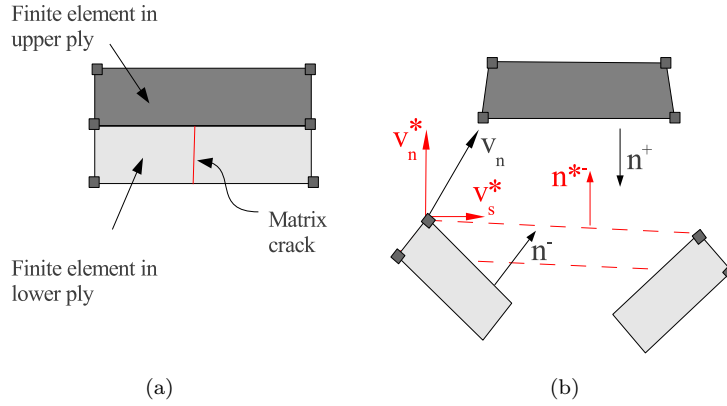


Figure 3.5 Incorrect fracture modes

quence the problem of traction oscillations will reappear which will cause numerical instabilities. Therefore, although the interfaces are cracked, the integration scheme for the interfaces is not adapted in this contribution.

3.4.2 Cracked or uncracked interfaces

The formation of a matrix crack in the ply requires the interfaces to be adapted accordingly. It implies the incorporation of a crack in one or both planes of the interface. Figure 3.5 shows two finite elements, one in the upper ply and one in the lower ply of the two-ply laminate. The formation of a matrix crack in the lower ply in a bending dominated problem, will cause the elements to deform as shown in figure 3.5. The interface will experience an opening displacement \mathbf{v} . Most cohesive laws are fracture-mode dependent and these opening modes are in turn related to the normal vector of the interface. For an interface which is adapted to take the presence of a crack into account, the normal vector to the interface is represented by \mathbf{n}^- . According to this reference frame, one may obtain only a mode-I interface opening, \mathbf{v}_n . On the other hand, if the interfaces are not adapted the components of the crack opening displacement, \mathbf{v} , based on an incorrect interface normal, \mathbf{n}^{*-} , may result in an unrealistic tangential, \mathbf{v}_s^* and normal, \mathbf{v}_n^* interface opening. This will ultimately result in unrealistic and incorrect computation of fracture modes and corresponding energy dissipation.

In the present contribution, if one or both plies connected to an interface are cracked, we adapt the planes of the interfaces accordingly. This results in the computation of the correct normal to the cracked interface and hence a correct fracture mode and energy dissipation.

3.4.3 Average cracked surface

For cracks which are undergoing large deformations, no unique normal to the crack surfaces can be identified [10, 158]. Usually the non-uniqueness of the normal plane to an interface is treated by defining an average crack surface [158]. The normal to an average crack surface can now be defined as:

$$\bar{\mathbf{n}} = \bar{J}(\bar{\mathbf{F}})^{-T} \mathbf{n}^\circ \frac{dA}{\bar{da}} \quad (3.14)$$

where $\bar{J} = \det(\bar{\mathbf{F}})$ is the Jacobian, \mathbf{n}° is the normal to the interface in the reference configuration, dA is the differential area of the interface in the reference configuration, while \bar{da} is the differential area of the assumed average crack surface in the deformed configuration. The average deformation gradient to an assumed average crack surface is defined as

$$\bar{\mathbf{F}} = \bar{\mathbf{g}}_i \otimes \mathbf{G}^i \quad (3.15)$$

in which $\bar{\mathbf{g}}_i$ is defined as

$$\bar{\mathbf{g}}_i = \frac{1}{2} [\mathbf{g}_i^+ + \mathbf{g}_i^-] \quad i = [\xi, \eta, \zeta] \quad (3.16)$$

$$\mathbf{g}_i^+ = \mathbf{x}_{,i}^+ \quad (3.17)$$

$$\mathbf{g}_i^- = \mathbf{x}_{,i}^- \quad (3.18)$$

Note that, due to improved kinematics of the shell interface model, the computation of the deformation gradient and normal to the interface becomes straightforward.

Remark 1. As explained above, non-uniqueness in defining the normal to an interface undergoing large deformations, is treated by defining an average crack surface. However, this assumption leads to an incorrect kinematic description of the interface. This can be demonstrated through a simple example. Consider an interface (figure 3.6), which is given a rigid rotation. The deformation gradients of the interfaces CD , $C'D$, and a fictitious average interface $E''D$ are given as:

$$F_{CD}^+ = \begin{bmatrix} 0 & 0 & 1 \\ 0 & 1 & 0 \\ -1 & 0 & 0 \end{bmatrix}, F_{C'D}^- = \begin{bmatrix} 1 & 0 & 0 \\ 0 & 1 & 0 \\ 0 & 0 & 1 \end{bmatrix}, \bar{F}_{E''D} = \begin{bmatrix} 0.5 & 0 & 0.5 \\ 0 & 1 & 0 \\ -0.5 & 0 & 0.5 \end{bmatrix} \quad (3.19)$$

Accordingly, the area ratios for the three surfaces are

$$da_{CD}^+/dA = 1.0, da_{C'D}^-/dA = 1.0, \bar{da}_{E''D}/dA = 0.7071 \quad (3.20)$$

in which da_{CD}^+ , $da_{C'D}^-$ and $\bar{da}_{E''D}$ are the deformed areas of the three surfaces and dA is the reference crack surface area. The above computation shows that there

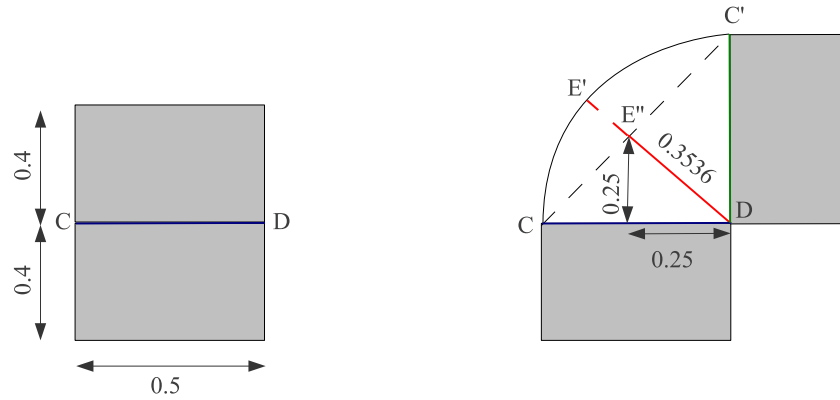


Figure 3.6 Cracked surface under large deformation/rotation

is a reduction of the deformed area, which is un-realistic for the problem under consideration. The reasons for such a behavior are obvious and are also schematically illustrated in figure 3.6. It can be derived from the figure that an average kinematic assumption for the interface, inherently assumes that the interface will not follow the curved path. The correct average crack surface should have been $E'D$, instead crack surface $E''D$ is predicted and the interface front is located at the chord. This results in a decreased interface length $l_c = 0.3536$. However, it is worth to note that the magnitude of the error induced by using averaging kinematics is also dependent upon the geometry, the boundary conditions of the body and the magnitude of interface rotation.

3.4.4 Computation of normal and rotation matrix

In large deformation problems, the local crack coordinate system also undergoes large rotations, hence the rotation matrix used for the transformation of kinematic quantities from the crack coordinate system to the global coordinate system does not remain constant. It becomes a function of deformation of the element [125, 158]. The rotation matrix \mathbf{Q} which transforms kinematic quantities from the crack coordinate system in the reference configuration to the global coordinate system and rotation matrix \mathbf{Q}^* which transforms kinematic quantities from the crack coordinate system

in the deformed configuration to the global coordinate system are given as

$$\mathbf{Q}_{ij} = \cos(\hat{\mathbf{e}}_{i,global}, \hat{\mathbf{e}}_{j,local}) \quad (3.21)$$

$$\mathbf{Q}_{ij}^* = \cos(\hat{\mathbf{e}}_{i,global}, \hat{\mathbf{e}}_{j,local}^*) \quad (3.22)$$

in which

$$\hat{\mathbf{e}}_{i,global} = \{\mathbf{i}_1, \mathbf{i}_2, \mathbf{i}_3\} \quad (3.23)$$

$$\hat{\mathbf{e}}_{i,local} = \{\mathbf{m}^o, \mathbf{p}^o, \mathbf{n}^o\} \quad (3.24)$$

$$\hat{\mathbf{e}}_{i,local}^* = \{\mathbf{m}, \mathbf{p}, \mathbf{n}\} \quad (3.25)$$

The Cartesian base vectors of the delamination interface in the reference configuration are given as

$$\mathbf{m}^o = \frac{\mathbf{G}_1}{\|\mathbf{G}_1\|}, \quad \mathbf{n}^o = \frac{\mathbf{G}_1 \times \mathbf{G}_2}{\|\mathbf{G}_1 \times \mathbf{G}_2\|}, \quad \mathbf{p}^o = \frac{\mathbf{n}^o \times \mathbf{m}^o}{\|\mathbf{n}^o \times \mathbf{m}^o\|} \quad (3.26)$$

The Cartesian base vectors to the average delamination interface in the deformed configuration are given as

$$\mathbf{m} = \frac{\bar{\mathbf{g}}_1}{\|\bar{\mathbf{g}}_1\|}, \quad \mathbf{n} = \frac{\bar{\mathbf{g}}_1 \times \bar{\mathbf{g}}_2}{\|\bar{\mathbf{g}}_1 \times \bar{\mathbf{g}}_2\|}, \quad \mathbf{p} = \frac{\mathbf{n} \times \mathbf{m}}{\|\mathbf{n} \times \mathbf{m}\|} \quad (3.27)$$

The covariant base vectors (\mathbf{G}_α , $\bar{\mathbf{g}}_\alpha$) in the reference and the deformed configuration are computed as

$$\mathbf{G}_\alpha = \frac{\partial \mathbf{X}}{\partial \xi^\alpha} = \mathbf{X}_{,\alpha} \quad (3.28)$$

$$\bar{\mathbf{g}}_\alpha = \frac{\partial \bar{\mathbf{x}}}{\partial \xi^\alpha} = \bar{\mathbf{x}}_{,\alpha} \quad \alpha = \{1, 2, 3\}, \quad \xi^\alpha = \{\xi, \eta, \zeta\} \quad (3.29)$$

Alternately, the deformed normal to an interface can also be computed as

$$\mathbf{n} = \frac{\bar{\mathbf{F}}^{-T} \mathbf{n}^o}{\|\bar{\mathbf{F}}^{-T} \mathbf{n}^o\|} \quad (3.30)$$

Note that it is due to the improved kinematic description of the interfaces using the shell interface model described above, which made it possible to compute the deformation gradient and derivatives of the kinematic quantities at the interface.

3.5 Constitutive laws

Bulk material is considered to be linear elastic and is modeled with Hooke's law for transversely-isotropic materials [72].

An exponentially decaying cohesive law is used for simulating cohesive matrix and delamination cracking. Micromechanical analysis of reinforced polymers shows three

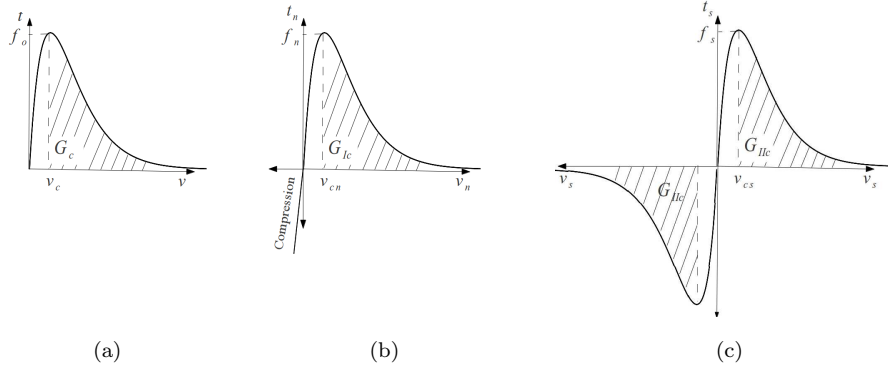


Figure 3.7 Exponentially decaying cohesive constitutive law, (a) mixed-mode cohesive law, (b) shape of cohesive law in pure mode I, (c) shape of cohesive law in pure mode II or mode III

distinct regions in their traction separation law. The initial plateau, denoting the formation and growth of micro-cracks in the material, the fast degrading branch, denoting the stage when the formation of micro-cracks has reached its saturation limit and crack coalescence starts and thirdly the region with low tractions levels, denoting the effect of cross-tie fibrils, which may delay the complete breakdown of crazes and the formation of traction-free crack surfaces.

Different cohesive interface laws have been suggested by several authors for modeling cohesive matrix and/or delamination cracks. For example rectangular [161], bi-linear [32, 148], trapezoidal [164] and exponentially decaying [22, 150] cohesive laws. However, it is well accepted that the shape of the cohesive constitutive law does not significantly affect the solution accuracy as long as a correct interfacial strength and fracture toughness are used [46]. However, the shape of the curve does affect the response at crack initiation. In [22] a delamination analysis using bi-linear and exponential cohesive laws was performed and it was observed that both laws gave approximately the same result but the exponential cohesive law showed better convergence behavior.

3.5.1 Constitutive law for delamination cracking

A mixed-mode, exponentially decaying cohesive constitutive law is presented, figure 3.7. The cohesive law uses a single scalar damage parameter ω , to describe damage in the fracture process zone (FPZ). The cohesive law has two key parameters, the mixed mode strength of an interface, f_o and fracture toughness, G_c .

The traction vector \mathbf{t} , parallel to the opening displacement \mathbf{v} is defined as:

$$\mathbf{t} = \mathbf{t}r \quad (3.31)$$

where \mathbf{r} is a unit vector in the direction of the opening displacement, $\mathbf{r} = \mathbf{v}/v$, and $v = \|\mathbf{v}\|$. The scalar function t is defined as:

$$t = (1 - \omega)f_o \quad (3.32)$$

where ω is a damage parameter which varies from 0, the undamaged state, to 1, the fully damaged state. The damage parameter ω , is defined as:

$$\omega = 1 - e \cdot \left(\frac{v}{v_c}\right) \cdot \exp\left(-\frac{v}{v_c}\right) \quad (3.33)$$

in which

$$e = \exp(1) \quad (3.34)$$

$$v_c = \frac{\tilde{G}_c}{e \cdot f_o} \quad (3.35)$$

$$\tilde{G}_c = G_c \left\{ 1 + \frac{1 - 2 \exp(-1)}{e \cdot f_o} \right\} \quad (3.36)$$

Note that \tilde{G}_c defines the area under the complete traction-separation curve, $\tilde{G}_c = \int_0^v t dv$, while G_c defines the area under the softening branch of the traction-separation curve, $G_c = \int_{v_c}^v t dv$. In order to be able to perform numerical analysis with variable mode mixities, parameters f_o and G_c are needed for each mixed-mode case. The mode mixity is incorporated using a phenomenological Benzeggagh-Kenane [26] mode interaction criterion according to:

$$f_o^2 = f_n^2 + (f_s^2 - f_n^2)\Pi^\eta \quad (3.37)$$

$$G_c = G_{I_c} + (G_{II_c} - G_{I_c})\Pi^\eta \quad (3.38)$$

with

$$\Pi = \left(\frac{G_{II}}{G_I + G_{II}} \right) = \frac{v_s^2}{v_s^2 + \langle v_n \rangle^2} \quad (3.39)$$

G_{I_c} and G_{II_c} are the fracture toughnesses in pure tension and shearing modes, respectively. G_I and G_{II} are the energy release rates in tension and shearing modes, respectively. f_n and f_s are the tensile and shearing interfacial strengths, respectively. η is a material parameter obtained from experiments. In order to prevent interpenetration of the interfaces in compression ($v_n < 0$), a penalty traction $t_p = K_p v_n$, normal to the interface, is applied. Since mixed-mode strength, f_o , and fracture toughness, G_c , are function of pure modes strengths and fracture toughnesses, the values can be determined experimentally using standard test methods.

3.5.2 Constitutive law for matrix cracking

As opposed to the shell interface model where cohesive surfaces are present from the beginning of the analysis, the partition of unity based approach for matrix cracking on the other hand introduces the crack in a stressed body. This requires an initially rigid cohesive law with a finite traction at zero crack opening displacement, as was also demonstrated by [75].

The traction-separation law used for cohesive matrix cracks is the same as the one described for delamination cracking. In order to obtain an initially rigid cohesive law an approach proposed in [65] is used. The idea is to simply translate the origin of displacement jump axis to a value of the displacement jump corresponding to the traction at crack initiation. Accordingly, considering f_o as the magnitude of traction for zero crack opening, we define the shifted displacement jump as $v_{shifted} = v + v_c$. Accordingly, the damage variable is computed with an updated displacement jump value as

$$\omega = 1 - e \cdot \left(\frac{v_{shifted}}{v_c} \right) \cdot \exp \left(- \frac{v_{shifted}}{v_c} \right) \quad (3.40)$$

In order to ensure continuity of the stress field, the tractions on the crack surface at zero crack opening should be in equilibrium with the stresses in the bulk material next to the crack [31], i.e.

$$\mathbf{t} = \boldsymbol{\sigma} \mathbf{n} \quad (3.41)$$

The same concept was later used by [124, 152] to define tractions at the moment of nucleation of a crack. In order to satisfy condition (3.41), it follows that f_o is required to be defined by

$$f_o = \|\boldsymbol{\sigma} \mathbf{n}\| \quad (3.42)$$

This ensures continuity of the stress field at the crack tip.

3.6 Implementation details

In this section implementation details of the progressive failure model are given.

3.6.1 Initiation and propagation of discontinuity

The phantom node method requires a failure criterion to insert new crack segments in a virgin material. To ensure continuity of the response and avoid sudden jumps in the stress field at the moment of insertion of a new crack segment, the failure criterion should match the damage evolution. Using a bulk constrained cohesive law,

as described above, this is automatically ensured. Consequently, the failure criterion is defined as

$$\frac{\langle \sigma_n \rangle^2 + \sigma_s^2}{f_n^2 + (f_s^2 - f_n^2) \Pi^\eta} = 1 \quad (3.43)$$

with

$$\Pi = \frac{\sigma_s^2}{\sigma_s^2 + \langle \sigma_n \rangle^2} \quad (3.44)$$

in which σ_n and σ_s are the normal and shear components of bulk stress at the crack surface. The operator $\langle x \rangle = (x + |x|)/2$ is used to nullify the influence of damage in normal direction in compression. Note that for orthotropic materials, in which matrix cracks propagate parallel to the fiber direction, $\sigma_n = \sigma_2$.

In order to initiate a new cohesive crack segment, the failure criterion is evaluated in all integration points of the critical elements. If the criterion is violated in one of the integration points, a new through-the-thickness crack segment is introduced in the center of an element, provided the distance between the new crack segment and existing cracks is larger than the minimum crack spacing. It is noted that for very thick plies, a single cracked element through the thickness of the ply may give inaccurate results and the interaction between matrix cracking and delamination interface may not be captured effectively, even if a discontinuous interface is modeled (section 3.4). This is due to inaccurate representation of the through-the-thickness stress field around the crack. This scale dependency of matrix cracking has been observed by [118]. However, using higher order finite elements or multiple elements through the thickness helps in obtaining a correct representation of crack tip field in thickness direction.

3.6.2 Matrix crack spacing

In order to simulate multiple cracking in a laminate, a criterion is required to determine the maximum number of cracks or minimum crack spacing. Unlike isotropic materials, where the formation of cracks in the bulk material results in stress relaxation and alteration of stress field around the crack. Laminated composites on the other hand, behave differently. The response is governed by different failure mechanisms as described in section 3.1.1. The formation of a crack in one of the plies does not instantaneously result in release of energy and opening of a crack unless some area underneath or above the crack delaminates. This means that for an interface which is extremely rigid, an infinite number of cracks can initiate with theoretically zero crack spacing. This makes it difficult to select an objective crack spacing for numerical analysis of laminated composites. This may be theoretically true, however real materials have a finite stiffness at the interface and in such cases the formation

of a matrix crack will result in an increase in interfacial stresses at places where matrix cracks are formed and hence may trigger delamination damage. This will therefore result in opening and growth of matrix cracks. Moreover, in real laminates matrix cracks are not the only source of stress enhancers at the inter-ply interfaces, which trigger delamination. Other mechanisms such as fiber breakage, bending stiffness mismatching and the effect of out-of-plane stresses also contribute to increase the stresses at the interface. This removes the non-uniqueness in crack spacing and results in a distributed crack formation in a laminate. Moreover, it has been observed, e.g. [86] that matrix cracking always reach a saturated crack density that is associated with local delamination in the vicinity of crack tips. These saturated crack density measurements from an experimental study may give a rough estimate of minimum crack spacing.

In the presented progressive failure model, this non-uniqueness is partially removed by performing a complete three-dimensional analysis which results in good predictions of interfacial and through-the-thickness stress distribution. Moreover, in addition to matrix cracking as a source of initiating delamination damage, the difference in bending stiffness of the connecting plies and its interaction with matrix cracking provides an additional source of triggering delamination damage and therefore helps in removing the non-uniqueness in crack spacing. In this contribution a minimum crack spacing is selected in such a way that the mesh being sufficiently fine to accurately represent the stress field, further decrease in crack spacing does not cause the response of the structure to change and the response converges to a unique solution upon decreasing crack spacing. The effect of crack spacing is further discussed in the next section.

3.7 Numerical examples

Several numerical tests are performed with realistic material properties to show the accuracy and efficiency of the proposed progressive failure model. The numerical examples are arranged in order of their complexity. The first numerical example presents numerical validation of the progressive failure model using a mesh convergence study. A parametric study is also performed to investigate the influence of different model parameters. In the second numerical example, we capture progressive damage mechanisms, as observed during experiments, for a laminated plate subjected to out-of-plane loading. Furthermore, the effect of crack spacing on the overall damage behavior is investigated. In the third example, we capture shear dominated matrix cracking and delamination damage and their mutual interaction, where trends in damage pattern and growth are observed. The numerical model is validated against experimental results in the fourth example.

3.7.1 Cross-ply laminated beam, $[0_2/90_2]$

Problem description

In order to demonstrate salient features of the progressive failure model, the initiation, growth and interaction of different failure mechanisms, a simply supported cross-ply $[0_2/90_2]$ laminated composite beam is analyzed. The geometry of the beam is shown in figure 3.8a. The beam is subjected to a quasi-static line load at the center. The ply thickness is considered to be 0.2 mm.

Individual plies are modeled with orthotropic material properties of HTA6376/C, a carbon fiber reinforced epoxy. The material properties used for the laminated beam test, extracted from [59], are given in table 3.1. In order to clearly demonstrate the different features of the model, the Poisson's ratio is set to zero. This allows the use of a coarse mesh discretization along the width of the beam. A more detailed analysis, considering the effect of the width of the beam/plate on damage growth, is considered in sections 3.7.2 and 3.7.3.

Table 3.1 Material properties for laminated beam test

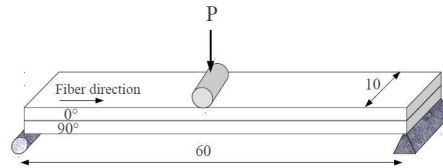
Laminate properties		Fracture properties	
E_{11} (GPa)	120	G_{Ic} (N/mm)	0.26
$E_{22} = E_{33}$ (GPa)	10.5	G_{IIc} (N/mm)	1.002
$G_{12} = G_{13}$ (GPa)	3.48	f_n (MPa)	30
$\nu_{12} = \nu_{13}$	0.0	f_s (MPa)	60
ν_{23}	0.0		

Finite element model

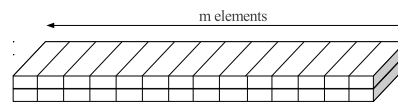
Each ply of the beam is modeled with a single solid-like shell element in thickness direction, 101 elements in longitudinal direction (element size = 0.6 mm) and a single element along the width, resulting in a mesh discretization of 101x1x2 elements for the whole beam. Figure 3.8b shows the schematic mesh discretization used for analysis. The mesh discretization was chosen based on the cohesive zone length, which is $\approx 1.2\text{mm}$ and minimum crack spacing, which is chosen to be 7 mm for the current analyses. For an efficient solution of the finite element system of equations a dissipation based arc-length method [155] is used to trace the equilibrium path.

Results and observations

Figure 3.9 shows the load displacement response. It is evident from the figure that the laminate behaves linear elastic until the stresses in the outermost layer reach



(a) Geometry and boundary conditions (All dimensions in mm)



(b) Schematic finite element mesh discretization

Figure 3.8 Cross-ply laminated beam

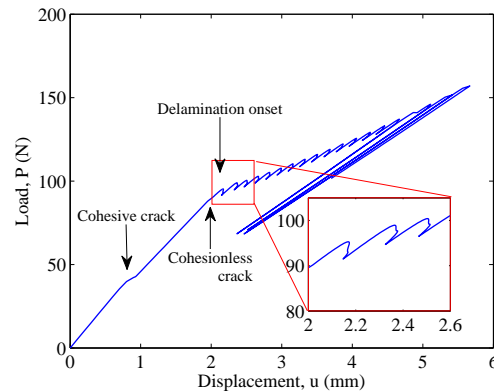


Figure 3.9 Load-displacement response of laminated beam

the material strength. At that moment a cohesive crack appeared in the bottom ply which slowly degraded the stiffness until a fully cohesionless or, in other words, a macro-crack developed. Moreover, the presence of a matrix crack did not significantly reduce the stiffness of the structure. Once the macro-crack developed, delamination damage starts. This not only resulted in an increase in displacements with smaller load increments but also resulted in significant stiffness degradation.

From figure 3.9 it can be observed that delamination growth is not smooth but shows small snap backs in the response after its onset. This is due to a sudden release of elastic energy from the surrounding bulk material as a result of softening

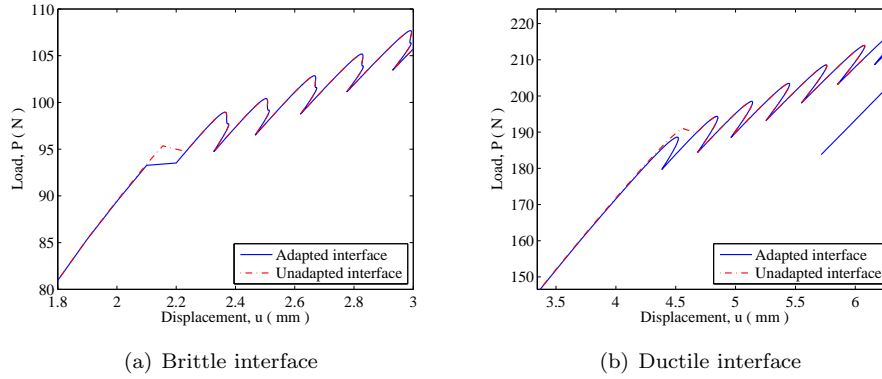


Figure 3.10 Load-displacement response of laminated beam-comparison between adapted and unadapted interface

in the interfacial strength. This results in an instantaneous failure of an interface which appeared as small snap backs in the global load-displacement response. In a displacement controlled analysis such a drop in energy appears in a stair-case pattern in the global load-displacement response as is usually observed with interface elements. However, the response get smooth with mesh refinement as is demonstrated in subsequent subsections. As the load increases, the beam starts to geometrically harden and hence failure of interfaces results in larger snap backs due to an increased elastic stored energy in the surrounding bulk material.

Effect of unadapted interface

In this section we shall investigate the effect of using adapted and unadapted interfaces (section 3.4.2) on the global response of the beam. In contrast to the previous section, the beam now contains an initial traction free crack in the center of the beam in the lower ply. The analysis is performed using adapted and unadapted interfaces. Two types of material properties are used. In the first case the analysis is performed with the set of material data presented in table 3.1. In order to simulate ductile interface, a second set of analyses was performed using a fracture toughness which is three times the value mentioned in table 3.1. Figure 3.10 shows the analysis results.

It can be observed that the response of the brittle and ductile interface is qualitatively similar. As was anticipated, the use of an unadapted interface resulted in an over-prediction of load capacity, and delay in the delamination onset. Moreover, the use of adapted or unadapted interfaces influence only the onset of damage while later the response of the two interfaces is the same. However, it is worth noting that the

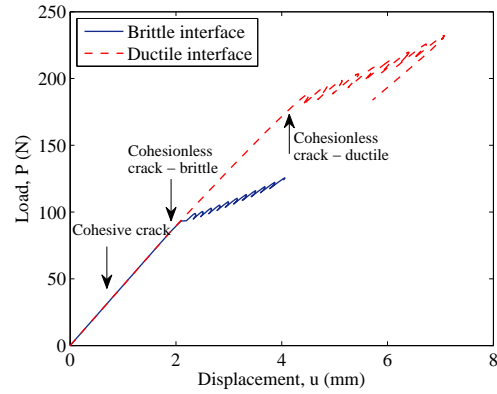


Figure 3.11 Load-displacement response of laminated beam-effect of interface brittleness

error induced due to the use of unadapted interfaces remains at element level and vanishes upon mesh refinement. Note that, the difference in the load-displacement curves of brittle and ductile interfaces at first yielding is due to coarse time stepping for the case of a brittle interface and is not consequence of a difference in the mechanical response of the two cases. As a result of coarse time-stepping, a small snap-back, as observed for the case of a ductile interface, is not captured for the case of a brittle interface analysis.

Effect of interface properties

In this section the effect of interface material properties over the response of laminated beam is investigated. The material and geometrical properties of the laminated beam are the same as used in section 3.7.1. In order to simulate ductile interface, analysis is performed using a fracture toughness which is three times the value mentioned in table 3.1. The response of a brittle interface is compared with a ductile interface in figure 3.11.

It can be observed that a brittle interface resulted in a lower load capacity than the ductile interface. Moreover, the increased fracture toughness of the ductile interface caused a delay in the onset of delamination or in other words, for a particular load level the brittle interface resulted in more delamination damage as compared to the ductile interface. It is also evident from figure 3.11 that, even though the cohesive matrix crack initiated at the same load level for both the brittle and ductile interfaces, the development of a traction free crack took place at higher load level for a laminated beam with a ductile interface due to a delay in delamination onset as a consequence of increased fracture toughness.

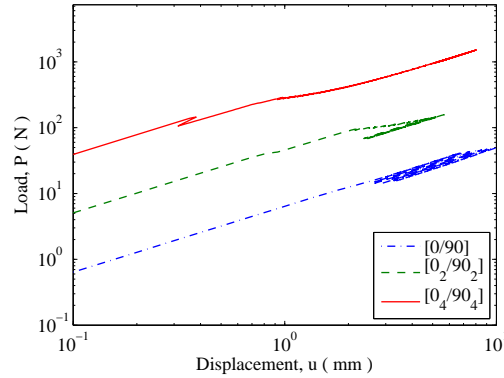


Figure 3.12 Load-displacement response of two ply beam-effect of thickness

Effect of thickness

Next the effect of laminate thickness on damage evolution is investigated. More specifically, the aim of this investigation is to assess the effect of scaling on initiation and growth of matrix and delamination cracking. For a true prediction of laminate strength, all failure mechanisms including compression failure need to be considered. Three laminate thicknesses were considered for analysis i.e. $[0/90]$, $[0_2/90_2]$ and $[0_4/90_4]$. Figure 3.12 shows the load-displacement response for the three cases. In order to show all three plots in one figure, the curves are plotted on a log-log scale. Table 3.2 compares the damage development in three analyses by comparing the displacement levels at which a matrix crack and a delamination crack initiated.

Table 3.2 Damage progression – displacement levels at which cracks initiated

	$[0_4/90_4]$	$[0_2/90_2]$	$[0/90]$
Cohesive matrix crack initiation	0.355	0.7	1.4
Fully developed matrix crack	0.72	2.019	6.3
Initiation of delamination	1.07	2.17	6.96

It can be observed that the load capacity increases with increasing thickness. The crack initiates at smaller displacement and larger load level with an increase in thickness. This is because, the formation of a crack is of more brittle nature while it is more ductile for smaller thickness laminates. It is worth to note that, in all the cases a through-the-thickness cohesive crack is inserted once the failure criterion is met. After this point damage progress was governed by the fracture energy included in the cohesive model. The observations made above are a clear indicator of the fact

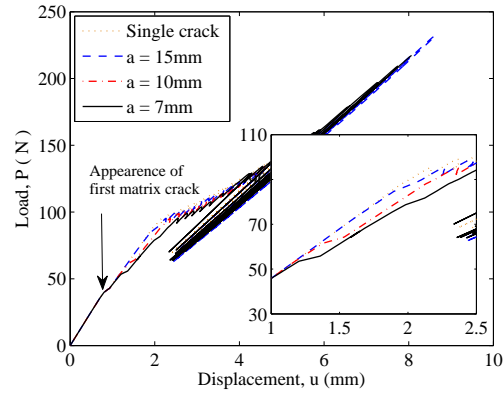


Figure 3.13 Load-displacement response of laminated beam - effect of crack spacing

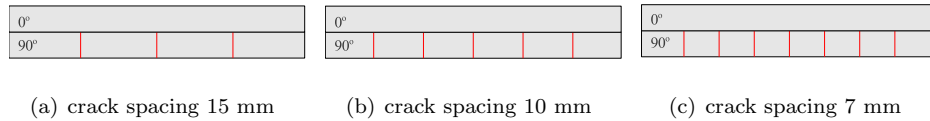


Figure 3.14 Crack locations at load $P \approx 140$ N

that size effects play a role in these laminates.

Effect of crack spacing

Next the effect of crack spacing is investigated for the laminated beam model. The analysis is performed with laminate configuration $[0_2/90_2]$. Three different crack spacings were used for the analysis, i.e. $a = 7$ mm, 10 mm and 15 mm. The same finite element mesh is used for all three analyses. The result of the analysis by means of load-displacement curves is shown in figure 3.13. Crack locations for the three cases are shown in figure 3.14. It can be observed from figure 3.13 that the initiation of the first matrix crack occurs at the same time in all three cases. However, the formation of more cracks in the case of a crack spacing of 7 mm resulted in degradation of the initial stiffness. Furthermore, the onset and growth of delamination is delayed for smaller crack spacing. After some time the responses of all three cases were approximately similar.

Effect of finite element discretization

In order to investigate the effect of mesh refinement on the response and damage of the laminated beam, four mesh discretizations are used along the length of beam.

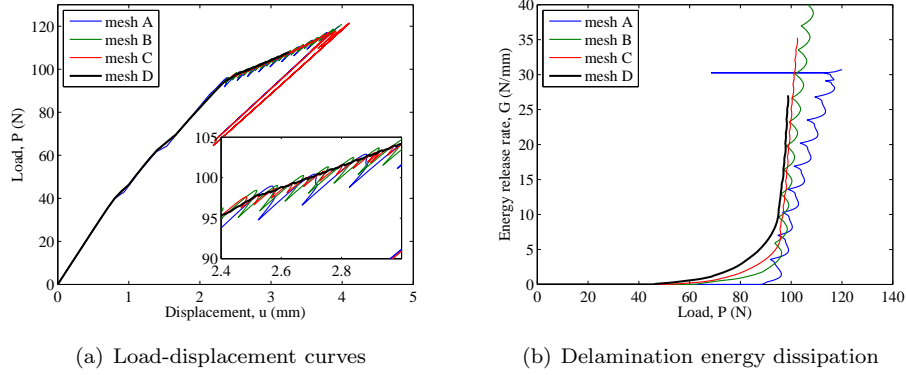


Figure 3.15 Laminated beam - effect of mesh discretization (Online version in colour.)

mesh-A consist of 101 elements, mesh-B consists of 202 elements, mesh-C consists of 303 elements and mesh-D consists of 403 elements along the length of beam per ply. The minimum crack spacing for the analysis was chosen to be 10 mm. The material and geometrical properties are the same as described in section 3.7.1. The analysis results are given in figure 3.15.

Figure 3.15a compares the load-displacement response of laminated beam modeled with three mesh discretizations. Figure 3.15a also shows a zoom-in to the region of the load-displacement curve during delamination. It is evident that the response of the three analyses is similar, however, the use of a finer mesh results in a gradual release of energy as an interface fails compared to a coarse mesh and results in a smooth load-displacement curve. Each bump of the load-displacement curve refers to the progression of the delaminated zone by a single element.

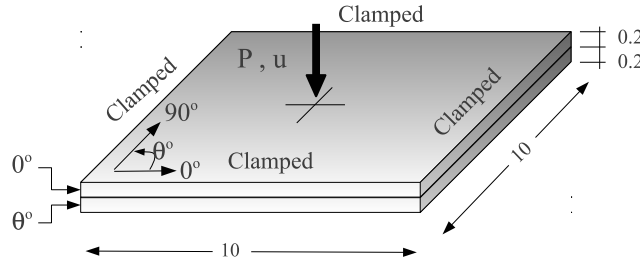
Figure 3.15b compares the total energy dissipation during delamination crack propagation as function of the load. It can be observed that the use of a fine mesh results in more energy dissipation for a particular load level compared to the coarse mesh. This is a direct consequence of using a nodal integration scheme, as usual with interface elements to avoid traction oscillations, due to under integration of the interface element. However, the solution converges to a unique solution with mesh refinement. The horizontal lines in figure 3.15b represent the snap backs in the load-displacement curve with zero or small energy dissipation.

3.7.2 Two-ply laminated plate

In order to investigate the performance of the developed progressive failure model in predicting the onset of damage, the interaction between matrix cracking and delamination cracking and their propagation along with mesh-independent propagation

Table 3.3 Material properties for laminated plate analysis

Laminate properties		Interfacial properties	
E_{11} (GPa)	140	G_{Ic} (N/mm)	0.3
$E_{22} = E_{33}$ (GPa)	10	G_{IIc} (N/mm)	0.7
$G_{12} = G_{13}$ (GPa)	5	f_n (MPa)	50
$\nu_{12} = \nu_{13}$	0.21	f_s (MPa)	30
ν_{23}	0.21		

**Figure 3.16** Plate model

of matrix cracking through the solid-like shell element, a two-ply laminated plate subjected to a center point load is analyzed. The geometry of the plate is shown in figure 3.16. The material properties used for the analysis are extracted from [164] and are given in table 3.3. The problem is studied for several laminate configurations and values for crack spacing. The cracks are allowed to develop only in the 90° plies, which are anticipated to affect the structural response more compared to the splitting cracks in 0° plies. It is noted that splitting cracks can influence the response of the laminate [4].

Single matrix crack analysis

In this section the capability of the model to predict arbitrary propagation of cracks through the finite element mesh and growth of delamination is studied. For analysis purpose two laminate configurations are considered, namely $[0/90]$ and $[0/75]$. It is noteworthy that the same finite element mesh is used for both analyses, which in case of interface elements would have required the generation of separate meshes in order to align the element edges with the cracks. The two cases are distinguished using a local material orientation. The average element size in the damage zone is $0.2 \times 0.2 \times 0.2$ mm. The analysis is performed with an uncracked plate and only a single crack is allowed to initiate and grow in fiber direction in each ply. Figures

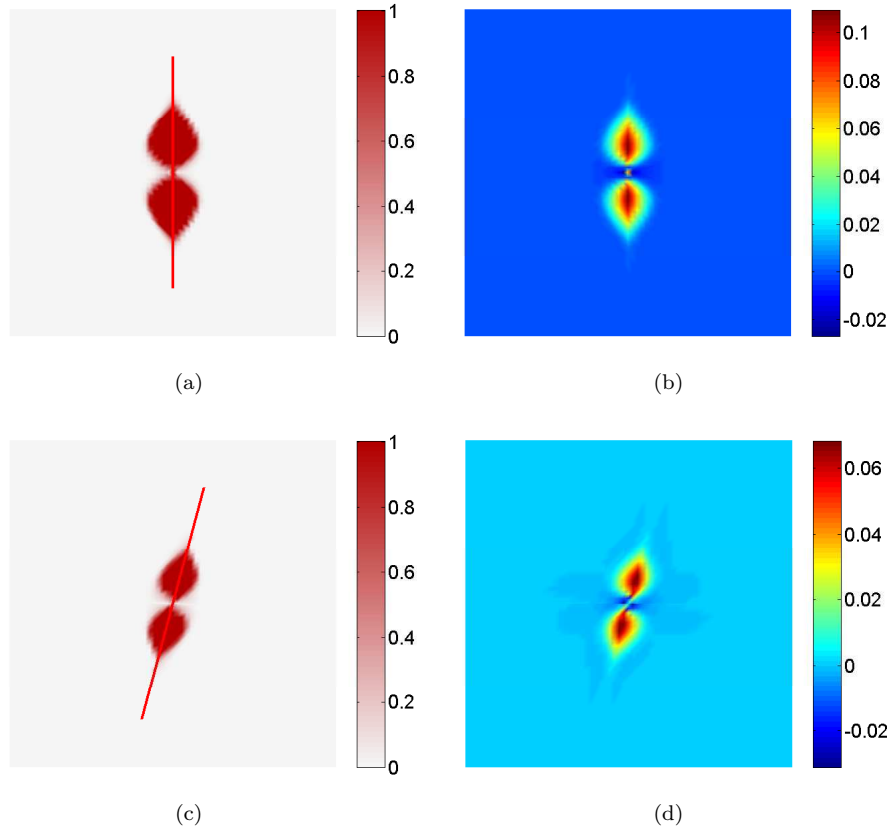


Figure 3.17 Analysis results for two-ply laminated plate with single matrix crack, Top: $[0/90]$, bottom: $[0/75]$, Left: delamination damage and matrix crack, Right: opening displacement at the interface

3.17 shows the analysis results for both laminate configurations. Figures 3.17a and c show the delamination damage along with the matrix cracks, while figures 3.17b and d show the opening displacement at the interface. As was expected, a bending crack appeared in the bottom ply oriented along the fiber direction. Moreover, the crack is propagating arbitrarily through the finite element mesh, figure 3.18. It is also evident from the figures that the model properly predicts the two lobe peanut-shape delamination areas for both laminate configurations. The delamination is aligned with the fiber direction of the lower ply along with the matrix crack. The results are qualitatively in good agreement with experimental observations of [98].

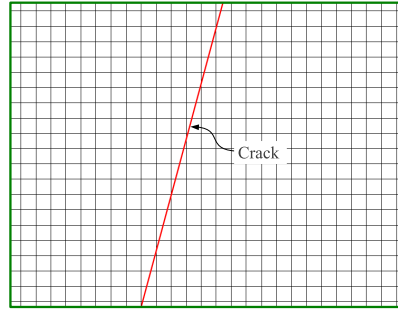


Figure 3.18 Zoom at crack [0/75]

Multiple matrix crack analysis- crack spacing 0.6 mm

In this section a two-ply [0/90] laminated plate is analyzed. The geometry and the material properties are the same as defined in the beginning of this section. Only one-half of the plate is modeled due to material and geometrical symmetry. Instead of allowing only one crack, multiple cracks are allowed to grow in the plate. However, the spacing between the cracks is kept fixed, i.e $a = 0.6$ mm.

Figure 3.19 shows the damage development at different load steps. Corresponding load steps are denoted in figure 3.20. It can be observed from figure 3.19 that damage begins by the formation of a bending matrix crack in the lower ply (90°). With increase in load, symmetric cracks appear on both sides of the center crack. A traction-free crack is shown by a thick light color line as part of the dark lines representing cohesive cracks. Once a traction-free crack is formed delamination damage is initiated in the shape of a half peanut, figure 3.19c. On a further increase of the load the delamination area propagates along with the propagation of a traction free crack and with the creation of more cohesive cracks. Note that the two processes i.e the formation of a traction-free crack and delamination, are growing side by side, signifying strong interaction between the two mechanisms. It can be observed that except for the center crack, the rest of the matrix cracks remain cohesive and did not develop into traction-free cracks. This is exactly what was observed in the experimental study of [98].

Figure 3.20b shows the total energy dissipation and energy dissipated in the shear-mode at the interface. It can be observed that delamination growth is taking place under mixed-mode conditions, in which there is equal contribution from the shearing and opening fracture modes.

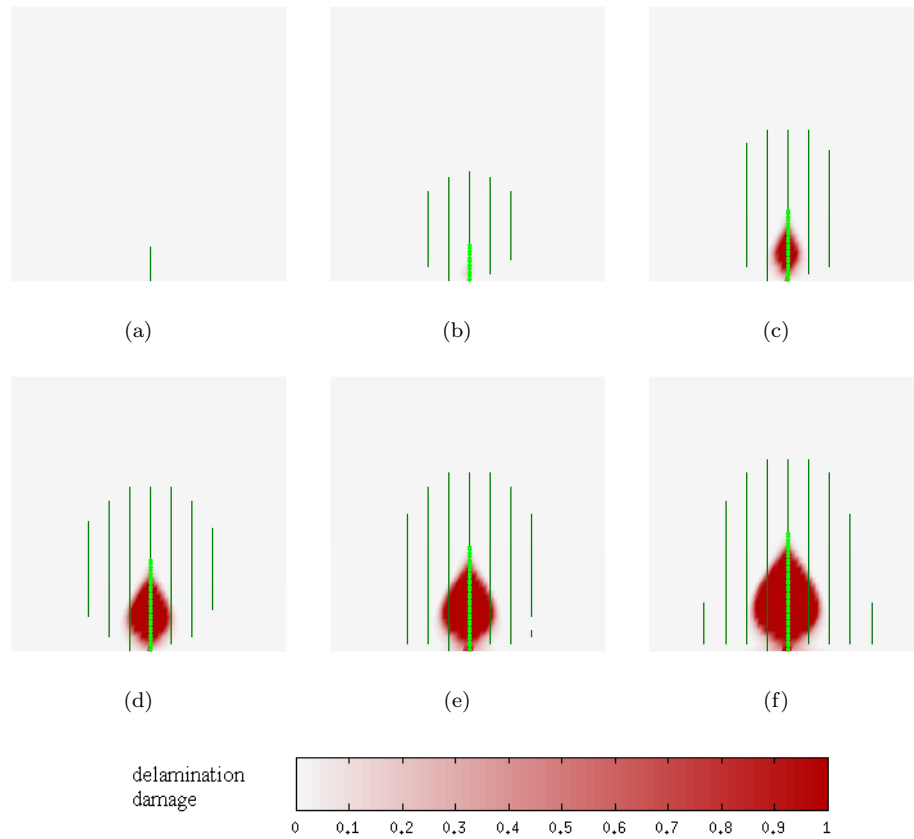


Figure 3.19 Damage development in two-ply laminated plate with crack spacing 0.6 mm- figure captions a – f indicates the load steps corresponding to figure 3.20a

Multiple matrix cracks analysis- crack spacing 0.3 mm

The same problem is now analyzed with reduced crack spacing, i.e $a = 0.3$ mm. Figure 3.21 shows the damage development in a plate at different load levels. It can be observed that the sequence of damage progress is the same as was observed for the analysis using 0.6 mm crack spacing. Comparing the damage at different instants for the two cases, it can be observed that more cohesive cracks are present in the analysis with smaller crack spacing. However, the corresponding delamination damage zone and the length of the traction-free crack are the same. Moreover, the zone over which matrix cracking takes place for both crack spacing remains the same. In spite of the formation of more matrix cracks, only the center crack becomes traction free while the rest of the cracks did not significantly contribute to damage development and

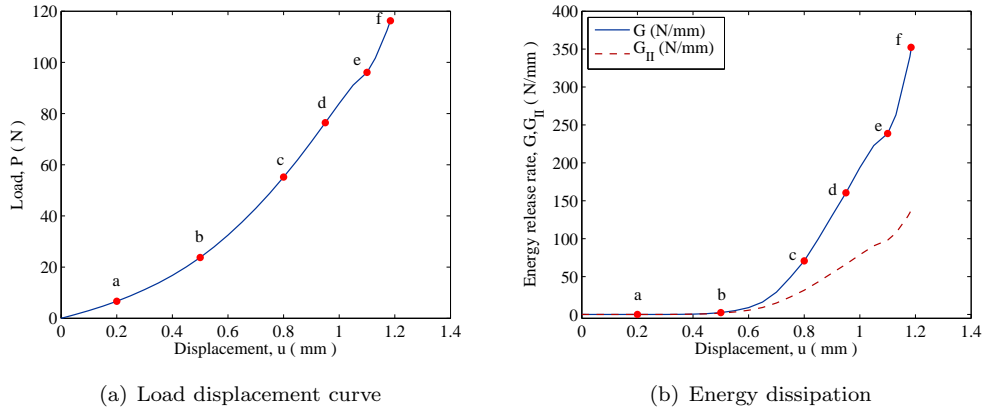


Figure 3.20 Load-displacement and energy dissipation of two-ply laminated plate with crack spacing 0.6 mm

remain closed. This signifies that the crack spacing parameter is not significantly influencing the response and overall damage development.

Influence of crack density

Next, a comparison is made between three different analyses (1) a multiple crack analysis with crack spacing 0.6 mm, (2) a multiple crack analysis with crack spacing 0.3 mm and (3) a single crack analysis. In case of the single crack analysis, in contrast to the multiple crack analyses, an initial traction free crack was inserted traversing the whole width of the plate. Note that this case is different from the single crack analysis of section 3.7.2 where the analysis was performed with an uncracked plate and a single cohesive crack was inserted and allowed to propagate based on failure and fracture criteria, respectively.

Figure 3.22a compares the load-displacement curves for the three analyses. It can be seen from the graph that the load displacement curves for single crack analysis and multiple crack analysis lie on top of each other. This indicates that the damage in this case is primarily dominated by a single centered bending matrix crack. The contribution of the other cracks is not so significant to initiate delamination damage and delamination propagation is mainly governed by the progressive opening of the center matrix crack. Indeed this is what was observed in the experimental studies e.g. in [47, 98] and it is for this reason, the investigators in [47] were able to model delamination damage with a single bending matrix crack.

The above conclusions are substantiated by figure 3.23a, which compares the history of the total energy dissipation during delamination damage for the three cases. It can be inferred from figure 3.23a that the delamination onset as well as energy

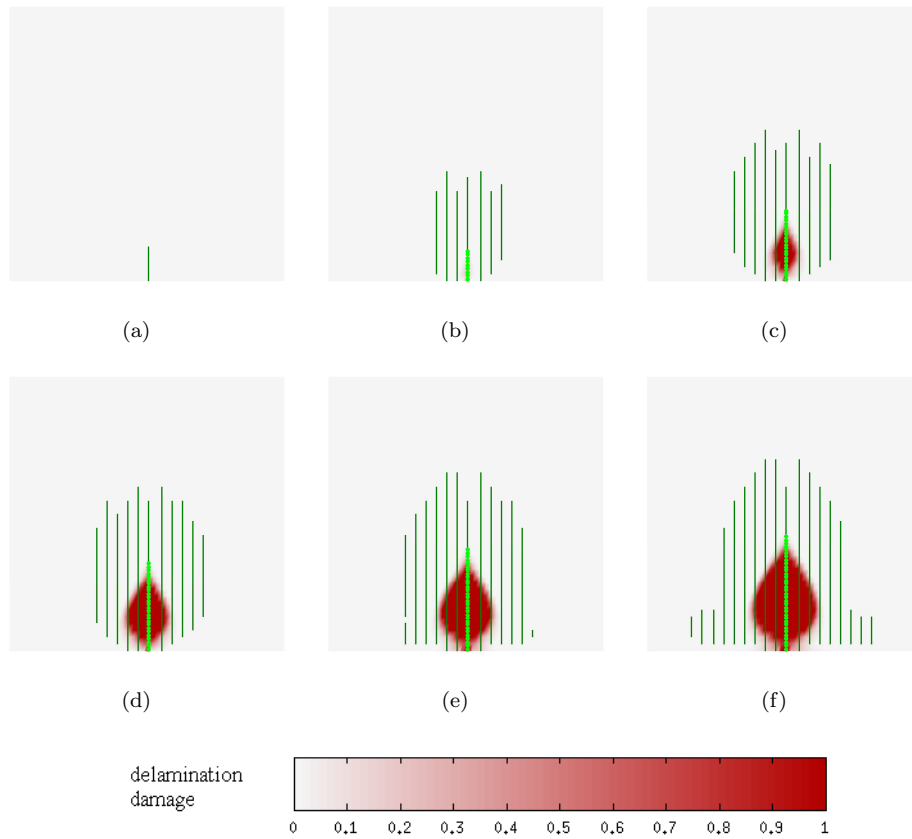


Figure 3.21 Damage development in two-ply laminated plate with crack spacing 0.3mm- figure captions a – f indicates the same load steps marked in figure 3.20a

dissipation is the same for the two cases of multiple crack analyses, i.e a multiple crack analysis with 0.6 mm and 0.3 mm crack spacing. A single crack analysis shows small deviation from the other two curves and gives more energy dissipation and an earlier delamination onset. This is due to the presence of an initial traction-free crack in the single crack analysis. The plate has only one source of energy dissipation i.e delamination damage, as compared to the multiple crack analysis where the energy input into the system is dissipated by two mechanisms i.e delamination damage and matrix cracking. Of course, a multiple crack analysis without initial cracks represents the real situation, where the progressive growth of matrix cracks together with delamination damage occurs concurrently.

Figure 3.23b compares the history of total energy dissipation by matrix cracking

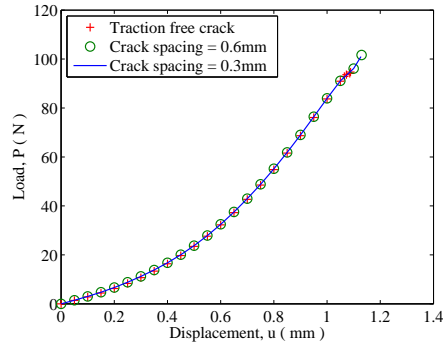
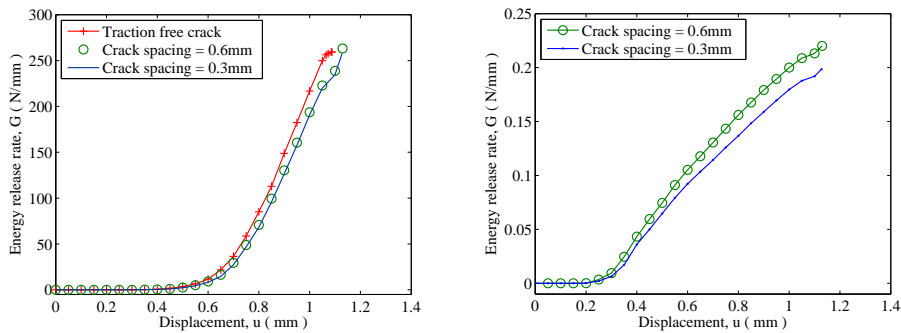


Figure 3.22 Load-displacement curves for multiple cracks analyses and single crack analysis



(a) Energy dissipation in delamination damage (b) Energy dissipation in matrix cracking damage

Figure 3.23 Comparison of energy dissipation

damage in the three analyses. Even though delamination damage for the two analysis with crack spacing 0.6 mm and 0.3 mm is approximately the same, it can be observed from figure 3.23b that the energy dissipated by matrix cracking damage is slightly more for the case of a larger crack spacing. It is noted that the magnitude of energy dissipation in matrix cracking is very small compared to the energy dissipation in delamination damage. Therefore this small difference in energy dissipation for smaller crack spacing compared to larger crack spacing analysis did not cause significant change in the response and damage development in the two-ply laminated plate. The reason for decreased energy dissipation for smaller crack spacing can be explained by the fact that the interface cohesive law has a finite initial stiffness, therefore incorporating more cracks resulted in more locations of stress enhancers for the interface. Since the magnitude of stresses was not too large, these cracks

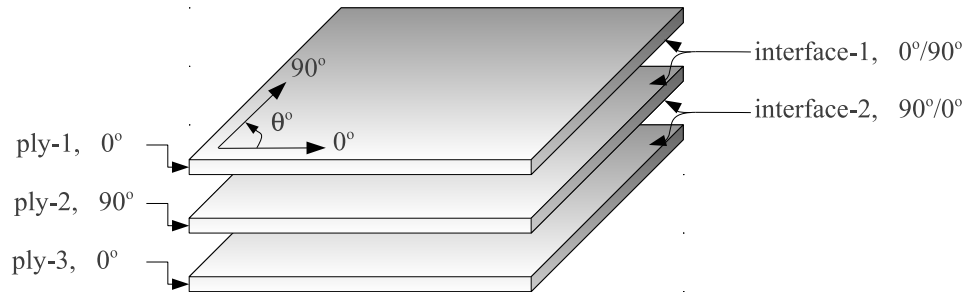


Figure 3.24 Three-ply laminated plate

did not result in onset and propagation of delamination damage, rather resulted in elastic opening of the interface. As a result the system becomes more flexible and prevented damage in matrix cracking compared to the case of large crack spacing analysis.

3.7.3 Three-ply laminated plate, [0/90/0]

In order to investigate the performance of the model in predicting damage due to shear matrix cracks, a three-ply laminated plate with stacking sequence [0/90/0] is analyzed. The in-plane dimensions of the plate, the boundary conditions and the material properties are the same as used in the previous section (section 3.7.2). A schematic three-ply laminated plate is shown in figure 3.24, representing different plies and interfaces. The thickness of each ply is 0.2 mm.

Figure 3.25 shows the damage development at different stages of loading. The damage pattern is the same as was observed during experiments [36, 98, 100], where minor delamination occurs at the top interface (interface-1) and major delamination at the bottom interface (interface-2) of the cracked ply. The damage starts with the formation of two matrix cracks in ply-2. The formation and propagation of cracks is accompanied with damage development at interface-1 and interface-2. Further increase in load results in the formation of more cohesive cracks distributed in ply-2 figure 3.25c. As soon as the two center cracks become traction free, major delamination occurred at the bottom interface (interface-2). The delaminated area is peanut-shaped and is oriented towards the fiber orientation of the lower ply (ply-3). On the contrary, the delamination area is confined near the center of the plate in the upper interface (interface-1).

Figure 3.26 shows the total energy release rate and the energy release rate in shear during delamination damage at interface-2. It can be observed that the damage is primarily dominated by shear damage with very little or no mode I opening at the

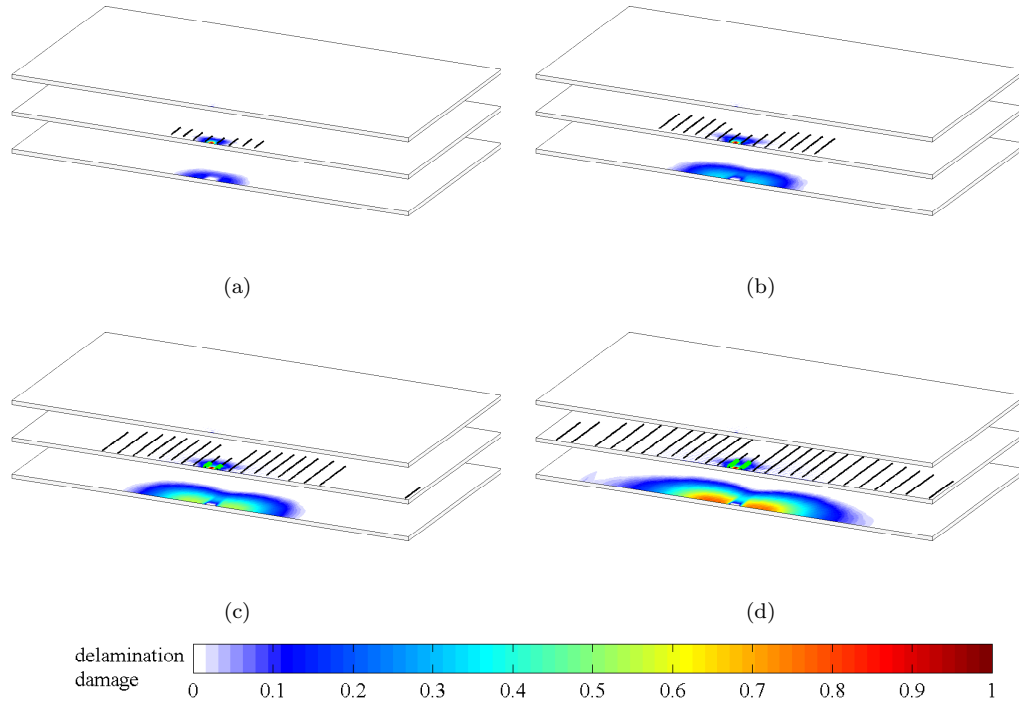


Figure 3.25 Damage development in three ply laminated plate at load levels $P = 77.7, 138.7, 181.6$ and 232.9 N

damage interface.

3.7.4 Verification of a square GFRP laminated plate

A square, $[0_{10}/90_{20}/0_{10}]$ graphite-fiber reinforced laminated plate is analyzed. Geometry and boundary conditions of the plate are shown in figure 3.27. The plate is simply supported on all edges and is loaded with a central transverse load. Material properties used for the analysis are given in table 3.4. Figure 3.28 shows the load displacement response in comparison with the experimental results of [79]. The numerical results show good agreement with the experimental results. Different labels on the graph show the sequence of different damage mechanisms. It is evident that formation of matrix cracking triggers delamination damage. Figure 3.29 shows delamination damage at the interfaces and matrix cracking in the plies. A peanut shape delamination damage area under mode-II fracture is evident from figure 3.29b.

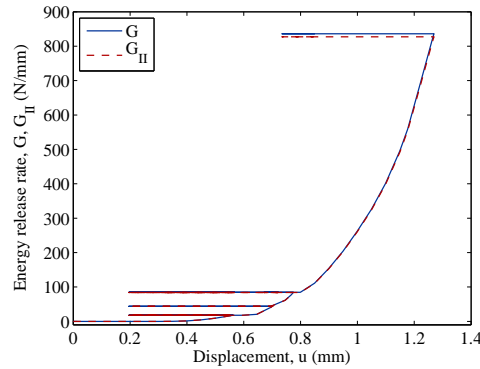


Figure 3.26 Energy release rate during delamination at interface-2

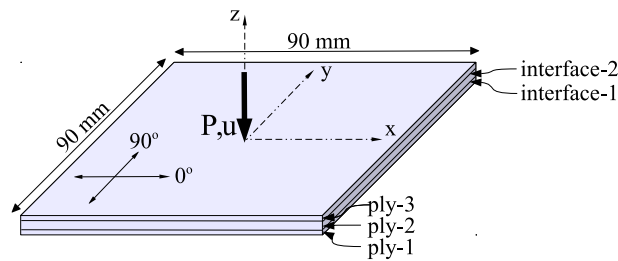


Figure 3.27 A GFRP laminated plate under transverse loading

3.8 Conclusions

A finite element model is presented to simulate progressive failure in laminated composites subjected to transverse loading conditions. The model uses solid-like shell elements which, on one hand, are able to model thin plies of a laminate and, on the other hand, give a complete three-dimensional state of stress. This is crucial for the proper modeling of delamination damage.

The model is capable of simulating mesh independent matrix cracking. This avoids the need of orienting the finite element edges along the cracks. As a result of this, modeling of arbitrary propagating cracks is possible and failure analysis can be performed with different laminate configurations using the same finite element mesh.

To model delamination phenomena an alternative approach compared to traditional interface elements is used, which allows for a full kinematic representation of the interface and makes computation of different kinematic quantities at the interface straightforward. Moreover, the model gives rapid convergence of the Newton-

Table 3.4 Material properties used for GFRP laminated plate

Ply level properties	
Longitudinal Young's modulus, E_{11} (GPa)	37.9
Transverse Young's modulus, $E_{22} = E_{33}$ (GPa)	9.07
In-plane shear modulus, $G_{12} = G_{13}$ (GPa)	3.72
Poisson's ratio, $\nu_{12} = \nu_{13}$	0.3573
Poisson's ratio, ν_{23}	0.4
Mode I fracture toughness, G_{Ic} (N/mm)	0.2
Mode II fracture toughness, G_{IIc} (N/mm)	0.6
Transverse tensile strength, f_{2t} (MPa)	20
In-plane shear strength, f_{12} (MPa)	35.5

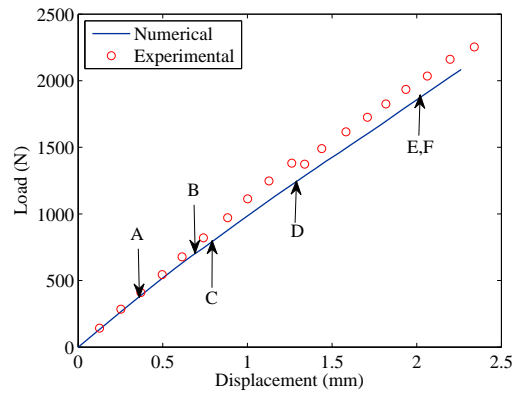
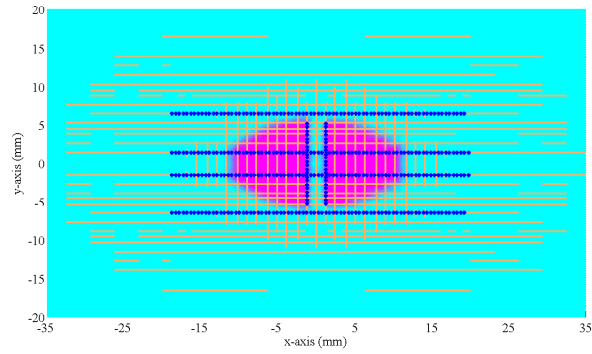


Figure 3.28 Load-displacement curve of a GFRP laminated plate; A-initiation of cohesive matrix cracking in ply-1, B-initiation of cohesive matrix cracking in ply-2, C-initiation of a traction-free matrix crack in ply-1, D-initiation of delamination at interface-2, E-initiation of a traction-free matrix crack in ply-2, F-initiation of delamination at interface-1

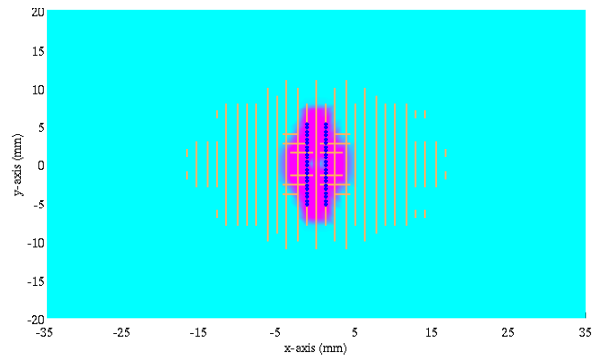
Raphson scheme due to the possibility of evaluating consistently the linearized tangent stiffness matrix for the interface contribution in large deformation problems.

A mixed-mode, exponentially decaying cohesive constitutive law is presented for both matrix cracking and delamination damage. The cohesive law uses a single scalar damage variable.

The presented computational framework is also able to take the strong interaction between matrix cracks and delamination damage into account. The combined modeling of matrix cracking and delamination is achieved without incorporation of additional degrees of freedom. Numerical simulations show that damage due to both bending cracks as well as shear cracks is predicted correctly and commonly observed



(a)



(b)

Figure 3.29 Delamination damage at the interfaces and matrix cracking in the connecting plies at $P = 2000$ N; (a) Delamination at interface-2 and matrix cracking in ply-3 (horizontal cracks) and ply-2 (vertical cracks), (b) Delamination at interface-1 and matrix cracking in ply-1 (horizontal cracks) and ply-2 (vertical cracks). Dark lines indicate traction-free portion of the cracks

peanut-shapes of delamination damaged zones aligned with the fiber orientation are observed. Moreover, the effect of crack density, for the problem investigated here, over the damage pattern is observed not to be so significant. The size of the damaged zone remains the same. However, differences in the lengths of the matrix cracks are observed.

Chapter 4

Solid-like shell element for dynamic analysis of plates and shells*

This chapter presents a full three-dimensional solid-like shell element for dynamic analysis of isotropic, orthotropic and anisotropic laminated composites. The dynamic variational formulation is based on a degenerated-shell concept which uses a compatible displacement field varying quadratically in the through-the-thickness direction in order to overcome Poisson-thickness locking. Mass discretization schemes for implicit and explicit dynamic analysis are presented. A selective mass scaling scheme is proposed for explicit analysis to avoid the use of extremely small time steps needed to resolve high element eigen-frequencies, introduced by the presence of internal degrees of freedom and a small thickness of the element. It is further explained, that a mid-surface and plane-stress constitutive law assumption lead to inaccurate results compared to realistic cases where the Neumann and Dirichlet boundary conditions are applied at the surface of the plates and shells.

4.1 Introduction

Shell structures are commonly used in many engineering applications, for example, automotive, space vehicles, pressure vessels etc. These structures are often subjected to static, dynamic, impact and thermal loading conditions. The analysis of these structures has been of interest for researchers for several decades. Owing to the fact that thickness of these structures is considerably smaller than the in-plane dimensions, two-dimensional (2-D) shell elements are appealing for finite element analysis. This resulted in several geometrically linear and nonlinear 2-D shell elements, see for instance [11, 117, 123, 144, 162] for dynamic analysis of shell/plate structures. However, these models are based on plane-stress constitutive relations and therefore thickness change was not taken into account in these formulations.

There are a number of instances where a complete three-dimensional (3-D) analysis is inevitable, such as sheet metal forming, damage analysis of plates/shells, delamination in laminated composites etc. Moreover, analysis of thick shells with pressure

* This chapter is extracted from [8]

acting on their surfaces result in a thickness change and corresponding stresses require three-dimensional evaluation. These are not accounted for in 2-D shell models. The thickness change and the corresponding stress are obtained in a post-processing stage. Moreover, in cases in which both surfaces of the shell are subjected to pressure, 2-D shell models neither give a thickness change nor a corresponding stress. In addition to this, due to the 2-D nature of shell elements, the kinematics are defined at the shell mid-surface. As a consequence, the boundary conditions can only be applied to the shell mid-surface. However, in reality the Neumann and the Dirichlet boundary conditions are usually applied at the shell surfaces. Application of boundary conditions at the shell mid-surface may be a good assumption for thin shells but not for thick shells, where thickness change and corresponding stresses may play a role. This may result in a different response compared to cases where the boundary conditions are applied at the shell surfaces, as is shown in this article.

Acknowledging the importance and the need of 3-D shell elements, several formulations have been presented based on a degenerated shell concept, see for example [1, 69]. However, these elements have a tendency to lock in thin shell applications due to Poisson-thickness locking. To overcome this problem extra degrees of freedom (dofs) are sometimes added to obtain a linearly varying strain field through-the-thickness, [27, 64, 84, 116]. This is usually achieved either by using enhanced assumed strain (EAS) methods, which enrich the strain field with incompatible strains to include higher-order strains in thickness direction, for example by [27, 84], or by using a quadratic displacement field in thickness direction, [116]. [123] presented a finite element procedure based on a degenerated shell element of [1], for dynamic analysis of laminated structures. However, the shell element uses a plane-stress constitutive law. [163] presented a degenerated continuum-based shell element for dynamic analysis. An improved displacement field was proposed with additional shear correction factors to take the transverse shear deformations into account. [157] presented a solid-shell element based on the mixed Hu-Washizu variational principle for dynamic analysis of multilayer composites. [94] used a continuum-based shell element having shell kinematics similar to [128] for damage analysis of isotropic shells under dynamic (impact) conditions. The analysis was performed with a full mass matrix.

Explicit dynamic simulations become extremely powerful when a lumped mass matrix is used. However, explicit integration schemes are only conditionally stable and the critical time step is limited by the maximum eigenfrequency of the system. For thin shell structures, the critical time is restricted by the eigenfrequencies of the thickness vibration modes. Moreover, for analysis cases, such as modelling cracking phenomena in shell structures e.g [2, 5], one may require internal dofs (included to remove Poisson-thickness locking) to be considered as global dofs to avoid poor conditioning of the element stiffness matrix used for static condensation of internal dofs. These internal dofs are associated with high frequency vibration modes and thus

will further reduce the critical time step. In these circumstances special mass lumping procedures are required for performing efficient and accurate explicit dynamic analysis. [70] presented a selective mass scaling procedure for plate elements with independent rotational degrees of freedom. [112] presented a mass scaling method where nodal accelerations are scaled such that only the higher eigenfrequency domain is affected. In [111], in contrast to acceleration scaling, the scaling was applied to the mass matrix. However, the resulting mass matrix was no longer diagonal.

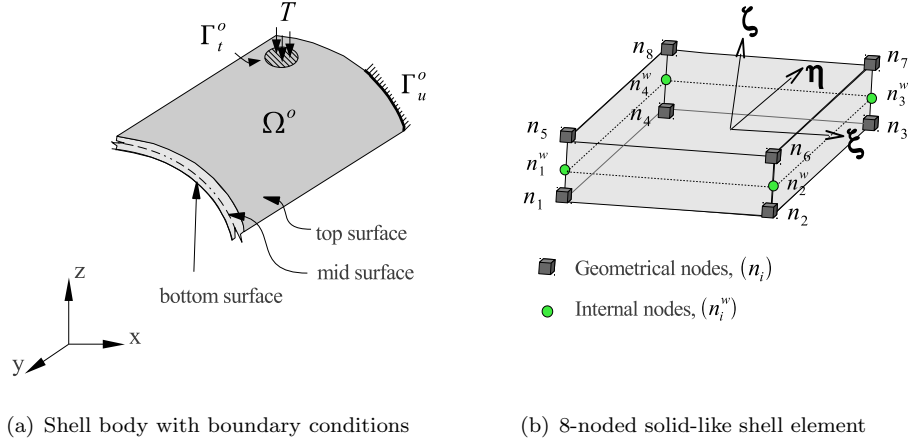
In this chapter a solid-like shell element for performing dynamic, geometrically linear and nonlinear analysis of plates/shells is presented. The dynamic variational formulation is an extension of the nonlinear shell theory of [116], which uses a compatible displacement field varying quadratically through-the-thickness of the shell. An improved finite element formulation of [10] is used, where the formulation of [116] is extended to incorporate strain terms corresponding to the higher-order thickness coordinate. These strain terms become important in the presence of large strains with bending deformations and shells with large bending curvatures [108]. The effects of mass discretization and inertial effects due to the internal degrees of freedom on the response of plates/shells are discussed. Mass discretization strategies for explicit and implicit dynamic analysis using solid-like shell elements are presented. The issue of defining masses corresponding to the internal degrees of freedom is addressed and procedures for defining consistent and lumped mass matrices are presented. A selective mass scaling method for solid-like shell elements is proposed to increase the critical time step in explicit dynamic simulations. Moreover, the effect of thickness change and the position of application of Neumann and Dirichlet boundary conditions on the dynamic response of plates and shells are also discussed.

An outline of the chapter is as follows. In the next section, the kinematics, the variational formulation and the finite element implementation details of the dynamic solid-like shell element are presented. Section 4.3 discusses in detail the mass discretization strategies for implicit and explicit dynamic analysis using solid-like shell elements. In section 4.4, finite element simulation results are presented for small and large deformations of isotropic, orthotropic and laminated composite plates/shells and are compared with the available reference solutions in literature.

4.2 Dynamic Solid-Like Shell Element (SLS) formulation

4.2.1 Kinematics

In this section, we review the kinematics of a solid-like shell element. The shell body is defined with a top surface, bottom surface and a degenerated mid-surface, figure 4.1. The displacement field, $\boldsymbol{\vartheta}$, of a solid-like shell element in a curvilinear coordinate



(a) Shell body with boundary conditions

(b) 8-noded solid-like shell element

Figure 4.1 Geometry and kinematics of solid-like shell

system (ξ, η, ζ) is defined as

$$\boldsymbol{\vartheta}(\xi, \eta, \zeta) = \mathbf{u}^o(\xi, \eta) + \zeta \mathbf{u}^1(\xi, \eta) + (1 - \zeta^2) \mathbf{u}^2(\xi, \eta) \quad (4.1)$$

where \mathbf{u}^o is the displacement of the shell mid-surface

$$\mathbf{u}^o(\xi, \eta) = [\mathbf{u}_t(\xi, \eta) + \mathbf{u}_b(\xi, \eta)] / 2 \quad (4.2)$$

\mathbf{u}^1 is the displacement of the shell director, \mathbf{D}

$$\mathbf{u}^1(\xi, \eta) = [\mathbf{u}_t(\xi, \eta) - \mathbf{u}_b(\xi, \eta)] / 2 \quad (4.3)$$

and \mathbf{u}^2 denotes internal stretching of an element, which is collinear with the deformed shell director, \mathbf{d} , and a function of thickness stretch variable, ω

$$\mathbf{u}^2(\xi, \eta) = \omega(\xi, \eta) \mathbf{d}(\xi, \eta) \quad (4.4)$$

The velocity of any material point is given by

$$\dot{\boldsymbol{\vartheta}}(\xi, \eta) = \dot{\mathbf{u}}^o + \zeta \dot{\mathbf{u}}^1 + (1 - \zeta^2)(\dot{\omega} \mathbf{d} + \omega \dot{\mathbf{d}}) \quad (4.5)$$

The acceleration of any material point is given by

$$\ddot{\boldsymbol{\vartheta}}(\xi, \eta) = \ddot{\mathbf{u}}^o + \zeta \ddot{\mathbf{u}}^1 + (1 - \zeta^2)(\ddot{\omega} \mathbf{d} + \omega \ddot{\mathbf{d}} + 2\dot{\omega} \dot{\mathbf{d}}) \quad (4.6)$$

4.2.2 Variational formulation

The conservation of linear momentum states

$$\text{DIV } \mathbf{P} + \hat{\mathbf{b}} = \rho \ddot{\boldsymbol{\vartheta}} \quad \text{in } \Omega^o \quad (4.7)$$

where \mathbf{P} is the first Piola-Kirchhoff stress tensor. $\hat{\mathbf{b}} = J\mathbf{b}$, is the body force in the current configuration with respect to the reference volume. $J = \det(\mathbf{F})$, is Jacobian, \mathbf{b} is the body force in the current configuration with respect to the current volume, \mathbf{F} is the deformation gradient and ρ is the density in the current configuration with respect to volume in the reference configuration.

By defining $\delta\boldsymbol{\vartheta}$ as the compatible variation of the displacement field and ignoring the integrands for brevity, the weak form of equilibrium is obtained as

$$\int_{\Omega^o} \nabla^o \delta\boldsymbol{\vartheta} : \mathbf{P} + \int_{\Omega^o} \delta\boldsymbol{\vartheta} \cdot \rho \ddot{\boldsymbol{\vartheta}} - \int_{\Gamma_t^o} \delta\boldsymbol{\vartheta} \cdot \mathbf{T} - \int_{\Omega^o} \delta\boldsymbol{\vartheta} \cdot \hat{\mathbf{b}} = \mathbf{0} \quad (4.8)$$

In equation (4.8), \mathbf{T} are the tractions in the current configuration with respect to the reference area, Γ_t^o . Since the term $\nabla^o \delta\boldsymbol{\vartheta} : \mathbf{P}$ is energetically equivalent to the work-conjugate term $\delta\mathbf{E} : \boldsymbol{\Sigma}$, the above equilibrium equation can be written as

$$\int_{\Omega^o} \delta\mathbf{E} : \boldsymbol{\Sigma} + \int_{\Omega^o} \delta\boldsymbol{\vartheta} \cdot \rho \ddot{\boldsymbol{\vartheta}} - \int_{\Gamma_t^o} \delta\boldsymbol{\vartheta} \cdot \mathbf{T} - \int_{\Omega^o} \delta\boldsymbol{\vartheta} \cdot \hat{\mathbf{b}} = \mathbf{0} \quad (4.9)$$

Equation (4.9) defines the principle of virtual work, in which \mathbf{E} and $\boldsymbol{\Sigma}$ are the Green-Lagrange strain and the Second-Piola Kirchhoff stress tensors, respectively. The variational strain field, $\delta\mathbf{E}$, is defined as

$$\delta E_{ij} = \frac{1}{2} (\mathbf{G}_i \cdot \delta\boldsymbol{\vartheta}_{,j} + \mathbf{G}_j \cdot \delta\boldsymbol{\vartheta}_{,i} + \delta\boldsymbol{\vartheta}_{,i} \cdot \boldsymbol{\vartheta}_{,j} + \boldsymbol{\vartheta}_{,i} \cdot \delta\boldsymbol{\vartheta}_{,j}) \quad (4.10)$$

in which the higher-order term $(\delta\boldsymbol{\vartheta}_{,i} \cdot \delta\boldsymbol{\vartheta}_{,j})$ is considered to be very small and may be neglected, [61, 116]. \mathbf{G}_i is the covariant base vector in the reference configuration. The variation of the displacement field is given as:

$$\delta\boldsymbol{\vartheta} = \delta\mathbf{u}^o + \zeta\delta\mathbf{u}^1 + (1 - \zeta^2)\delta\mathbf{u}^2 \quad (4.11)$$

The variation of the gradients of the displacement field is given as:

$$\delta\boldsymbol{\vartheta}_{,\alpha} = \delta\mathbf{u}_{,\alpha}^o + \zeta\delta\mathbf{u}_{,\alpha}^1 \quad \alpha = 1, 2 \quad (4.12a)$$

$$\delta\boldsymbol{\vartheta}_{,3} = \delta\mathbf{u}^1 - 2\zeta\delta\mathbf{u}^2 \quad (4.12b)$$

in which the terms corresponding to $\delta\mathbf{u}_{,\alpha}^2$ can be neglected [61, 116]. The variation of \mathbf{u}^2 yields

$$\delta\mathbf{u}^2 = \delta\omega\mathbf{d} + \omega\delta\mathbf{u}^1 \quad (4.13)$$

4.2.3 Constitutive relations

A linear elastic relationship between the Second-Piola Kirchhoff stress tensor, $\boldsymbol{\Sigma}$, and the Green-Lagrange strain tensor, \mathbf{E} , is used

$$\boldsymbol{\Sigma} = \mathbb{C} : \mathbf{E} \quad (4.14)$$

in which \mathbb{C} is the fourth-order material tangent stiffness tensor with

$$[\mathbf{C}]^{-1} = \begin{bmatrix} \frac{1}{E_{11}} & \frac{-\nu_{21}}{E_{22}} & \frac{-\nu_{31}}{E_{33}} & 0 & 0 & 0 \\ \frac{-\nu_{12}}{E_{11}} & \frac{1}{E_{22}} & \frac{-\nu_{32}}{E_{33}} & 0 & 0 & 0 \\ \frac{\nu_{13}}{E_{11}} & \frac{-\nu_{23}}{E_{22}} & \frac{1}{E_{33}} & 0 & 0 & 0 \\ 0 & 0 & 0 & \frac{1}{G_{12}} & 0 & 0 \\ 0 & 0 & 0 & 0 & \frac{1}{G_{23}} & 0 \\ 0 & 0 & 0 & 0 & 0 & \frac{1}{G_{13}} \end{bmatrix} \quad (4.15)$$

in which \mathbf{C} is the matrix form of tensor \mathbb{C} [72], obtained using a Voigt notation. The subscript 1,2 and 3 denote the orthogonal axis of the principal material coordinate system. A special case of anisotropic material i.e transversely isotropic material such as a fiber reinforced composite material, is considered by assuming axis 1 to be aligned with the fiber direction, the axis 2 in the plane of the lamina and perpendicular to the fiber and axis 3 perpendicular to the plane of lamina. Material symmetry is assumed to be in the 2-3 plane. A transformation matrix \mathbb{T} defined in [72] can be used to transform the material tangent matrix \mathbf{C} from material frame reference (1-2-3) to global frame reference (x-y-z).

4.2.4 Finite element discretization

The solid-like shell element considered in this work is an eight-noded solid element. The node numbering and geometry of the element are shown in figure 4.1. Each geometrical node i is associated with three degrees of freedom $\mathbf{u}(u_x, u_y, u_z)_i$ and each internal node is associated with one degree of freedom ω_i . This leads to a total of 28 degrees of freedom. For an element e , the displacement vector is arranged as:

$$\hat{\boldsymbol{\vartheta}} = [\hat{\mathbf{u}}_1, \hat{\mathbf{u}}_2, \dots, \hat{\mathbf{u}}_8, \hat{\omega}_1, \dots, \hat{\omega}_4]^T = [\hat{\mathbf{U}}, \hat{\mathbf{W}}]^T \quad (4.16)$$

The discretized displacement field of a shell mid-surface (\mathbf{u}^o), shell director (\mathbf{u}^1) and internal stretching variable (ω) in equation (4.1) and corresponding velocities and accelerations in equations (4.5) and (4.6), respectively, for element e are given as:

$$\mathbf{u}_e^o = \mathbf{N}^o \hat{\mathbf{U}}_e, \quad \dot{\mathbf{u}}_e^o = \mathbf{N}^o \hat{\dot{\mathbf{U}}}_e, \quad \ddot{\mathbf{u}}_e^o = \mathbf{N}^o \hat{\ddot{\mathbf{U}}}_e \quad (4.17a)$$

$$\mathbf{u}_e^1 = \mathbf{N}^1 \hat{\mathbf{U}}_e, \quad \dot{\mathbf{u}}_e^1 = \mathbf{N}^1 \hat{\dot{\mathbf{U}}}_e, \quad \ddot{\mathbf{u}}_e^1 = \mathbf{N}^1 \hat{\ddot{\mathbf{U}}}_e \quad (4.17b)$$

$$\omega_e = \mathbf{N}^\omega \hat{\mathbf{W}}_e, \quad \dot{\omega}_e = \mathbf{N}^\omega \hat{\dot{\mathbf{W}}}_e, \quad \ddot{\omega}_e = \mathbf{N}^\omega \hat{\ddot{\mathbf{W}}}_e \quad (4.17c)$$

in which \mathbf{N}^o , \mathbf{N}^1 and \mathbf{N}^ω are the shape function matrices of the solid-like shell element, see [10]. The nodal quantities are represented with a hat over the quantity.

The discretization of the variational equilibrium, equation (4.9), requires evaluation of $\delta\mathbf{E}$ and $\delta\boldsymbol{\vartheta}$. The vector of virtual strain components is arranged as

$$[\delta\mathbf{E}]_{6 \times 1} = \{\delta E_{11}, \delta E_{22}, \delta E_{33}, 2\delta E_{12}, 2\delta E_{23}, 2\delta E_{13}\} \quad (4.18)$$

The vector of virtual strains is related to the nodal displacement vector through a gradient operator matrix \mathbf{B} as

$$\delta\mathbf{E} = (\mathbf{B}_L + \mathbf{B}_{NL}) \delta\hat{\boldsymbol{\vartheta}} = \mathbf{B} \delta\hat{\boldsymbol{\vartheta}} \quad (4.19)$$

with $\mathbf{B} = \mathbf{B}_L + \mathbf{B}_{NL}$. \mathbf{B}_L and \mathbf{B}_{NL} are the strain-displacement matrices defined in [10].

The discrete form of the variation of the compatible displacement field for the solid-like shell element is given as

$$\delta\boldsymbol{\vartheta} = \mathbf{N} \delta\hat{\boldsymbol{\vartheta}} \quad (4.20)$$

The matrix \mathbf{N} is given as

$$[\mathbf{N}] = [\mathbf{N}^o + \zeta\mathbf{N}^1 + (1 - \zeta^2)\omega\mathbf{N}^1, (1 - \zeta^2)\mathbf{dN}^\omega] \quad (4.21)$$

Moreover, since the load can only be applied on the geometrical nodes ([116]), a modified variational field $\delta\boldsymbol{\vartheta}^*$ is defined, which replaces the variational terms corresponding to external load parts of the variational equilibrium equation. The modified variational field is defined as

$$\delta\boldsymbol{\vartheta}^* = \delta\mathbf{u}^o + \zeta\delta\mathbf{u}^1 \quad (4.22)$$

The corresponding discretized form of the modified variational field is given as

$$\delta\boldsymbol{\vartheta}^* = \mathbf{N}^* \delta\hat{\mathbf{U}} \quad (4.23)$$

where the matrix \mathbf{N}^* is defined as

$$\mathbf{N}^* = \mathbf{N}^o + \zeta\mathbf{N}^1 \quad (4.24)$$

Incorporating the variations in the variational equations (4.9), we obtain

$$\int_{\Omega^o} 2\rho(1 - \zeta^2)\mathbf{N}^T \dot{\omega} \dot{\mathbf{d}} + \int_{\Omega^o} \mathbf{N}^T \rho \mathbf{N} \ddot{\boldsymbol{\vartheta}} + \int_{\Omega^o} \mathbf{B}^T \boldsymbol{\Sigma} - \int_{\Gamma_i^o} \mathbf{N}^{*T} \mathbf{T} - \int_{\Omega^o} \mathbf{N}^{*T} \hat{\mathbf{b}} \quad (4.25)$$

Note that, the first term of equation (4.25) involving velocities of unknown variables, appears due to the last term in equation (4.6). Equation (4.25) can be written in a more compact form as

$$\mathbf{f}_{conv} + \mathbf{f}_{inert} + \mathbf{f}_{int} - \mathbf{f}_{ext} = \mathbf{0} \quad (4.26)$$

in which

$$\mathbf{f}_{conv} = \int_{\Omega^o} 2\rho(1 - \zeta^2) \mathbf{N}^T \dot{\omega} \dot{\mathbf{d}} \quad (4.27a)$$

$$\mathbf{f}_{inert} = \int_{\Omega^o} \mathbf{N}^T \rho \mathbf{N} \ddot{\boldsymbol{\theta}} \quad (4.27b)$$

$$\mathbf{f}_{int} = \int_{\Omega^o} \mathbf{B}^T \boldsymbol{\Sigma} \quad (4.27c)$$

$$\mathbf{f}_{ext} = \int_{\Gamma_i^o} \mathbf{N}^{*T} \mathbf{T} + \int_{\Omega^o} \mathbf{N}^{*T} \hat{\mathbf{b}} \quad (4.27d)$$

From equation (4.26), it can be observed that the variational formulation of the solid-like shell element results in two distinct contributions of mass to the equilibrium equation: (1) the inertial force vector \mathbf{f}_{inert} and (2) the convective force vector \mathbf{f}_{conv} . The force \mathbf{f}_{conv} acts as a damping force. Numerical increase in the convective force, such that $\mathbf{f}_{conv} > \mathbf{f}_{int}$, either due to loading conditions or due to numerical error in numerical computation of $\dot{\omega}$ and/or $\dot{\mathbf{d}}$, may result in an overly damped system. However, since the magnitude of the internal stretching variable, ω , is small compared to the other degrees of freedom, the contribution of the convective force will usually be small.

4.2.5 Shear locking

An eight-node solid-like shell element suffers from transverse shear locking as observed by [116]. To remedy this problem an assumed natural strain (ANS) method is exploited. The idea is to compute the transverse shear strains ($\delta E_{\alpha 3}$) at special points which are located at the center of the element edges. These strain components are then linearly interpolated between opposite edges to the actual integration point. A detailed finite element procedure for removing shear locking through the ANS method can be found in [10].

4.3 Mass discretization schemes

4.3.1 Consistent mass matrix

The variational or consistent mass matrix can be obtained from \mathbf{f}_{inert} (see equation 4.27b) and is given as

$$\mathbf{M} = \int_{\Omega^o} \mathbf{N}^T \rho \mathbf{N} \quad (4.28)$$

The discretized mass in matrix form can be written as (see C.1)

$$\mathbf{M} = \begin{bmatrix} \mathbf{M}^{uu} & \mathbf{M}^{u\omega} \\ \mathbf{M}^{\omega u} & \mathbf{M}^{\omega\omega} \end{bmatrix} \quad (4.29)$$

in which

$$\begin{aligned} \mathbf{M}^{uu} &= \int_{\Omega^o} \mathbf{M}^o + ((1 - \zeta^2)\omega + \zeta)^2 \mathbf{M}^1 \\ &\quad + \int_{\Omega^o} ((1 - \zeta^2)\omega + \zeta) \mathbf{M}^{1o} + ((1 - \zeta^2)\omega + \zeta) \mathbf{M}^{o1} \end{aligned} \quad (4.30a)$$

$$\mathbf{M}^{u\omega} = \int_{\Omega^o} (\mathbf{M}^{o\omega} + \zeta \mathbf{M}^{1\omega} + (1 - \zeta^2)\omega \mathbf{M}^{1\omega}) (1 - \zeta^2) \mathbf{d} \quad (4.30b)$$

$$\mathbf{M}^{\omega u} = \int_{\Omega^o} (\mathbf{M}^{\omega o} + \zeta \mathbf{M}^{\omega 1} + (1 - \zeta^2)\omega \mathbf{M}^{\omega 1}) (1 - \zeta^2) \mathbf{d} \quad (4.30c)$$

$$\mathbf{M}^{\omega\omega} = \int_{\Omega^o} (1 - \zeta^2)^2 \mathbf{d}^2 \mathbf{M}^\omega \quad (4.30d)$$

Note that, the sub-matrix \mathbf{M}^{uu} contains a major contribution coming from mass matrix \mathbf{M}^o corresponding to the mid-surface translational vibration modes, whereas mass matrices \mathbf{M}^1 and \mathbf{M}^{1o} , corresponding to the higher-order vibration modes, have comparatively smaller contributions. Moreover, sub-matrix \mathbf{M}^{uu} also contains terms which have a contribution due to the internal degrees of freedom, ω . Since the internal degree of freedom, ω , represents a measure for the gradient of internal stretching [10, 116], the magnitude of ω will be very small compared to the other degrees of freedom and consequently there will be only a small inertial contribution to the global equilibrium equation. The contribution of sub-matrices $\mathbf{M}^{u\omega}$, $\mathbf{M}^{\omega u}$ and $\mathbf{M}^{\omega\omega}$ will be very small, partly because of the presence of the internal stretching variable and partly due to the presence of higher order terms in ζ . This implies that these sub-matrices can be assumed to be zero in numerical simulation. As a consequence, for the case where internal degrees of freedom are required to be eliminated at element level using a static condensation method [116], the static condensation of mass matrix \mathbf{M} is not required anymore.

4.3.2 Lumped mass matrix and selective mass scaling

For an efficient solution of the dynamic equilibrium equations, explicit algorithms with lumped mass matrices are often preferred. However, explicit algorithms such as the central difference method are only conditionally stable. The critical time step is restricted by the maximum eigenfrequency (λ_{max}) of the system. The eigenfrequency increases with decreasing thickness of plates and shells, modeled with solid or solid-like shell elements, rendering a very small time step for explicit dynamic simulations.

Moreover, as motivated in section 4.3.1, mass corresponding to the internal degrees of freedom can be assumed zero in consistent mass matrices. However, in explicit simulations where internal stretching variables are considered as global dofs and are not condensed out at element level, it is required to assign inertia to these dofs. Additionally, the presence of internal dofs will give rise to higher-order vibration modes having eigenfrequencies higher than the eigenfrequencies corresponding to the standard dofs. This will further reduce the critical time step.

To circumvent the problem of very small time steps in explicit simulations of thin plates and shells, a new mass lumping scheme for the solid-like shell element

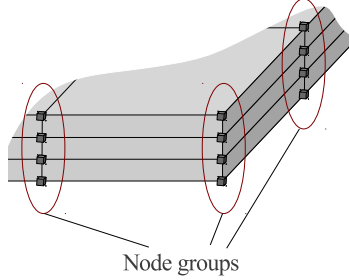


Figure 4.2 Node groups for acceleration scaling

is presented. A selective mass lumping strategy is employed to increase the density corresponding to higher-order modes without influencing the lower-order modes. To decrease the eigenfrequencies corresponding to thickness vibration modes, acceleration scaling is used by means of parameter α_u , applied to standard dofs, following [112]. The eigenfrequencies corresponding to the internal dofs are decreased by directly applying a scaling of the mass matrix through parameter α_ω .

For explicit simulations the assembled, diagonal mass matrix is defined as:

$$\mathbf{M} = \begin{bmatrix} \widetilde{\mathbf{M}}^{uu} & \mathbf{0} \\ \mathbf{0} & \widetilde{\mathbf{M}}^{\omega\omega} \end{bmatrix} \quad (4.31)$$

where $\widetilde{\mathbf{M}}^{uu}$ and $\widetilde{\mathbf{M}}^{\omega\omega}$ are the diagonal mass matrices corresponding to standard and internal dofs. The dynamic equilibrium equations can be written as

$$\widetilde{\mathbf{M}}^{uu} \hat{\mathbf{U}} = \widetilde{\mathbf{R}}^u \quad (4.32)$$

$$\widetilde{\mathbf{M}}^{\omega\omega} \hat{\mathbf{W}} = \widetilde{\mathbf{R}}^\omega \quad (4.33)$$

in which $\widetilde{\mathbf{R}}^u$ and $\widetilde{\mathbf{R}}^\omega$ are the force vectors. These will be defined later in this section.

To increase the time step, the selective mass scaling procedure of [112] is used for standard dofs. The idea is to apply acceleration scaling to a group of nodes such that rigid body translational acceleration is not affected. Each standard/geometrical node i belongs to a particular node group, see figure 4.2. The scaled acceleration of the geometrical node i is given as

$$\hat{\mathbf{U}}_i = \frac{\mathbf{R}_g^u}{\mathbf{m}_g} + \frac{1}{\alpha_u} \left(\frac{\mathbf{R}_i^u}{\mathbf{m}_i} - \frac{\mathbf{R}_g^u}{\mathbf{m}_g} \right) \quad (4.34)$$

in which \mathbf{m}_g and \mathbf{R}_g^u are the sum of nodal masses and forces of all nodes within a

node group and are given as

$$\mathbf{m}_g = \sum_{i=1}^{ng} \mathbf{m}_i, \quad \mathbf{R}_g^u = \sum_{i=1}^{ng} \mathbf{R}_i^u \quad (4.35a)$$

$$\mathbf{m}_i = \sum_{e=1}^{numElem} \mathbf{m}_i^e, \quad \mathbf{R}_i^u = \sum_{e=1}^{numElem} \mathbf{R}_i^{e/u} \quad (4.35b)$$

$$\mathbf{m}_i^e = \frac{\rho V_e}{8} \mathbf{I}_{3 \times 3}, \quad \mathbf{R}_i^{e/u} = \mathbf{f}_{i/ext}^{e/u} - \mathbf{f}_{i/int}^{e/u} - \mathbf{f}_{i/conv}^{e/u} \quad (4.35c)$$

in which \mathbf{m}_i^e and $\mathbf{R}_i^{e/u}$ represent the i th node mass and force vector of element e , respectively. ng is the number of nodes in a particular node group, $numElem$ is the total number of elements in a finite element mesh and \mathbf{I} is a unit identity tensor. Note that, equations (4.35b) and (4.35c) represent the standard element assembly procedure.

Equation (4.34) can be used to obtain nodal accelerations. In case, displacements are considered as primary unknowns instead of accelerations, it is required to compute $\widetilde{\mathbf{M}}^{uu}$ and $\widetilde{\mathbf{R}}^u$ to solve equation (4.34) for unknown displacements. They are then given by

$$\widetilde{\mathbf{M}}_i^{uu} = \mathbf{m}_i \quad (4.36)$$

$$\widetilde{\mathbf{R}}_i^u = \frac{\mathbf{R}_i^u}{\alpha_u} + \left(1 - \frac{1}{\alpha_u}\right) \left(\frac{\mathbf{m}_i}{\mathbf{m}_g}\right) \mathbf{R}_g^u \quad (4.37)$$

Note that, the mass matrix remains unadapted and scaling is applied only to the force vector.

To decrease the eigenfrequencies corresponding to the internal dofs, a mass scaling is applied through parameter α_ω . It is evident from equation 4.30d, that mass matrix $\mathbf{M}^{\omega\omega}$ is scaled with the square of the deformed shell director. Consequently, $\mathbf{M}^{\omega\omega}$ has the dimension of weight * length². This suggests, that parameter α_ω should have the dimension of length² and is not a dimensionless quantity. The mass of the internal dofs can be increased with parameter α_ω , such that the critical time step is determined by the eigenfrequencies corresponding to the standard dofs, as will be explained in the next section. The scaled nodal masses $\widetilde{\mathbf{M}}^{\omega\omega}$ and force vector $\widetilde{\mathbf{R}}^\omega$ corresponding to the internal dofs are given as

$$\widetilde{M}_i^{\omega\omega} = \alpha_\omega m_i^\omega \quad (4.38)$$

$$\widetilde{R}_i^\omega = R_i^\omega \quad (4.39)$$

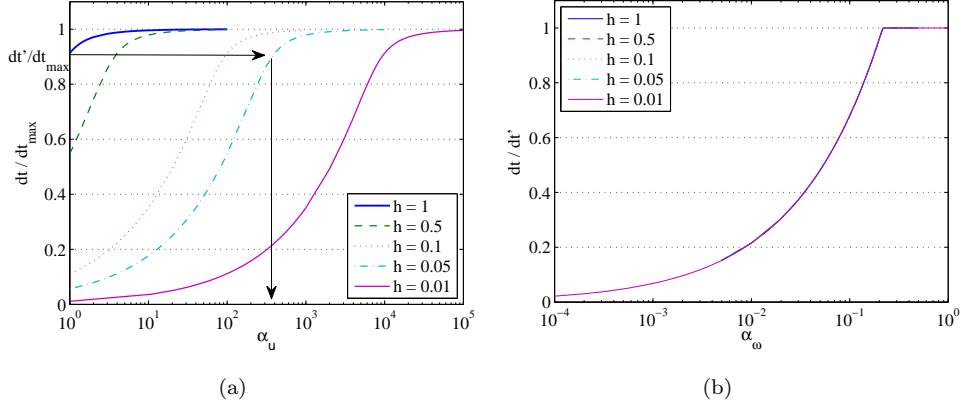


Figure 4.3 Effect of mass scaling parameters α_u (left) and α_ω (right) on critical time step

in which \mathbf{m}^ω and \mathbf{R}^ω are computed in a standard fashion as

$$m_i^\omega = \sum_{e=1}^{numElem} m_i^{e/\omega}, \quad R_i^\omega = \sum_{e=1}^{numElem} R_i^{e/\omega} \quad (4.40a)$$

$$m_i^{e/\omega} = \frac{\rho V_e}{4}, \quad R_i^{e/\omega} = -f_{i/int}^{e/\omega} - f_{i/conv}^{e/\omega} \quad (4.40b)$$

Note that, in equation (40b₁) it is assumed that the mass corresponding to internal dofs is equal to the total mass of the element which is equally distributed over the internal nodes of the element. This mass is then scaled with parameter α_ω to obtain a correct measure of the mass corresponding to the internal dofs. A method for determining parameters α_u and α_ω is given in the next section.

4.3.3 Critical time step

The parameters α_u and α_ω can be estimated by solving an eigenvalue problem for a single element. As a first step, the eigenvalue problem for a single element assuming $\alpha_\omega \rightarrow \infty$ for a range of α_u is performed. For demonstration purpose, an eigenvalue problem for a solid-like shell element with unit in-plane dimensions is performed and a critical time step (dt) is plotted against α_u in a semi-log plot for various element thicknesses (h), figure 4.3a. The critical time step (dt) is calculated using $dt = 2/\lambda_{max}$. The critical time step (dt) in figure 4.3a is normalized with the value of the critical time step corresponding to $\alpha_u \rightarrow \infty$, denoted as dt_{max} . It can be observed, that increasing values of α_u results in an increase of the critical time step until it reaches an asymptotic value after which there is no considerable increase in critical time step. At this stage, there is no further decrease in thickness related

eigenfrequencies of the element, instead increasing α_u starts to affect the in-plane vibration modes. Moreover, it can be observed that with decreasing thickness of the element, the trend in the curve remains the same and all curves finally converges to the same asymptotic value. For analysis purpose, an eigenvalue problem for a range of α_u can be solved to determine the critical time step for each corresponding value of α_u . Hereafter, any value of α_u after which there is no significant increase in critical time step can be selected. This value is denoted as dt' and will be referred to as the *selected critical time step*. The value of α_u used in section 4.4.2 corresponds to the critical time step $dt'=0.9dt_{max}$

The parameter α_ω is established in a second step by performing an eigenfrequency analysis using the value of α_u determined in the first step. Figure 4.3b shows the variation of critical time step corresponding to parameter α_ω . The critical time step is normalized with the *selected critical time step*, dt' . It is evident from figure 4.3b, that for $\alpha_\omega \rightarrow 0$, the critical time step is lower than the *selected critical time step*, dt' , which corresponds to the dofs of geometrical nodes. This suggests that mass scaling corresponding to internal dofs is also required in addition to mass scaling of dofs corresponding to geometrical nodes. As parameter α_ω increases, the critical time step also increases until it reaches the critical time step, dt' . After this point the maximum eigenfrequency of the element is dictated by the eigenfrequencies corresponding to the dofs of geometrical nodes. Moreover, it can be observed from figure 4.3b that α_ω is independent of the thickness of the element.

For analysis purpose, a value of α_ω can be selected from the critical time step (dt) vs α_ω curve. The value of α_ω which corresponds to a point after which there is no increase in critical time step can be selected. This allows to use the critical time step corresponding to the dofs of geometrical nodes without further decrease in critical time step due to internal dofs. Moreover, as discussed in section 4.3.1, the mass corresponding to internal dofs, $\mathbf{M}^{\omega\omega}$, is only a fraction of the mass, \mathbf{M}^{uu} , assigned to standard dofs. The value of α_ω will always be less than 1. This suggests, that parameter α_ω is scaling mass \mathbf{m}^ω , in equation (4.38), similar to the term $((1 - \zeta^2)^2 \mathbf{d}^2)$ in equation 4.30d. Furthermore, since internal dofs contribute to higher-order vibration modes, its contribution to the total kinetic energy of the system will be negligibly small. This implies that large values of $\alpha_\omega > 1$ can be used in numerical analysis. This is further elaborated through the numerical examples in section 4.4.2. Moreover, using a value of $\alpha_\omega = 1$ makes the determination of mass scaling parameters simpler and only requires the determination of parameter α_u for mass scaling in explicit simulations.

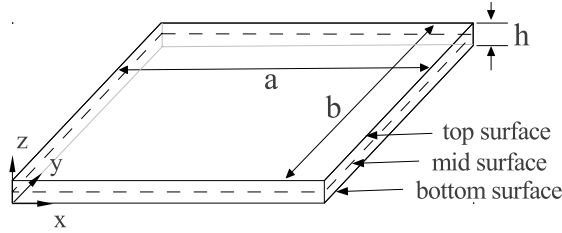


Figure 4.4 Geometry of a schematic plate

4.4 Numerical examples

In this section several numerical examples are presented to show the performance of the solid-like shell element in dynamic analysis of isotropic and laminated shells and plates. Numerical analysis of composite laminates performed at meso-scopic level of observation often requires modeling of each ply of the laminate separately, instead of using a multilayer plate/shell elements. Therefore, in all numerical examples presented here, each lamina of the laminate is modeled with a single layer of solid-like shell elements in thickness direction. Note that, this results in performing analysis with elements of large aspect ratios in addition to the small thickness of the plate/shell itself. The Newton-Raphson method is employed to solve the nonlinear finite element equations in implicit simulations. The equations are solved iteratively until residual force norm is less than a tolerance value. The convergence tolerance is taken to be $1.0\text{E-}5$. Integration in the time domain is performed with the Newmark time-stepping method for implicit analysis with parameters α and β equal to 0.5 and 0.25 respectively, whereas the second-order accurate central difference method is used for time integration in explicit dynamic simulations.

The geometry of a schematic plate used for analysis is shown in figure 4.4. The boundary conditions used for simply supported and clamped shells are as follows:

Simply supported (SS1)

along x-axis: $\hat{u}_y = 0$, $\hat{u}_z = 0$ at bottom or mid-surface of plate/shell

along y-axis: $\hat{u}_x = 0$, $\hat{u}_z = 0$ at bottom or mid-surface of plate/shell

Simply supported (SS2)

$\hat{u}_x = 0$ at $(x = 0, y = 0)$ and $(x = 0, y = b)$

$\hat{u}_y = 0$ at $(x = 0, y = 0)$

along all edges: $\hat{u}_z = 0$ at bottom or mid-surface of plate/shell

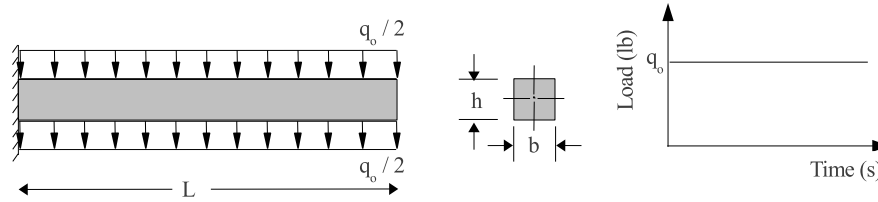


Figure 4.5 Geometry and boundary conditions of a cantilever beam

Clamped (C)

along all edges: $\hat{u}_x = \hat{u}_y = \hat{u}_z = 0$

Different analysis cases are identified by a name consisting of the name of type of boundary conditions used and the position of applied load. For example the analysis case "SS2,bot-top" implies that the analysis is performed with SS2 boundary conditions, $\hat{u}_z = 0$ are applied at the bottom-surface of the plate/shell and the load is applied at the top-surface of the plate/shell.

4.4.1 Cantilever beam subjected to impulsive load

A cantilever beam of length, $L = 254\text{mm}$ (10in), width, $b = 25.4\text{mm}$ (1in) and thickness, $t = 25.4\text{mm}$ (1in) is analyzed, figure 4.5. The beam is subjected to a suddenly applied uniformly distributed load, q_0 . The material properties used for the analysis are: modulus of elasticity, $E = 82.74\text{MPa}$ (1.2E04psi), Poisson ratio, $\nu = 0.2$ and density $\rho = 1.0687\text{E-}10\text{N-s}^2/\text{mm}^4$ (10E-6lb-s²/in⁴). The time step used for the analysis is 1.5E-4s. An implicit dynamic analysis with a full variational mass matrix (equation (4.29)) is performed. Several authors have analyzed this problem, e.g. [23, 25, 132] using different finite elements.

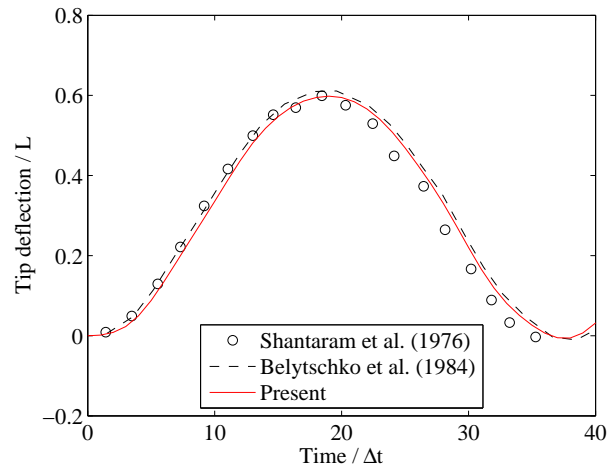
A geometrically linear analysis is performed with a uniformly distributed load, $q_0 = 0.01\text{psi}$ and the results are summarized in table 4.1. A geometrically nonlinear analysis is performed with a uniformly distributed load, $q_0 = 2.85\text{psi}$. A finite element mesh of 10 elements is used for the geometrically nonlinear analysis. The tip displacement, in comparison with reference solutions [25, 132], is given in figure 4.6. The analysis results of the present formulation, both for geometrically linear and nonlinear analysis cases, are in good agreement with the reference solutions.

4.4.2 A square plate subjected to impulsive load

To investigate the inertial effect contribution from the internal degrees of freedom ω in implicit simulations, two types of consistent mass matrices are used

Table 4.1 Linear analysis of cantilever beam

Element type	No. of elements	Max; deflection (in)	period (ms)
Triangular plate element, [25]	20	0.02408	5.662
Quadrilateral plate element, [25]	5	0.02454	5.68
Analytical, [25]	-	0.025	5.719
Present	5	0.025162	5.6
Present	10	0.025305	5.7
Present	20	0.025371	5.7

**Figure 4.6** Displacement time history of cantilever beam - large displacement analysis

- CMM1 : consistent mass matrix, equation (4.29);
- CMM2 : consistent mass matrix, equation (4.29) but assigning zero masses to internal degrees of freedom, ω , i.e. the sub-matrices $\mathbf{M}^{u\omega}$, $\mathbf{M}^{\omega u}$ and $\mathbf{M}^{\omega\omega}$ in mass matrix \mathbf{M} are zero.

To investigate the behavior of the solid-like shell element in explicit simulations, an analysis using the lumped mass matrix (LM), defined in section 4.3.2, is performed.

Square plate - implicit analysis

An isotropic, simply supported (SS2, bot-top) square plate of [25] is analyzed. The material and geometrical properties used for the analysis are obtained from [25]. A quadrant of a plate modeled with 8x8 equidistant elements is used for analysis. An implicit dynamic analysis with a time step of 1.5E-5s, is performed. Figures 4.7a and 4.7b show the displacement and velocity time history of a geometrical

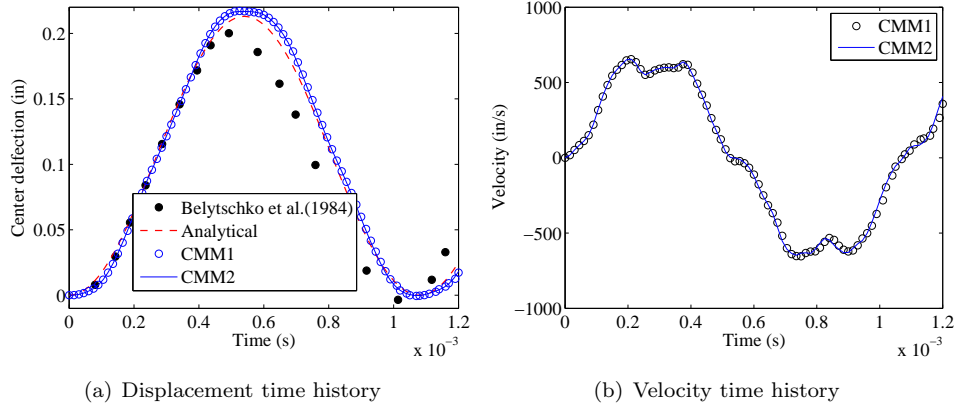


Figure 4.7 Effect of mass discretization - Isotropic plate (response of geometrical node)

node at the plate center. The numerical results show a slight increase in the peak displacement and the period compared to the reference solution ([25]). It is noted that the reference solution was obtained with two-dimensional plate elements with a plane stress constitutive law. Moreover, the boundary conditions were applied at the plate mid-surface which has an effect on the shell response as will be explained in section 4.4.4. However, the numerical results of the solid-like shell element from the present investigation, i.e. maximum center deflection ≈ 0.2184 in and period ≈ 1.08 ms, are in good agreement with the analytical solution [142, 147], i.e. maximum center deflection = 0.2129in and period = 1.0796ms, figure 4.7a. Comparing the time histories obtained with different mass discretizations (figures 4.7a and 4.7b), it can be observed that the mass discretization has no significant effect on the response of the plate.

Figure 4.8 shows the time history of an internal degree of freedom at the center of the plate. The time histories of the two analyses, i.e. CMM1 and CMM2, are in good agreement with each other. This also suggests that assigning a zero mass to the internal dofs has no significant effect on the response.

Square plate - explicit analysis

Three analysis cases are considered in this section, namely "LM(a/h=20)", "LM,2L(a/h=20)", "LM(a/h=40)". The analysis case "LM(a/h=20)" refers to the analysis, in which the isotropic plate of section 4.4.2, is analyzed with a lumped mass matrix. The boundary conditions, load and mesh discretizations are the same as used in section 4.4.2

Moreover, in order to investigate the effect of element and structural slenderness

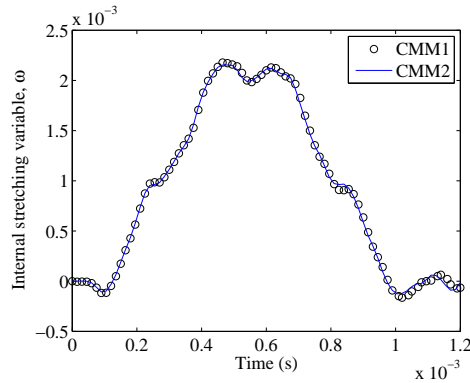


Figure 4.8 Effect of mass discretization - Isotropic plate (response of internal node)

Table 4.2 Parameters for explicit analysis

Analysis case	α_u	α_ω	dt' (s)	dt' (s) $\alpha_u = \alpha_\omega = 1$	dt (s) (Hinton, 1976; Mallikarjuna and Kant, 1988)
Isotropic plate					
LM (a/h=20)	1.5	0.079	2.08E-6	1.824E-6	1.5275E-6
LM,2L (a/h=20)	4	0.077	2.08E-6	1.06E-6	1.07E-6
LM (a/h=40)	4	0.077	2.08E-6	1.06E-6	1.07E-6
Laminated cylindrical panel					
LM	100	1	1.5E-6	2.384E-7	6.88E-8

the analysis cases "LM,2L(a/h=20)" and "LM(a/h=40)" are used. A structural slenderness is defined as the ratio of length of the plate to its thickness (a/h). The element slenderness is defined as the ratio of a minimum element in-plane dimension to its thickness (a_e/h_e). In analysis case "LM,2L(a/h=20)", the isotropic plate of section 4.4.2 is analyzed with a mesh discretization of 8x8x2. This results in an element slenderness of 2.5. The analysis case "LM(a/h=40)" is simulated with a thin plate. The in-plane geometry and boundary conditions of the plate are the same as defined in section 4.4.2 but having a thickness h/2. A uniformly distributed load of $q_o=100$ psi is applied. The mesh discretization used to model a quarter of a plate is 8x8x1. This result in element and structural slenderness of 2.5 and 40, respectively. The time step dt' and the mass scaling factors used for the analysis are presented in table 4.2. The critical time step for the case $\alpha_u = \alpha_\omega = 1$ and a Mindlin plate according to [66, 102], is also presented in table 4.2 as a reference.

It can be observed from table 4.2, that mass scaling results in an increase of the critical time step for explicit dynamic analysis. Figures 4.9a-d show the displacement and velocity time histories of a geometrical node in comparison with the

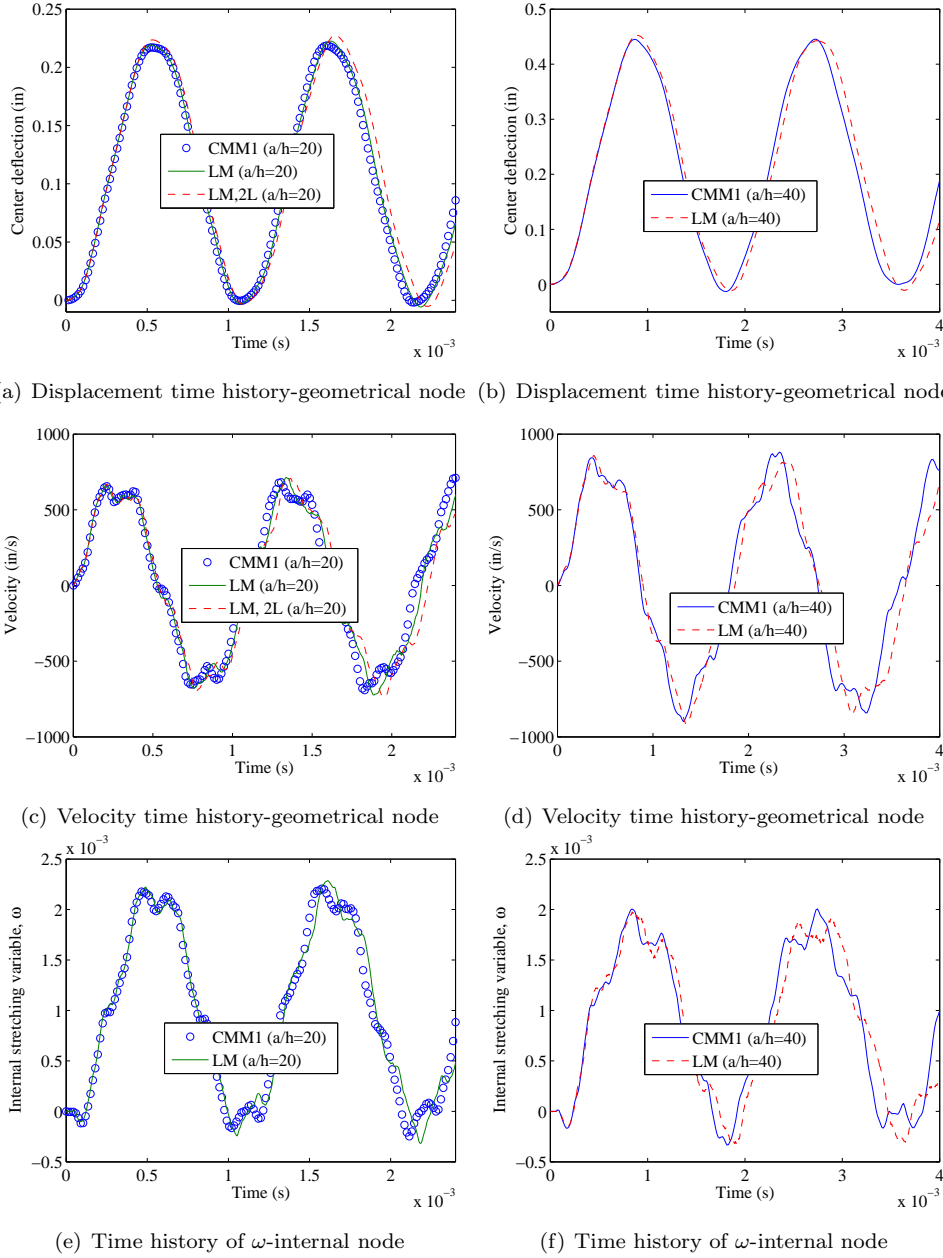
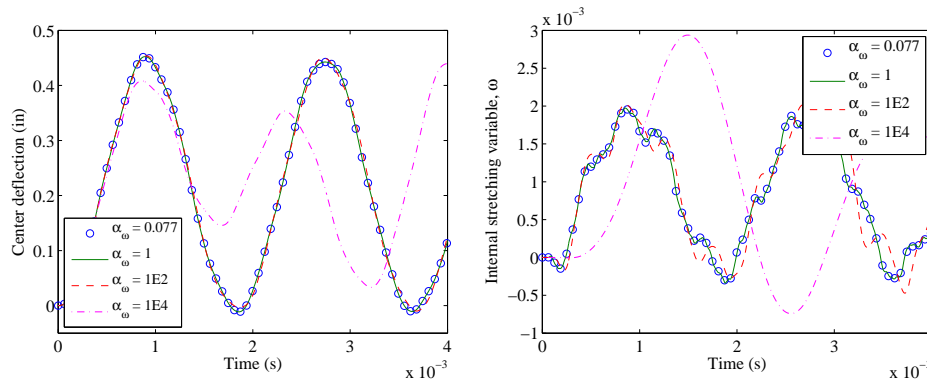


Figure 4.9 Effect of mass discretization (isotropic plate)- Left: thick plate, Right: thin plate



(a) Displacement time history-geometrical node (b) Displacement time history-internal node

Figure 4.10 Effect of parameter α_ω - Isotropic thin plate

implicit analysis results. Figures 4.9e-f show the time histories of the internal degrees of freedom. Note that for the analysis case "LM,2L(a/h=20)", the location of the internal dofs is different compared to the analysis case "LM(a/h=20)", hence a comparison cannot be made. It can be observed from the figures that results of the explicit analysis are in good agreement with the results of the implicit analysis. However, for the case of a thin plate a small increase in the period is observed. Note that, all analyses are performed with the same time step and the response of geometrical and internal nodes, as well as the time step is not affected by element and/or structural slenderness.

Square plate - effect of parameter α_ω in explicit analysis

To investigate the effect of parameter α_ω on the the dynamic response of plates, the thin plate ($a/h = 40$) of section 4.4.2 is analyzed with increasing values of α_ω . Figure 4.10 shows the results of the analysis. It can be seen that the dynamic response is not affected by increasing values of α_ω . However, very large values of α_ω affect the thickness related vibration modes due to increased inertia of the internal dofs and therefore result in an amplitude decrease and period lengthening of the displacement time histories of the geometrical nodes.

4.4.3 Clamped laminated cylindrical panel under impulsive load

Clamped laminated cylindrical panel - implicit analysis

The dynamic response of a thin cross-ply ($0^\circ/90^\circ$), laminated cylindrical panel is investigated and a convergence study is performed. An implicit dynamic analysis is

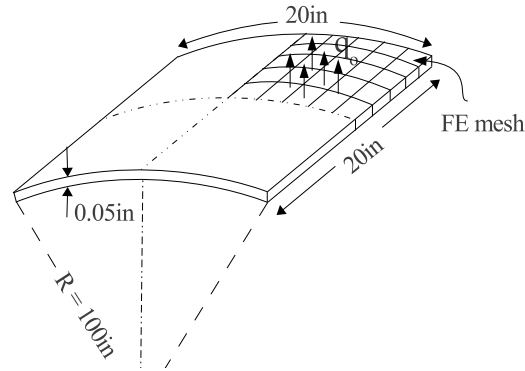


Figure 4.11 Geometry of clamped cylindrical panel

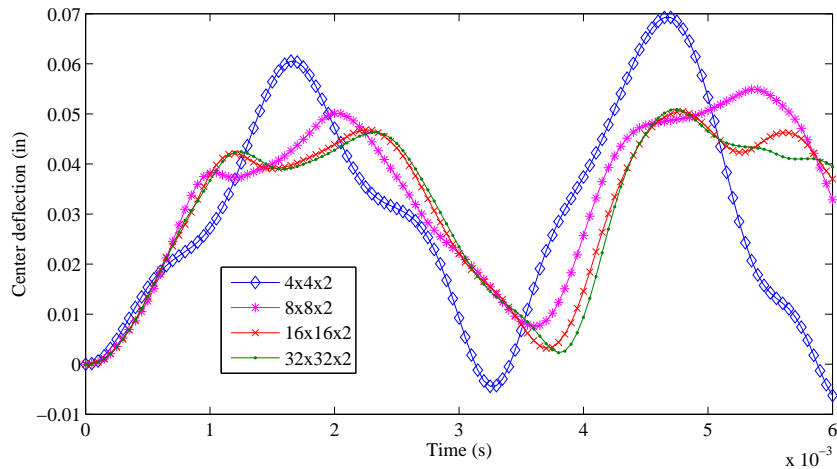


Figure 4.12 Displacement time histories of laminated cylindrical panel

performed with a full mass matrix (equation (4.29)). The geometry of the model is shown in figure 4.11. The panel is clamped on all four edges and is subjected to a uniformly distributed step load q_o , acting normal to the shell surface. The material properties used for the analysis are that of graphite-epoxy and are as follows: $E_{11} = 20E6\text{psi}$, $E_{22} = 1.43E6\text{psi}$, $\nu_{12} = \nu_{13} = \nu_{23} = 0.3$, $G_{12} = G_{13} = G_{23} = 0.76E6\text{psi}$, $\rho = 0.146E-3\text{lb-sec}^2/\text{in}^4$, $q_o = 1\text{psi}$. The analysis is performed with a time step, $dt = 5.0E-5\text{s}$. A quadrant of the shell is modeled for analysis.

Figure 4.12 shows the results of the analysis with different mesh discretizations.

It can be observed, that for the mesh 4x4x2 the response is primarily dominated by the first mode of vibration. However, there is the presence of higher-order vibration modes. Further, mesh refinement resulted in a larger contribution of higher-order vibration modes and once the mesh is sufficiently refined the result converges to a unique solution.

In order to show that the assumption of assigning zero mass corresponding to internal dofs is also valid for curved shell structures, an implicit analysis is performed using the consistent mass matrices CMM1 and CMM2. Figures 4.13a,c and e show the displacement and velocity time histories of the geometrical and internal nodes at the center of the panel for a mesh discretization of 16x16x2. It can be observed from the figures that the response of analysis cases CMM1 and CMM2 are almost identical both for standard and internal degrees of freedom.

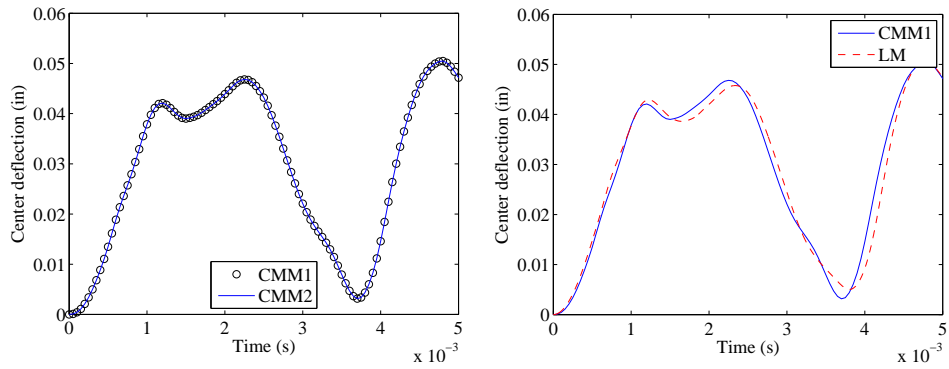
Clamped laminated cylindrical panel - explicit analysis

An explicit analysis of a laminated cylinder is performed using the scaled lumped mass matrix as defined in section 4.3.2. Motivated by the results of section 4.4.2, the analysis is performed with $\alpha_\omega = 1$. The mass scaling parameters and time step used for the analysis are given in table 4.2. It is noteworthy, that mass scaling results in an increase of the critical time step compared to the reference solution given by [66, 102]. Figures 4.13b,d and f show the response of the explicit analysis in comparison with the analysis results of the implicit analysis. The results of the explicit analysis are in good agreement with the reference solution.

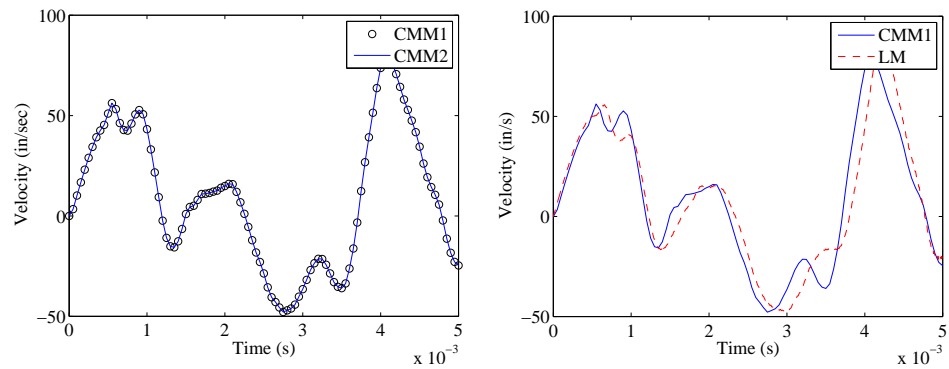
4.4.4 Effect of boundary conditions and thickness change

Geometrically non-linear analysis of two-ply laminate

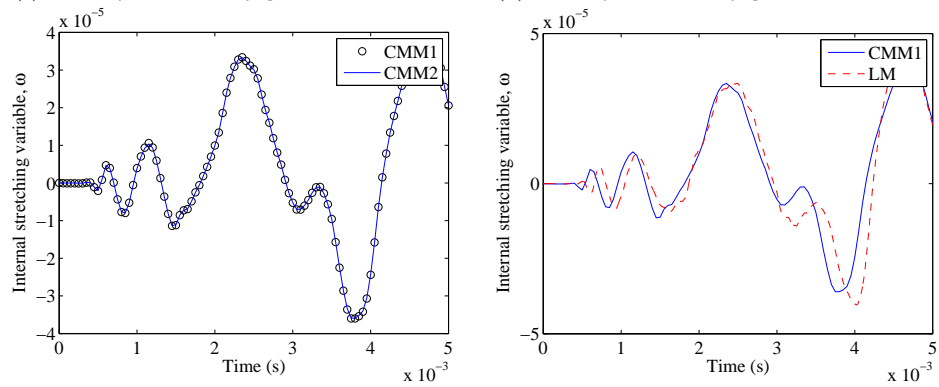
When performing a numerical analysis with plane-stress 2-D and 3-D shell elements, the boundary conditions and the load are often applied to the mid-surface of the plate. However, in reality the load is applied on the top or bottom surfaces of the shell structure. Numerical analysis of shells with plane-stress and mid-surface assumption, especially for thick plates, may influence the numerical response of the plate/shell due to the thickness change and the position of application of boundary conditions. To illustrate the effect of positioning of boundary conditions, a thick unsymmetric cross-ply ($0^\circ/90^\circ$) laminate with $a/h = 10$ is analyzed. The material and geometrical properties are taken from [80]. The plate is simply supported and loaded with uniform pressure. The simply supported boundary conditions SS1 and SS2 with different positions of the application are used in the numerical analysis. The analysis is performed by modeling only a quadrant of a plate, discretized into 8x8 equidistant elements in the in-plane direction. The numerical results are compared with double



(a) Displacement time history - geometrical node (b) Displacement time history-geometrical node



(c) Velocity time history-geometrical node (d) Velocity time history-geometrical node



(e) Time history of ω -internal node (f) Time history of ω -internal node

Figure 4.13 Effect of mass discretization (laminated cylindrical panel)- Left: implicit analysis, Right: explicit analysis

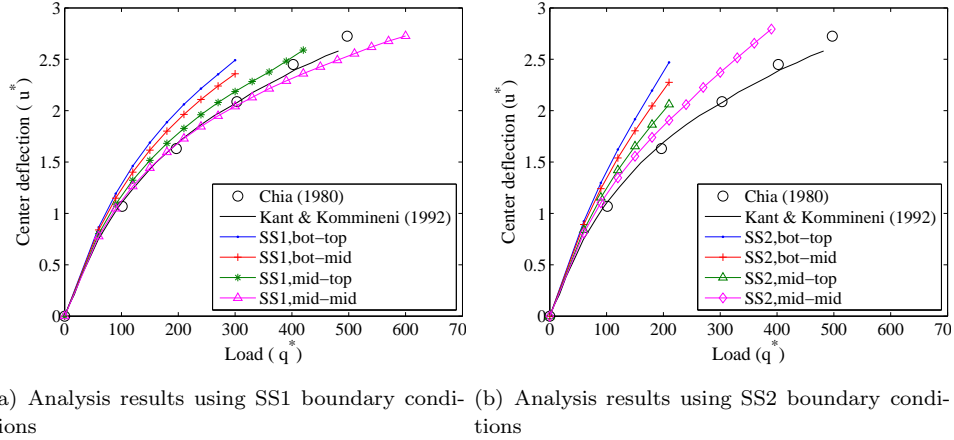


Figure 4.14 Effects of boundary conditions - two-ply laminated plate

Fourier series results of [35] and finite element results based on higher-order shear deformation theory of [80]. The following non-dimensional parameters are used:

$$u^* = \frac{u_z}{h}, \quad q^* = \frac{1}{E_{22}} \left(\frac{a}{h} \right)^4$$

Figure 4.14 shows the result of the analysis in comparison with the reference solution. It can be observed that for the case of SS1,mid-mid a good agreement with the reference solution is obtained, while for the case of SS2,mid-mid the result is close to the reference solution but not in exact correspondence with the reference solution. The reason for this difference is that in the reference solution it is assumed that the boundary conditions are of type SS1.

It can also be observed from figure 4.14, that the response is significantly affected by the position of application of boundary conditions and the load. It can be seen from the figures 4.14a and 4.14b, that the response of the plate with the analysis cases SS1,bot-top and SS2,bot-top show a compliant response and the response becomes stiffer as the boundary conditions and the load are applied at the mid-surface. This is due to membrane action in the case of mid-surface boundary conditions. A good agreement of the analysis case SS1,mid-mid, in contrast to the analysis case SS1,bot-top, with the reference solution, is due to the fact that in the reference solutions it is assumed that the boundary conditions and the load are applied at the mid-surface of the plate.

A strong influence of the position of application of boundary conditions in the SS2 case compared to the SS1 case, is due to the boundary conditions effect. The SS1 boundary conditions restrain the torsional moments at the edges of the plate, which

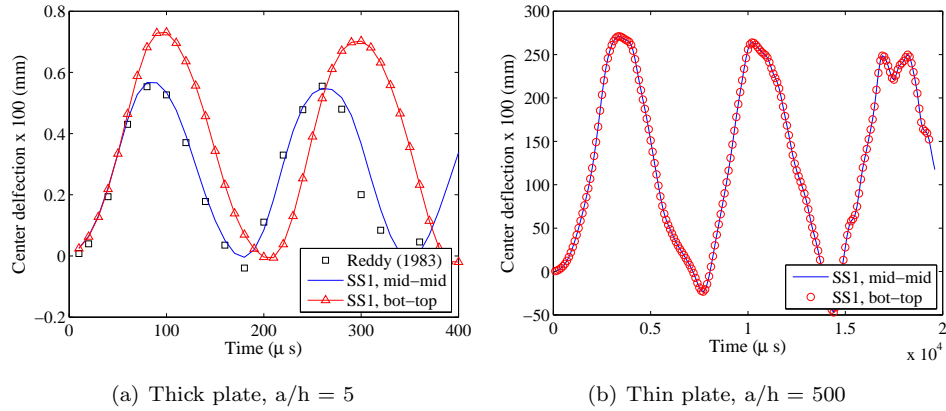


Figure 4.15 Displacement time histories of orthotropic plate in comparison with reference solution

causes a stiffer response compared to the case of the SS2 boundary conditions, [11]. The investigation clearly reveals the importance of correct application of boundary conditions and careful use of plane-stress and shell mid-surface assumption in performing numerical analysis of shell/plate structures. Moreover, the analysis results suggests that the effect of boundary conditions become significant as the thickness of the plate increases.

Dynamic analysis of orthotropic plate

An implicit dynamic analysis of a square, simply supported, orthotropic plate is performed. The analysis is performed with consistent mass matrix (equation (4.29)) and a time step of $1.0E-5$ s. The material properties considered for analysis are: $E_{11} = 52.5E4N/cm^2$, $E_{22} = 2.1E4N/cm^2$, $\nu_{12} = \nu_{13} = \nu_{23} = 0.25$, $G_{12} = G_{13} = G_{23} = 1.05E4N/cm^2$, $\rho = 0.8E-9Ns^2/cm^4$, $q_o = 0.1N/cm^2$. The plate has a length $a = 25$ cm and thickness $h = 5$ cm. The analysis is performed with a quarter of a plate discretized into $6 \times 6 \times 2$ solid-like shell elements. The results of the analysis are given in figure 4.15a. It can be observed that the results are in good agreement with the reference solution [123], when the boundary conditions are applied at the mid-surface of the plate (SS1,mid-mid). Analysis case SS1,bot-top shows that application of the boundary conditions at the plate surface results in increased displacements. Moreover, the fundamental period of the plate also increases.

Figure 4.15b shows the analysis results of a thin plate with $a/h = 500$. The plate is subjected to a suddenly applied load of $1.0E-4N/cm^2$. The analysis is performed with a time step size of $1.0E-4$ s. It can be observed from the figure that there is no influence of the location of application of boundary conditions for thin plates.

This suggests that the effect of the positioning of the boundary conditions becomes significant as the thickness of the plate increases. Moreover, the response of the plate is observed to be slightly irregular compared to the thick plate. This is due to the presence of higher-order vibration modes.

4.5 Concluding remarks

A three-dimensional solid-like shell element for performing nonlinear dynamic analysis of plates and shells structures is presented. Mass discretization schemes for performing implicit and explicit dynamic simulations using solid-like shell elements are proposed. A new mass scaling procedure for a solid-like shell element is presented in order to increase the critical time step in explicit dynamic analysis. Numerical results obtained with the present formulation suggest that the element is accurate in predicting the response in small and large deformation analysis of various thick and thin, isotropic, anisotropic shells and anisotropic laminated composite shells.

Moreover, it was observed that the inertial contribution of internal degrees of freedom to the global dynamic equilibrium is negligibly small and the solution is not affected by the change in mass discretization corresponding to the internal degrees of freedom. As a consequence, in implicit dynamic simulations the mass matrix corresponding to the standard dofs, assuming a zero mass to the internal dofs, can be used for analysis. This avoids the need of obtaining a condensed mass matrix in cases where internal degrees of freedom are required to be condensed out at element level using static condensation. For explicit dynamic simulations α_ω can be assumed to be unity and therefore only one parameter, i.e. α_u is required to be determined for mass scaling.

Numerical results of thick shells show that the response of shells is also significantly affected by the plane-stress constitutive law and shell-mid-surface assumption due to the 3-D stress state in the shell body. It is observed, that for static analysis, application of loads and boundary conditions at the shell mid-surface results in a stiff response of the shells compared to cases where the boundary conditions are applied at the top/bottom surfaces of the shell. In case of dynamic analysis, the application of boundary conditions at the shell mid-surface results in shortening of the fundamental period in addition to smaller amplitudes of peak displacements compared to the case of surface boundary conditions. The difference in response is attributed to the presence of a three-dimensional stress state, thickness change and membrane action in the shell body. However, it is observed that this difference in response vanishes as the thickness of the shell becomes smaller.

Chapter 5

Dynamic fracture in laminated composite plates*

This chapter presents a meso-scopic, time-dependent finite element model for the simulation of dynamic fracture in laminated composite plates. The analyses are performed with an emphasis on the quantification of the effect of the loading rate on interacting damage mechanisms, i.e. matrix cracking and delamination. In particular, rate effects on damage initiation, propagation and interaction between matrix cracking and delamination under low and high velocity impact are studied. Moreover, the chapter addresses computational issues related to time continuity in stress/strain and velocity fields, during dynamic simulation, at the time of incorporation of new degrees of freedom in a mesh-objective crack modeling approach. Illustrative numerical examples are presented to show the performance of the model. The model is validated with a fast crack growth simulation in a unidirectional laminate. An impact test on a cross-ply laminated plate is performed in order to study the rate effects on structural response and damage mechanics.

5.1 Introduction

Dynamic fracture in solids has remained a subject of interest for many researchers in the last century. Significant work has been done to understand the mechanisms and mechanics of crack propagation under dynamic loading conditions in isotropic materials, see for example [19, 52, 53, 77, 122, 133]. However, characterizing and understanding the mechanics of damage growth in fiber-reinforced laminated composite materials under dynamic loading conditions, has become an active area of research in the last couple of decades. This is primarily due to (a) increasing use of fiber-reinforced laminated composite materials in various fields of engineering, (b) the anisotropic nature of fiber-reinforced composites, which results in anisotropic wave speeds in the fibre and transversal directions, and (c) the property of fiber-reinforced composites that crack growth takes place in preferential directions.

Experimental studies on crack growth in bi-material plates, e.g [41, 89, 97, 137], revealed that crack propagation along weak planes or predefined paths, in Mode-II, can exceed the shear wave speed of the material and propagate intersonically,

* This chapter is extracted from [6]

approaching the longitudinal wave speed of the material. Fiber-reinforced composite laminates belong to a class of materials which inherently contains preferential crack propagation directions. For example matrix cracking/splitting occurs in the direction of fibers and delamination cracks grow along the interfaces of the connecting plies. In [40, 90] dynamic crack propagation in unidirectional fiber composite plates was studied and it was observed that in mode-I fracture, the crack propagation speed does not exceed the shear wave speed of the material, similar to isotropic materials. However, when cracks are subjected to high rate shear loading, the crack propagates in Mode-II with a speed approaching the longitudinal wave speed of the material.

Damage in structural composites usually appears as a combination of matrix cracking/splitting, delamination, fibre failure and buckling failure modes. Apart from studying and understanding the characteristics of each individual damage mode, it is equally crucial to understand the interaction between different failure modes and their combined effect on the global structural response. It is one of the motivations of the current chapter to numerically study the interaction between different damage mechanisms under dynamic transverse loads in composite plates. In [36, 37] low-velocity impact tests on composite laminated plates were performed and it was observed that matrix cracking is the initial failure mode, which may induce delamination damage. The experimental study in [33] revealed that the structural response of laminated composites significantly differ under high and low impact velocity impact and damage increases with increasing in loading rate. In [91] impact tests on laminated plates were carried out and it was observed that delamination damage grows in bursts. This type of non-smooth damage growth under dynamic loading was also observed in [29, 139]. Moreover, it was also observed in [91] that the response is more localized under high velocity impact and results in an increase of impact load with a small increase in displacement. Therefore, it is crucial to understand the interaction between matrix cracking and delamination damage under a range of loading rates, in order to understand damage initiation and evolution in composite laminates. The same knowledge can then be used to design new materials and architectures and to predict the susceptibility of composite laminates to failure.

The motivation of this chapter is three-fold. Firstly, to present a time dependent progressive failure model based on a solid-like shell element, which is able to simulate dynamic fracture in laminated composite plates. Secondly, to numerically simulate and study fast crack propagation in laminated composite plates under transverse loads. Thirdly, to study the effect of the loading rate on damage initiation, interaction between matrix cracking and delamination and evolution of damage. Moreover, the chapter also discusses computational issues related to dynamic fracture modeling in composite laminates.

Several numerical models have been proposed to model impact induced damage in laminated composites. A detailed survey of the computational models proposed

for the analysis of failure in laminated composites can be found in [114]. For an accurate numerical representation and to understand the mechanisms of cracking in laminated composites, such as matrix cracking/splitting and delamination, a cohesive interface element model [13, 30, 42, 47, 61, 99] is often preferred over continuum damage, plasticity and failure based models. However, a drawback of the interface element model is, that it requires the finite element mesh to be aligned with the crack geometry and the cracks can only propagate along predefined locations. Therefore, the model requires different finite element meshes to be generated for different ply orientations with special attention to element stacking in thickness direction [30]. Some of the preferred computational approaches to model cracking in a material are the partition-of-unity (PoU) based approaches, such as the extended finite element method (XFEM) [107, 159] and the phantom node method [106]. PoU based methods allows for the mesh-independent simulation of matrix cracking in laminated composites. As a result, the crack geometry needs not to be aligned with the finite element mesh and the same finite element mesh can be used for different stacking sequences. Such an approach has been used to model the in-plane response of laminated composites in [74, 153] and to model the out-of-plane response in [5], under quasi-static loading.

In this chapter a time-dependent progressive failure model is presented to numerically model and study the damage evolution in composite laminates under dynamic loading conditions. The dynamic variational formulation is an extension of the progressive failure model presented in [5]. The model uses solid-like shell elements to model thin plies of the laminate. The computational model allows for mesh-objective simulation of matrix cracking/splitting through shell finite elements and effectively take the coupling between matrix cracking and delamination damage into account. Moreover, the chapter also discusses the issue of numerical instabilities arising due to imbalance of equilibrium at the interface at the time of insertion of new crack segments. It has been argued in [115], that sudden incorporation of new crack segments into the finite element mesh may lead to numerical problems due to numerical oscillations in the spatial and time derivatives of displacement field. It is shown in this chapter, that if proper equilibrium conditions are met at the interface at the time of insertion of new crack segments, such type of numerical oscillations can be avoided for cohesive cracking.

The chapter is organized as follows. Section 5.2 briefly discusses the time-dependent progressive failure model. In section 5.3 numerical aspects of dynamic fracture modeling are discussed. The application of the method is illustrated through several numerical examples in section 5.4.

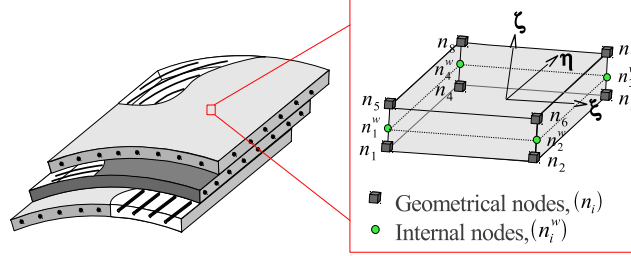


Figure 5.1 Meso-scopic finite element model

5.2 Meso-level progressive failure model

A meso-scopic computational model is presented for the simulation of dynamic damage in laminated composites. The dynamic variational formulation is an extension of the progressive failure model in [5]. Each ply of the laminated composite is modeled with a single layer of solid-like-shell (SLS) elements, figure 5.1. Matrix cracking in individual plies is modeled using the phantom node method [106], whereas delamination damage is modeled with shell interface elements. The model carefully takes the interaction between matrix cracking and delamination damage into account. Detailed variational formulation and finite element implementation aspects can be found in [5]. A brief overview of the time-dependent discontinuous progressive failure model is given in the subsequent sub-sections. The progressive failure model is formulated in a large deformation framework.

5.2.1 Ply-level model

In order to model thin plies of the laminate solid-like shell elements are used. The displacement field, $\boldsymbol{\vartheta}$, of a solid-like shell element in a curvilinear coordinate system (ξ, η, ζ) is defined as

$$\boldsymbol{\vartheta}(\xi, \eta, \zeta) = \mathbf{u}^o(\xi, \eta) + \zeta \mathbf{u}^1(\xi, \eta) + (1 - \zeta^2) \mathbf{u}^2(\xi, \eta) \quad (5.1)$$

in which \mathbf{u}^o is the displacement of the shell mid-surface, \mathbf{u}^1 is the displacement of the shell director \mathbf{D} and \mathbf{u}^2 denote internal stretching of an element which is collinear with the deformed shell director \mathbf{d} and a function of thickness stretch variable ω . Mathematically they are defined as

$$\mathbf{u}^o(\xi, \eta) = [\mathbf{u}_t(\xi, \eta) + \mathbf{u}_b(\xi, \eta)] / 2 \quad (5.2a)$$

$$\mathbf{u}^1(\xi, \eta) = [\mathbf{u}_t(\xi, \eta) - \mathbf{u}_b(\xi, \eta)] / 2 \quad (5.2b)$$

$$\mathbf{u}^2(\xi, \eta) = \omega(\xi, \eta) \mathbf{d}(\xi, \eta) \quad (5.2c)$$

in which \mathbf{u}_t and \mathbf{u}_b are the displacements at top and bottom surface of the shell, respectively cf. figure 5.1.

The weak form of the momentum balance equation is given as

$$\int_{\Omega^o} \delta \mathbf{E} : \boldsymbol{\Sigma} + \int_{\Omega^o} \delta \boldsymbol{\vartheta} \cdot \rho \ddot{\boldsymbol{\vartheta}} - \int_{\Gamma_t^o} \delta \boldsymbol{\vartheta} \cdot \mathbf{T} - \int_{\Omega^o} \delta \boldsymbol{\vartheta} \cdot \hat{\mathbf{b}} = \mathbf{0} \quad (5.3)$$

in which \mathbf{E} and $\boldsymbol{\Sigma}$ are the Green-Lagrange strain and the Second-Piola Kirchhoff stress tensors, respectively. \mathbf{T} are the tractions in the current configuration with respect to the reference area Γ_t^o , $\hat{\mathbf{b}}$ is the body force in the current configuration with respect to the reference volume Ω^o and ρ is the material density in the current configuration with respect to the reference volume. The acceleration of any material point denoted by $\ddot{\boldsymbol{\vartheta}}$ can be found by differentiating equation (5.1), twice respect to time:

$$\ddot{\boldsymbol{\vartheta}}(\xi, \eta) = \ddot{\mathbf{u}}^o(\xi, \eta) + \zeta \ddot{\mathbf{u}}^1(\xi, \eta) + (1 - \zeta^2) \ddot{\mathbf{u}}^2(\xi, \eta) \quad (5.4)$$

in which $\ddot{\mathbf{u}}^2$ is given as

$$\ddot{\mathbf{u}}^2 = \ddot{\omega} \mathbf{d} + \omega \ddot{\mathbf{d}} + 2\dot{\omega} \dot{\mathbf{d}} \quad (5.5)$$

The weak form (equation 5.3) is discretized with standard Galerkin procedures. The discretized weak form for an element e can be written as

$$\mathbf{f}_{conv_e} + \mathbf{f}_{inert_e} + \mathbf{f}_{int_e} - \mathbf{f}_{ext_e} = \mathbf{0} \quad (5.6)$$

in which

$$\mathbf{f}_{conv_e} = \int_{\Omega_e^o} 2\rho(1 - \zeta^2) \mathbf{N}^T \dot{\omega} \dot{\mathbf{d}} \quad (5.7a)$$

$$\mathbf{f}_{inert_e} = \int_{\Omega_e^o} \mathbf{N}^T \rho \mathbf{N} \ddot{\boldsymbol{\vartheta}} \quad (5.7b)$$

$$\mathbf{f}_{int_e} = \int_{\Omega_e^o} \mathbf{B}^T \boldsymbol{\Sigma} \quad (5.7c)$$

$$\mathbf{f}_{ext_e} = \int_{\Gamma_t^o} \mathbf{N}^{*T} \mathbf{T} + \int_{\Omega_e^o} \mathbf{N}^{*T} \hat{\mathbf{b}} \quad (5.7d)$$

\mathbf{f}_{conv_e} , \mathbf{f}_{inert_e} , \mathbf{f}_{int_e} and \mathbf{f}_{ext_e} are the convective, inertial, internal and external force vectors. The shape function matrices (\mathbf{N} and \mathbf{N}^*) and gradient operator matrix (\mathbf{B}) for a linear solid-like shell element with 28 degrees of freedom are defined in [10]. Note that, the convective force contribution to the equilibrium is due to the presence of internal stretching field \mathbf{u}^2 , cf. equation (5.5).

Matrix cracking is modeled with the phantom node method [106], which allows for a mesh-independent simulation of cracking through shell finite elements. The

cracked element with domain Ω_e^o is replaced with a pair of elements, e.g. referred to as element A and element B with domains Ω_e^{oA} and Ω_e^{oB} such that $\Omega_e^o = \Omega_e^{oA} \cup \Omega_e^{oB}$. For the cracked elements, the equilibrium equation (5.6) is modified as

$$\mathbf{f}_{conv_e}^A + \mathbf{f}_{inert_e}^A + \mathbf{f}_{int_e}^A + \mathbf{f}_{coh_e}^A - \mathbf{f}_{ext_e}^A = \mathbf{0} \quad (5.8a)$$

$$\mathbf{f}_{conv_e}^B + \mathbf{f}_{inert_e}^B + \mathbf{f}_{int_e}^B - \mathbf{f}_{coh_e}^B - \mathbf{f}_{ext_e}^B = \mathbf{0} \quad (5.8b)$$

Note that, the definitions of $\mathbf{f}_{conv_e}^{A/B}$, $\mathbf{f}_{inert_e}^{A/B}$, $\mathbf{f}_{int_e}^{A/B}$ and $\mathbf{f}_{ext_e}^{A/B}$ remain similar to equation (5.7) for uncracked elements apart from the integration domains. The cracked elements are only integrated over their active part [106]. An additional term (\mathbf{f}_{coh_e}) appears for the cracked elements, which is the contribution of cohesive tractions to simulate nonlinear processes ahead of the crack tip. \mathbf{f}_{coh_e} is given as

$$\mathbf{f}_{coh_e}^A = \mathbf{f}_{coh_e}^B = \int_{\Gamma_e^c} \mathbf{N}^T \mathbf{T}_c \quad (5.9)$$

in which \mathbf{T}_c are the First-Piola Kirchhoff cohesive tractions.

5.2.2 Delamination interface model

To model delamination damage, a zero-thickness shell interface element based on the kinematics defined in [5, 93] is used. The shell interface model allows computationally efficient simulation of delamination and evaluation of a consistently linearized tangent for large deformation problems. Accordingly the following additional equilibrium equation is required to be solved for the interface contribution

$$\int_{\Gamma_e^c} \bar{\mathbf{N}}^T \mathbf{T}_c^d = \mathbf{0} \quad (5.10)$$

in which \mathbf{T}_c^d are the First-Piola Kirchhoff cohesive tractions at the delamination interface and $\bar{\mathbf{N}}$ is the interface shape function matrix, as defined in [5].

The presence of a matrix crack in the plies connected to an interface requires, that interface elements used to model delamination phenomena should be able to represent cracking in the connecting plies. This is crucial to properly take the effect of matrix cracking on delamination damage into account, as is also discussed in [87]. The present model takes the interaction between matrix cracking and delamination damage into account through an enhanced shell interface model [5]. If the coupling between matrix cracking and delamination damage is not taken into account, it may result in inaccurate predictions of the amount of delamination fracture and the load carrying capacity of the laminate [5].

5.3 Implementation aspects

5.3.1 Constitutive relations

In principle, any kind of constitutive law can be used in combination with the present model. However, in this chapter the material is considered to be rate independent and all rate effects are considered to be due to inertial effects and the presence of cohesive inter-ply/intra-ply cracking. The bulk material response is considered to be orthotropic, linear elastic. The stress-strain relation is given as

$$\boldsymbol{\Sigma} = \mathbb{C} : \mathbf{E} \quad (5.11)$$

in which \mathbb{C} is the fourth-order material tangent stiffness tensor according to

$$[\mathbf{C}]^{-1} = \begin{bmatrix} \frac{1}{E_1} & \frac{-\nu_{21}}{E_2} & \frac{-\nu_{31}}{E_3} & 0 & 0 & 0 \\ \frac{-\nu_{12}}{E_1} & \frac{1}{E_2} & \frac{-\nu_{32}}{E_3} & 0 & 0 & 0 \\ \frac{\nu_{13}}{E_1} & \frac{-\nu_{23}}{E_2} & \frac{1}{E_3} & 0 & 0 & 0 \\ 0 & 0 & 0 & \frac{1}{G_{12}} & 0 & 0 \\ 0 & 0 & 0 & 0 & \frac{1}{G_{23}} & 0 \\ 0 & 0 & 0 & 0 & 0 & \frac{1}{G_{13}} \end{bmatrix} \quad (5.12)$$

in which \mathbf{C} is the matrix form of tensor \mathbb{C} , obtained using Voigt notation. The subscripts 1,2 and 3 denote the orthogonal axes of the principal material coordinate system.

A mixed mode, exponentially decaying cohesive law is used for simulating cohesive matrix cracking and delamination damage. The cohesive traction at the interface is defined as

$$\mathbf{t} = (1 - \omega) f_o \mathbf{r} \quad (5.13)$$

in which \mathbf{r} is a unit vector in the direction of the opening displacement, $\mathbf{r} = \llbracket \mathbf{u} \rrbracket / \llbracket u \rrbracket$, and $\llbracket u \rrbracket = \|\llbracket \mathbf{u} \rrbracket\|$. ω is a damage parameter which varies from 0, the undamaged state, to 1, the fully damaged state. The damage variable ω , is defined as:

$$\omega = 1 - e \cdot \left(\frac{\llbracket u \rrbracket}{\llbracket u \rrbracket_c} \right) \cdot \exp \left(- \frac{\llbracket u \rrbracket}{\llbracket u \rrbracket_c} \right) \quad (5.14)$$

in which

$$e = \exp(1) \quad (5.15)$$

$$\llbracket u \rrbracket_c = \frac{\tilde{G}_c}{e \cdot f_o} \quad (5.16)$$

$$\tilde{G}_c = G_c \left\{ 1 + \frac{1 - 2\exp(-1)}{e \cdot f_o} \right\} \quad (5.17)$$

The parameters G_c and f_o are determined as

$$f_o^2 = f_n^2 + (f_s^2 - f_n^2)\Pi^\eta \quad (5.18)$$

$$G_c = G_{Ic} + (G_{IIc} - G_{Ic})\Pi^\eta \quad (5.19)$$

with

$$\Pi = \left(\frac{G_I}{G_I + G_{II}} \right) = \frac{\llbracket u \rrbracket_s^2}{\llbracket u \rrbracket_s^2 + \langle \llbracket u \rrbracket_n \rangle^2} \quad (5.20)$$

G_{Ic} and G_{IIc} are the fracture toughness in pure tension and shear, respectively. G_I and G_{II} are the energy release rates in tension and shear, respectively. f_o is a mixed mode strength of an interface, f_n and f_s are the tensile and shear interfacial strengths, respectively and η is a mode interaction parameter [26]. The operator $\langle x \rangle = (x + |x|)/2$ is used to nullify the influence of damage in normal direction in compression.

In order to obtain an initially rigid cohesive constitutive law for matrix cracking, the displacement jump $\llbracket u \rrbracket$ in equation (5.14) is replaced with a shifted displacement jump $\llbracket u \rrbracket_{shifted}$. Considering f_o as the magnitude of traction for zero crack opening, the shifted displacement jump is given as $\llbracket u \rrbracket_{shifted} = \llbracket u \rrbracket + \llbracket u \rrbracket_c$. More details on the interface constitutive law can be found in [5].

5.3.2 Mass matrix

In order to solve the dynamic equilibrium equation, a consistent mass matrix for the solid-like shell element [8] is used, for implicit dynamic analysis. The mass matrix for a solid-like shell element is given as

$$\mathbf{M}_e = \int_{\Omega_e} \mathbf{N}^T \rho \mathbf{N} = \begin{bmatrix} \mathbf{M}^{uu} & \mathbf{M}^{u\omega} \\ \mathbf{M}^{\omega u} & \mathbf{M}^{\omega\omega} \end{bmatrix} \quad (5.21)$$

in which the submatrices $\mathbf{M}^{u\omega}$, $\mathbf{M}^{\omega u}$ and $\mathbf{M}^{\omega\omega}$ are assigned a zero mass. It is observed in [8] that assigning a zero mass to these submatrices does not influence the accuracy of the solution and results in an efficient finite element implementation. Moreover, the contribution of the convective force term, \mathbf{f}_{conv_e} in equation (5.7a), is considered to be small [8] and is ignored.

In explicit dynamic simulations, a lumped mass matrix for solid-like shell elements is used. A mass scaling can be used to increase the critical time step. However, in the present contribution, the mass scaling parameters α_u and α_ω for solid-like shell elements are considered to be unity (see reference [8]). A lumped mass matrix for an element e is given as

$$\mathbf{M}_e = \begin{bmatrix} \widetilde{\mathbf{M}}^{uu} & \mathbf{0} \\ \mathbf{0} & \widetilde{\mathbf{M}}^{\omega\omega} \end{bmatrix}_{28 \times 28} \quad (5.22)$$

in which

$$\widetilde{\mathbf{M}}^{uu} = \frac{\rho V_e}{8} \mathbf{I}_{24} \quad , \quad \widetilde{\mathbf{M}}^{\omega\omega} = \frac{\rho V_e}{4} \mathbf{I}_4 \quad (5.23)$$

in which \mathbf{I}_n is an identity matrix of dimensions $n \times n$ and V_e is the volume of element e in the reference configuration.

One of the computational issues in explicit dynamic analysis using the XFEM/phantom node method is that the critical time step reduces due to the presence of cracks. A critical time step is often limited by the size of the element. When a crack divides an element into two parts, the two parts can be considered as individual elements whose sizes are smaller than the parent element. Therefore reducing the critical time step is necessary. The problem becomes worse when the crack crosses the element such that one of the separated parts becomes so small that the critical time step becomes infinitesimal. To remedy this problem, a lumped mass matrix for the uncracked elements, equations (5.22) and (5.23), is used even for the cracked elements. This avoids assigning a nearly zero mass to any of the nodes of a structure. Moreover, it has been observed in [105], that using such a mass discretization for the cracked elements does not significantly reduce the critical time step of the cracked element compared to an uncracked element.

5.3.3 Matrix crack initiation and propagation

In order to model mesh-objective cracking using PoU methods a crack initiation and propagation criterion is required. The failure criterion is defined according to [5], as

$$\frac{\langle \sigma_n \rangle^2 + \sigma_s^2}{f_n^2 + (f_s^2 - f_n^2) \Pi^\eta} = 1 \quad (5.24)$$

with

$$\Pi = \frac{\sigma_s^2}{\sigma_s^2 + \langle \sigma_n \rangle^2} \quad (5.25)$$

in which σ_n and σ_s are the normal and shear components of bulk stress at the crack surface.

To initiate a crack in a virgin material, the failure criterion is evaluated at all integration points in the elements in which cracking is allowed. When the failure criterion is violated in any of the integration points, a new crack segment is introduced at the centroid of the element. For isotropic materials the new crack segment is oriented perpendicular to the direction of principal stresses. For orthotropic materials, it is known that matrix cracks grow in the direction of the fiber orientation, therefore the crack direction is set equal to the fiber direction in a ply.

In order to propagate an existing crack, the failure criterion is required to be evaluated ahead of the crack tip. Since the stress state ahead of the crack tip is not

exact, the average stress in the vicinity of the crack tip using Gauss averaging is often used [159]. In this contribution, instead of using the average stress, the failure criterion is evaluated in the prospective crack element ahead of the existing crack tip. After the failure criterion is violated, the existing crack is extended in fiber direction. A similar propagation criterion was also used in [5, 153] for laminate analysis under quasi-static loading conditions.

The choice of using a local stress field instead of the average stress state is motivated by the following arguments. The average stress state is normally too low compared to the local stress state ahead of a crack tip. As a result, the stress state ahead of the crack tip is underestimated and the crack segment is extended too late. Consequently, too much internal energy is stored in the bulk prior to crack extension. At the time of crack extension, the sudden release of stored energy may result in undesirable structural vibrations and oscillations in the stress/strain and velocity fields. Moreover, when performing a multi-axial cohesive crack analysis using the XFEM/phantom node method, incorporation of new degrees of freedom may lead to substantial noise due to imbalance of cohesive tractions and the stresses in the bulk at the time of injection of new crack segments [115]. Additionally, using the average stress to evaluate the failure criterion means that at the time of crack extension local stresses will be higher than the failure strength of the material. On the other hand, the maximum cohesive tractions prescribed by the cohesive constitutive law are often limited by the material strength parameters. Therefore, a mismatch between the stresses in the bulk and cohesive tractions at the time of insertion of new crack segments is created. As a result the cohesive traction does not satisfy the time continuity which results in oscillations in nodal velocities and forces.

Following the above argument, the failure criterion is evaluated based on a local stress state in the prospective crack element ahead of a cohesive crack tip. Mesh refinement is used in the prospective cracked areas to resolve the characteristic cohesive zone and to obtain better predictions of the stress/strain field ahead of a crack tip. It is argued in [3] that the use of linear quadrilateral and solid elements, for modeling of cohesive cracking through the XFEM/phantom node method, may result in un-realistic predictions of the stress/strain field in the vicinity of a cohesive crack. This is due to the unsuccessful transformation of the displacement jump from integration points to the element nodes as a rigid body motion and is a direct consequence of using linear element shape functions for the approximation of the displacement jump field. Since, the solid-like shell element used in this contribution is also a linear element, the same arguments hold. However, it is shown in [3] that the error in the approximation of the displacement jump field and consequently in the stress/strain fields can be minimized with mesh refinement.

In order to ensure the continuity of the stress/strain and velocity field at the time of insertion of new crack segments, tractions at the time of insertion of new crack

segments are enforced to be in equilibrium with the stresses in the bulk at the crack location, i.e.

$$f_o = \|\mathbf{t}_c\| = \|\boldsymbol{\sigma} \cdot \mathbf{n}_c\| \quad (5.26)$$

This avoids the need of any regularization technique [104], for cohesive cracking, and time continuity in the velocity and stress/strain fields is obtained in a physical manner.

5.4 Numerical examples

In this section numerical examples are presented to simulate fast crack growth in laminated composite plates. Fast crack growth under high rate shear loading in an isotropic material is simulated to show the performance of the numerical scheme in ensuring time continuity in spatial and time derivatives of the displacement field. Next, fast crack growth under Mode-I and Mode-II loading conditions, in a single-edge notch laminated plate, is simulated and the numerical results are compared with the available experimental results. In third and fourth example, a detailed dynamic fracture analysis of a cross-ply laminated plate subjected to different loading rates is presented. Characteristic features of damage growth and interaction between matrix cracking and delamination damage and the effect of loading rate on damage growth are discussed.

5.4.1 Dynamic crack growth in isotropic plate under mixed-mode loading conditions

Dynamic crack growth under high rate shear loading in a single edge notch plate is analyzed, figure 5.2. The plate is considered to be made of PMMA material. The geometry and material properties used for the analysis are extracted from [124]. It has been observed in the experimental studies of [78, 121] that at sufficiently high rate of loading, the crack propagates at an angle between 60° and 70° with the x-axis.

Here, the aim is to examine the efficiency of equation (5.26), for the case of mixed-mode dynamic crack propagation, in ensuring time continuity at the time of insertion of new crack segments. The plate is modeled with 4-node plane stress elements. A refined mesh is used in the prospective crack growth area with a minimum element size equals to $17 \mu\text{m}$. The analysis is performed using both a Newmark constant average-acceleration method (implicit scheme) with consistent mass matrix and a central difference method (explicit scheme) with lumped mass matrix. In the present analysis, the mass is equally lumped on all four nodes for the cracked and uncracked elements. The plate is loaded with a velocity, which increases linearly to a constant

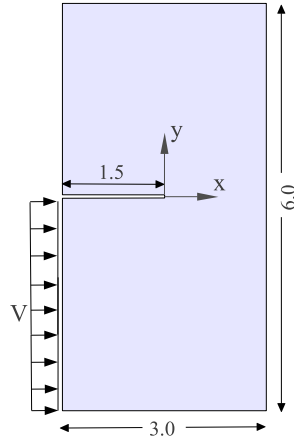


Figure 5.2 Geometry and boundary conditions of a single-edge notch isotropic plate under high rate shear loading (All dimensions in mm)

velocity $V = 25$ m/s within a rise time, $t_r = 1.0E-7$ s, [124]. Explicit as well implicit analyses are performed with a time step, $dt = 1.0E-10$ s.

Figure 5.3a shows the crack tip positions for both implicit and explicit analyses cases. It can be observed that the crack propagates at an angle of approximately 65° to 70° for both analyses cases. Figure 5.3b shows the crack-tip speed. It is evident that the velocity is smooth and no oscillations appear as were observed in in [104]. Small differences in implicit and explicit analysis can be attributed to the different mass discretization.

5.4.2 Dynamic crack growth in a UD composite plate

Numerical simulations of fast crack growth under Mode-I and Mode-II loading in a single-edge notched unidirectional (UD) composite plate, are performed. Plate geometry and boundary conditions are shown in figure 5.4. The longitudinal wave speed in the fiber direction (C_l) and the shear wave speed (C_s) of the material are 7500 m/s and 1600 m/s, respectively [40]. The Rayleigh wave speed in fiber direction is $0.99C_s$. The plate is modeled with solid-like shell elements. A locally refined mesh is used in the prospective crack growth region with an average element size of 0.15 mm. The finite element discretization is shown in figure 5.5. The plate is subjected to impact either by prescribed velocities or forces, uniformly distributed over a length, $l_o = 75$ mm, on the right or left edge of the UD plate, see figure 5.4. An explicit dynamic analysis is performed and integration in the time domain is performed with a second-order accurate central difference method. A lumped mass

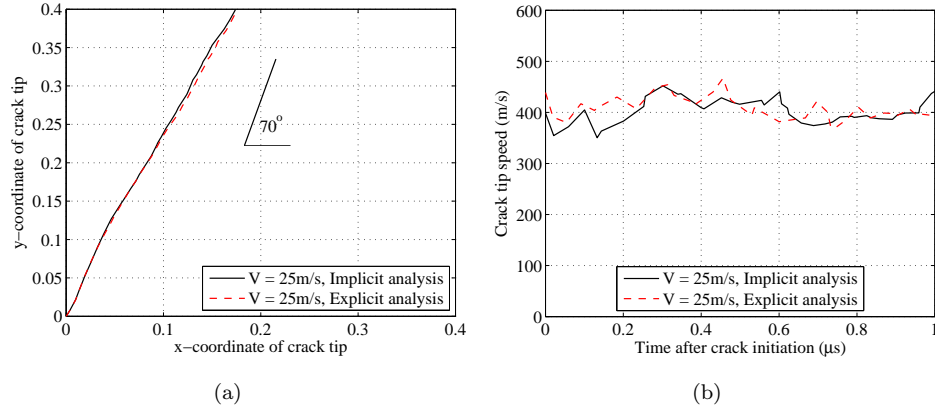


Figure 5.3 Analysis results of crack propagation in an isotropic plate – Effect of time continuity; (a) crack tip position, (b) crack tip speed history

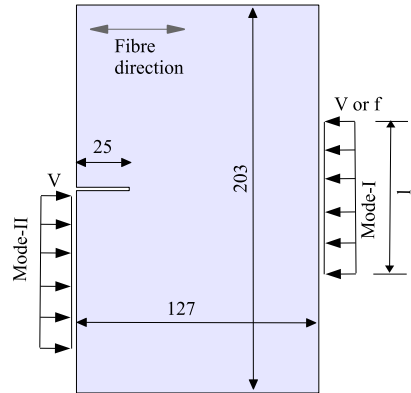


Figure 5.4 Geometry and boundary conditions of a unidirectional plate under impact (all dimensions in mm)

matrix for the solid-like shell elements is used. The numerical results are validated against experimental observations in [40, 126].

Mode-I dynamic crack growth

Low velocity, mode-I crack growth in a UD composite plate is first analyzed. The right edge of the plate is subjected to an impact velocity V defined as

$$V(t) = \begin{cases} V_o \cdot t/t_r & \text{for } t < t_r \\ V_o & \text{for } t \geq t_r \end{cases} \quad (5.27)$$

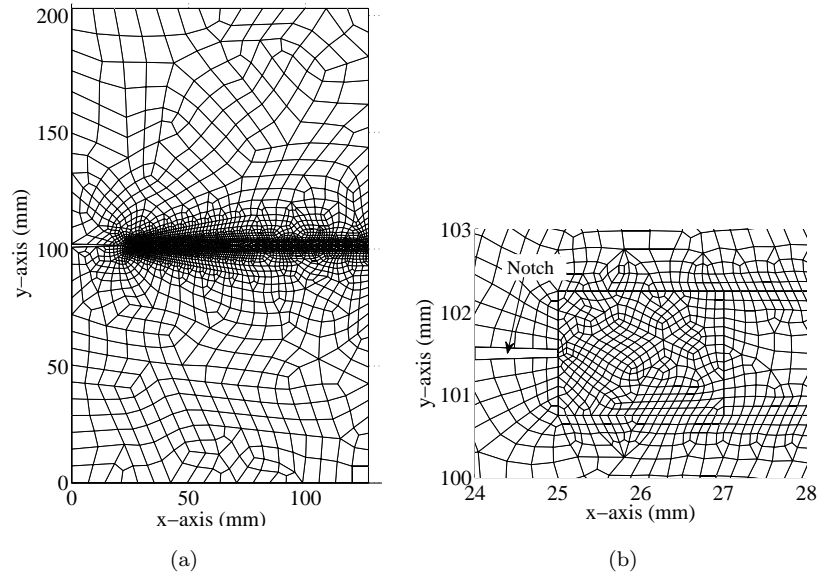


Figure 5.5 Finite element mesh of a UD composite plate; (a) finite element discretization of a UD plate, (b) zoom-in at the finite element mesh around a notch

in which $t_r = 2.0 \mu\text{s}$ is the rise time and $V_o = 12 \text{ m/s}$. The analysis is performed with a time step, $dt = 1.0\text{E-}9 \text{ s}$. The effects of impact velocity and duration are discussed in [7]. The displacement components u_x , u_y and u_z are set to 0 at the bottom-left corner of the plate whereas displacement components u_x and u_z are set to 0 at the top-left corner of the plate.

Figure 5.6 compares the numerically computed crack-tip speed with the experimental result [126]. It can be observed that the numerical crack-tip speed is in good agreement with the experimental result.

Next, dynamic crack growth under Mode-I loading, subjected to high velocity impact, is simulated. The plate is subjected to prescribed loads on the right edge of the plate instead of prescribed displacements. At high impact velocities, the prescribed displacements on the right edge of the plate provide a stiff boundary condition and result in multiple reflections from the boundary before the crack traverses the whole plate. This results in non-smooth crack propagation. Consequently, the crack-tip velocity is non-smooth and shows oscillations. Therefore, in order to simulate high velocity impact, prescribed forces are used to avoid boundary condition effects. Note that, the aim here is to show that at high impact load the crack-tip speed, under Mode-I loading, does not exceed the Rayleigh wave speed of the material. In this case the crack-tip speed is equal to the shear wave speed of the material. This is validated by performing numerical analyses with impact loads of different amplitude.

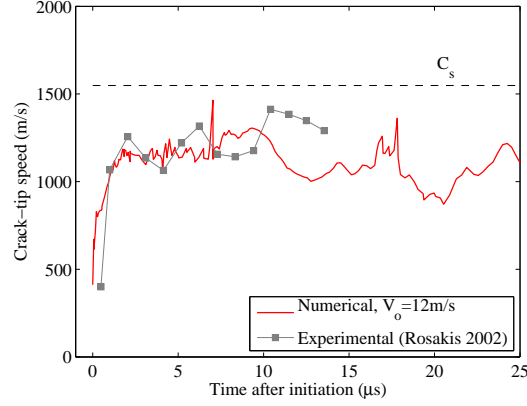


Figure 5.6 Crack-tip speed history for crack growth under Mode-I loading ($V_o = 12$ m/s) in a UD composite plate

Therefore, using Neumann boundary conditions for this analysis case, causes that the results cannot directly be related to the impact speed observed in the experiment of [40]. The loading force history is defined as

$$f(t) = \begin{cases} f_o \cdot l_o \cdot \sin\left(\frac{\pi t}{t_{imp}}\right) & \text{for } t < t_{imp} \\ 0 & \text{for } t \geq t_{imp} \end{cases} \quad (5.28)$$

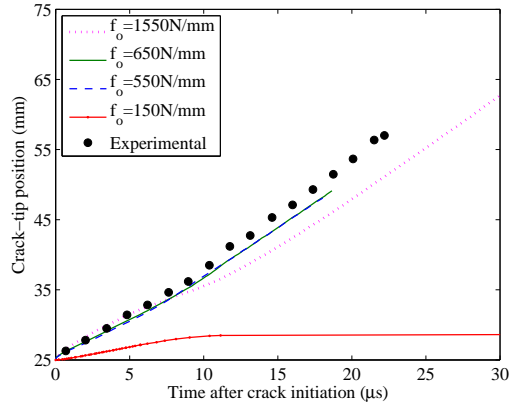
in which $t_{imp} = 27.3 \mu\text{s}$ is the impulse duration. The analysis is performed with a time step, $dt = 1.0\text{E-}9$ s. The load intensity is varied with the loading parameter f_o .

Figure 5.7 shows the analysis results. It can be observed from figure 5.7b that the crack-tip speed increases with increasing load intensity but does not exceed the shear wave speed of the material, as observed by [40] for Mode-I crack propagation.

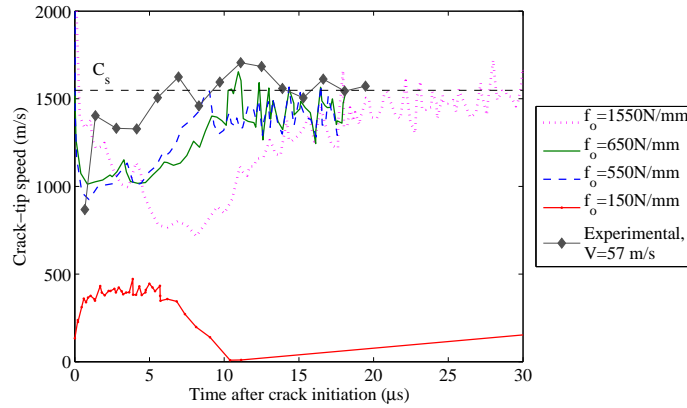
Mode-II dynamic crack growth

Mode-II, dynamic crack propagation in a UD composite plate is simulated. Here, the attention is focused on numerical simulation of cracks propagating at speeds higher than the shear wave speed of the material. The plate is subjected to a prescribed velocity, on the left edge of the plate, figure 5.4, and is defined as

$$V(t) = \begin{cases} V_o t / t_r & \text{for } 0 \leq t < t_r, \\ V_o & \text{for } t_r \leq t < t_p, \\ V_o (1 - (t - t_p) / t_s) & \text{for } t_p \leq t < (t_p + t_s), \\ 0 & \text{for } t \geq (t_p + t_s). \end{cases} \quad (5.29)$$



(a)



(b)

Figure 5.7 Mode-I crack growth in a UD plate subjected to high impact loads; (a) crack-tip position, (b) crack-tip speed

in which t_r is the rise time, t_p is the pulse time and t_s is the step down time. In the calculations t_r and t_s are taken to be $2 \mu\text{s}$, t_p is taken to be $25.3 \mu\text{s}$ and V_o is equal to 28 m/s . The displacement components u_x , u_y and u_z are set to 0 at the top-left corner of the plate whereas displacement components u_y and u_z are set to 0 at the top-right corner of the plate. The numerical analysis is performed with a time step, $dt = 5.0\text{E-}10 \text{ s}$.

Figures 5.8a and 5.8b show the crack-tip position and speed in comparison with the reference solution [40]. The numerical results are in good agreement with the

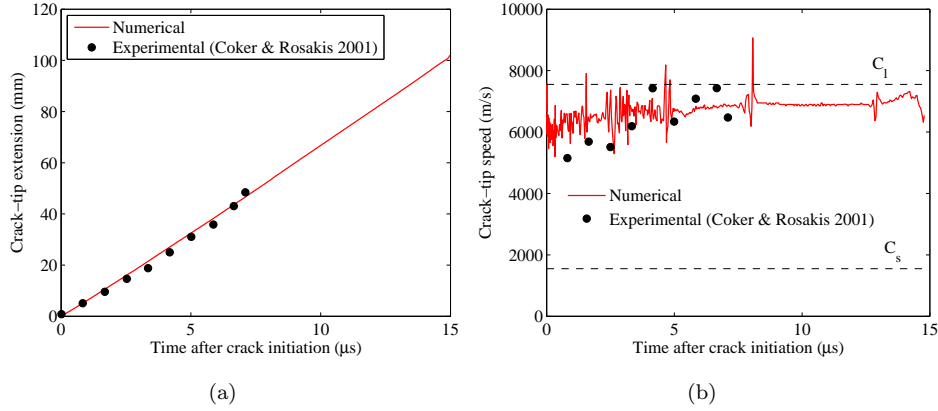


Figure 5.8 Mode-II crack growth in a UD plate subjected to high velocity impact; (a) crack-tip position, (b) crack-tip speed

reference solution. It is evident from figure 5.8b that the crack-tip speed is greater than the shear wave speed of the material and the crack tip propagates at a constant speed, close to the longitudinal wave speed of the material. This is due to the development of a shock wave behind the crack tip. Figure 5.9 shows the stress profiles around the crack at different times. The initial compressive wave, reflected as tensile wave from the lower edge of the notch, loaded the notch tip in a shear mode, figure 5.9a. After some time, the crack accelerates and a shock wave appears behind the crack tip, which suggests that the crack is propagating intersonically, figure 5.9b. The crack propagates intersonically until it traverses the whole width of the plate.

5.4.3 Impact induced damage in [0/90] laminated plate

A two-layered, un-symmetric, cross-ply laminated plate is analyzed. The laminated plate is considered to be made of carbon-fibre-reinforced epoxy composite (HTA-6376C). The orthotropic material properties used for the analysis are extracted from [18] and are given in table 5.1. The density, ρ of the material is considered to be 1620 kg/m^3 . The plate geometry and boundary conditions are shown in figure 5.10a, where $L = 10 \text{ mm}$ and $W = 4.8 \text{ mm}$. The ply thickness is considered to be 0.2 mm . The plate is clamped on two sides and is impacted at the middle of the plate. The laminated plate is loaded with load P , linearly increasing with time at a rate r_p . The plate is impacted with different loading rates (r_p) varying from 0.03 MN/s to 30 MN/s .

The main focus of this example is to study the effect of the loading rate on the damage development and to gain further insight into the damage growth and interaction

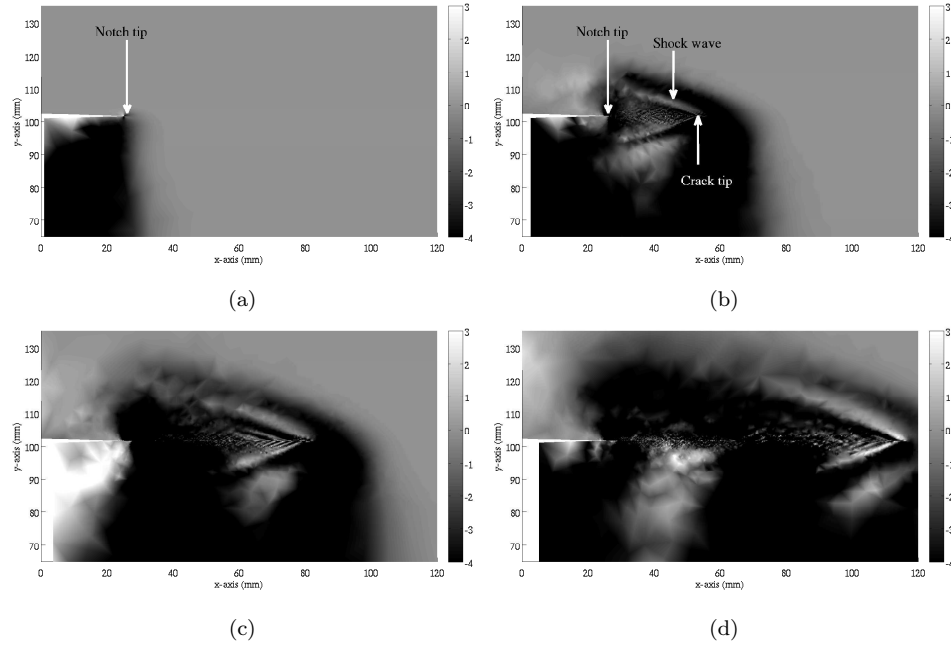
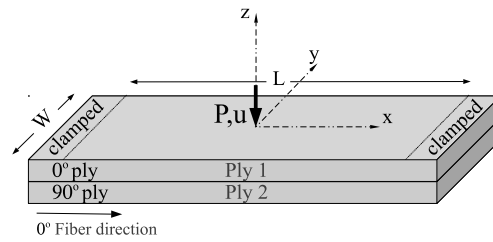


Figure 5.9 Stress component σ_{yy} (MPa) at (a) time, $t = 4 \mu\text{s}$, (b) time, $t = 10 \mu\text{s}$, (c) time, $t = 14 \mu\text{s}$ and (d) time, $t = 19 \mu\text{s}$

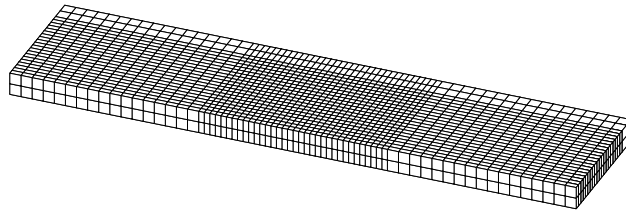
between matrix cracking and delamination damage in laminated composite plates, under dynamic loading conditions. An implicit analysis is performed for the sake of accuracy and to ensure, that the balance of momentum is satisfied at each time step, especially when damage growth takes place. Integration in the time domain is performed with a Newmark constant-average-acceleration method. A consistent mass matrix, as defined in section 5.3.2, is used for the analysis. The numerical analysis is performed with a time step, $dt = 2.5\text{E-}5$ s. Each ply of the laminate is modeled with a single layer of solid-like shell elements in thickness direction, figure 5.10b. A fine mesh with an average element size of 0.10 mm in the in-plane dimension is used near the center of the plate, where damage is likely to grow. The finite element mesh consists 2992 elements with 6348 nodes. Matrix cracks are allowed to initiate with a minimum crack spacing of 0.25 mm.

Load-displacement behavior

Figure 5.11 compares the load-displacement curves for the three characteristic loading rates. These curves can be roughly classified into three main categories for further discussions. (1) Low loading rate case, e.g. $r_r = 0.03$ MN/s. At these loading rates,



(a)



(b)

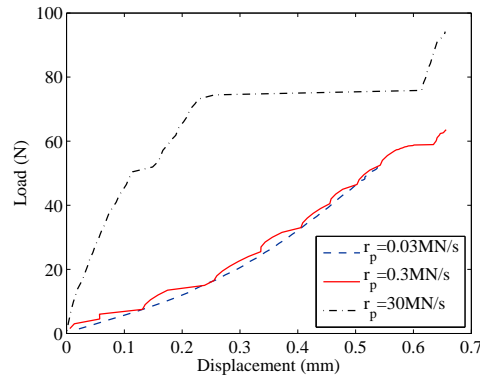
Figure 5.10 Two ply laminated plate; (a) Geometry and boundary conditions of a plate, (b) Finite element mesh of half of a plate

the curves are smooth and the displacement increases monotonically with applied load. Moreover, the damage also grows smoothly without hiccups. (2) An intermediate loading rate case, e.g. $r_p = 0.3$ MN/s. In this case the curves show small flexural vibrations. (3) High loading rate case, e.g. $r_p = 30$ MN/s. In this case, there is significant increase in initial impact load with small displacements, until material failure occurs. This is the moment at which point the elastically stored energy is suddenly released and displacement of the structure increases with little increase in load.

It can be observed from figure 5.11, that dynamic effects due to flexural vibrations start to appear as the loading rate increases. Successive arrivals of compressive and tensile stress waves hinder a smooth growth of damage. During the time of arrival of a compressive wave, damage does not grow and the energy is stored as elastic energy in the body resulting in a stiff response, e.g. the curves of $r_p = 0.3$ MN/s and 30 MN/s (figure 5.11). The arrival of a next tensile wave results in a sudden release of energy with little or no load increase. This effect appears as a plateau in the load-displacement curve. Moreover, this effect increases with the increase in loading rate due to increasing magnitude of compressive wave. This shows that damage growth becomes non-smooth with increasing loading rates, as observed in [29, 33, 91]. Furthermore, it can be observed that increasing loading rate results in an increasing impact load compared to low loading rate case.

Table 5.1 Material properties used for analysis

Material properties of HTA-6376C	
Longitudinal Young's modulus, E_{11} (GPa)	120
Transverse Young's modulus, $E_{22} = E_{33}$ (GPa)	10.5
In-plane shear modulus, $G_{12} = G_{13}$ (GPa)	3.48
Poisson's ratio, $\nu_{12} = \nu_{13}$	0.3
Poisson's ratio, ν_{23}	0.5
Mode I fracture toughness, G_{Ic} (N/mm)	0.26
Mode II fracture toughness, G_{IIc} (N/mm)	1.002
Transverse tensile strength, f_n (MPa)	30
In-plane shear strength, f_s (MPa)	60

**Figure 5.11** Load-displacement response of a two-ply laminated plate under dynamic loading*Damage characteristics at intermediate loading rate, $r_p = 0.3$ MN/s*

Since, there are no significant differences in dynamic effects between the intermediate and low loading rate cases, except the presence of flexural vibrations in case of intermediate loading rate case, the damage development in low loading rate case is not discussed. Figure 5.12 shows the sequence of damage development by means of delamination damage at an interface and matrix cracking in the lower ply, at different times. A thick blue line over a crack represents the traction-free portion of the crack. The damage initiates with the formation of cohesive matrix cracking in the lower ply, as observed in [37], at time, $t = 7.5 \mu\text{s}$ ($P = 4.5$ N). Once the middle matrix crack starts to become traction free, it triggers delamination damage at an interface, figure 5.12a. This delamination damage grows in the shape of two

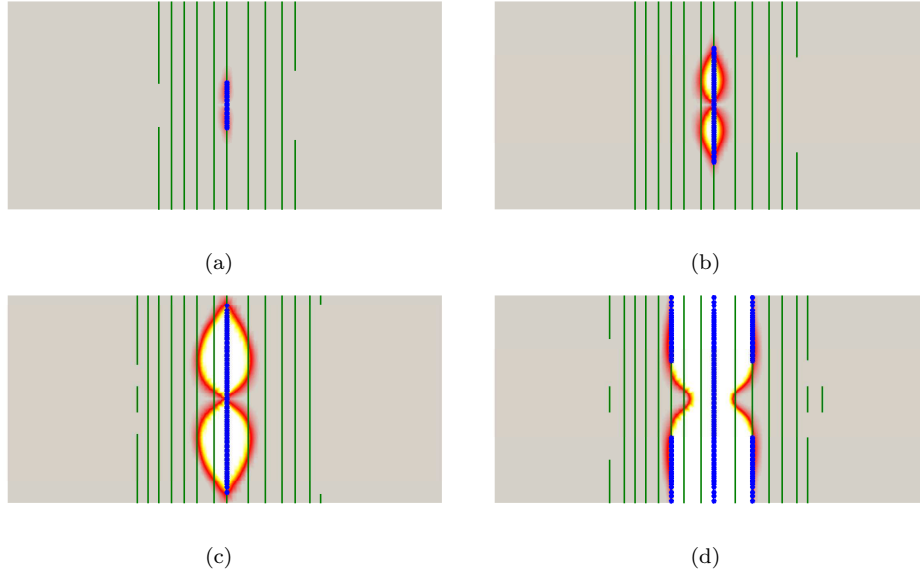


Figure 5.12 Damage development in a two-ply laminated plate subjected to a loading rate $r_p = 0.3$ MN/s; (a) $P = 22.51$ N, $t = 37.5 \mu\text{s}$, (b) $P = 45.0$ N, $t = 75 \mu\text{s}$, (c) $P = 57.29$ N, $t = 95.5 \mu\text{s}$ and (d) $P = 58.95$ N, $t = 98.25 \mu\text{s}$

lobes, oriented along the fibre direction of the lower ply. Notably, it can be observed from the figures that the tip of the delamination zone coincides with the tip of the traction free center matrix crack. This suggests that there is a strong interaction between these two damage mechanisms. As time progresses, a larger portion of the center matrix crack becomes traction free along with the formation of more matrix cracking, concentrated in the center of the plate. Consequently, the delamination at an interface grows in size and at $98.25 \mu\text{s}$ (stage d in figure 5.12) the delamination spreads over a significant portion of the plate. At this time other cohesive matrix cracks along the edges of the delamination area also become traction free in a very short time. Moreover, it can also be observed that almost all of the cohesive matrix cracks extend over the full width of the plate.

It can be seen from figure 5.12c, that the delamination area reached the edge of the plate at $95.5 \mu\text{s}$. This takes a relatively long time. During the same period, dilatational waves travel through the thickness of the specimen approximately 8 times. This results in flexural vibration of the plate, see figure 5.11. However, these flexural vibrations do not significantly influence the damage growth compared to the response of the laminate at $r_p = 30$ MN/s. The damage pattern and sequence of damage growth at loading rates 0.03 MN/s upto 0.3 MN/s are similar which suggests

that flexural vibrations up till a loading rate equal to 0.3 MN/s do not significantly influence the response. After 95.5 μs , there is an abrupt increase in the delamination area and matrix cracking and the whole damage process takes place in a relatively short time. These observations are consistent with the experimental observations in [91], in which delamination growth was observed to occur non-smoothly. Moreover, the shape of the delamination area is more elongated, which underlines the anisotropic nature of delamination growth in the fibre and transverse directions at low and intermediate loading rates. The average speed of delamination growth in the fibre and transverse direction, between 75 μs and 95.5 μs , is calculated to be 43 m/s and 31 m/s, respectively.

Damage characteristics at high loading rate, $r_p = 30 \text{ MN/s}$

Figure 5.13 shows the sequence of damage development at high loading rate, $r_p = 30 \text{ MN/s}$. The damage initiates with the formation of a cohesive matrix crack at time, $t = 0.275 \mu\text{s}$ ($P = 16.2 \text{ N}$). As the time progresses, delamination damage begins to grow in the shape of a peanut. Note that, this behavior is different from the low/intermediate loading rate cases (see figure 5.12), in which the delamination damage initiated after the formation of a traction free matrix crack in the middle of the plate. As time progresses, the center matrix crack starts to open up and becomes traction free along with the growth of delamination damage. After time, $t = 1.325 \mu\text{s}$, there is a sudden growth of damage, i.e formation and growth of a higher number of cohesive as well traction-free matrix cracks and growth of delamination damage to a significant area of the interface, figure 5.13f. Moreover, it can be observed that the whole damage process takes place in a very short time compared to the low/intermediate loading rate cases.

It is observed, that the duration of damage development in the case of a high loading rate is much shorter than in the intermediate loading rate case. Moreover, the number of matrix cracks is smaller compared to the low/intermediate loading rate cases. In contrast to the low loading rate case, matrix cracks are now more distributed over the whole plate instead of being concentrated at the center of the plate. Moreover, it can be observed from figure 5.13 that not all matrix cracks extend to the full width of the plate.

It is also evident from the damage growth (figure 5.13), that in contrast to the case of low/intermediate loading rate, the tip of the two lobes of the delaminated area does not coincide with the tip of the traction free matrix crack. Moreover, the delaminated area for the case of high loading rate is more rounded compared to the intermediate loading rate case. This is due to a difference in structural response at high and low loading rates [33, 113]. The average delamination growth velocity in fibre and transverse direction during the interval 1.05 μs and 1.325 μs is the same

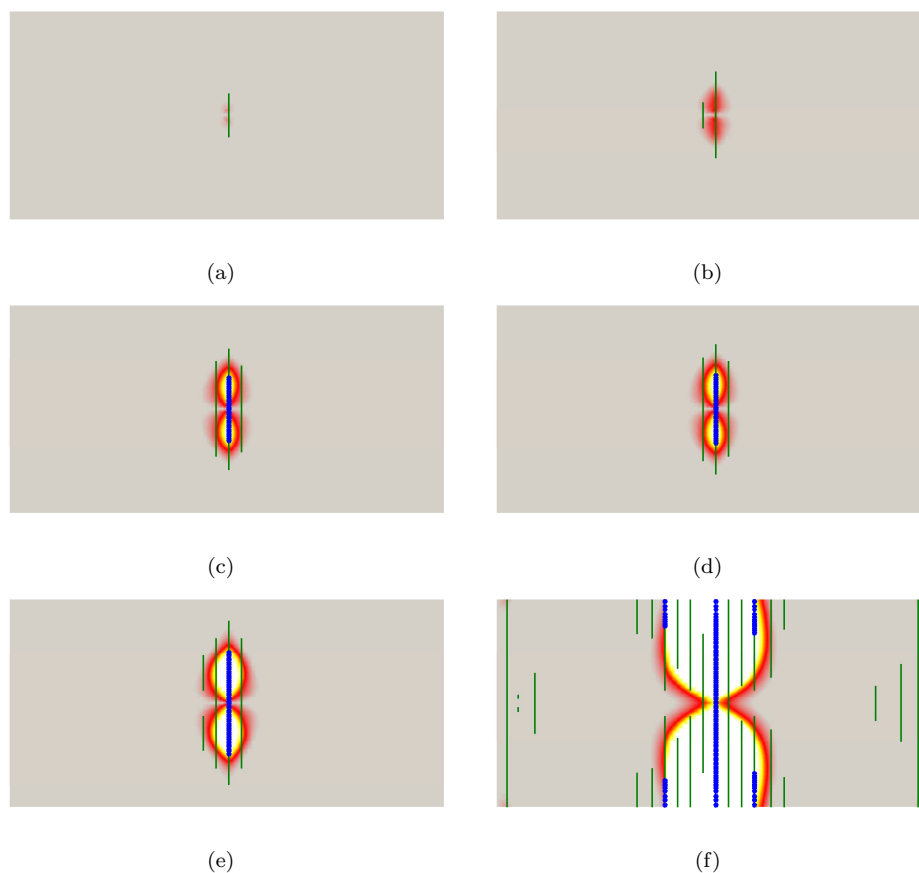


Figure 5.13 Damage development in a two-ply laminated plate subjected to a loading rate $r_p = 30$ MN/s; (a) $P = 22.34$ N, $t = 0.4 \mu\text{s}$, (b) $P = 45.10$ N, $t = 0.8 \mu\text{s}$, (c) $P = 57.14$ N, $t = 1.025 \mu\text{s}$, (d) $P = 59.23$ N, $t = 1.05 \mu\text{s}$, (e) $P = 74.45$ N, $t = 1.325 \mu\text{s}$ and (f) $P = 75.84$ N, $t = 1.35 \mu\text{s}$

and is calculated to be 1164 m/s. It is approximately 80% of the shear wave speed of the bulk material. Such high rates of delamination growth were also observed in [91].

Stress waves at intermediate loading rate, $r_p = 0.3$ MN/s

Figure 5.14 shows contours of stress components σ_{xx} and σ_{yy} of the bottom surface of ply-2. It can be observed from the stress component σ_{xx} that at intermediate loading rate the deformation of the plate is uniform and the stress contours are uniformly smeared over the whole specimen. Moreover, a small zone of compression, of smaller magnitude, can be seen ahead of the traction-free matrix crack tip. The

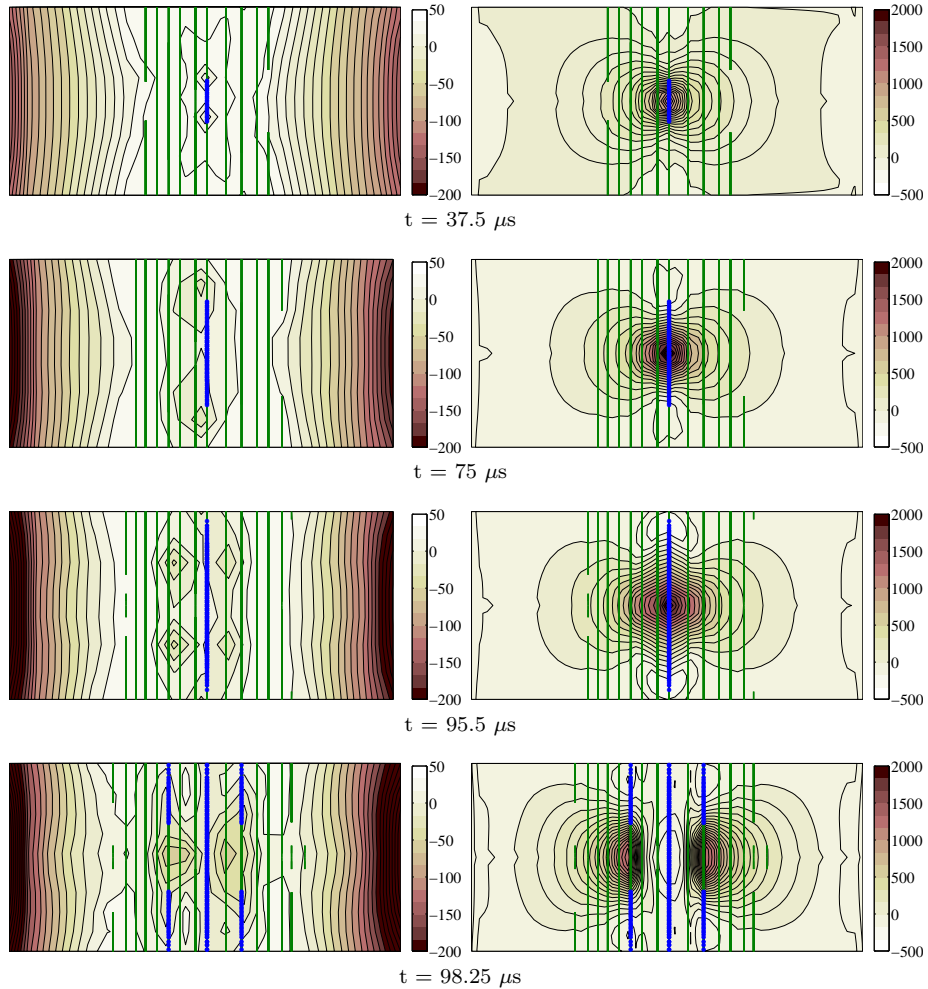


Figure 5.14 Contours of stress components at different time instants for loading rate $r_p = 0.3$ MN/s; Left: stress component σ_{xx} (MPa), Right: stress component σ_{yy} (MPa)

appearance of these compressive zones due to successive flexural vibrations results in a non-smooth damage growth. As the magnitude of these small zones of compression is not significant, damage growth in each successive burst is also small and therefore the load-displacement curve followed the load-displacement curve of the low loading rate. Damage growth takes place gradually in small bursts until significant damage has taken place. Similar observations can also be made from the stress contours σ_{yy} .

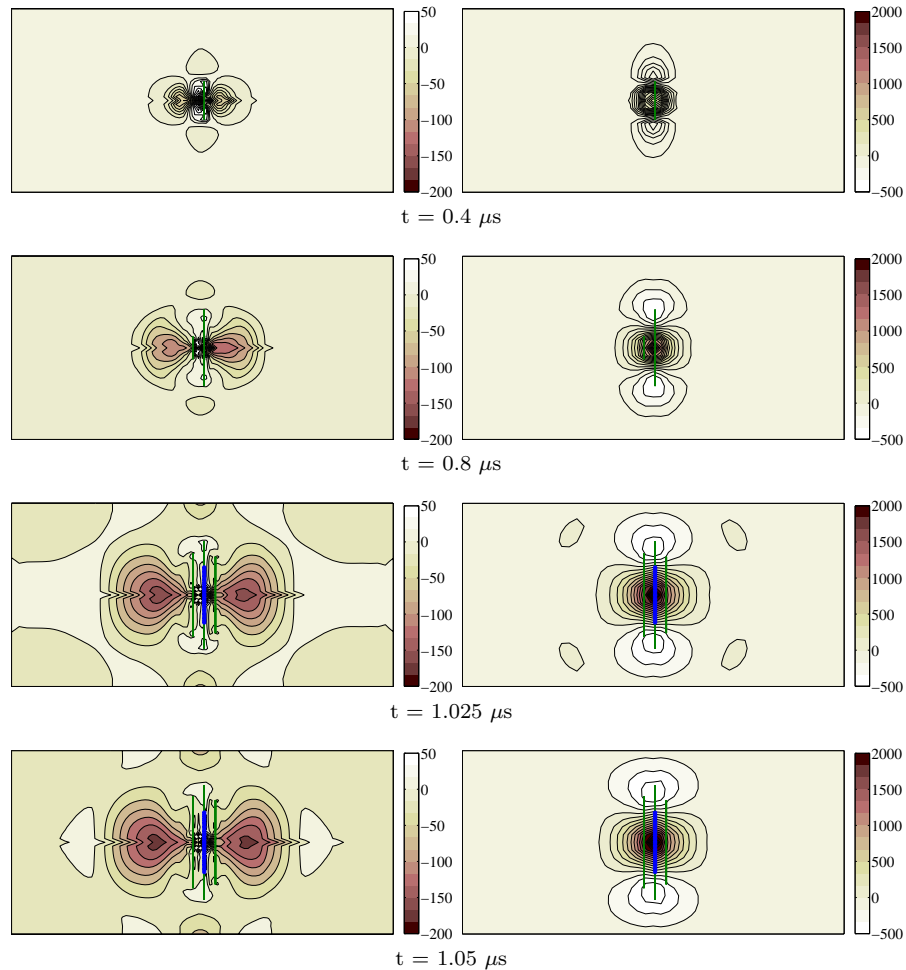


Figure 5.15 Contours of stress at different time instants for loading rate $r_p = 30$ MN/s; Left: stress component σ_{xx} (MPa), Right: stress component σ_{yy} (MPa)

Stress waves at high loading rate, $r_p = 30$ MN/s

Figures 5.15 and 5.16 show the stress wave profiles for the case of high loading rate, $r_p = 30$ MN/s, at different times. It can be observed from figures 5.15 and 5.16, that stress contours show large stress gradients compared to the case of intermediate loading rate, figure 5.14. Moreover, the stress contours are much more localized to the center of the plate. This suggests that at high loading rate the deformation is more localized. It is also evident from figures 5.15 and 5.16, that there is a zone of

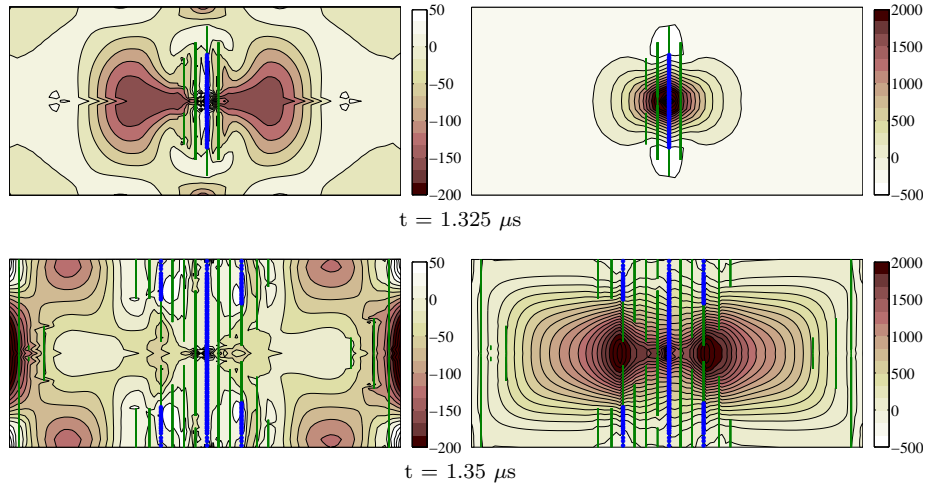


Figure 5.16 Contours of stress at different time instants for loading rate $r_p = 30$ MN/s; Left: stress component σ_{xx} (MPa), Right: stress component σ_{yy} (MPa)

large amplitude compressive stresses ahead of the crack tip compared to the case of intermediate loading rate. The presence of this compressive wave results in an arrest of the matrix crack, which also prevents the growth of delamination damage for some time. As time progresses, the tension wave arrives at time $t = 1.325 \mu\text{s}$. The arrival of the tension wave results in an instantaneous growth of matrix cracking and delamination damage at time $1.35 \mu\text{s}$ due to the stored energy in the bulk during the crack arrest period. It can also be observed from the stress contours σ_{xx} that higher order modes are present in case of higher loading rate compared to the intermediate loading rate case.

Energy dissipated during matrix cracking and delamination damage

Figure 5.17 compares the energy dissipated during matrix cracking and delamination damage as a function of displacement at the center of the plate, at different loading rates. It is observed from figure 5.17a that there is no significant effect loading rate on energy dissipation during matrix cracking. On the other hand, energy dissipation during delamination damage increases at high loading rate, see figure 5.17b.

Figure 5.18a compares the energy dissipation during matrix cracking as a function of time, at different loading rates. It can be observed that at low loading rate the energy dissipation is gradual and smoothly varying with time. However, for the case of intermediate loading rate the energy dissipation is non-smooth which represents stick-slip behavior of crack growth, as observed in [29, 139]. Moreover, at low and intermediate loading rates e.g. $r_p = 0.03$ MN/s and 0.3 MN/s, energy dissipation

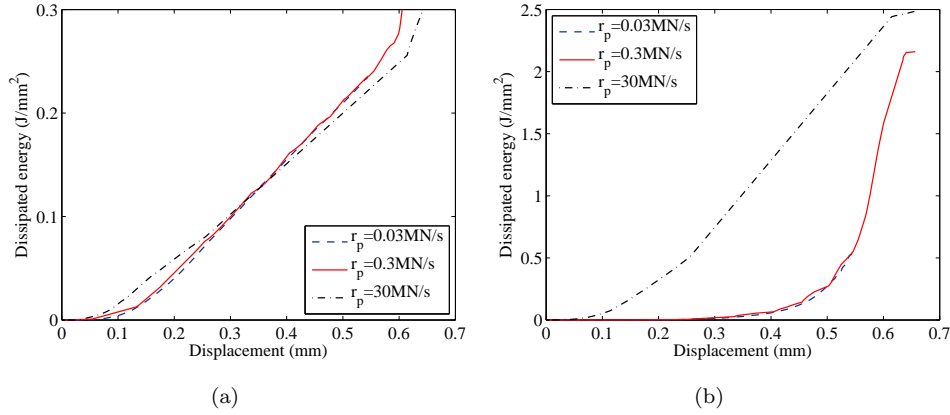


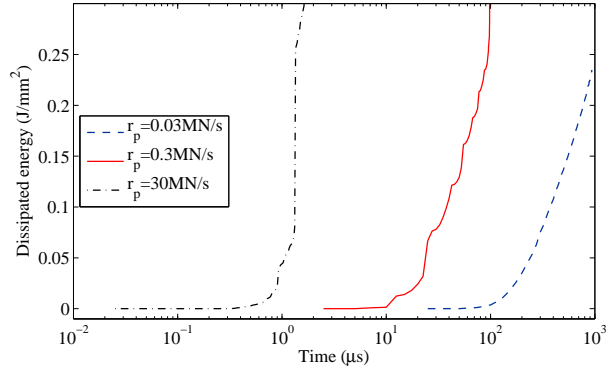
Figure 5.17 Comparison of energy dissipation as function of plate deflection in a two-ply laminated plate; (a) Energy dissipation during matrix cracking, (b) Energy dissipation during delamination

is gradual whereas at high loading rate $r_p = 30$ MN/s, the energy dissipation is instantaneous which shows that damage process takes place abruptly.

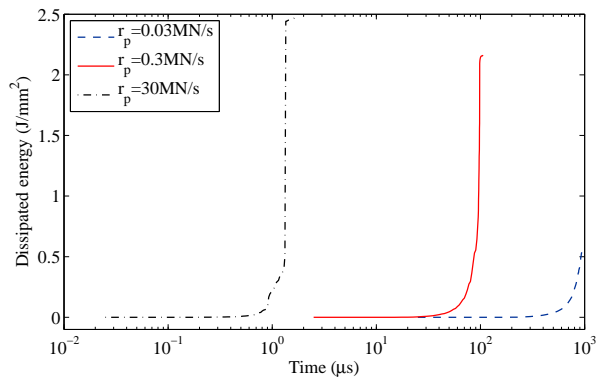
Figure 5.18a compares the energy dissipation during delamination damage as a function of time, at different loading rates. Comparing figures 5.18a and 5.18b, it can be observed that matrix cracking and delamination damage initiate approximately at the same time, which shows a strong interaction between the two damage mechanisms. However, for the case of low and intermediate loading rate, matrix cracking continues to dissipate energy gradually with time after damage initiation whereas, delamination damage start to grow with some delay. On the contrary, at high loading rate $r_p = 30$ MN/s matrix cracking and delamination damage grow simultaneously. Similar observations are made in sections 5.4.3 and 5.4.3, in which delamination damage is observed to grow after the formation and growth of a traction free matrix crack at low and intermediate loading rates. However, for the case of high loading rate, the two damage mechanisms grow simultaneously.

Matrix crack propagation speed

Figure 5.19 compares the crack-tip speed of the center matrix crack, propagating from the center of the plate to the edge of the plate, for different loading rates. It can be observed from figure 5.19a that for low and intermediate loading rates the crack propagates at approximately constant speed except at the time of initiation and the time at which the crack is very close to the edge of the plate. However, the crack propagation speed is very low, less than 100 m/s, but the crack speed increases with increasing loading rate.



(a)



(b)

Figure 5.18 Comparison of energy dissipation as a function of time in a two-ply laminated plate; (a) Energy dissipation during matrix cracking, (b) Energy dissipation during delamination

Figure 5.19b represents the crack-tip speeds for the case of high loading rate. It can be observed that for the loading rate 30 MN/s, the crack starts propagating at a speed close to the shear wave speed of the material and accelerates to a speed close to the longitudinal wave speed of the material. Soon after that crack arrest occurs and later on, the crack propagates at a speed close to the shear wave speed followed by a rapid crack propagation towards the edge of the plate, as discussed in section 5.4.3. The increased crack-tip speed beyond longitudinal wave speed is due to numerical artefact.

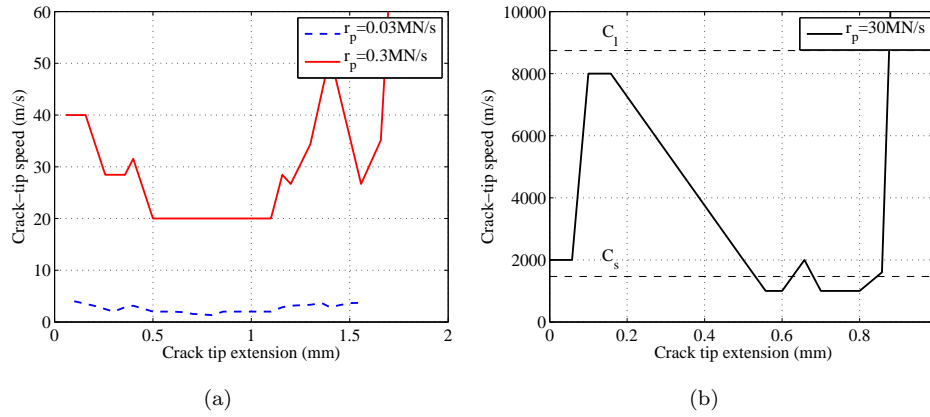


Figure 5.19 Crack-tip speed of the center matrix crack, propagating from the center to the edge of the plate

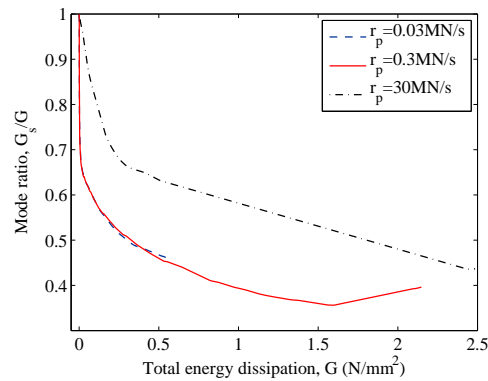
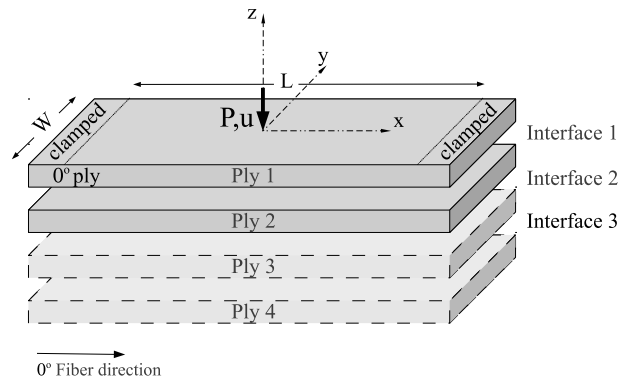


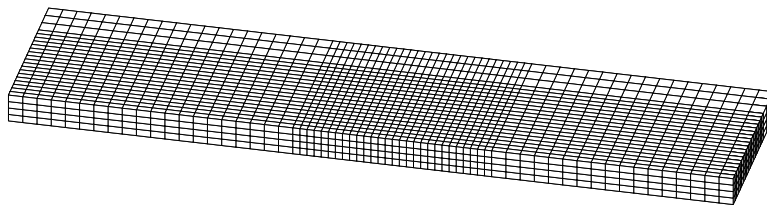
Figure 5.20 Fracture mode ratio during delamination damage

Effect of loading rate on delamination mode ratio

Figure 5.20 shows the effect of loading rate on the interface fracture mode ratio during delamination. It is evident from the figure that for the case of low and intermediate loading rate case, soon after the initiation of delamination damage, the delamination interface tends to open in mixed mode (mode ratio ≈ 0.7) which further decreases gradually to a value below 0.5 and has a major contribution from the Mode-I fracture mode. This suggests that for low and intermediate loading rates, Mode-I delamination cracking dominates delamination growth. On the other hand, for the case of high rate of loading, the shearing fracture mode dominates the re-



(a)



(b)

Figure 5.21 Four-ply laminated plate; (a) Geometry and boundary conditions, (b) Finite element mesh

sponse and delamination damage initiates in a pure shearing mode and the fracture mode gradually shifts to mixed-mode fracture.

5.4.4 Laminate with multiple delamination

To examine the behavior of dynamic fracture in a laminate with multiple delaminating interfaces, a four-ply laminated plate is analyzed. For this purpose, the laminate of section 5.4.3 is scaled by a factor 2, using a sub-laminate level scaling technique. The resulting laminate has a length, $2L = 20$ mm, width, $2W = 9.6$ mm and a stacking sequence $[0/90/0/90]$, see figure 5.21a. Note that, the resulting laminate has three potential interfaces for delamination damage. This is done in order to analyze a laminate which is geometrically similar to the laminate of section 4.3 except having more interfaces. It should be noted, that the aim here is not to study scaling effects in laminates. The impact analysis is performed with two loading rates $r_p = 0.09$ MN/s and 0.3 MN/s. Matrix cracks are allowed to initiate with a minimum crack spacing of 0.5 mm. A fine mesh with an average element size of 0.15 mm is

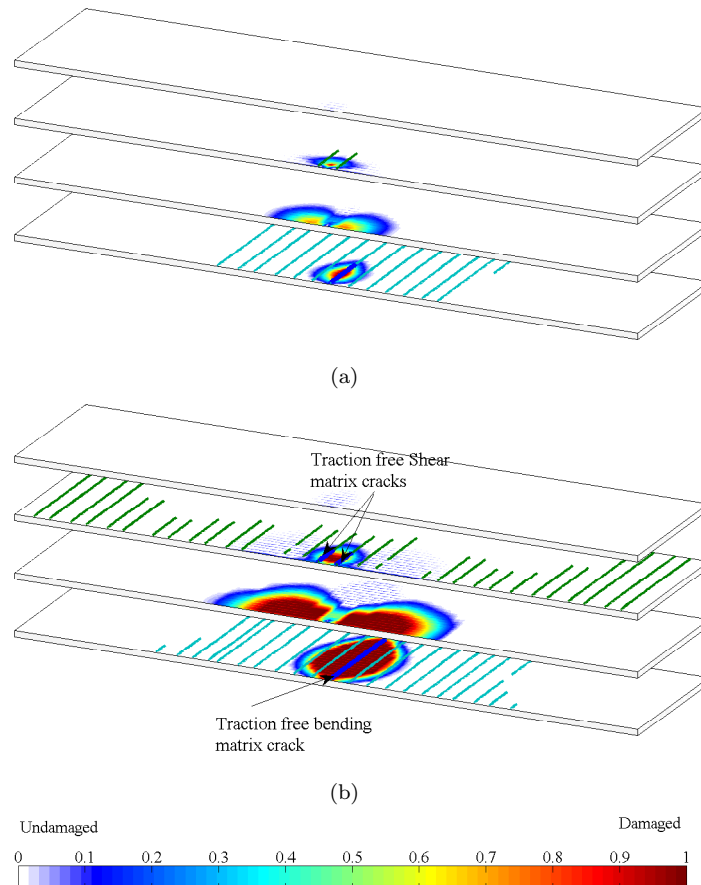


Figure 5.22 Damage development in a four-ply laminated plate subjected to loading rate 0.09 MN/s ; (a) $P = 135 \text{ N}$, $t = 750 \mu\text{s}$, (b) $P = 259.2 \text{ N}$, $t = 1440 \mu\text{s}$

used near the center of the plate, where damage is likely to grow. The finite element model consists of 11615 elements with 11616 nodes, figure 5.21b.

Figure 5.22 shows the damage development by means of matrix cracking in the plies and delamination damage at the interface for the case of $r_p = 0.09 \text{ MN/s}$, at different times. As expected, damage initiates with a bending matrix crack in the outermost ply. As time progresses the center matrix crack becomes traction free and starts to open up upon bending resulting in a progressive delamination opening in mixed mode, figure 5.23a. Delamination grows in the shape of a half peanut, oriented along the fiber direction of the lowermost ply, ply-4. As time progresses, matrix cracking also develops in inner ply-2. Two of the matrix cracks in the center of

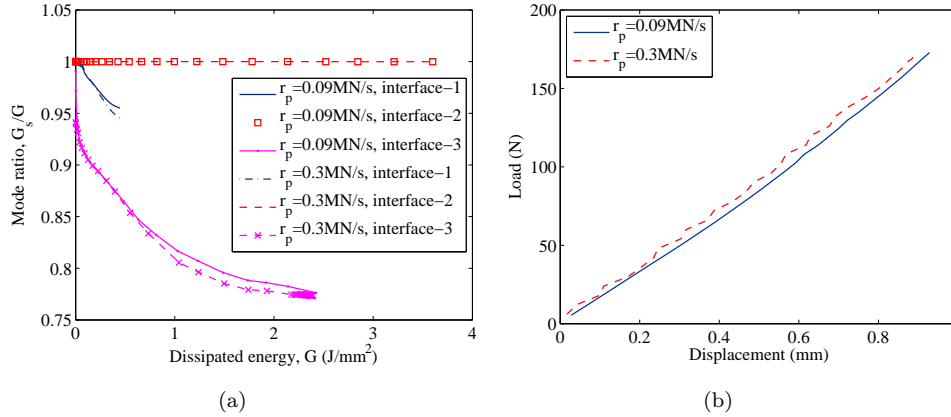


Figure 5.23 Analysis results of a four-ply laminated plate; (a) Delamination mode-ratio, (b) load-displacement response

ply-2 become traction free under combined bending and shear stresses. Additionally, growth of these matrix cracks results in substantial growth of delamination at the lower interface (interface-2, (90/0)) and small delamination at the upper interface (interface-1, (0/90)) of the cracked ply-2. Delamination grows in a pure shearing fracture mode at interface-2, figure 5.23a. These numerical results are consistent with experimental observations in [36, 37]. Note that initiation and growth of different matrix cracks and the selection of appropriate matrix crack to become open and become traction free, at different interfaces is done automatically by the present model as opposed to the use of interface elements in which the location of matrix cracks had to be defined a priori.

Figure 5.23b compares the load-displacement response for two loading rates. It can be observed, that for case $r_p = 0.09$ MN/s, load and displacement of the plate are in phase and the curve is smooth. On the other hand, for the case $r_p = 0.3$ MN/s, bumps appears in the load-displacement curve. Therefore, the cases $r_p = 0.09$ MN/s and 0.3 MN/s can be classified as low and intermediate loading rate cases, respectively, based on the classification defined in section 5.4.3. Moreover, it can be observed that the impact load is slightly larger for the case of intermediate loading rate compared to the case of low loading rate.

Figure 5.24 compares the energy dissipation during matrix cracking and delamination damage at two different loading rates. It can be observed from figure 5.24a, that the curves for the case of $r_p = 0.3$ MN/s shows a staircase response, which is again due to successive arrivals of compressive and tensile waves resulting in a non-smooth crack growth. Consequently, delamination at the interfaces also grows non-smoothly, figure 5.24b. Moreover, it can be observed from figure 5.24 that energy dissipation

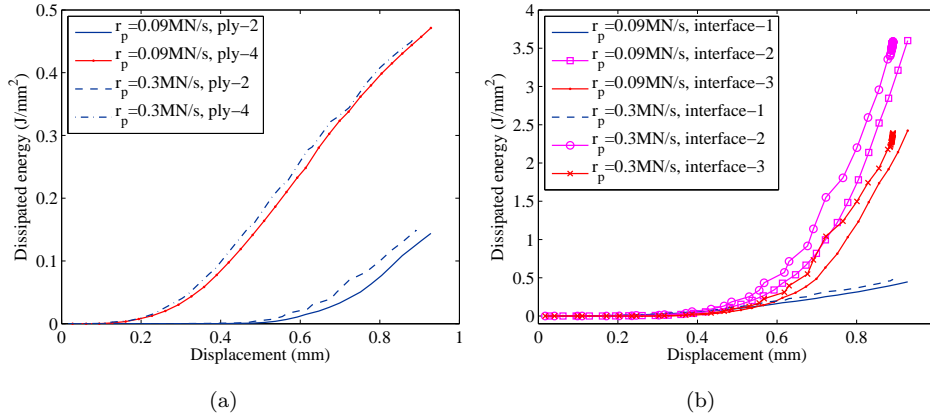


Figure 5.24 Energy dissipated during impact in a four-ply laminated plate; (a) energy dissipated during matrix cracking, (b) energy dissipated during delamination

increases with increasing loading rate. It can also be observed from the figures that the energy dissipated during delamination damage is approximately 10 times larger than the energy dissipated during matrix cracking. Moreover, most of the energy during delamination damage is dissipated at the inner interface (interface-2, (90/0)), at which delamination is growing in a pure shear fracture mode. This is not surprising, as observed during experiments [40, 91] and in section 5.4.2, cracks in fiber-reinforced composites propagate faster under shear and thus result in more damage and energy dissipation. The results here are clear evidence of this phenomenon; delamination at interface-2 propagates faster under shear than the mixed-mode delamination at interface-3. These observations are confirmed by figure 5.25, which shows the plot of the rate of energy dissipation during delamination damage at different interfaces.

It can be observed from figure 5.25, that the rate of energy dissipation during delamination damage at the interface-2, at a particular time is larger than the rate of energy dissipation at interface-3. Moreover, delamination damage at the inner interface, interface-2, starts earlier than at interface-3.

5.5 Conclusions

A time-dependent progressive failure model based on a solid-like shell element is presented to simulate fast crack growth in laminated composite plates. Special attention is focused on studying and understanding the effect of the loading rate on damage initiation, interaction between matrix cracking and delamination and evolution of damage in laminated composite plates. Moreover, numerical aspects of stability in implicit/explicit simulations of mesh-objective cracking are discussed.

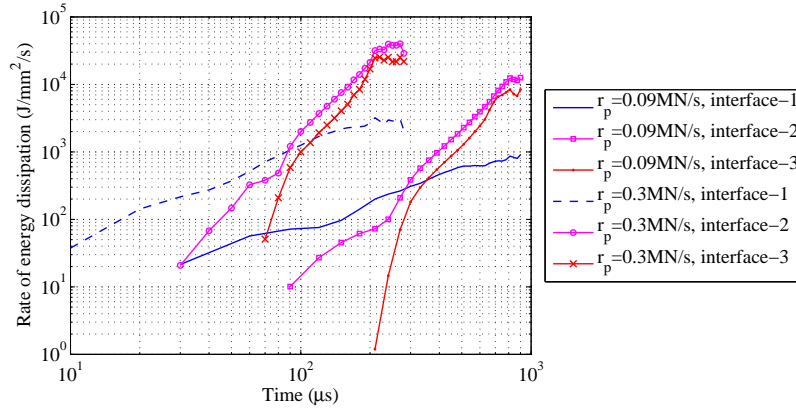


Figure 5.25 rate of energy dissipation at the interface of a four-ply laminated plate

Numerical results on mixed mode fracture in an isotropic plate show that incorporation of new degrees of freedom, during a simulation, does not influence the stability of the solution. The time continuity in velocity and stress/strain fields is ensured successfully. The proposed approach for cohesive cracks helps to stabilize the solution at the crack tip.

The validity of the model in simulating fast crack growth is assessed with numerical simulations of Mode-I and Mode-II crack propagation in a single-edge-notch unidirectional composite plate. Key features of dynamic crack growth in composite plates, under Mode-I and Mode-II, are captured and the numerical results were in good agreement with the experimental observations.

The performance of the presented model is further illustrated in an impact test on two- and four-cross-ply laminated plates. A full laminate analysis is performed including multiple cracking and extended delamination. The numerical model is able to simulate not only the key damage mechanisms and their interaction and evolution but is also able to simulate the sequence of damage mechanisms under impact. Promising results are obtained in which key characteristics of dynamic fracture in laminated composite plates such as fast crack growth, non-smooth damage growth, strong interaction between matrix cracking and delamination, differences in structural response and damage distribution with loading rate and rate effects on damage development are simulated successfully.

It is envisioned that the present numerical approach can be combined with numerical models for fiber failure and compressive failure to allow for complete damage analysis of composite laminated plates.

Chapter 6

Discontinuous thermo-mechanical computational model*

A finite element approach to model thermo-mechanical cracking in fiber reinforced composites is proposed. A phantom-node method is used to allow for the modeling of discontinuities in the displacement, temperature and heat flux fields. This allows for modeling of adiabatic as well as isothermal cracks, propagating arbitrarily through the finite element mesh. The simultaneous modeling of heat transfer through an interface and heat generation during fracture is achieved by coupling the equation of motion to the energy equation, accounting for the effects of cohesive interfaces, friction, inertia and heat conduction. A mixed-mode cohesive interface law coupled with a constitutive law for contact friction between crack flanks is used for an accurate representation of interface phenomena. Numerical results are presented to demonstrate salient features of the model. The model is validated against analytical and experimental results.

6.1 Introduction

In many engineering applications, fiber-reinforced composite structures are often subjected to extreme loading conditions such as impact, thermal shock, thermal cycles etc. In the event of impact loading, the energy which is in excess of the energy required for the creation of new crack surfaces, is dissipated as heat. This may result in a substantial increase in local temperature near the crack tip region [28, 96, 126]. This internal heat generation process can significantly influence the mechanical response of the material. Furthermore, localized increase of temperature in the crack-tip region may affect the energy release rate of the crack and consequently, the crack propagation speed [28]. Numerical analysis of such a coupled multi-physics problem including crack growth, requires the use of efficient and reliable computational tools.

In this paper, a coupled thermo-mechanical finite element model is presented for the analysis of crack growth in fiber-reinforced composite plates subjected to impact. The objective of this paper is twofold. Firstly, to present a coupled thermo-mechanical model for mesh-independent cohesive crack growth in fiber-reinforced

* This chapter is extracted from [9]

composites. Such a discontinuous approach has not been explored before for these materials. Secondly, to present an integrated numerical model based on the phantom node method for combined modeling of mesh-independent adiabatic as well as isothermal cracking. This allows simultaneous modeling of heat transfer through an interface and heat generation during fracture at the interface.

The presence of matrix and/or delamination cracks in fiber-reinforced composites results in a discontinuity in the displacement field. In case of thermo-mechanical problems, the presence of a crack also results in a discontinuity in the thermal field (temperature field in case of adiabatic cracks and heat flux field in case of isothermal cracks) and hinder the flow of heat. Such a problem can be efficiently addressed, if the kinematics, momentum and energy balance equations carefully take the discontinuity in the mechanical and thermal fields into account, [57].

Discontinuities in the displacement and/or temperature fields across the crack surfaces are most often modeled by means of interface elements, [62, 166]. However, these methods require the finite element mesh to be aligned with the crack geometry. Consequently, cracks can only grow along predefined boundaries and the locations of the cracks have to be known in advance. One of the preferred computational paradigms to model mesh-independent cracking within the framework of finite element method, is the Partition-of-Unity (PoU) approach [103, 106, 107, 159]. Even though, this method has been employed for modeling mesh-independent cracking in laminated composites subjected to mechanical loads, e.g. [5, 125, 152], it has not been explored for modeling coupled thermo-mechanical problems in fiber-reinforced laminated composites. This paper aims at filling this gap.

Another important feature of the presented finite element model is, that it provides a unified approach to model adiabatic and isothermal cracking in contrast to the work of [62], which deals with modeling of only adiabatic cracks. The model in [62] was only able to simulate heat transfer through an interface. [28] on the other hand, presented a thermally dissipative cohesive zone model to simulate only isothermal cracking, able to generate heat during dynamic fracture in amorphous polymers. In [49] a thermo-mechanical model based on the extended finite element method (XFEM) [107] was presented, for brittle fracture in isotropic materials. However, in [49] modeling of adiabatic and isothermal cracking required separate finite element treatment. In [51] a thermo-mechanical cohesive zone model for adiabatic/isothermal cracking was introduced. The numerical framework was based on a cohesive finite element model of citeWells2001. In order to simulate both isothermal and adiabatic cracking, an interface temperature relative to a fictitious crack surface was defined. In contrast to the work of [51], the notion of fictitious crack surface is not used in the present contribution. Instead all kinematics have been defined on real crack flanks (surfaces) and hence no assumptions have been made concerning the distribution of temperature and/or heat flux field within the cohesive zone. This gives a more

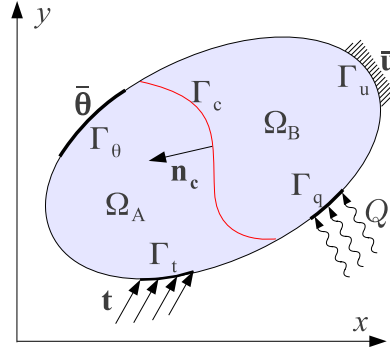


Figure 6.1 Body $\Omega = \Omega_A \cup \Omega_B$ crossed by a crack Γ_c

physical meaning to the kinematics at the crack surfaces. Furthermore, in contrast to [51], the numerical framework presented in this paper is based on the phantom node method [106], which provides an efficient finite element implementation compared to traditional XFEM [107, 159].

An outline of the paper is as follows. In the next section, the basic kinematic equations and variational formulation pertaining to discontinuous thermo-mechanical model are presented. Section 6.3 discusses the bulk and cohesive interface constitutive relations. Finite element discretization of the equilibrium equations is presented in section 6.4. In section 6.5, finite element simulation results are presented to illustrate salient features of the model. The model is validated against analytical and experimental results.

6.2 Thermo-mechanical discrete damage model

In this section, the basic kinematic and equilibrium equations concerning thermo-mechanical modeling of cracked fiber-reinforced polymer (FRP) composites are described.

6.2.1 Weak form of balance of linear momentum

Consider a body with domain Ω crossed by an internal boundary (crack), Γ_c , with unit normal \mathbf{n}_c , figure 6.1. External tractions, \mathbf{t} are applied at the boundary Γ_t whereas displacements are imposed at boundary Γ_u . Assuming small strains and displacements, and ignoring the integrands for brevity, the balance of linear momen-

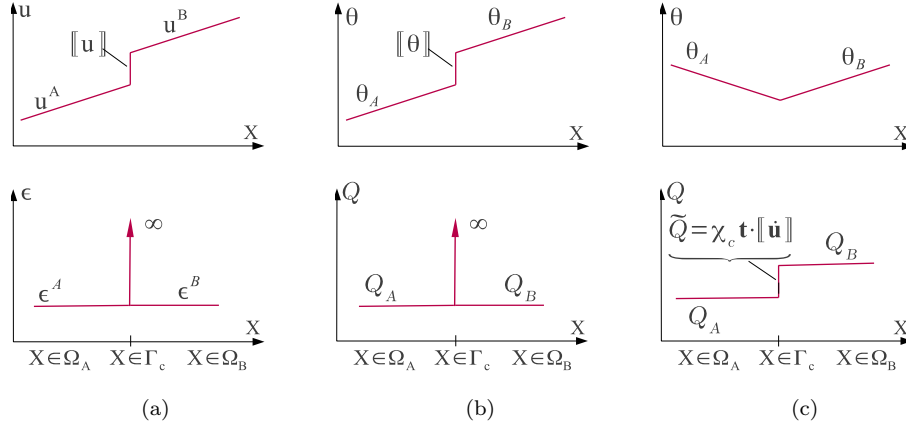


Figure 6.2 One dimensional representations of displacement, temperature, strain and heat flux fields; (a) Discontinuous displacement at the crack and continuous strain field across the crack surface, (b) Discontinuous temperature at the crack and continuous heat flux field across the crack surface (adiabatic crack), and (c) Discontinuous heat flux field at the crack surface (isothermal crack)

tum in the current configuration is given as

$$\int_{\Omega} (\nabla \cdot \boldsymbol{\sigma} + \mathbf{b} - \rho \ddot{\mathbf{u}}) = \mathbf{0} \quad (6.1)$$

in which $\boldsymbol{\sigma}$ is the Cauchy stress tensor, \mathbf{b} is the body force, ρ is the current material density, $\ddot{\mathbf{u}}$ is the acceleration and ∇ is the divergence with respect to the current configuration.

The presence of a crack in a body results in a discontinuity in the displacement field across the crack. Consequently, due to a jump in the displacement field, the proper strain field cannot be defined at the crack, figure 6.2a. Partition-of-unity based methods [107, 159] allow for efficient modeling of propagating discontinuities, such as cracks, through the finite element mesh. The crack geometry not necessarily needs to be aligned with the element boundaries in a finite element mesh. To simulate mesh independent matrix cracking/splitting in individual plies of the laminate, the phantom node method, [106] is exploited. The idea is to replace the cracked element, with domain Ω^{elem} , with a pair of partially active overlapping elements with domains Ω_A^{elem} and Ω_B^{elem} , respectively, such that $\Omega^{elem} = \Omega_A^{elem} \cup \Omega_B^{elem}$. The superscript *elem* represents a particular element in a finite element mesh crossed by a discontinuity. The singularity in the stress field is removed due to the presence of cohesive tractions at the interface. Fracture is modeled as a gradual process with cohesive tractions at the crack surfaces.

The displacement field \mathbf{u} of a cracked element is given as

$$\mathbf{u}(\mathbf{x}) = \begin{cases} \mathbf{u}_A(\mathbf{x}) & \forall \mathbf{x} \in \Omega_A \\ \mathbf{u}_B(\mathbf{x}) & \forall \mathbf{x} \in \Omega_B \end{cases} \quad (6.2)$$

The displacement jump $\llbracket \mathbf{u} \rrbracket$ over the crack is defined as the difference of the displacement fields of the two elements

$$\llbracket \mathbf{u} \rrbracket(\mathbf{x}) = \mathbf{u}_A(\mathbf{x}) - \mathbf{u}_B(\mathbf{x}) \quad \forall \mathbf{x} \in \Gamma_c \quad (6.3)$$

At the crack, the continuity condition $\mathbf{t}_{c_A} = -\mathbf{t}_{c_B} = -\mathbf{t}_c$ has to be satisfied. Moreover, under the assumption of small deformations at the interface, the unit normal at the interface can be uniquely defined as $\mathbf{n}_{c_A} = -\mathbf{n}_{c_B} = -\mathbf{n}_c$.

By applying a standard Galerkin procedure to equation (6.1) and using the definition of displacement field, equation (6.2), the following weak form of the balance of linear momentum is obtained

$$\begin{aligned} \int_{\Omega_A} \rho \delta \mathbf{u}_A \cdot \ddot{\mathbf{u}}_A + \int_{\Omega_A} \delta \boldsymbol{\epsilon}_A : \boldsymbol{\sigma}_A + \int_{\Gamma_{c_A}} \delta \mathbf{u}_A \cdot \mathbf{t}_c - \int_{\Gamma_{t_A}} \delta \mathbf{u}_A \cdot \mathbf{t} \\ - \int_{\Omega_A} \delta \mathbf{u}_A \cdot \mathbf{b} = \mathbf{0} \end{aligned} \quad (6.4a)$$

$$\begin{aligned} \int_{\Omega_B} \rho \delta \mathbf{u}_B \cdot \ddot{\mathbf{u}}_B + \int_{\Omega_B} \delta \boldsymbol{\epsilon}_B : \boldsymbol{\sigma}_B + \int_{\Gamma_{c_B}} -\delta \mathbf{u}_B \cdot \mathbf{t}_c - \int_{\Gamma_{t_B}} \delta \mathbf{u}_B \cdot \mathbf{t} \\ - \int_{\Omega_B} \delta \mathbf{u}_B \cdot \mathbf{b} = \mathbf{0} \end{aligned} \quad (6.4b)$$

6.2.2 Weak form of balance of energy

The energy balance for a material exhibiting plasticity is given as [28, 146, 169]

$$\int_{\Omega} \rho C_p \dot{\theta} - \int_{\Omega} \chi_b \boldsymbol{\sigma} \cdot \dot{\boldsymbol{\epsilon}}_p - \int_{\Omega} \rho s + \int_{\Omega} \nabla \mathbf{q} = \mathbf{0} \quad (6.5)$$

in which θ is the temperature field. A superimposed dot denotes differentiation with respect to time. C_p is the specific heat, χ_b is the fraction of plastic work converted to heat, $\dot{\boldsymbol{\epsilon}}_p$ is the plastic strain rate due to fiber failure/shear nonlinear behavior, ρ is the current density, s is the heat power per unit mass and \mathbf{q} is the heat flux vector. The integrands are ignored for brevity. In the above equation, it is considered that the thermo-elastic contribution on the internal work is small and a major part of the plastic work, due to fiber failure and/or other failure mechanisms such as shear nonlinearity, is converted into heat.

The temperature field in a cracked element is defined similar to the displacement discontinuity [106], as

$$\theta(\mathbf{x}) = \begin{cases} \theta_A(\mathbf{x}) & \forall \mathbf{x} \in \Omega_A \\ \theta_B(\mathbf{x}) & \forall \mathbf{x} \in \Omega_B \end{cases} \quad (6.6)$$

Note that, independent definitions of the temperature field on both sides of the crack allows to model a discontinuity in the temperature field across the crack surface. The temperature jump $[[\theta]]$ over the crack is defined as the difference of the temperature fields of the two elements

$$[[\theta]](\mathbf{x}) = \theta_A(\mathbf{x}) - \theta_B(\mathbf{x}) \quad \forall \mathbf{x} \in \Gamma_c \quad (6.7)$$

After applying a weighted test function $\delta\theta$ to equation (6.5), the weak form of energy equation takes the form

$$\int_{\Omega} \delta\theta \rho C_p \dot{\theta} - \int_{\Omega} \delta\theta (\chi_b \boldsymbol{\sigma} \cdot \dot{\boldsymbol{\epsilon}}_p) - \int_{\Omega} \rho \delta\theta s + \int_{\Omega} \delta\theta \nabla \mathbf{q} = \mathbf{0} \quad (6.8)$$

In particular, the divergence term in equation (6.8) can be expanded by means of integration by parts and applying the divergence theorem as

$$\begin{aligned} \int_{\Omega} \delta\theta \nabla \mathbf{q} &= - \int_{\Omega} \nabla \delta\theta \cdot \mathbf{q} + \int_{\Gamma_q} \delta\theta (\mathbf{n} \cdot \mathbf{q}) + \int_{\Gamma_{c_A}} \delta\theta_A (\mathbf{n}_{c_A} \cdot \mathbf{q}_A) \\ &\quad + \int_{\Gamma_{c_B}} \delta\theta_B (\mathbf{n}_{c_B} \cdot \mathbf{q}_B) \end{aligned} \quad (6.9a)$$

$$= - \int_{\Omega} \nabla \delta\theta \cdot \mathbf{q} + \int_{\Gamma_q} \delta\theta Q + \int_{\Gamma_{c_A}} \delta\theta_A Q_A + \int_{\Gamma_{c_B}} \delta\theta_B Q_B \quad (6.9b)$$

in which Γ_{c_A} and Γ_{c_B} are the crack surfaces corresponding to domains Ω_A and Ω_B , respectively. Q is the external heat flux applied at boundary Γ_q , Q_A and Q_B are the heat fluxes in to the crack surface Γ_{c_A} and Γ_{c_B} , respectively. Substituting equations (6.9) and (6.6) in equation (6.8) and then exploiting the additive property of integrals, equation (6.8) can be written as two independent energy balance equations for the domains Ω_A and Ω_B as

$$\begin{aligned} \int_{\Omega_A} \delta\theta_A \rho C_p \dot{\theta}_A - \int_{\Omega_A} \delta\theta_A (\chi_b \boldsymbol{\sigma}_A \cdot \dot{\boldsymbol{\epsilon}}_{p/A}) - \int_{\Omega_A} \nabla \delta\theta_A : \mathbf{q} + \int_{\Gamma_{c_A}} \delta\theta_A Q_A \\ - \int_{\Omega_A} \delta\theta_A \rho s + \int_{\Gamma_{q_A}} \delta\theta_A Q = \mathbf{0} \end{aligned} \quad (6.10a)$$

$$\begin{aligned} \int_{\Omega_B} \delta\theta_B \rho C_p \dot{\theta}_B - \int_{\Omega_B} \delta\theta_B (\chi_b \boldsymbol{\sigma}_B \cdot \dot{\boldsymbol{\epsilon}}_{p/B}) - \int_{\Omega_B} \nabla \delta\theta_B : \mathbf{q} + \int_{\Gamma_{c_B}} \delta\theta_B Q_B \\ - \int_{\Omega_B} \delta\theta_B \rho s + \int_{\Gamma_{q_B}} \delta\theta_B Q = \mathbf{0} \end{aligned} \quad (6.10b)$$

The definitions of interface heat fluxes Q_A and Q_B , appearing in equation 6.10a and 6.10b, are given in the subsequent sections for adiabatic, isothermal and combined modeling of adiabatic-isothermal cracking.

Adiabatic crack

The case of an adiabatic crack in a material results in a discontinuous temperature and a continuous heat flux field across the crack surface, figure 6.2b. The continuity of heat flux at the crack surface is enforced by, [63]

$$Q_A(\mathbf{x}) = -Q_B(\mathbf{x}) = Q_c(\mathbf{x}) \quad \forall(\mathbf{x}) \in \Gamma_c \quad (6.11)$$

in which Q_c is the heat flux transferred through the interface and is defined as

$$Q_c(\mathbf{x}) = k_c \llbracket \theta \rrbracket(\mathbf{x}) \quad \forall(\mathbf{x}) \in \Gamma_c \quad (6.12)$$

in which k_c is the interface conductance coefficient. The explicit expression for k_c depends upon the effect of crack bridging, damage at the interface, displacement jump, crack surface roughness etc. For more details, see for example [63]. Note that, the presented formulation for adiabatic cracking is similar to [63], however, the present formulation allows mesh-independent modeling of adiabatic cracking through a finite element mesh.

Isothermal crack

The case of isothermal cracking (isothermal across the crack) in a material results in a discontinuity in the heat flux field and not in the temperature field, figure 6.2c. As a result, the heat flux field on both sides of the discontinuity is not necessarily the same, i.e. $Q_A \neq -Q_B$.

In order to take the heat generated due to the dissipative processes during fracture into account, the *thermo-fracture heating* term $\int_{\Omega} \tilde{Q}$, can be added to the energy balance equation (6.5), following the work of [28]. The *thermo-fracture heating* \tilde{Q} is related to the rate of work done by the cohesive tractions, \mathcal{W} , as

$$\int_{\Omega} \tilde{Q} = \chi_c \int_{\Omega} \frac{\dot{\mathcal{W}}}{h_c} \quad (6.13)$$

in which χ_c is the fraction of cohesive work converted into heat. \mathcal{W} is the rate of cohesive work given as

$$\dot{\mathcal{W}} = \mathbf{t} \cdot \llbracket \dot{\mathbf{u}} \rrbracket \quad (6.14)$$

and h_c is the thickness of the cohesive interface. The parameter h_c appeared in equation (6.13), due to the fact that \mathcal{W} defines the rate of cohesive work per unit area. In the limit of a zero thickness interface, such that $h_c \rightarrow 0$, the volume integral on the right hand side of equation (6.13) is converted into an area integral over the cohesive surface (see appendix D).

Consequently, equation (6.13) takes the form

$$\int_{\Omega} \tilde{Q} = \chi_c \int_{\Gamma_c} \dot{\mathcal{W}} \quad (6.15)$$

Substituting equation (6.14) in equation (6.15), yields

$$\int_{\Omega} \tilde{Q} = \chi_c \int_{\Gamma_c} \mathbf{t} \cdot \llbracket \dot{\mathbf{u}} \rrbracket \quad (6.16a)$$

$$= \chi_c \left(\int_{\Gamma_c^A} \mathbf{t} \cdot \dot{\mathbf{u}}_A - \int_{\Gamma_c^B} \mathbf{t} \cdot \dot{\mathbf{u}}_B \right) \quad (6.16b)$$

$$= \chi_c \left(\int_{\Gamma_c^A} \tilde{Q}_A + \int_{\Gamma_c^B} \tilde{Q}_B \right) \quad (6.16c)$$

Consequently, heat fluxes Q_A and Q_B in equations 6.10a and 6.10b, can be defined for isothermal cracking as

$$Q_A(\mathbf{x}) = -\tilde{Q}_A(\mathbf{x}) \quad (6.17a)$$

$$Q_B(\mathbf{x}) = -\tilde{Q}_B(\mathbf{x}) \quad (6.17b)$$

Note that the above equation also allows for an unsymmetric distribution of heat fluxes to the crack interface.

Adiabatic-isothermal crack

In order to simulate both adiabatic as well as isothermal cracking phenomena in a material, the heat flux on both sides of the discontinuity is defined as

$$Q_A(\mathbf{x}) = Q_c(\mathbf{x}) - \tilde{Q}_A(\mathbf{x}) \quad \forall \mathbf{x} \in \Gamma_{cA} \quad (6.18a)$$

$$Q_B(\mathbf{x}) = -Q_c(\mathbf{x}) - \tilde{Q}_B(\mathbf{x}) \quad \forall \mathbf{x} \in \Gamma_{cB} \quad (6.18b)$$

This allows for the simultaneous modeling of heat transfer through the interface and heat generation during fracture at the interface.

6.3 Constitutive relations

6.3.1 Bulk constitutive laws

The bulk material response is considered to be orthotropic, linear elastic. The stress-strain relation is given as

$$\boldsymbol{\sigma} = \mathbb{C} : (\boldsymbol{\epsilon} - \boldsymbol{\epsilon}_\theta) \quad (6.19)$$

in which \mathbb{C} is the fourth-order material tangent stiffness tensor according to

$$[\mathbf{C}]^{-1} = \begin{bmatrix} \frac{1}{E_1} & \frac{-\nu_{21}}{E_2} & \frac{-\nu_{31}}{E_3} & 0 & 0 & 0 \\ \frac{-\nu_{12}}{E_1} & \frac{1}{E_2} & \frac{-\nu_{32}}{E_3} & 0 & 0 & 0 \\ \frac{\nu_{13}}{E_1} & \frac{-\nu_{23}}{E_2} & \frac{1}{E_3} & 0 & 0 & 0 \\ 0 & 0 & 0 & \frac{1}{G_{12}} & 0 & 0 \\ 0 & 0 & 0 & 0 & \frac{1}{G_{23}} & 0 \\ 0 & 0 & 0 & 0 & 0 & \frac{1}{G_{13}} \end{bmatrix} \quad (6.20)$$

in which \mathbf{C} is the matrix form of tensor \mathbb{C} , obtained using Voigt notation. The subscripts 1,2 and 3 denote the orthogonal axes of the principal material coordinate system. ϵ_θ is the thermal strain tensor and is considered to be purely volumetric. The thermal strain tensor in Voigt notation is given as

$$\{\epsilon_\theta\} = \{\alpha_1\theta, \alpha_2\theta, \alpha_3\theta, 0, 0, 0\}^T \quad (6.21)$$

in which α_1, α_2 and α_3 are linear coefficients of thermal expansion in material principle directions. In principle, any constitutive law can be used, but in the present contribution a rate-independent, linear elastic behavior is assumed.

The constitutive assumption for heat conduction is given by Fourier's law as

$$\mathbf{q} = -\mathbf{k}\nabla\theta \quad (6.22)$$

in which matrix \mathbf{k} is the conductivity matrix given as

$$[\mathbf{k}] = \text{diag}[k_1, k_2, k_3] \quad (6.23)$$

and k_1, k_2 and k_3 are the thermal conductivities in material principle directions.

6.3.2 Cohesive constitutive law

A mixed-mode, bi-linear cohesive constitutive law, [148], is used to model cohesive cracking. Mode-mixity is taken into account through a phenomenological mode-mixity criterion proposed by [26]. In order to take the friction between the crack flanks into account, a coulomb friction model is also included in the cohesive zone, following the work of [12]. The method is based on the hypothesis that, at mesomechanical level, a representative elementary area, dA , of the interface can be partitioned into an undamaged ($dA_{el} = (1 - \omega)dA$) and damaged part ($dA_d = \omega dA$). ω is a damage variable varying from 0, undamaged to 1, fully damaged state. The mathematical form of damage variable can be found in [148]. The damage variable depends on three material parameters, i.e. mode-I fracture toughness G_{Ic} , mode-II fracture toughness (G_{IIc}) and a mode-interaction parameter η [26]. The material parameter η takes into account the dependence of fracture toughness on mode ratio, which can be obtained by a curve fitting (fracture toughness G_c Vs mode ratio

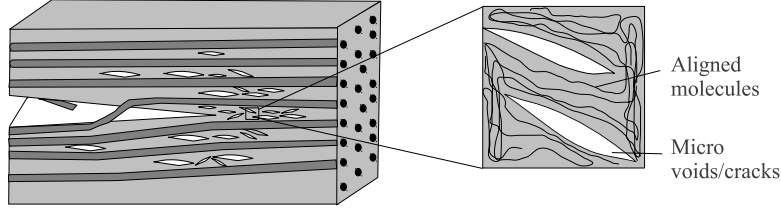


Figure 6.3 Molecular chain alignment and creation of small voids between fibrils ahead of crack tip

plot) of a set of experimental data. Cohesive tractions at the interface are defined according to [12], as

$$\mathbf{t} = \underbrace{(1 - \omega)\mathbf{t}_o}_{\mathbf{t}_{el}} + \underbrace{\omega\mathbf{t}_f}_{\mathbf{t}_d} \quad (6.24)$$

where \mathbf{t}_o is the mixed-mode material strength defined in [148] and \mathbf{t}_f is the traction due to cohesive friction, defined in [12]. For more details on the cohesive interface law formulation, see [12, 148].

Note that, cohesive tractions, $(1 - \omega)\mathbf{t}_o$, taking into account the effect of fiber-bridging, craze formation and breakdown are related to the undamaged part of the interface whereas the cohesive tractions, $\omega\mathbf{t}_f$, due to frictional sliding between surfaces of micro-voids/cracks or fully developed crack flanks are related to the damaged part of the interface.

Remark 1. The *thermofracture heating* term, $\tilde{Q}(\mathbf{t}, \llbracket \dot{\mathbf{u}} \rrbracket)$, encompasses heat generated during craze formation and breakdown, molecular chain alignment and frictional sliding between damaged interfaces, figure 6.3. As \tilde{Q} is a function of cohesive tractions and following the discussion of section 6.3.2, a more detailed physical meaning can be given by partitioning it into \tilde{Q}_{el} and \tilde{Q}_d , such that

$$\tilde{Q} = \tilde{Q}_{el} + \tilde{Q}_d \quad (6.25)$$

in which \tilde{Q}_{el} is the heat generated due to craze formation and breakdown, which includes molecular chain alignment ahead of the crack tip as the craze fibrils form, stretch and eventually fail, [85]. \tilde{Q}_d is the heat generated in the fully damaged part of the interface during frictional sliding between micro-voids/cracks and fully developed cracks.

Remark 2. In equation (6.16a), a single parameter χ_c is used to describe the fraction of total cohesive work converted into heat. However, based on the

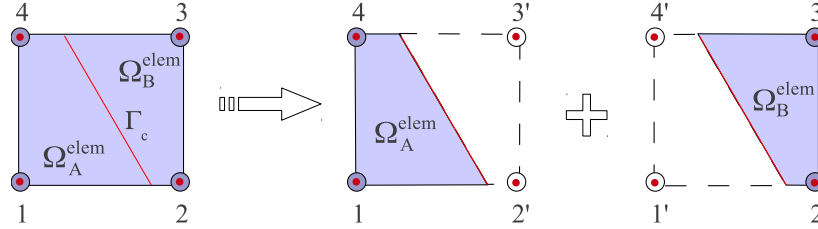


Figure 6.4 Connectivity of a cracked thermo-mechanical finite element in the phantom node method

arguments of section 6.3.2 and remark 1, a more general description of the fraction of mechanical work converted into heat can be used, as

$$\int_{\Omega} \tilde{Q} = \chi_{c_1} \int_{\Gamma_c} \underbrace{\mathbf{t}_{el} \cdot [[\dot{\mathbf{u}}]]}_{\tilde{Q}_{el}} + \chi_{c_2} \int_{\Gamma_c} \underbrace{\mathbf{t}_d \cdot [[\dot{\mathbf{u}}]]}_{\tilde{Q}_d} \quad (6.26)$$

in which χ_{c_1} is the fraction of cohesive work converted into heat due to craze formation and breakdown and χ_{c_2} is the fraction of the cohesive work converted into heat due to frictional sliding at the crack flanks.

6.4 Finite element formulation

In this section a coupled thermo-mechanical finite element formulation is briefly presented. The domain Ω is discretized into ne isoparametric elements such that $\Omega = \bigcup_{elem=1}^{ne} \Omega^{elem}$, in which \bigcup symbolizes the assembly operator. Each node i of the finite element is associated with displacement degrees of freedom (\mathbf{u}) and a temperature degree of freedom (θ).

In order to model the adiabatic/isothermal crack using the phantom node method, the cracked element is replaced with two partially active overlapping elements, namely A and B, with the addition of phantom nodes i' , figure 6.4. Accordingly, phantom degrees of freedom are added corresponding to displacement as well as thermal degrees of freedom. Note that, if phantom degrees of freedom are added corresponding to only displacement degrees of freedom, it will result in a discontinuity in the displacement field and the thermal field will remain unaltered, i.e thermal field remains continuous across the crack similar to uncracked elements. The displacement field \mathbf{u} , the temperature field θ , their time derivatives and admissible

variations are approximated by isoparametric shape functions as

$$\mathbf{u}_e(\mathbf{x}) = \mathbf{N}(\mathbf{x})\hat{\mathbf{u}}_e, \quad \dot{\mathbf{u}}_e(\mathbf{x}) = \mathbf{N}(\mathbf{x})\dot{\hat{\mathbf{u}}}_e \quad (6.27a)$$

$$\delta\mathbf{u}_e(\mathbf{x}) = \mathbf{N}(\mathbf{x})\delta\hat{\mathbf{u}}_e, \quad \delta\dot{\mathbf{u}}_e(\mathbf{x}) = \mathbf{N}(\mathbf{x})\delta\dot{\hat{\mathbf{u}}}_e \quad (6.27b)$$

$$\theta_e(\mathbf{x}) = \mathbf{N}^\theta(\mathbf{x})\hat{\theta}_e, \quad \dot{\theta}_e(\mathbf{x}) = \mathbf{N}^\theta(\mathbf{x})\dot{\hat{\theta}}_e \quad (6.27c)$$

$$\delta\theta_e(\mathbf{x}) = \mathbf{N}^\theta(\mathbf{x})\delta\hat{\theta}_e, \quad \delta\dot{\theta}_e(\mathbf{x}) = \mathbf{N}^\theta(\mathbf{x})\delta\dot{\hat{\theta}}_e \quad e = A, B \quad (6.27d)$$

in which \mathbf{N} and \mathbf{N}^θ are standard finite element matrices containing shape functions of polynomial order p , $\hat{\mathbf{u}}$ is a vector of nodal displacement degrees of freedom and $\hat{\theta}$ is a vector of nodal thermal degrees of freedom. Incorporating the discrete admissible variations, equation (6.27), into equations (6.4) and (6.10), the following discretized weak forms of balance of linear momentum and energy for an element $elem$ cut by a crack are obtained

$$\int_{\Omega_e^{elem}} \rho \mathbf{N}^T \mathbf{N} \dot{\hat{\mathbf{u}}}_e + \int_{\Omega_e^{elem}} \mathbf{B}^T \boldsymbol{\sigma}_e + \int_{\Gamma_{ce}} \beta_e \mathbf{N}^T \mathbf{t}_c - \int_{\Gamma_{te}} \mathbf{N}^T \mathbf{t} - \int_{\Omega_e^{elem}} \mathbf{N}^T \mathbf{b} = \mathbf{0} \quad (6.28a)$$

$$\int_{\Omega_e^{elem}} \rho C_p \mathbf{N}^{\theta T} \mathbf{N}^\theta \dot{\hat{\theta}}_e - \int_{\Omega_e^{elem}} \mathbf{N}^{\theta T} (\chi_b \boldsymbol{\sigma}_e \cdot \dot{\boldsymbol{\epsilon}}_{p/e}) - \int_{\Omega_e^{elem}} \mathbf{B}^{\theta T} \mathbf{q} + \int_{\Gamma_{ce}} \mathbf{N}^{\theta T} Q_e - \int_{\Omega_e^{elem}} \mathbf{N}^{\theta T} \rho s + \int_{\Gamma_{qe}} \mathbf{N}^{\theta T} Q = 0 \quad (6.28b)$$

in which \mathbf{B} and \mathbf{B}^θ are the standard finite element displacement- and temperature-gradient interpolation matrices, respectively. β_e is defined as

$$\beta_e = \begin{cases} 1 & \text{for } e = A \\ -1 & \text{for } e = B \end{cases} \quad (6.29)$$

6.5 Numerical examples

In this section different numerical examples are presented to demonstrate the validity and salient features of the discontinuous thermo-mechanical model. First a simple uni-directional (UD) square plate is tested under thermal loading to demonstrate the performance of the model in simulating discontinuities in temperature and heat flux fields. Next, a cracked isotropic plate is analyzed to show the accuracy of the proposed model under thermo-mechanical conditions. The third example demonstrates the performance of the model in simulating heat generation under impact loading conditions.

To simulate mesh-independent cracking, a failure criterion is required to initiate and propagate the cracks. In order to ensure continuity of the response under mixed-mode loading conditions, the crack initiation criterion should match the damage

evolution. The failure criterion is defined according to [148], as

$$\frac{\langle \sigma_n \rangle^2 + \sigma_s^2}{f_n^2 + (f_s^2 - f_n^2) \Pi \eta} = 1 \quad (6.30)$$

with

$$\Pi = \frac{\sigma_s^2}{\sigma_s^2 + \langle \sigma_n \rangle^2} \quad (6.31)$$

in which f_n and f_s are the tensile and shearing interfacial strengths, respectively. σ_n and σ_s are the normal and shear components of bulk stress at the crack surface and η is a mode interaction parameter [26]. The operator $\langle x \rangle = (x + |x|)/2$ is used to nullify the influence of damage in normal direction in compression.

To initiate new crack segments in a virgin material, the failure criterion is evaluated at all integration points in the critical elements. If the failure criterion is violated in one of the integration points, a new crack segment is introduced in the center of the element in the direction of the fiber. In order to propagate an initially existing crack, the failure criterion is evaluated in the prospective crack element ahead of the existing cohesive crack tip. After the failure criterion is violated, the existing crack is extended in fiber direction.

In this contribution, two-dimensional four node bi-linear and three-dimensional eight node tri-linear elements are used. In order to avoid spurious stresses [119], the order of polynomial approximation for thermal strains should be lower than that of the mechanical strains. Therefore, for a linear element thermal strains are computed from a constant thermal field at the element centroid.

The equilibrium equations are solved in a fully coupled manner. The Newton-Raphson method is used to solve the non-linear coupled equations, equation (6.28). The equations are solved iteratively until residual force norm is less than a tolerance value. The convergence tolerance is taken to be 1.0E-4. Integration in the time domain is performed using the Newmark average acceleration method.

6.5.1 Adiabatic/isothermal cracking in UD plate

In order to show the performance of the discontinuous thermo-mechanical model in simulating mesh-objective adiabatic/isothermal cracking, thermal analysis on an edge-cracked square unidirectional (UD) plate is performed. Several cases are considered with various crack geometries, fiber-orientations and thermal boundary conditions. The plate is modeled with orthotropic material properties with $E_1 = 25\text{E}4\text{MPa}$, $E_2 = E_3 = 1\text{E}4\text{MPa}$, $G_{12} = 12.5\text{E}4\text{MPa}$, $\nu_{12} = 0.25$, $\nu_{23} = 0.25$, $k_1 = 1.65\text{E}-4\text{W}/(\text{mC})$, $k_2 = k_3 = 2.46\text{E}-6\text{W}/(\text{mC})$, $\alpha_1 = -0.3\text{E}-6\text{C}^{-1}$, $\alpha_2 = \alpha_3 = 30\text{E}-6\text{C}^{-1}$. The plate is discretized with a uniform finite element mesh of $51 \times 51 \times 1$ eight-node solid elements. The thickness of the plate is 10mm. In-plane geometry

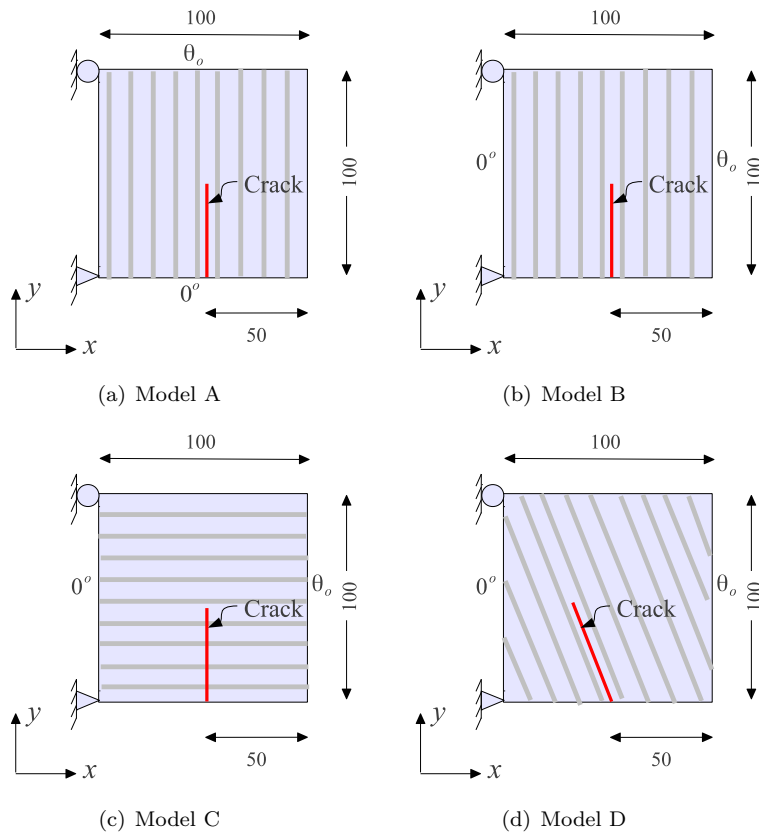


Figure 6.5 Geometry and boundary conditions of a cracked unidirectional composite plate— adiabatic crack, thermal analysis (All dimensions in mm); (a) Model A, (b) Model B, (c) Model C and (d) Model D

and boundary conditions are described separately for each example below. Initial temperature of the plate is assumed to be 0°C .

Adiabatic crack in a UD plate – Model A

A unidirectional edge-cracked plate is analyzed to see the performance of the thermo-mechanical model. The aim here is to examine the accuracy of the model in predicting a thermal profile in the presence of a crack, crossing the finite elements arbitrarily. Model geometry and boundary conditions are shown in figure 6.5a. The fiber orientation is in the direction of the y -axis. The plate is subjected to a uniform temperature $\theta_o = -22^{\circ}\text{C}$ on the top surface, while the temperature at the bottom surface is prescribed as 0°C . The crack is modeled as a traction free crack with

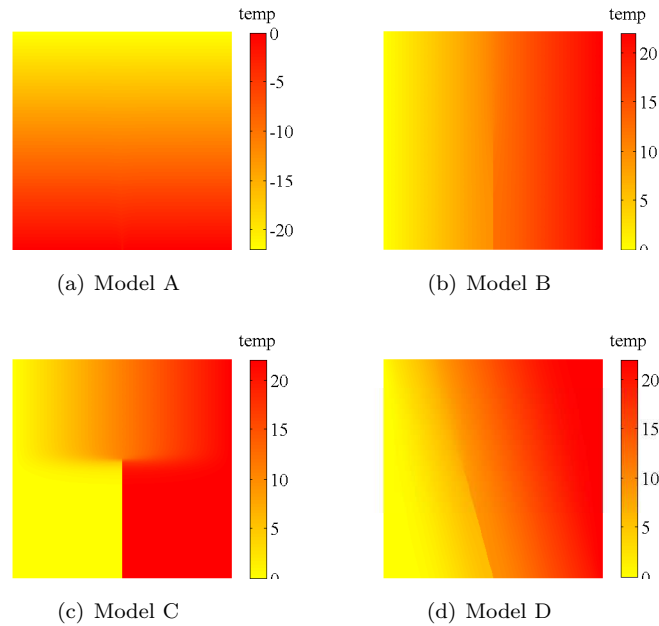


Figure 6.6 Temperature distribution ($^{\circ}\text{C}$) in a laminae– adiabatic crack, thermal analysis; (a) Model A, (b) Model B, (c) Model C and (d) Model D

insulating surfaces.

Since the crack has no influence on the response for this particular case, the exact solution for the temperature distribution is given by $\theta = \frac{y}{100}\theta_o$. The numerical result in the form of the temperature distribution over the plate surface is presented in figure 6.6a. Figure 6.7a compares the temperature profile along the length of the crack at the two crack faces. It can be observed from the figures 6.6a and 6.7a that the temperature field is indeed unaffected by the crack and the thermal field is predicted accurately.

Adiabatic crack in a UD plate – Model B

The purpose of this example is to show the behavior of the model in simulating a discontinuity in the temperature field. Model geometry and boundary conditions are shown in figure 6.5b. An initial traction free crack is present in the direction of fiber orientation.

To simulate adiabatic cracking the plate is subjected to a uniform temperature $\theta_o = 22^{\circ}\text{C}$ on the right edge and the temperature at the left edge is 0°C , figure 6.6b. Note that the fiber direction is parallel to the edge at which thermal boundary

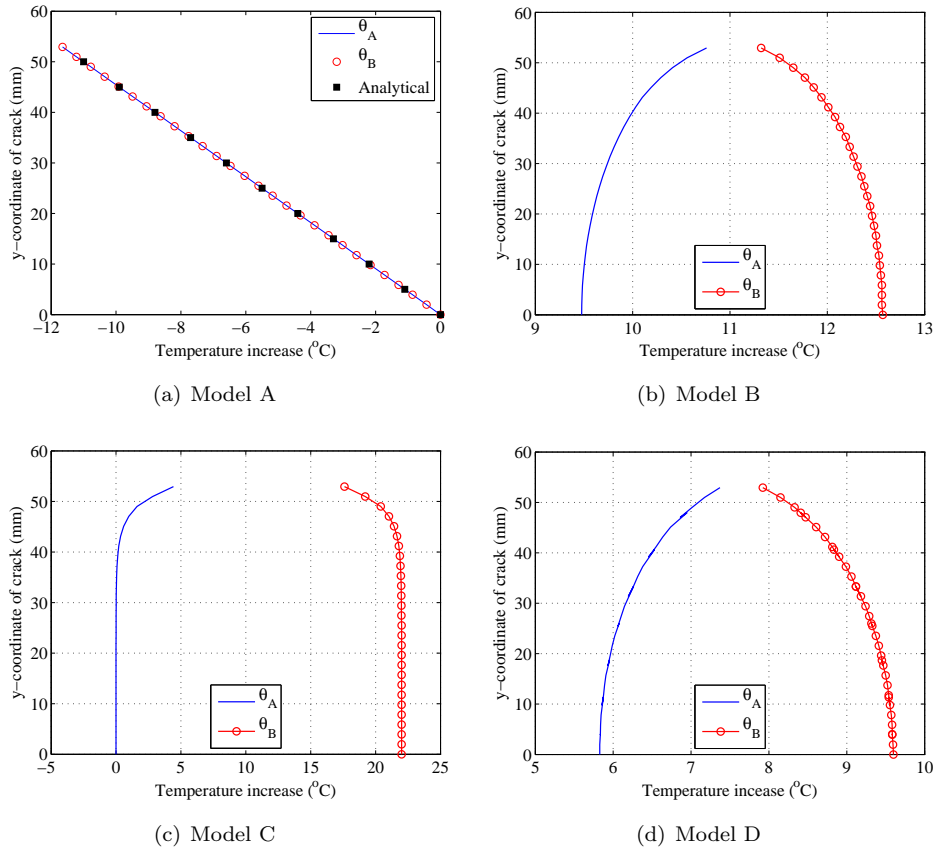


Figure 6.7 Temperature distribution on two faces of the crack– adiabatic crack, thermal analysis; (a) Model A, (b) Model B, (c) Model C and (d) Model D

conditions are applied. Figure 6.6b shows the thermal field over the plate. Figure 6.7b shows the temperature profile along the two faces of the crack. It can be observed from the results that a discontinuity in the thermal field is present across the crack surface and the two faces of the crack have different temperatures. This shows that the discontinuity in the temperature field is properly modeled. However, the difference in temperature field on both sides of the crack is not significant, even though, the crack faces are insulated and no heat transfer takes place through the crack. This is due to a high thermal conductivity of the material in fiber direction. As a result the heat quickly conducts through the uncracked area above the crack tip, to the other side of the crack.

Adiabatic crack in a UD plate – Model C

Model C is similar to Model B, however, the fiber direction is now parallel to the x -axis, figure 6.5c. Figure 6.6c shows the distribution of thermal field over the plate and figure 6.7c shows the temperature distribution on the two faces of the crack along the crack line. It can be observed from figure 6.7c that the discontinuity in the temperature field is properly modeled and the temperature on the left side of the crack is nearly zero.

Models B and C clearly show the effect of anisotropic thermal conductance in a cracked body. It can be concluded that since matrix cracks run parallel to the fiber direction, the discontinuity in the thermal field will not be significant and heat transfer to the other side of the crack will take place through the uncracked portion of the body. It is also noted, that in Model C, a crack/notch was introduced which was not parallel to the fiber direction. This example was specifically designed to show the effects of anisotropic thermal conductance on a thermal field in a cracked body. In the remainder of the article, cracks are only allowed to initiate and propagate parallel to the fiber direction.

Adiabatic crack in a UD plate – Model D

To show the capability of the model for inclined cracks, a unidirectional plate with an inclined crack is considered. The geometry and boundary conditions are shown in figure 6.5d. The fiber direction is at an angle of 105° with the x -axis. Finite element mesh and crack geometry are not aligned in this example, which is properly accounted for in the phantom node method. The crack is modeled as a traction free crack with thermal insulation. Figure 6.6d shows the thermal field over the cracked plate. Figure 6.7d shows the temperature distribution on the two faces of the crack. It can be observed from the analysis results that the discontinuity is properly modeled even for the case of an inclined crack arbitrarily aligned with the finite element mesh. However, as was observed in the case of Model B, the difference of the thermal field on both sides of the crack is not significant due to thermal conductance from the uncracked domain of the plate to the other side of the crack. Again, this effect is due to a high thermal conductivity in fiber direction.

Isothermal crack in a UD plate

A square unidirectional edge cracked plate is considered to simulate isothermal cracking. The model geometry and boundary conditions are shown in figure 6.8a. The fiber orientation is parallel to the y -axis. To simulate isothermal cracking, a rate of interface dissipation ($\mathbf{t} \cdot \llbracket \dot{\mathbf{u}} \rrbracket$) is given as input in this example. However, it is noted that in real simulations this is not the true input but will be computed from the

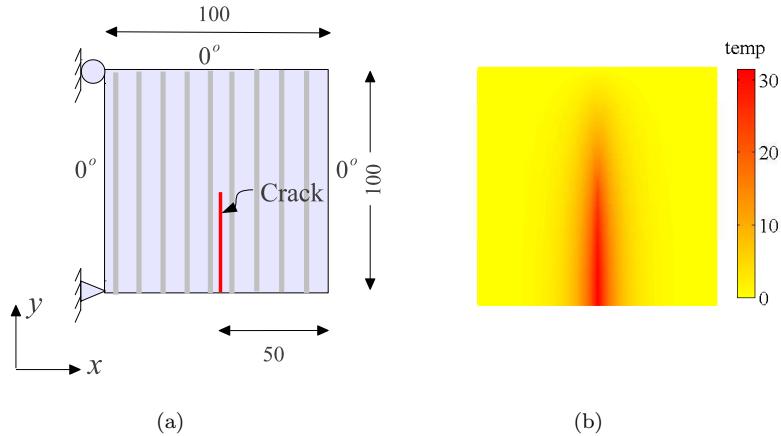


Figure 6.8 Isothermal cracking in a unidirectional laminae; (a) geometry and boundary conditions of the cracked plate (All dimensions in mm) and (b) temperature distribution ($^{\circ}\text{C}$) in a laminae

mechanical part of the equilibrium equations. In this example a constant rate of dissipation ($2.0\text{E-}5\text{Nmm}^{-1}\text{s}^{-1}$) is prescribed along the crack surface. The parameter χ_c is assumed to be unity in this example. The crack is modeled as a traction free crack without thermal insulation.

Figure 6.8b shows the analysis result by means of the temperature distribution. The temperature distribution on the two faces of the crack is shown in figure 6.9. It is evident from figures 6.8b and 6.9, that the discontinuous thermo-mechanical model is also able to simulate a weak discontinuity in the temperature field, cf. figure 6.2c.

Mesh size effect

A mesh refinement study is performed in order to investigate the mesh size effect on modeling adiabatic-isothermal cracks, arbitrarily aligned in the finite element mesh. The UD square plate is discretized into four different meshes, namely Mesh1, Mesh2, Mesh3 and Mesh4, which consist of uniform finite element meshes of $11 \times 11 \times 1$, $31 \times 31 \times 1$, $51 \times 51 \times 1$ and $71 \times 71 \times 1$ eight node solid elements, respectively.

Figures 6.10a and 6.10b show mesh sensitivity results in the form of temperature profiles along the crack surface corresponding to the analysis case adiabatic crack (Model-B) and isothermal crack, respectively. It is evident from the figures that the numerical results converge to a unique solution upon mesh refinement.

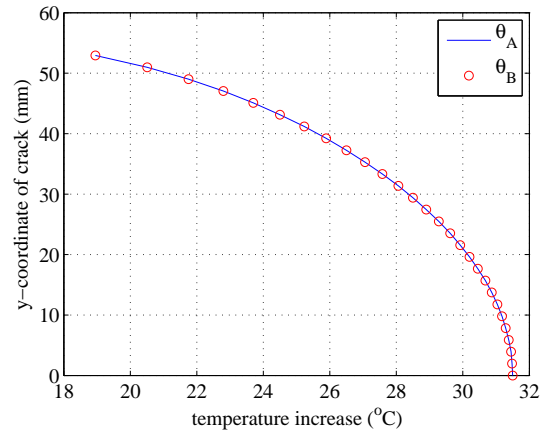


Figure 6.9 Temperature distribution on two faces of the crack– Isothermal cracking

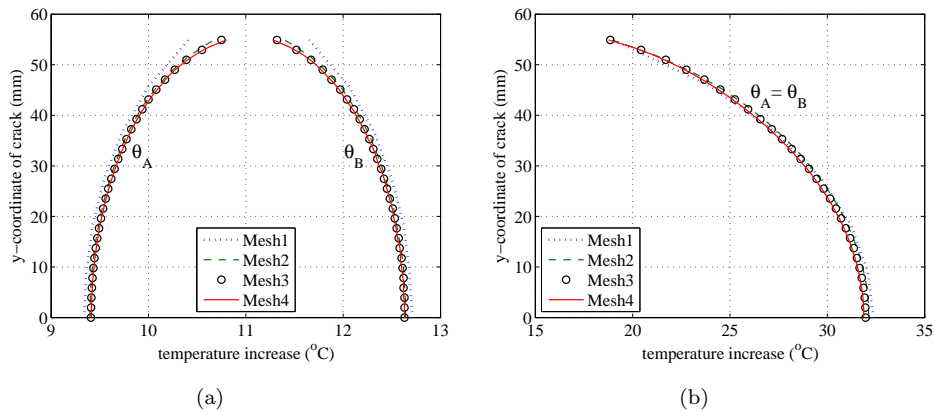


Figure 6.10 Mesh sensitivity analysis; (a) Adiabatic crack, Model-B and (b) Isothermal crack

6.5.2 Thermo-mechanical analysis of a notch plate

To examine the accuracy of the model, a thermo-mechanical crack analysis is performed. An edge cracked strip is subjected to a uniform temperature $\pm\theta_0$ on left and right edges. This results in a linear variation of the thermal field through the width of the strip such that the temperature at the crack tip is zero. The geometry and boundary conditions of the edge cracked strip are shown in figure 6.11a. The length (L) and width (W) of the specimen is 2mm and 0.5mm, respectively. The plate is considered to be made of alumina with a Young's Modulus, $E = 200\text{GPa}$,

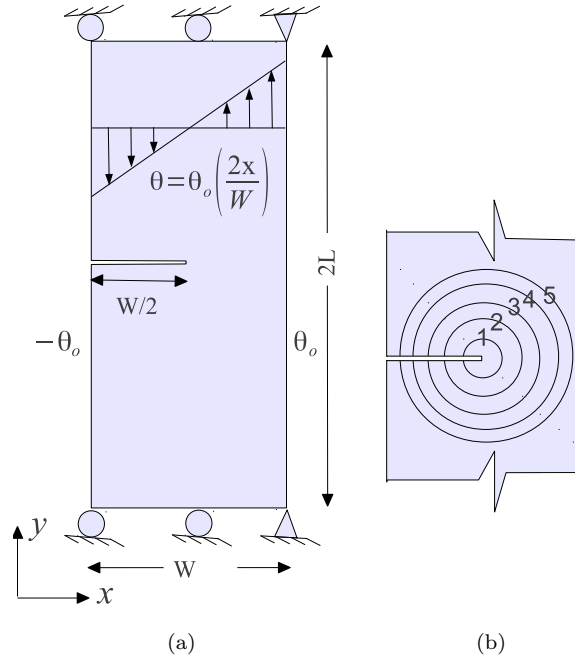


Figure 6.11 Edge cracked strip subjected to thermal load (a) plate geometry and boundary conditions (b) domains for computing J-integral

Poisson ratio, $\nu = 0.25$, coefficient of thermal expansion, $\alpha = 8.6\text{E-}6 / ^\circ\text{C}$ and thermal conductance, $k = 30 \text{ W}/(\text{m} \cdot \text{K})$. A fine mesh with a minimum element size of 0.0064mm is used around the crack-tip zone, in order to accurately capture the near-tip stress field.

Two analyses are performed. First, a thermo-mechanical crack analysis is performed by subjecting the strip to a thermal field. This analysis case will be referred to as analysis case I. The crack faces are considered to be traction free in analysis case I. Second, a mechanical analysis is performed on a cracked strip by applying tractions at the crack interface, to assess the accuracy of the model for modeling cohesive cracks. This analysis case will be referred to as analysis case II. In order to make a direct comparison of analysis case I with the results of analysis case II, a thermo-mechanical analysis of an uncracked strip is performed to obtain the magnitude and direction of cohesive tractions for case II, following [134, 160]. The tractions obtained at the prospective crack surfaces, after a thermo-mechanical analysis of an uncracked strip, are applied to the crack surfaces of the cracked strip in the analysis case II with opposite directions. The accuracy of the numerical results is judged by computing the stress intensity factor K_I at the crack tip. Stress intensity factors are

Table 6.1 Normalized stress intensity factors

Domain	thermal loading	crack face traction
1	0.4913	0.4944
2	0.4900	0.4962
3	0.4939	0.4906
4	0.5099	0.4948
5	0.5141	0.4835
Average	0.4998	0.4919
Average[Shih 1986]	0.4857	0.4951
Average[Wilson 1979]	0.5035	0.5043

computed by $K_I = \sqrt{JE/(1-\nu^2)}$, in which J is energy release rate computed using the J -integral [134], as

$$J = \int_{\Omega_A} [(\sigma_{ij}u_{j,1} - W\delta_{1i})q_1]_{,i} d\Omega + \int_{\Gamma_c^A} t_i \llbracket u \rrbracket_{i,1} q_1 d\Gamma \quad (6.32)$$

in which W is the strain energy density and q is a smooth function over the domain of integration for the J -integral. The J -integral is computed on five different domains bounded by the circles shown in figure 6.11b. Plane-strain conditions are assumed for the analyses. The values of K_I are normalized by $E\alpha\theta_o\sqrt{\pi(W/2)}/(1-\nu)$. The normalized stress intensity factors in comparison with reference solutions, [134, 160], are given in table 6.1. The results of the present analyses are in good agreement with the reference solution, for both thermo-mechanical and mechanical analyses cases. Figure 6.12a shows the temperature distribution over a zoomed-in region near the crack. A linear distribution of temperature across the width of the plate is clearly visible. Figure 6.12b shows the distribution of thermal strain near the cracked zone and figure 6.12c shows the distribution of stress σ_{yy} with peak values near the crack tip. It should be noted, that a more accurate description of the crack-tip field can be obtained using crack-tip enrichment functions [107]. However, this contribution deals with modeling of cohesive cracks, in which case the stress singularity is removed due to the presence of cohesive tractions at the crack surface [159].

6.5.3 Dynamic fracture in a single edge notch composite plate

Dynamic crack propagation in a unidirectional (UD), fiber-reinforced composite plate subjected to high rate shear loading is analyzed. In the experimental study of [40], an edge cracked UD composite plate was impacted, resulting in a shear-dominated propagating crack. It was observed that the crack which is constrained to move along the fiber direction of a ply, propagates intersonically and the speed

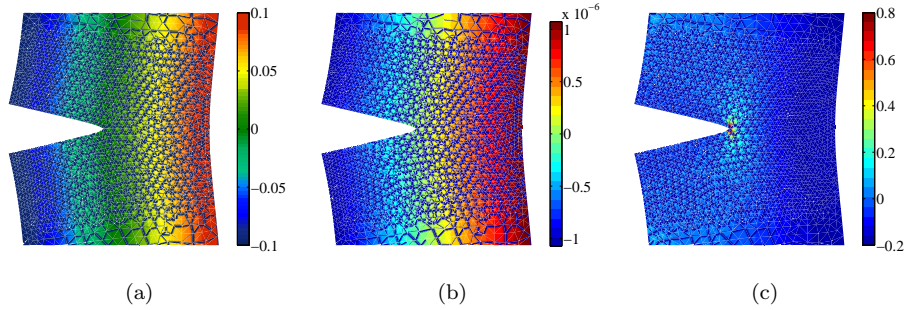


Figure 6.12 Temperature and stress profile over a deformed mesh (zoom in to the crack zone); (a) temperature distribution ($^{\circ}\text{C}$), (b) thermal strain, ϵ_{θ} and (c) stress component σ_{yy} (MPa)

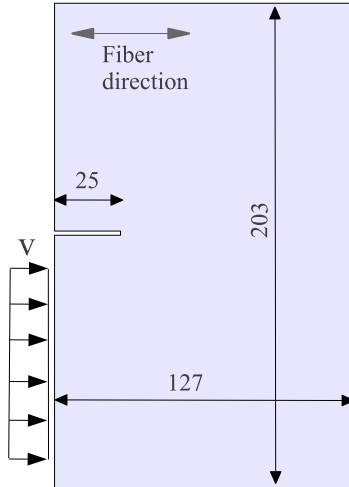


Figure 6.13 Geometry and boundary conditions of a single edge notch composite plate (All dimensions in mm)

of the crack may reach the longitudinal wave speed of the material. Heat dissipation during intersonic crack growth near the cracked flanks was observed and was attributed to the non-uniform frictional contact between crack flanks, [126]. This example aims at numerically simulating heat dissipation during intersonic crack growth in a UD composite plate. Note that, in [40, 126] impact tests on single edge notch plates were performed with two different notch types, i.e. sharp and blunt notch. In this section, the notch is modeled as a blunt notch.

The geometry and boundary conditions of the specimen are shown in figure 6.13. Material properties used for the analyses are extracted from [165] and are given in table 6.2. Thermal material properties, for a typical graphite-epoxy composite, are

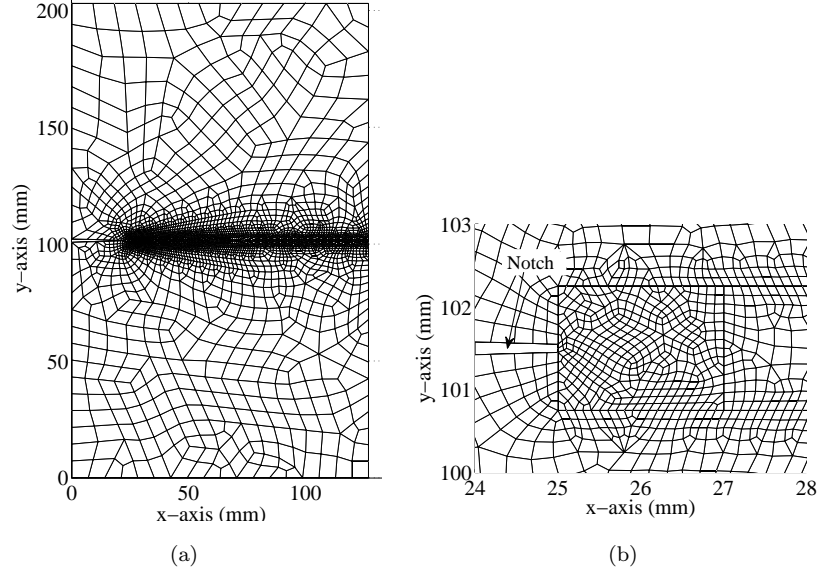


Figure 6.14 Finite element mesh of a UD composite plate; (a) finite element discretization of a UD plate, (b) zoom-in at the finite element mesh around the notch

extracted from [45]. The plate is modeled with tri-linear solid elements. A fine mesh with an average element size, in the in-plane dimension, of 0.25mm is used along the prospective crack growth path. The finite element discretization is shown in figure 6.14. Note that, the finite element mesh is not aligned with the direction of the prospective crack growth path. In order to avoid rigid body modes, displacement components u_x, u_y and u_z are set to 0 at the top-left corner of the plate whereas displacement components u_y and u_z are set to 0 at the top-right corner of the plate. The plate is impacted with a velocity V defined as

$$V(t) = \begin{cases} V_1 t/t_r & \text{for } 0 \leq t < t_r, \\ V_1 & \text{for } t_r \leq t < t_p, \\ V_1(1 - (t - t_p)/t_s) & \text{for } t_p \leq t < (t_p + t_s), \\ 0 & \text{for } t \geq (t_p + t_s). \end{cases} \quad (6.33)$$

in which t_r is the rise time, t_p is the pulse time and t_s is the step down time. In the calculations t_r and t_s are taken to be $2\mu\text{s}$, t_p is taken equal to $25.3\mu\text{s}$ and V_1 is 28m/s . The shear wave speed, C_s and longitudinal wave speed, C_l for the considered material is equal to 7500m/s and 1600m/s , respectively, [40]. The analysis is performed with a timestep of $0.01\mu\text{s}$.

Figure 6.16 shows the crack tip position and speed of an intersonically propagating crack in comparison with the reference solution [40]. The numerical results are in

Table 6.2 Material properties of the FRP composite plate

Ply level properties		Interfacial properties		Thermal properties	
E_{11} (GPa)	80	G_{Ic} (N/mm)	0.474	k_1 (W/(mK))	42
$E_{22} = E_{33}$ (GPa)	8.9	G_{IIc} (N/mm)	0.344	k_2 (W/(mK))	15
$G_{12} = G_{13}$ (GPa)	3.6	f_n (MPa)	35.8	$\alpha_1(10^{-6}/^{\circ}C)$	0.1
$\nu_{12} = \nu_{13}$	0.25	f_s (MPa)	26	$\alpha_2(10^{-6}/^{\circ}C)$	26
ν_{23}	0.43	η	1	C_p (J/kg K)	1170
ρ (kg/m ³)	1478			μ_f (friction coefficient [12])	0.7

good agreement with the reference solution. The crack accelerates and propagates at a velocity close to the longitudinal wave speed of the material, as was observed during experiments [40]. However, it can be observed that the crack tip speed history shows some oscillations. The oscillations in the velocity profile are due to imbalance of the cohesive tractions and the stresses in the bulk at the time of insertion of new crack segments. The problem can be circumvented by making the tractions in equilibrium with the stresses in the bulk at the time of insertion of new crack segments, [115].

Figure 6.15 shows the temperature profiles over an area ahead of the notch corresponding to different time steps. At time $t = 6\mu s$, the shear crack is cohesive. The formation and growth of the cohesive crack resulted in localized heat generation along the length of the crack. At time $t = 10\mu s$, the shear crack tip has passed the window plotted in figure 6.15, therefore, the energy dissipation in the form of heat is due to frictional contact and sliding of the crack flanks. The formation of “hot spots” (localized zones of high temperature) are visible. This is due to non-uniform frictional contact and sliding between crack flanks. This confirms the presence of experimentally observed hot spot formation ahead of the notch. As time progresses the magnitude as well as the shape of the hot spots vary with time. The numerically observed localized heating zones and the temperature profiles are qualitatively in good agreement with the experimental observations in [126]. Note that, the experimental results related to temperature profiles in [126] correspond to the case of a sharp notch.

Effect of mesh size

A mesh refinement study is performed in order to investigate the effect of mesh size on the plate response. Three different mesh discretizations are used for the analyses, namely Mesh-I, Mesh-II and Mesh-III. Average element sizes along the prospective crack growth path in Mesh-I, Mesh-II and Mesh-III are 0.25mm, 0.2mm and 0.15mm, respectively.

Figure 6.17 compares the crack tip position and speed for the three mesh discretizations. It can be observed that numerical results converge to a unique solution

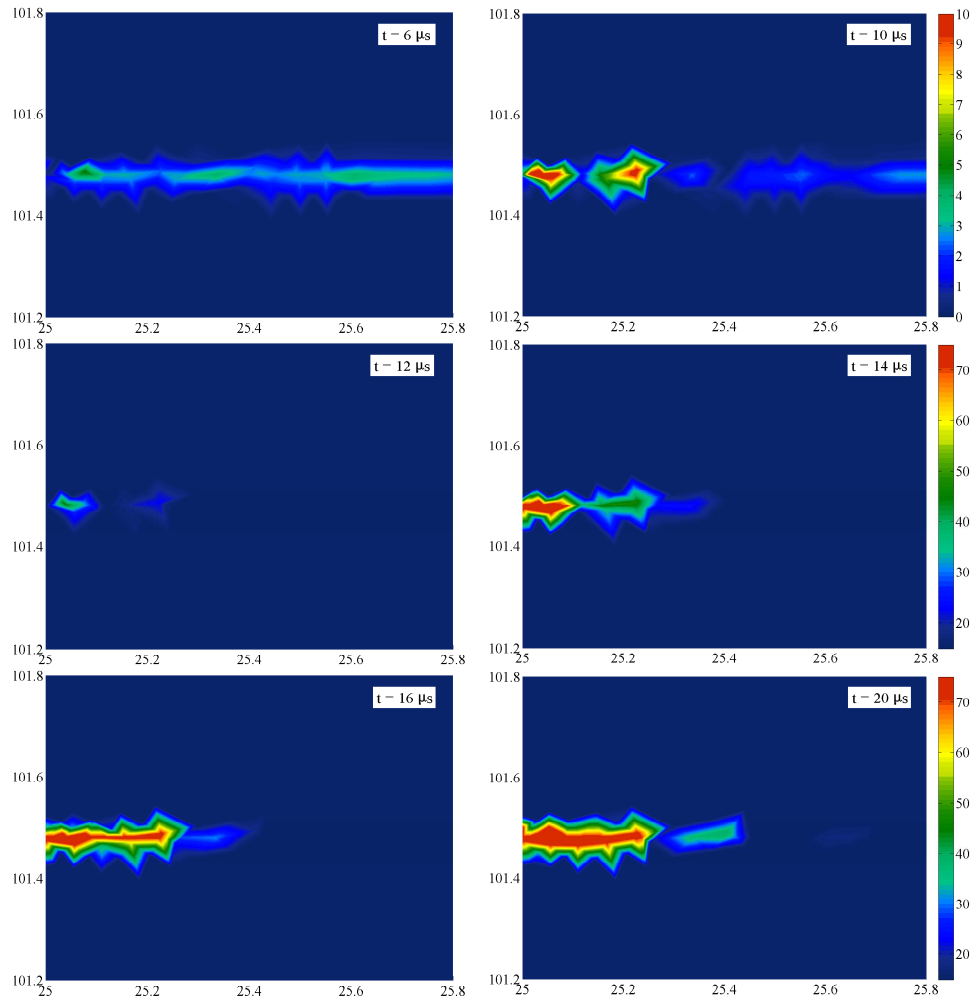


Figure 6.15 Temperature field ($^{\circ}\text{C}$) ahead of a notch (notch tip is at 25 mm) due to fracture at different time instants

upon mesh refinement. Moreover, it is observed from figure 6.17b that the crack tip speed shows more oscillations for the coarse mesh (Mesh-I) compared to the fine mesh (Mesh-III). Figure 6.18 compares energy dissipation due to cohesive cracking for different mesh discretizations. It is evident from the figure that the numerical results are objective with respect to the mesh size.

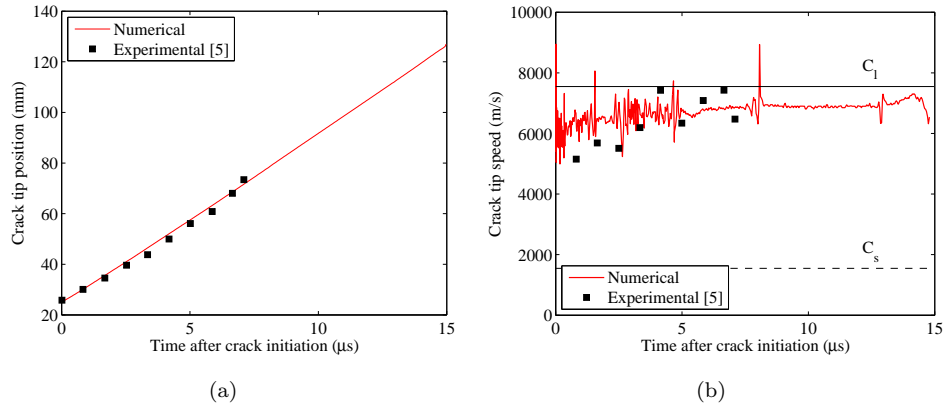


Figure 6.16 Crack tip position and speed of an intersonically propagating shear crack

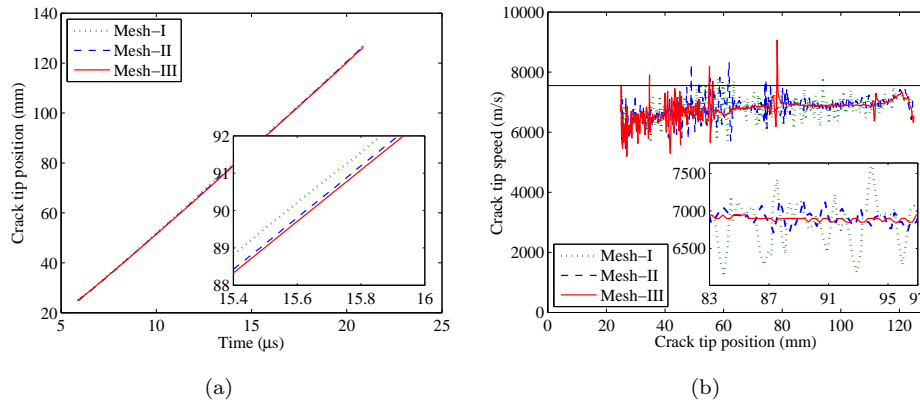


Figure 6.17 Mesh size effect; (a) crack tip position and (b) crack tip speed history

Effect of thermo-fracture heating

A parametric study is performed to study the influence of the thermo-fracture heating term on the response of the composite plate analyzed in section 6.5.3. The analysis is performed for three different cases. Case-I refers to the analysis case in which both parts of \tilde{Q} , i.e. \tilde{Q}_{el} and \tilde{Q}_d are taken into account. Case-II refers to the analysis case in which it is assumed that heat dissipation is only due to craze formation and breakdown (\tilde{Q}_{el}) and heating due to frictional contact (\tilde{Q}_d) is ignored. In Case-III, heat generation due to fracture is completely ignored, i.e. $\tilde{Q} = 0$.

Figures 6.19a and 6.19b compare the crack-tip position and speed of the crack for the three cases. It can be observed that the response in all three cases is almost

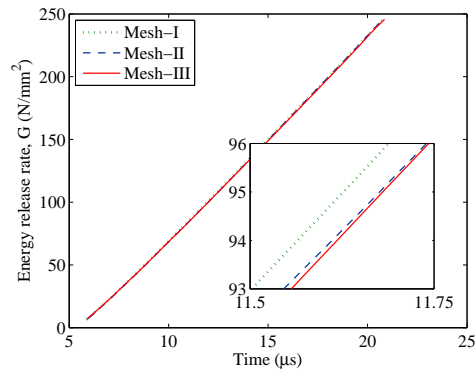


Figure 6.18 Energy dissipation during crack propagation – effect of mesh discretization

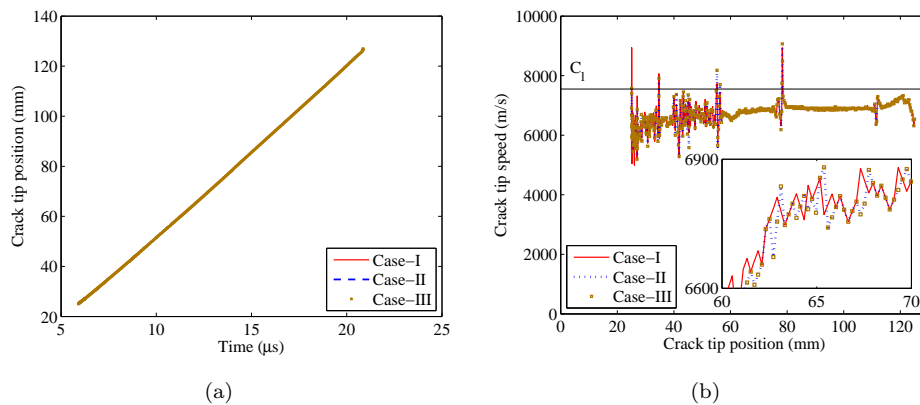


Figure 6.19 Effect of thermo-fracture heating on plate response; (a) crack tip position and (b) crack tip speed history

similar. However, at a closer look (cf. figures 6.20a, 6.20b and inset in figure 6.19b), it can be seen that the response of Case-I is slightly different from the other two cases. This suggests that *thermo-fracture* heating is primarily produced by frictional sliding and not by craze formation and breakdown. It is also evident from figure 6.20a, that failure for Case-I is delayed due to the presence of interface friction compared to the other two cases and at a given time the crack tip is behind the crack tip in analyses cases Case-II and Case-III. However, as time progresses, the crack tip in analysis Case-I overtakes the crack tip of the analyses Case-II and Case-III, figure 6.20b. This is due to thermal softening of the material, resulting in rapid crack growth. However, after time $t = 15\mu\text{s}$ the crack tip in Case-I again is behind the crack tip

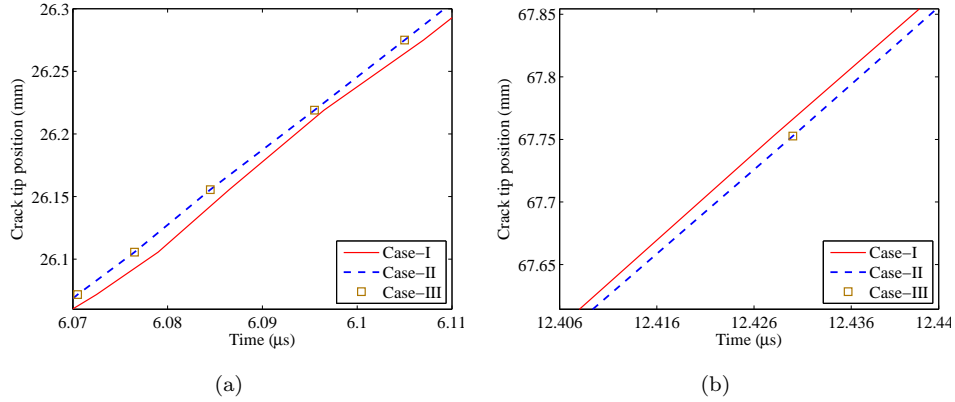


Figure 6.20 Effect of thermo-fracture heating on plate response – zoom in to the plot of crack tip position

of the analyses Case-II and Case-III. This is due to minor friction and consequently minor heat generation near the crack tip zone away from the pre-notched region. These observations are also confirmed by the temperature field profiles (figure 6.15) in which heat generation took place near the notch region. This suggests that there is a strong interplay between interface friction and thermal softening and shows that thermally induced rate effects can be captured.

Effect of friction coefficient

To investigate the effect of the friction coefficient (μ_f) on dynamic crack propagation, the analysis is performed with three different values, $\mu_f = 0.5, 0.7$ and 0.9 (see [12] for description of the coulomb friction model). The analyses results in the form of crack-tip position and speed are given in figure 6.21. It can be observed from the crack-tip history, figure 6.21a, that an increase in friction coefficient results in delay in cohesionless crack initiation and propagation. Moreover, an increased friction coefficient also results in a more smooth crack growth, cf. 6.21b.

Figure 6.22 shows the temperature field ahead of the notch for different values of friction coefficient, at a particular time step. It can be observed, that the temperature increase with an increase of friction coefficient. Moreover, the position and shape of the temperature field ahead of the notch also varies with the change in friction coefficient. It can be concluded, that the spatial and temporal variations of temperature field, ahead of the notch, are affected by the inertia of the structure and contact friction between crack flanks.

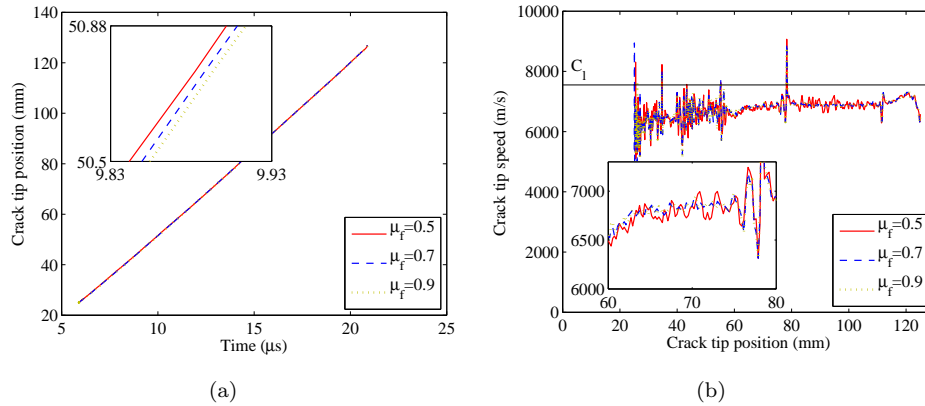


Figure 6.21 Effect of friction coefficient on plate response; (a) crack tip position and (b) crack tip speed history

6.6 Concluding remarks

A discontinuous, coupled thermo-mechanical model for cracking in fiber reinforced composite plates is presented. The model is able to simulate mesh-independent discontinuities in the displacement, temperature and heat flux fields under static and dynamic loading conditions. The discontinuity is incorporated using the phantom node method which allows for the crack being modeled at arbitrary location in the finite element mesh. The computational model allows for combined modeling of adiabatic and isothermal cracking. Consequently, simultaneous modeling of heat transfer through a cracked interface and heat generation at the interface during fracture is possible. A thermo-fracture heating term is proposed, which takes into account the heat generation due to craze formation and breakdown, molecular chain alignment and frictional contact between crack flanks. This is incorporated via a mixed-mode bi-linear cohesive zone model coupled with a constitutive law for contact friction. The presented numerical results show good agreement with existing analytical, numerical and experimental results.

A numerical study on a thermally loaded cracked unidirectional square plate shows that the computational model is able to simulate adiabatic as well as isothermal cracking arbitrarily aligned with the finite element mesh. It is also observed, that in partially cracked fiber reinforced composites, in which the crack is often aligned with the fiber orientation of the ply, the anisotropic nature of heat flow in these materials does not completely prevent the flow of heat from one side of the crack to the other side. This is true, even if the cracked surfaces are insulated. It is observed that this behavior is due to rapid heat conductance through the uncracked areas above the

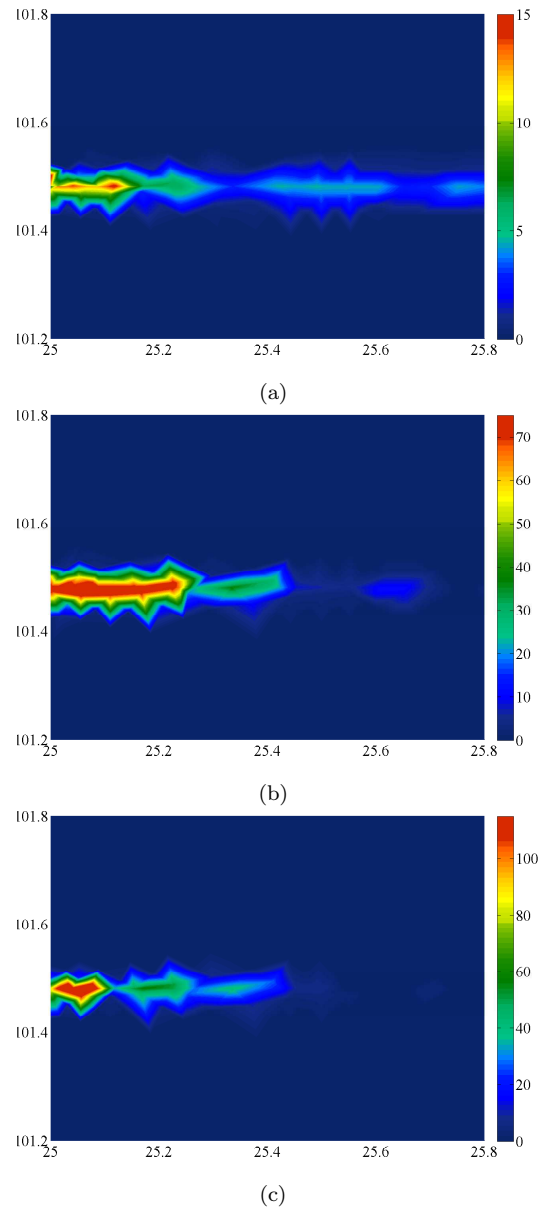


Figure 6.22 Temperature field ($^{\circ}\text{C}$) ahead of a notch due to frictional contact between crack flanks at time, $t = 18\mu\text{s}$; (a) $\mu_f = 0.5$, (b) $\mu_f = 0.7$ and (c) $\mu_f = 0.9$

crack-tip to the other side of the crack.

Thermo-mechanical analysis of a cracked isotropic plate shows that the proposed model is able to accurately simulate the coupled thermo-mechanical response in the presence of a crack. Promising results are obtained and numerically computed thermal as well as mechanical fields are in good agreement with the reference solutions.

The performance of the model in simulating heat generation during dynamic crack growth in a fiber-reinforced composites is illustrated through an impact test on a single edge notch composite plate. The model successfully simulated fast crack growth along with the formation of hot spots during fracture in a FRP composite. Crack initiation time, crack-tip position and speed is observed to be affected by the thermal field. The spatial and temporal distribution of heat generation during fracture is observed to be dependent upon the dynamics of the structure and contact friction between crack flanks. Moreover, the magnitude of temperature, crack tip position and speed is observed to be affected by the coefficient of friction. Larger values of the friction coefficient result in delay in crack initiation. Moreover, the model is able to capture thermally induced rate effects.

It is envisioned that the present numerical approach can be combined with numerical models for fiber failure and shear nonlinear behavior to allow for a complete damage analysis of fiber-reinforced composites.

Chapter 7 Conclusions

An integrated computational framework for the modeling of failure in laminated composite plates/shells subjected to transverse quasi-static and dynamic loading has been developed. To arrive at an efficient and accurate computational model, state of the art numerical tools have been exploited and further developed. The performance and accuracy of the model as a whole and individual components of it have been illustrated through several numerical examples. The main conclusions of the thesis are:

- The discontinuous solid-like shell element (DSLS) provides an efficient means for modeling mesh-independent cohesive cracking in isotropic/orthotropic shells and plates and has the favourable properties of both a 2D shell and a 3D solid elements for numerical analysis of laminated composite plates/shells.
- The DSLS element is able to simulate material and geometrical nonlinearities.
- The DSLS element is coupled with a shell interface element to model progressive damage in laminated composite plates. Promising results are obtained and characteristic damage mechanisms of impact damage and their correct sequence are predicted.
- The effect of coupling between matrix cracking and delamination damage is carefully taken into account using an enriched shell interface model. If the interaction between matrix cracking and delamination is not modeled properly, it may result in incorrect predictions of fracture mode, energy dissipation and load capacity.
- The numerical results are insensitive to the crack spacing parameter. The objectivity of the analysis results, i.e. the global structural response, energy dissipation due to matrix cracking and delamination damage, with respect to crack spacing is ensured.
- Application of the DSLS element to simulate progressive damage in laminated composite plates subjected to rapidly applied loads reveals that the DSLS element can be used in dynamic applications without loss of accuracy. The proposed mass discretization schemes for implicit as well as explicit analysis using a solid-like shell element gives accurate and stable numerical results. Moreover, the mass corresponding to the internal degrees of freedom can be taken as zero in implicit simulations, using solid-like shell elements, without loss of accuracy.

- The proposed mass scaling technique, for solid-like shell elements in laminate analysis, is useful which enables an increase of the critical timestep in explicit dynamic simulations.
- Numerical instability due to insertion of new crack segments during fracture analysis, in mesh-independent crack modeling approaches (e.g XFEM, phantom node method etc.), can be avoided if force equilibrium is enforced at the crack interface, at the time of insertion of new crack segment.
- The rate dependent progressive failure model is able to simulate fast crack growth in laminated composites and rate effects on progressive damage evolution are captured.
- Heat transfer through an interface and heat generation at the interface can be modeled using the unified computational approach. The proposed discontinuous, coupled thermo-mechanical model successfully simulate adiabatic-isothermal cracks propagating arbitrarily through the finite element mesh.
- Mesh size objectivity of the individual models as well as the whole framework is ensured.

The thesis presented a comprehensive computational framework for modeling failure in fiber-reinforced composite laminates subjected to quasi-static and dynamic transverse loads, discussing in detail algorithmic and implementation aspects of the model. It is envisioned that the computational framework can be combined with a more realistic constitutive model, including a model for fiber failure, matrix non-linearity and rate dependence of the matrix material for a complete analysis of laminate failure.

Appendix A

Modeling cohesive cracking using XFEM – Computational anomalies*

The performance of partition-of-unity (PoU) based methods such as the generalized finite element method (GFEM), the extended finite element method (XFEM) or the phantom node method is studied for the simulation of cohesive cracking. The focus of investigation is on the performance of bi-linear quadrilateral finite elements using these methods. In particular, the approximation of the displacement jump field, representing cohesive cracks, by XFEM/GFEM and its effect on the overall behavior at element and structural level is investigated. A single element test is performed with two different integration schemes namely the Newton-Cotes/Lobatto and the Gauss integration scheme, for the cracked interface contribution. It was found that cohesive crack segments subjected to a non-uniform opening in un-structured meshes (or an inclined crack in a structured finite element mesh) results in an un-realistic crack opening. The reasons for such behavior and its effect on the response at element level are discussed. Furthermore, a mesh refinement study is performed to analyze the overall response of a cohesively cracked body in a finite element analysis.

A.1 Extended finite element method (XFEM) basics

In this section a brief introduction of the XFEM displacement approximation is presented followed by a discretized weak form of equilibrium equation, which will be used in the subsequent sections for the analysis of cohesively cracked bodies.

A.1.1 Kinematic relations

Partition-of-unity based methods such as the generalized finite element method (GFEM) [110], or the extended finite element method (XFEM) [24], explore the idea of enriching the displacement field of a cracked body. The displacement approximation is considered to be the sum of the standard finite element method (FEM)

* This appendix is extracted from [3]

polynomial displacement assumption \mathbf{u}_{std} and an enriched displacement field \mathbf{u}_{enr} .

$$\mathbf{u} = \mathbf{u}_{std} + \mathbf{u}_{enr} \quad (\text{A.1})$$

For modeling cohesive cracking phenomena in a material, this is accomplished by [159]:

$$\mathbf{u} = \sum_{i \in I} \Psi_i \hat{\mathbf{u}}_i + \sum_{j \in J} \Psi_j \mathcal{H}_{\Gamma_c} \hat{\mathbf{a}}_j \quad (\text{A.2})$$

where Ψ_i are the smooth functions satisfying the property of partition of unity, i.e. $\sum_{i=1}^n \Psi_i = 1$. $\hat{\mathbf{u}}$ and $\hat{\mathbf{a}}$ are the standard and additional degrees of freedom, respectively. I is a set of all nodes and J is a set of enriched nodes. \mathcal{H}_{Γ_c} is a Heaviside function at the crack surface, Γ_c (figure A.1), defined as

$$\mathcal{H}_{\Gamma_c}(\mathbf{x}) := \begin{cases} 1 & \forall \mathbf{x} \in \Omega_B \\ 0 & \forall \mathbf{x} \in \Omega_A \end{cases}$$

in which \mathbf{x} denotes the position of the material point in a body.

Using the above definition of Heaviside function \mathcal{H}_{Γ_c} , \mathbf{u}_{enr} in equation (A.1) defines the displacement jump, $[[\mathbf{u}]]$ at the crack surface. Moreover, [145] showed that different partition of unity functions can be embedded into the approximation space. Hence, equation (A.2) generalizes to

$$\mathbf{u} = \sum_{i \in I} \Psi_i^p \hat{\mathbf{u}}_i + \sum_{j \in J} \tilde{\Psi}_j^q \mathcal{H}_{\Gamma_c} \hat{\mathbf{a}}_j \quad (\text{A.3})$$

in which Ψ^p and $\tilde{\Psi}^q$ are the partition of unity functions of order p and q , respectively. This opens the possibility of using different interpolation functions for the standard and enriched parts of the displacement field.

Within the finite element method (FEM) framework, since the standard FEM shape functions also possess the property of partition of unity, equation (A.2) can be written as (see [24, 159])

$$\mathbf{u} = \sum_{i \in I} N_i \hat{\mathbf{u}}_i + \sum_{j \in J} N_j \mathcal{H}_{\Gamma_c} \hat{\mathbf{a}}_j \quad (\text{A.4})$$

in which N_i and N_j are the standard FEM shape functions. Note that both fields \mathbf{u}_{std} and \mathbf{u}_{enr} are approximated with the same interpolation functions.

A.1.2 Weak form of equilibrium equation

Following standard methods, the weak form of the momentum balance equation for quasi-static analysis reads (see for instance [24, 159])

$$\int_{\Omega \setminus \Gamma_c} \delta \boldsymbol{\epsilon} : \boldsymbol{\sigma} + \int_{\Gamma_c} [[\delta \mathbf{u}]] \cdot \mathbf{t}_c - \int_{\Gamma_t} \delta \mathbf{u} \cdot \mathbf{t} - \int_{\Omega \setminus \Gamma_c} \delta \mathbf{u} \cdot \mathbf{b} = 0 \quad (\text{A.5})$$

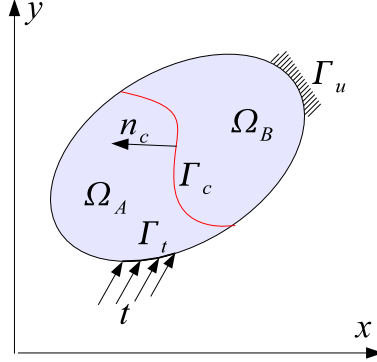


Figure A.1 Body Ω crossed by a crack Γ_c

where ϵ and σ are small strain and Cauchy stress tensors, \mathbf{t} and \mathbf{t}_c are the traction vectors acting on the surface Γ_t and Γ_c , respectively, \mathbf{b} are the body forces and $\delta \mathbf{u}$, $[[\delta \mathbf{u}]]$ denotes variations in displacement and jump field.

Next, the phantom node method [58] is used, a variant of XFEM, where the element crossed by a discontinuity is replaced by two partially active elements with domains Ω_A^{elem} and Ω_B^{elem} , respectively, such that $\Omega^{elem} = \Omega_A^{elem} \cup \Omega_B^{elem}$. The superscript *elem* represents a particular element in a finite element mesh crossed by a discontinuity. The displacement field of a cracked element can be represented as

$$\mathbf{u}(\mathbf{x}) = \begin{cases} \mathbf{u}_A(\mathbf{x}) & \forall \mathbf{x} \in \Omega_A \\ \mathbf{u}_B(\mathbf{x}) & \forall \mathbf{x} \in \Omega_B \end{cases} \quad (\text{A.6})$$

The displacement jump over the crack is defined as the difference of the displacement fields of the two elements

$$[[\mathbf{u}]](\mathbf{x}) = \mathbf{u}_B(\mathbf{x}) - \mathbf{u}_A(\mathbf{x}) \quad \forall \mathbf{x} \in \Gamma_c \quad (\text{A.7})$$

The equivalence of degrees of freedoms $\hat{\mathbf{u}}_A$ and $\hat{\mathbf{u}}_B$ with the conventional XFEM degrees of freedom, equation (A.2), for the case when subtracted form of enrichment ($\bar{H} = \mathcal{H}_{\Gamma_c} - \mathcal{H}_{\Gamma_c}^j$, where $\mathcal{H}_{\Gamma_c}^j$ denotes the nodal value of \mathcal{H}_{Γ_c}) is used instead of \mathcal{H}_{Γ_c} , is given by [140]:

$$\hat{\mathbf{u}}_{A_i} = \begin{cases} \hat{\mathbf{u}}_i & \forall \hat{\mathbf{x}}_i \in \Omega_A \\ \hat{\mathbf{u}}_i - \hat{\mathbf{a}}_i & \forall \hat{\mathbf{x}}_i \in \Omega_B \end{cases} \quad \hat{\mathbf{u}}_{B_i} = \begin{cases} \hat{\mathbf{u}}_i + \hat{\mathbf{a}}_i & \forall \hat{\mathbf{x}}_i \in \Omega_A \\ \hat{\mathbf{u}}_i & \forall \hat{\mathbf{x}}_i \in \Omega_B \end{cases} \quad (\text{A.8})$$

Note that the nodal quantities are represented with a hat over the quantity.

When using the additive property of integrals in combination with equation (A.6)

and taking $\delta \mathbf{u}_A = 0$ and $\delta \mathbf{u}_B = 0$, the following two variational statements are obtained

$$\int_{\Omega_A} \delta \epsilon_A : \boldsymbol{\sigma} + \int_{\Gamma_c} -\delta \mathbf{u}_A \cdot \mathbf{t}_c - \int_{\Gamma_{t,A}} \delta \mathbf{u}_A \cdot \mathbf{t} - \int_{\Omega_A} \delta \mathbf{u}_A \cdot \mathbf{b} = \mathbf{0} \quad (\text{A.9a})$$

$$\int_{\Omega_B} \delta \epsilon_B : \boldsymbol{\sigma} + \int_{\Gamma_c} \delta \mathbf{u}_B \cdot \mathbf{t}_c - \int_{\Gamma_{t,B}} \delta \mathbf{u}_B \cdot \mathbf{t} - \int_{\Omega_B} \delta \mathbf{u}_B \cdot \mathbf{b} = \mathbf{0} \quad (\text{A.9b})$$

Note that in case of traction free cracks, the term involving integration over the crack surface, Γ_c , vanishes and the two equations act independently i.e. there is no interaction between the two domains separated by the crack and hence the equations can be solved independently of each other. Additionally, the two variational statements thus obtained are similar to the standard variational forms for the uncracked domains, and therefore standard FEM procedures can be used for their solution. Importantly, the fields of the two domains will only interact when cohesive tractions are active on the cracked surface.

The discretized displacement field and its variations are given as

$$\begin{aligned} \mathbf{u}_e &= N \hat{\mathbf{u}}_e \quad , \quad \delta \mathbf{u}_e = N \delta \hat{\mathbf{u}}_e \\ \llbracket \mathbf{u} \rrbracket &= N \llbracket \hat{\mathbf{u}} \rrbracket \quad , \quad \llbracket \delta \mathbf{u} \rrbracket = N \llbracket \delta \hat{\mathbf{u}} \rrbracket \end{aligned} \quad (\text{A.10})$$

in which $e = A, B$ and N is a standard shape function matrix for element e . The quantities $\llbracket \hat{\mathbf{u}} \rrbracket$ and $\llbracket \delta \hat{\mathbf{u}} \rrbracket$ are defined as

$$\llbracket \hat{\mathbf{u}} \rrbracket = \hat{\mathbf{u}}_B - \hat{\mathbf{u}}_A \quad (\text{A.11})$$

$$\llbracket \delta \hat{\mathbf{u}} \rrbracket = \delta \hat{\mathbf{u}}_B - \delta \hat{\mathbf{u}}_A \quad (\text{A.12})$$

Using equations (A.6), (A.9) and (A.10), the corresponding discretized form of equilibrium equation is obtained

$$\int_{\Omega_A} B^T \boldsymbol{\sigma} + \int_{\Gamma_c} -N^T \mathbf{t}_c - \int_{\Gamma_{t,A}} N^T \mathbf{t} - \int_{\Omega_A} N^T \mathbf{b} = \mathbf{0} \quad (\text{A.13a})$$

$$\int_{\Omega_B} B^T \boldsymbol{\sigma} + \int_{\Gamma_c} N^T \mathbf{t}_c - \int_{\Gamma_{t,B}} N^T \mathbf{t} - \int_{\Omega_B} N^T \mathbf{b} = \mathbf{0} \quad (\text{A.13b})$$

in which B is the standard finite element matrix containing derivatives of shape functions for element e .

The remainder of the chapter is ordered as follows. In the next section the model problem is described and a finite element analysis based on discretized equation (A.13) is performed for a cohesively cracked body. To communicate the idea of anomalous behavior of cohesive cracking in a transparent way, elements completely cut by cohesive segments are considered. The aim of the analysis is to highlight (a) how the displacement jump field is approximated in PoU based methods?, especially

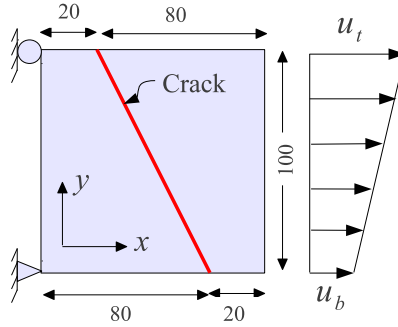


Figure A.2 Single element model geometry (All dimensions are in mm)

for un-structured meshes and (b) what is the response of a cohesively cracked element modeled using PoU based methods?. Section A.3, explains the observations made after the analysis of a single element test in section A.2. Section A.4 presents the analysis of a cohesively cracked element using interface elements. A mesh refinement study is conducted in section A.5 to see the performance of PoU methods at structural level (where a body is discretized with a finite number of elements).

A.2 Model problem

To investigate the performance of PoU based methods for arbitrarily propagating cohesive cracks in a finite element mesh, a single element test is performed. In finite element simulations, especially using unstructured meshes, where PoU cracks cross the element arbitrarily, the crack segments in an element may not be parallel to the element edges. This situation is simulated by modeling an inclined crack in a square shaped quadrilateral element, such that it divides the element into two parts. The geometry of the element and crack is shown in figure A.2. The thickness of the element is 10mm. Since the displacement approximation of tri-linear solid elements is similar to bi-linear quadrilateral elements, except the presence of a third dimension, the analysis is performed only using quadrilateral elements for the sake of simplicity and to avoid repetition of results. However, the conclusions drawn afterwards are also valid for modeling three-dimensional cohesive cracks using tri-linear solid elements.

Plane stress conditions are assumed for the analysis. The bulk material is considered to be linear elastic with a Young's modulus, $E = 40\text{GPa}$ and Poisson ratio, ν equals zero. An isotropic linear elastic cohesive constitutive law is assumed for the crack, which relates the interface tractions, \mathbf{t}_c and the displacement jump, $[[\mathbf{u}]]$ through a tangent, $\mathbb{C}_{[[u]]} = k_{el}\mathbb{I}$. Where $k_{el} = 1.0\text{E}+05\text{N}/\text{mm}^3$ is the elastic interface

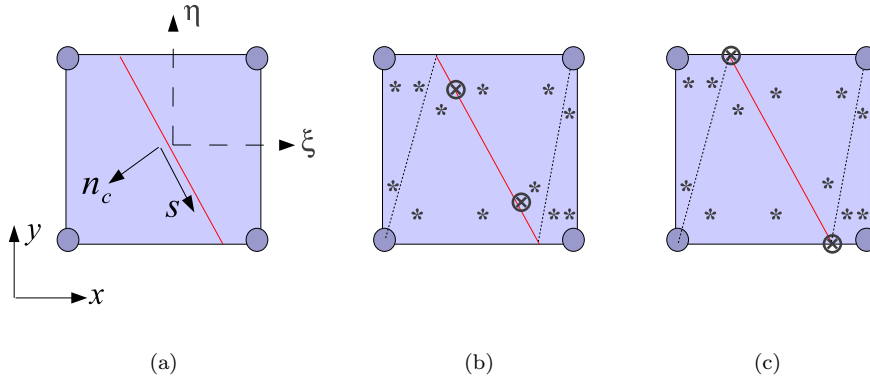


Figure A.3 Integration schemes for the bulk and cohesive interface and different coordinate axes used for analysis; (a) Parent element local axes (ξ, η) , crack local axes (n_c, s) and global axes (x, y) , (b) Gauss integration scheme for cohesive interface, (c) NC/Lobatto integration scheme for cohesive interface, $*$ Bulk integration point, \otimes Cohesive integration point

stiffness and \mathbb{I} is 2x2 identity matrix.

A displacement controlled analysis is performed by subjecting the body to prescribed displacements at the right end, see figure A.2. Two different loading conditions are considered for the analysis, (1) Uniform prescribed displacements, $u_b = u_t$, to simulate uniform crack opening and (2) linearly varying prescribed displacements along the height of the bar, $u_b = 0$, to simulate non-uniform crack opening. The analysis was performed with a 4-node quadrilateral element. For the integration of the bulk material on both sides of the crack, Delaunay triangulation is used with three integration points per triangle. Two different integration schemes were used for the integration of cohesive stiffness, namely a Newton-Cotes/Lobatto and a Gauss integration scheme. The numerical integration schemes for the bulk and the cohesive zone along with the crack local axes, parent element axes and global axes are shown in figure A.3.

A.2.1 Analysis results and observations

Uniform crack opening

The uniform crack opening test was performed by subjecting the element to a prescribed displacement of $u_b = u_t = 1.0\text{E-}03\text{mm}$. The numerical results have been compared with the analytical solution, which yields a total load, $P = 398.6327\text{N}$ at the loaded ends and a constant displacement jump along the length of the crack,

$\llbracket u \rrbracket_x = 3.4182\text{E-}06\text{mm}$, $\llbracket u \rrbracket_y = 0.0\text{mm}$. Where $\llbracket u \rrbracket_x$ and $\llbracket u \rrbracket_y$ denote the x and y components of the displacement jump. The observations made during the analysis are as follows

- The displacement jump is constant, as expected, along the length of the crack, when Gauss integration is used, figure A.4a.
- The displacement jump shows a curved variation along the length of the crack when Newton-Cotes/Lobatto integration scheme is used, figure A.4b.

It is noteworthy that this un-realistic opening of the crack is not because of the mapping of a discontinuity line from the reference element domain to the parent element domain as identified by [154]. Since, in our case the element is a perfect square, the straight discontinuity will be mapped to a parent element as a straight line. This is an additional source of error which resulted due to un-successful transformation of the displacement jump from integration points to the element nodes as rigid body motion, as will be explained in section A.3.

- By applying a slightly linearly varying displacement field, $u_b = 0.9999u_t$, such that it can still be considered as uniform displacement field ($u_b \approx u_t$), the displacement jump shows a curved behavior along the length of the crack also with a Gauss integration scheme, figure A.4a.
- The error in the approximation of the displacement jump field is more significant when Newton-Cotes/Lobatto integration is used as compared to the case when Gauss integration is used. This effect can be attributed to underintegration of the displacement jump field when nodal integration is used.
- The unrealistic opening of the interface in x -direction also resulted in an unrealistic displacement jump in y -direction, figure A.4c.
- The un-realistic opening of the interface also resulted in inaccurate straining of the element, figure A.5. The element experienced a non-uniform distribution of strains in x -direction, instead of constant strains, figure A.5a. In addition to this, the element also experienced straining in y -direction, instead of zero strains. More importantly, the order of magnitude of strain ϵ_{yy} is the same as the strain ϵ_{xx} , figure A.5b.

Similar observations can be made for the case of a Gauss integration scheme with $u_b = 0.9999u_t$. However the magnitude of unrealistic straining is small compared to a Newton-Cotes/Lobatto integration scheme, figure A.6. This follows from the small error in the approximation of displacement jump field, see figure A.4.

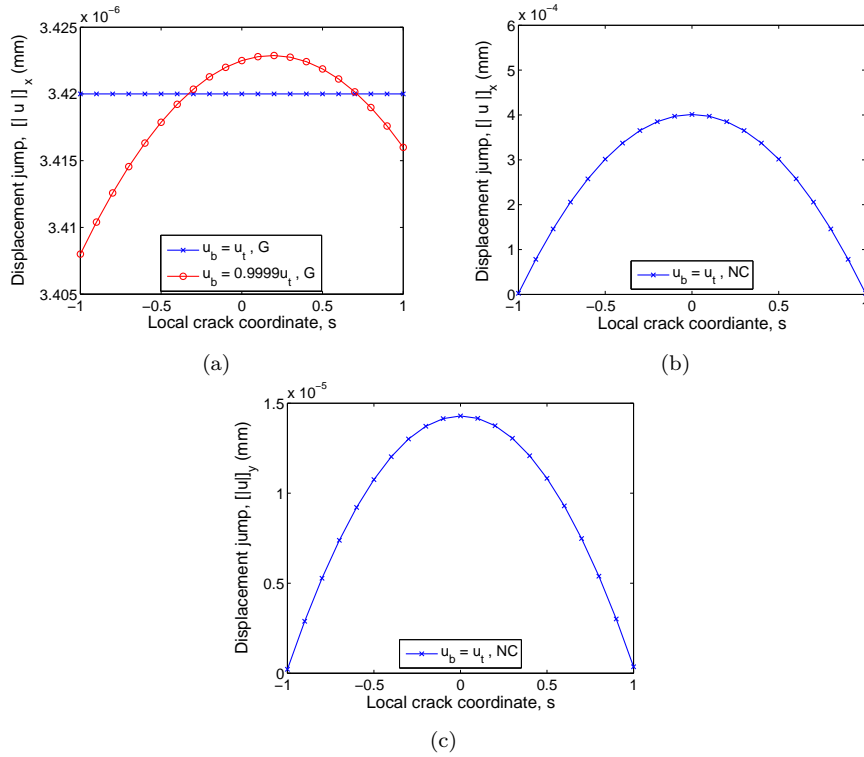


Figure A.4 Variation of displacement jump along the crack ($\llbracket \mathbf{u} \rrbracket(\mathbf{x}) = N(\mathbf{x})\llbracket \hat{\mathbf{u}} \rrbracket \quad \forall \mathbf{x} \in \Gamma_c$) - Uniform crack opening; (a) Horizontal displacement jump $\llbracket u \rrbracket_x$ when Gauss integration is used, (b) Horizontal displacement jump $\llbracket u \rrbracket_x$ when NC/Lobatto integration is used, (c) Vertical displacement jump $\llbracket u \rrbracket_y$ when NC/Lobatto integration is used

- Figure A.7 shows the x -component of the tractions at a particular integration point on both sides of the discontinuity for increasing load levels. The negative sign of tractions shows that the x -component of traction is acting in opposite direction of global x -axis and in the direction of x -component of normal to the interface. It can be observed from figure A.7b that for the simple case of $u_b = u_t$, where the trial solution is supposed to be capable of representing linear functions and exact results can be obtained, traction continuity at the interface is also not properly enforced due to an error in the approximation of the displacement jump field. This error increases with increasing magnitude of tractions.

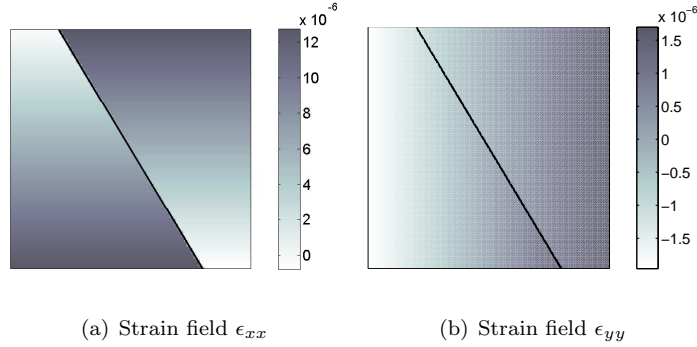


Figure A.5 Analysis result using Newton-Cotes integration - Uniform crack opening

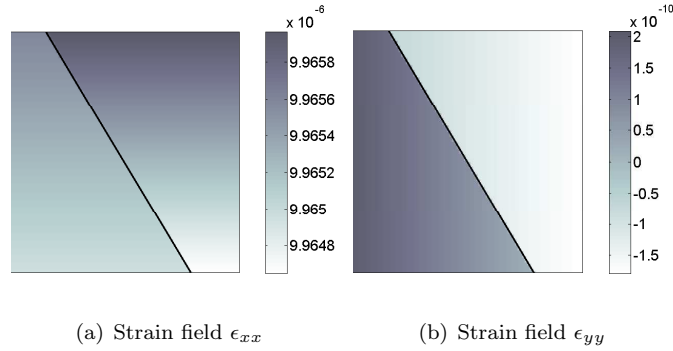


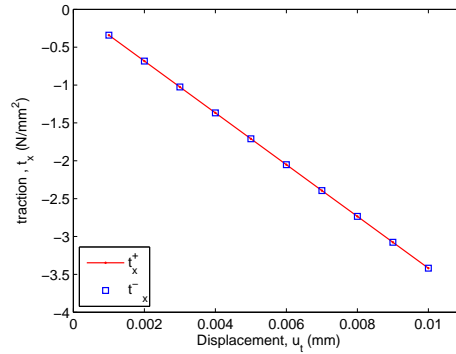
Figure A.6 Analysis result using Gauss integration - Uniform crack opening, $u_b = 0.9999u_t$

Non-uniform crack opening

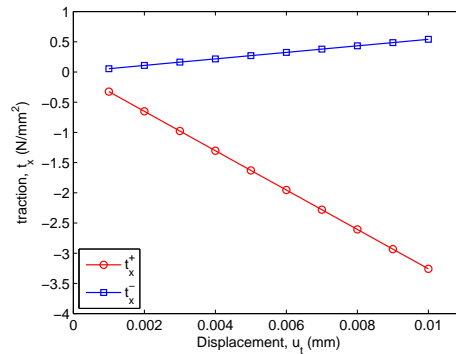
In real simulations, cracks are subjected to non-uniform openings. To investigate the performance of the element for non-uniform openings, we consider the case where $u_b = 0$. Figure A.8 represents the x -component of the displacement jump for both integration schemes. The analysis results are qualitatively similar to the results obtained for uniform crack opening. The displacement jump showed a curved shape along the crack surface for both integration schemes. Furthermore, the error in the approximation of displacement jump field is larger when a nodal integration scheme is used as compared to Gauss integration.

A.3 Explanation of analysis results

- The standard finite element method is a node-based approximation method, where unknown variables are defined at the nodes. In addition to external



(a) Analysis result using Gauss integration



(b) Analysis result using Newton-Cotes integration

Figure A.7 Traction continuity at a particular integration point for increasing load levels - Uniform crack opening

nodal forces, if a body contains external surface tractions and/or body forces, they are transferred to the nodes as equivalent nodal forces by the interpolation function of the element. The extended finite element method is a nodal enrichment method, where extra degrees of freedom are added at existing nodes to represent the displacement jump across the crack. The displacement jump is approximated as a function of additional nodal degrees of freedom, using element shape functions, equation (A.10). As a result the traction forces which are evaluated along the crack surface are transferred to the nodes as equivalent tractions $\left(\int_{\Gamma_c} N^T \mathbf{t}_c\right)$, similar to the external forces. This is schematically illustrated in figure A.9. Since the interpolation functions which compute the contribution of forces on a particular node are based on bi-linear element shape

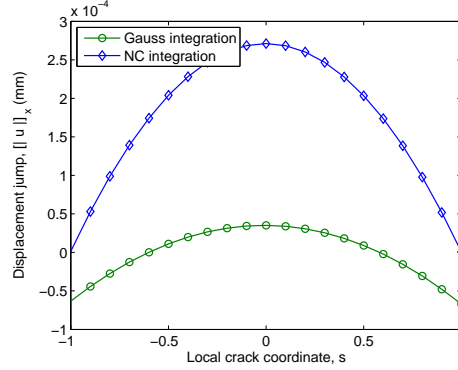


Figure A.8 Variation of displacement jump along the crack ($[[\mathbf{u}]](\mathbf{x}) = N(\mathbf{x})[[\hat{\mathbf{u}}]] \forall \mathbf{x} \in \Gamma_c$) - Non-uniform crack opening

functions, a constant traction on an interface may result in un-equal nodal forces. As a consequence, it is possible that in such a situation, force equilibrium is satisfied, $\sum \mathbf{F} = 0$ but the moment equilibrium is not, $\sum \mathbf{M} \neq 0$. This results in an un-realistic moment couple and will cause rotation of the interface. Hence, the interface which should have experienced an opening only in the x -direction, such as in the model problem with uniform applied displacements at the ends, may also experience an un-realistic movement in the y -direction, see figure A.4c.

- Since the tractions at the interface are a function of the displacement field, the equilibrium equation is a nonlinear equation and is required to be solved with iterative methods like the Newton-Raphson method. This requires computation of tangent matrices. The above discretized equilibrium equation (eqn: (A.13)) reduces to a standard form

$$(\mathbf{K}_{e,Bulk} + \mathbf{K}_{e,coh}) \hat{\mathbf{u}} = f_{ext_e} \quad (\text{A.14})$$

where $\mathbf{K}_{e,Bulk}$ and $\mathbf{K}_{e,coh}$ are the element tangent stiffness matrices for the bulk and cohesive parts, respectively and f_{ext_e} is the equivalent external nodal forces for an element e .

Since matrix $\mathbf{K}_{e,coh}$ is directly affected by the way the jump is transferred to the nodes and hence depends upon the chosen interpolation function for the variational jump field, it automatically contaminates the whole stiffness matrix and consequently will result in a wrong equilibrium and evaluation of un-realistic nodal displacements. As a result the internal force vectors, $f_{int,Bulk}$ and $f_{int,coh}$ are also affected. Furthermore, increasing the interface stiffness

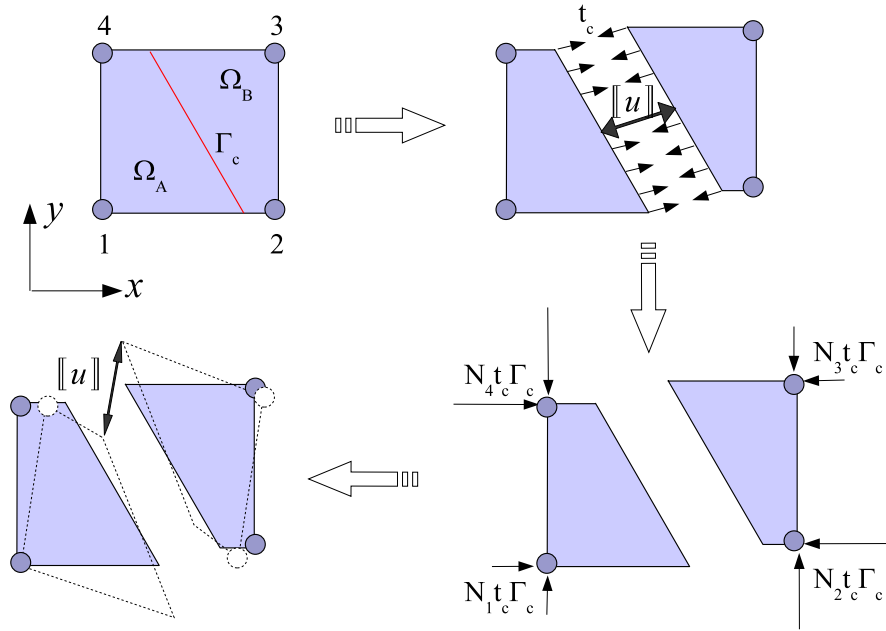


Figure A.9 Transmission of tractions to equivalent nodal tractions

will increase the above mentioned effects and the error in the solution will also increase, as was observed by [44].

It is noteworthy that in the absence of cohesive terms, equation (A.13) simplifies to a standard equilibrium equation of a finite element method. Therefore for cohesionless cracks no un-realistic displacements will be observed and the displacement jump along the discontinuity will not represent the strange curved shape even when bi-linear element shape function for the approximation of the jump field are used.

- Due to the fact, that the error in the solution is coming from the cohesive terms of equation (A.13), increase or decrease in the magnitude of tractions will affect the accuracy of the solution accordingly.
- As a consequence of the development of an un-realistic moment couple, as explained above, un-realistic equivalent nodal jumps will be observed. Hence the nodes having a larger contribution of traction forces will have smaller displacements and *vice versa*. The interpolation of these nodal displacement

jumps will result in a bi-linear curved surface over an element, figure A.10. Indeed, it is this phenomenon that was observed earlier in figures A.4 and A.8.

- The bi-linear approximation of the displacement jump has another severe effect, i.e. as a consequence of bi-linear approximation the element experiences un-realistic straining. For a simple case of $u_b = u_t$ with a nodal integration scheme, the strain field within an element should be constant. On the contrary, a linear variation of the strain field within the element due to un-realistic crack opening is observed. Indeed, the strains are function of the derivatives of the displacement field and since the displacement field is bi-linear, its derivatives will be linear, hence the strains will show a linear variation in such cases, figure A.11.
- For the case of uniform crack opening good numerical results were observed using a Gauss integration scheme. This is not surprising, since the displacement jump is approximated by the finite element shape functions as:

$$[[u]](\mathbf{x}) = \sum_I N_I(\mathbf{x}) [[\hat{\mathbf{u}}_I]] \quad \forall \mathbf{x} \in \Gamma_c \quad (\text{A.15})$$

For the case of uniform crack opening, a trivial solution of the above equation exist, when all nodes are rigidly displaced, i.e $[[\hat{\mathbf{u}}_I]] = a_o$

$$[[u]] = \sum_I N_I a_o \quad (\text{A.16})$$

$$[[u]] = a_o \quad \because \sum_I N_I = 1 \quad (\text{A.17})$$

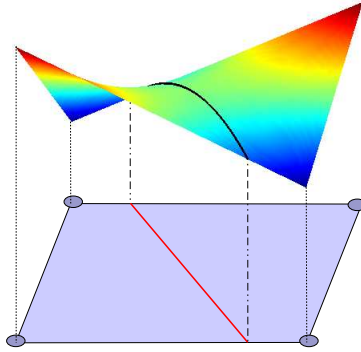


Figure A.10 Displacement jump field, $N[[\hat{\mathbf{u}}]]$, over an element

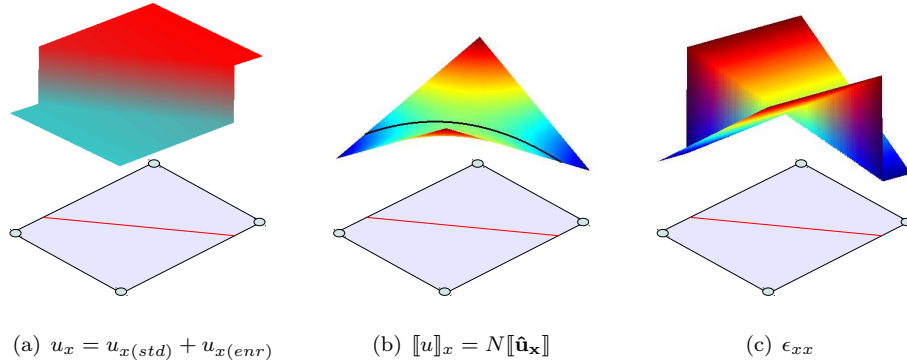


Figure A.11 Displacement and stress field in a cracked element

hence, for the case of uniform crack opening, the displacement jump can be transmitted as a rigid body motion, to the nodes without causing straining in the element. However for the case of non-uniform crack opening, where both normal and tangential components of the displacement jump are present and if the crack local axes are not aligned with the element local axes, the bi-linear approximation of the displacement jump field will result in un-realistic opening of the crack and the transmission of the displacement jumps as rigid body motion from the integration point to the nodes is no more guaranteed. This also results in un-realistic straining of the element.

- From the analysis cases $u_b = 0.9999u_t$ and $u_b = 0$, it is observed that the problem of un-realistic crack opening persists regardless of the type of integration scheme used for the interface contribution. However, the error is magnified when a Newton-Cotes/Lobatto integration scheme is used as compared to a Gauss integration scheme due to underintegration. The influence of the choice of integration scheme for the cohesive interface on the numerical accuracy and efficiency can be found in [136].
- Moreover, it is observed that the problem of unrealistic straining of the element persists irrespective of the orientation of the crack. Figure A.12 shows the strain field over an element subjected to a uniform displacement at the right edge. However, no unrealistic straining is observed for the case when the local crack axis is aligned with the local element axis, see figures A.12a and A.12d.

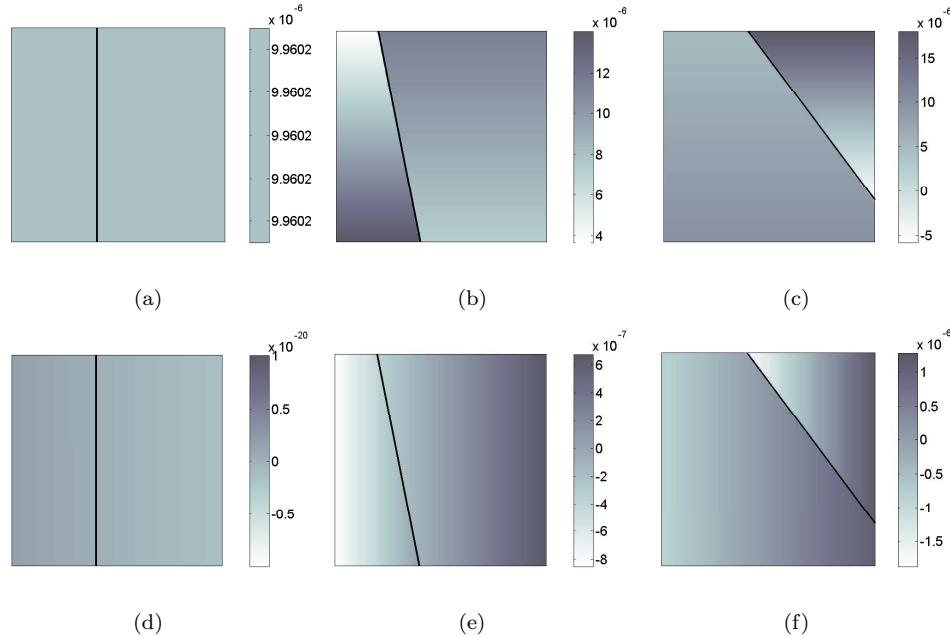


Figure A.12 Analysis results using Newton-Cotes/Lobatto integration scheme; Figures a, b and c shows the strain field ϵ_{xx} and figures d, e and f shows the strain field ϵ_{yy} for different crack orientations

A.4 Interface element analysis

For the sake of comparison, we analyze the same problem by explicitly modeling the crack using interface elements. An eight noded linear interface element was used to model the crack. In order to compare the results with a PoU analysis, we also used 2 integration points with Newton-Cotes/Lobatto and Gauss integration schemes for the interface elements. First a uniform crack opening analysis was performed. The numerically computed displacement jump along the crack surface and traction continuity for increasing load levels is shown in figure A.13. Noting that, the traction continuity plots using Gauss and Newton-Cotes/Lobatto integration schemes were exactly the same. For this reason only results using one of the integration schemes in figure A.13b have been presented. The numerically computed displacement jump across the crack surface and load P_x at the loaded boundary is $3.4182\text{E-}06\text{mm}$ and 398.6327N , respectively. Thus, the analytical solution presented in section A.2 is accurately predicted using interface elements. Moreover, no un-realistic opening of the crack is observed, i.e neither the jump was observed to be curved along the interface nor a displacement jump in the y -direction was observed and consequently

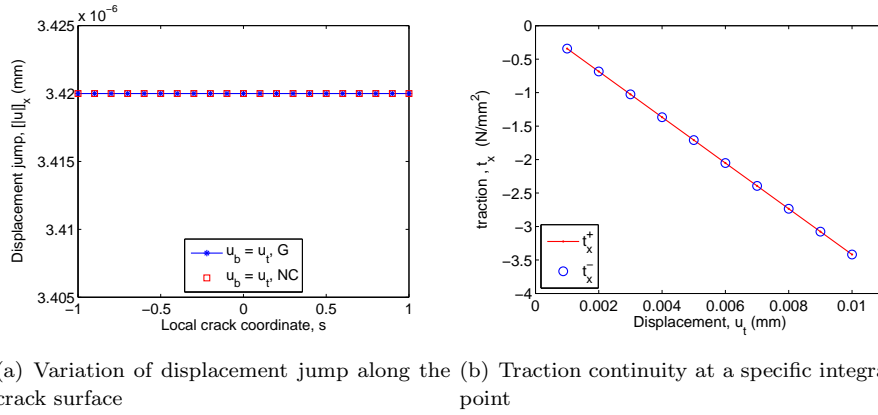


Figure A.13 Analysis results using interface elements, Uniform crack opening

a constant strain, ϵ_{xx} , is observed. Figure A.15a shows the strain field, ϵ_{xx} , over a mesh. The excellent performance of interface elements was due to the fact that

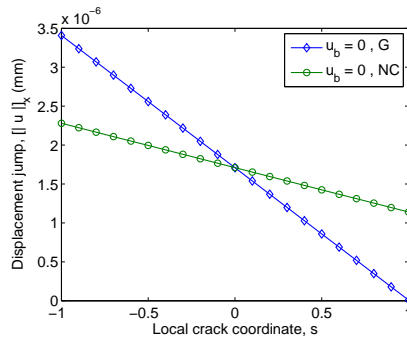


Figure A.14 Variation of displacement jump along the crack surface, Non-uniform crack opening

all kinematic quantities at the interface were evaluated at the nodes defined on the interface in contrast to a PoU cohesive crack, where the kinematics at the interface are approximated using element nodal quantities. Moreover, the displacement jump in interface elements is approximated using the shape functions defined in the local coordinate system of crack or interface elements while in PoU based methods the jump is approximated using the bi-linear shape functions of the element. This has a serious effect regarding the performance of elements as was explained in the previous section.

For the sake of completeness the analysis was also performed with non-uniform prescribed displacements, $u_b = 0$. The displacement jump field along the crack sur-

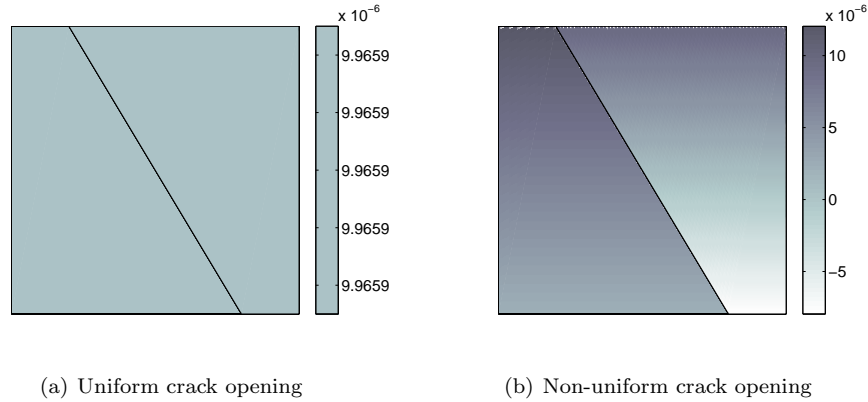


Figure A.15 Strain field, ϵ_{xx}

face is shown in figure A.14. It can also be observed that the displacement jump at $s = 1$ is not zero when Newton-Cotes/Lobatto integration scheme is used in contrast to Gauss integration scheme. However, the effect of integration scheme on cohesive crack modeling is out of scope of this article and is not discussed here. Figure A.15b shows the strain field, ϵ_{xx} over the mesh. The numerically computed end loads are $P_x = 199.3188\text{N}$ and $P_y = 40.7658\text{N}$.

Figure A.16 shows a comparison between the interface element and XFEM/GFEM analysis results for uniform crack opening using Newton-Cotes integration scheme for interface contribution, in a summarized form. The inaccuracy of the numerical results using XFEM/GFEM is evident from the figure.

A.5 Mesh refinement study

In order to investigate mesh sensitivity, the model problem is studied using different mesh discretizations. These are shown in figure A.17, where the position of a crack is shown by a thick line over the mesh. Meshes a-c represent structured meshes with different mesh refinement. Meshes d and e represent a discretization in which the elements crossed by a discontinuity are oriented such that the edges of the elements become parallel to the crack. Note that, orienting the elements in this way forces one of the local axes of the elements to be parallel to the local crack axis, figure A.18. Meshes f-h represents un-structured meshes with different mesh refinement near the crack.

The analysis results are compared with the reference solution and the accuracy of the numerical solution is judged by computing the relative error. The relative error in any quantity q is computed as, $\text{Error}_q = \frac{|q_{num} - q_{ref}|}{|q_{ref}|}$. For the case of uniform crack

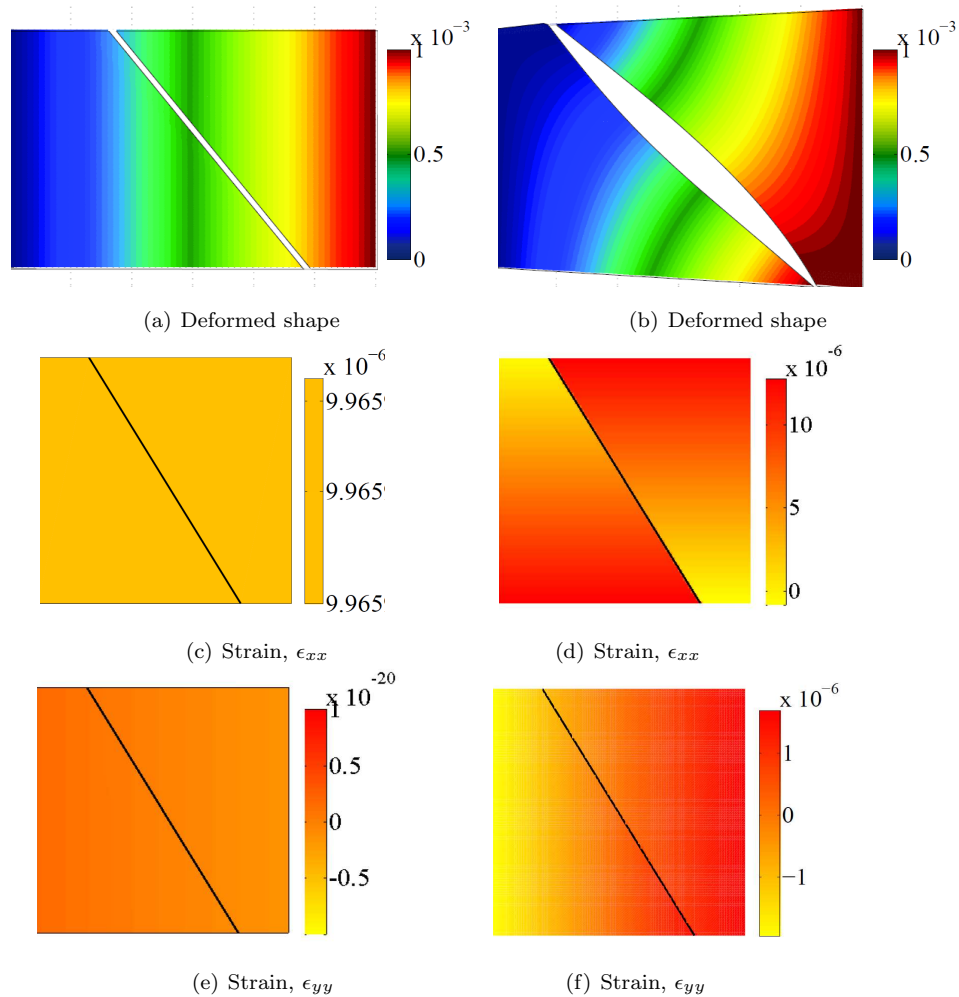


Figure A.16 Comparison between interface element and XFEM/GFEM analyses results; Left: interface element analysis, Right: XFEM/GFEM analysis

opening the analytical solution of the model problem given in section A.2, is used as a reference solution while for the case of non-uniform crack opening the reference solution is obtained from an analysis using interface elements and a very fine mesh for the whole body, to model the in-plane bending of the element accurately.

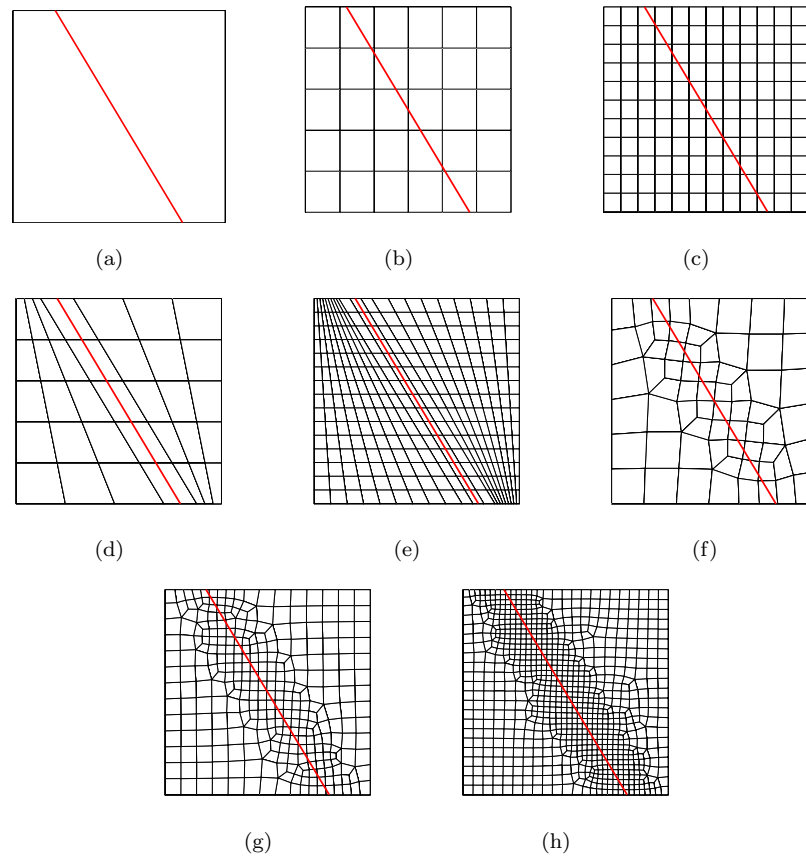


Figure A.17 Different meshes for mesh refinement study

A.5.1 Uniform crack opening

Analysis results using Gauss integration yielded exact results for uniform crack opening, as was observed earlier (section A.2), hence only results obtained using nodal integration scheme are presented here. Figures A.19 and A.20 show a variation of displacement jump components along the crack for various meshes, computed at the integration points, in comparison with reference solution. It is evident from figures A.19a and A.20a that meshes d and e performed well in comparison to all other mesh configurations and their data points almost overlapped the data points of the reference solution. This is not a surprise, as aligning one of the local axes of the element with the local crack axis removed the source of error partially (partially because only one of the local axes of the element is aligned with one of the local crack axes, figure A.18). The bi-linear effect of element shape functions in computing equivalent

nodal jumps and tractions, was considerably reduced and the transmission of jumps to the nodes and hence their contribution to the total element displacements almost consists of rigid body motion.

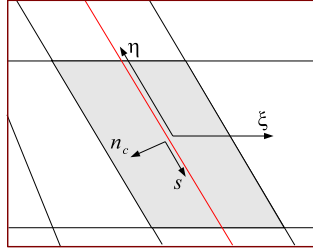


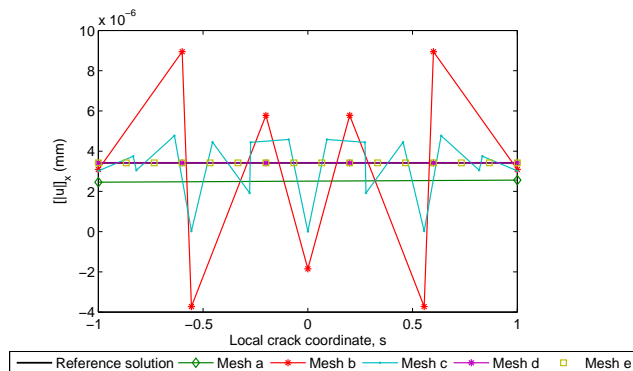
Figure A.18 Zoom at the cracked element - Mesh d

On the other hand, mesh configurations b and c do not give correct approximations to the jump at the interface and show oscillations. One of the reasons is that different elements were cut in different configurations and hence different magnitudes of moment couples contributed to the total element displacements, which may also be sometimes positive and sometimes negative. However, refining the mesh did reduce the error. This is due to the fact that by decreasing the element size, the moment arm of the moment couple forces also decreased, consequently decreasing the magnitude of moment. This ultimately resulted in smaller un-realistic displacements and a closer approximation to the correct solution.

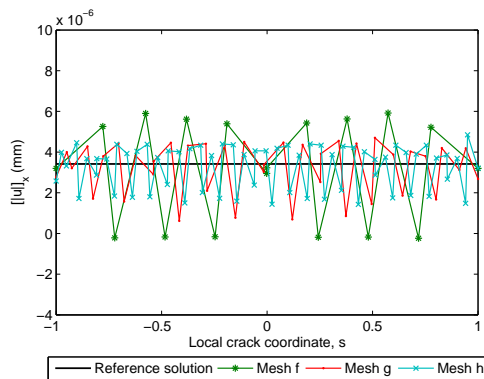
Figures A.19b and A.20b show the results of mesh configurations f, g and h. These mesh configurations also show a similar kind of behavior as was observed with meshes b and c. Thus, it can be concluded that mesh refinement does not solve the problem, however it may help to reduce the error. The observation is also confirmed by table A.1, which represents the relative error in the computed total load at the boundary, where prescribed displacements were applied.

A.5.2 Non-uniform crack opening

A mesh refinement study is also performed with non-uniform prescribed displacements. First analysis results using Newton-Cotes/Lobatto integration scheme are considered. Figures A.21 and A.22 show the variation of displacement jump components along the length of the crack in comparison with the reference solution. Table A.1 gives the error in the computed numerical solution. Similar conclusions as in section A.5.1 can be also drawn here. The approximation of the displacement jump field shows oscillations, however with mesh refinement these oscillations reduce and a good approximation of the correct solution is obtained. A larger error in the P_y



(a)

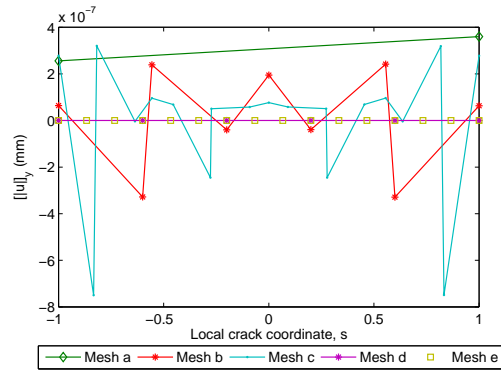


(b)

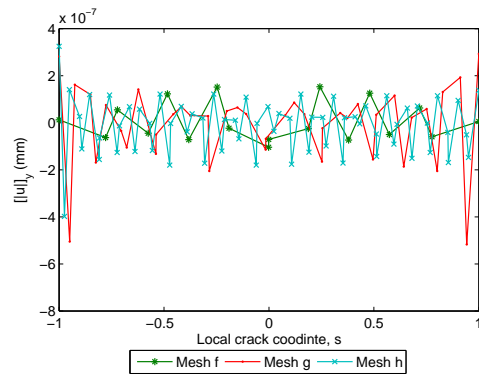
Figure A.19 Analysis results using Newton-Cotes/Lobatto integration scheme; horizontal displacement jump $[[u]]_x$

is due to the fact that the problem at hand involves in-plane bending and mesh refinement is only done near the cracked zone whereas for the reference solution with the interface element analysis, a refined mesh was used for the whole domain, which resulted in a more compliant response. However, this does not make any difference for the general conclusions drawn earlier regarding the error in the approximation of the displacement jump field and the resulting errors in the nodal forces and strain fields, which is subject and main focus of this contribution.

The same analysis is then performed using a Gauss integration scheme for the interface contribution. The analysis results are presented in table A.1 and figures A.23 and A.24. It can be observed that the PoU solution approaches the correct solution as the mesh near the crack becomes finer. Moreover, as was observed earlier,



(a)



(b)

Figure A.20 Analysis results using Newton-Cotes/Lobatto integration scheme; vertical displacement jump $[[u]]_y$

the Gauss integration performed well as compared to the Newton-Cotes/Lobatto integration scheme.

A.6 Conclusions

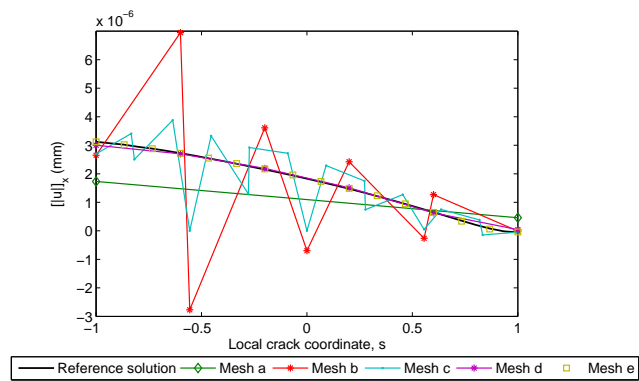
The main aim of this work was to assess the performance of a PoU based finite element for cohesive cracking. More importantly, the effect of using element shape functions for the approximation of the displacement jump field in a finite element analysis is studied. A single element test, modeled with a 4-node quadrilateral element, is used for analysis. The main conclusion of the chapter is that the use of bi-linear element shape functions of a quadrilateral element for the approximation

Table A.1 Error in numerical solution with mesh refinement

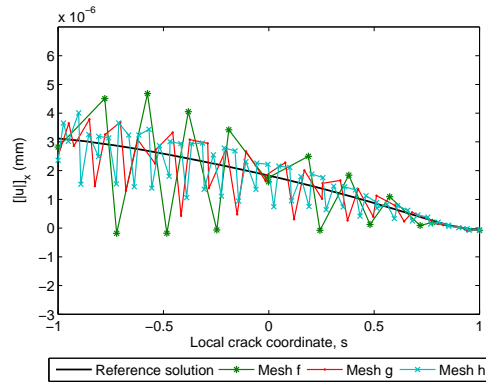
	Uniform crack opening	Non-Uniform crack opening			
	Error $_{P_x}$ NC	Error $_{P_x}$ NC	Error $_{P_y}$ NC	Error $_{P_x}$ G	Error $_{P_y}$ G
Mesh a	2.658E-01	3.608E-01	4.385E-01	1.158E-03	1.889E+00
Mesh b	3.997E-02	4.001E-02	5.908E-01	1.308E-03	5.867E-01
Mesh c	1.885E-02	1.936E-02	2.975E-01	1.118E-03	2.934E-01
Mesh d	1.159E-04	1.268E-03	5.228E-01	1.198E-03	5.228E-01
Mesh e	8.200E-05	1.191E-03	1.633E-01	1.197E-03	1.633E-01
Mesh f	1.814E-02	1.905E-02	4.793E-01	1.348E-03	4.861E-01
Mesh g	6.348E-03	7.710E-03	2.154E-01	1.123E-03	2.178E-01
Mesh h	3.529E-03	4.628E-03	9.560E-02	1.184E-03	9.601E-02

of the displacement jump field in PoU based methods such as XFEM and GFEM, may result in an error in the approximation of the displacement jump field and un-desirable rotation of the interface. This has a severe effect in the sense that it results in un-realistic straining of the element and even for a simple case where the element is subjected to a linear displacement field, the XFEM/GFEM trial solution is incapable of representing the linear function. This ultimately result in incorrect nodal displacements and forces and an inaccurate stress field. However, it was found from a mesh refinement study that although the PoU methods give an error in the approximation of the displacement jump field at element level, the significance of such an error vanishes upon mesh refinement. Similar conclusions also hold for an 8-node linear solid element for modeling 3D cohesive cracking using PoU.

Moreover, a secondary outcome of the analysis also showed that the error in the approximation of the displacement jump is more pronounced in case of Newton-Cotes/Lobatto integration schemes as compared to the Gauss integration scheme, which is because of under-integration of the cohesive stiffness. Nevertheless, there are cases (see e.g [136], [44]) where the former performed better than the latter and it is envisioned that if the Newton Cotes/Lobatto integration scheme is to be used for an interface contribution, mesh refinement near the cohesive zone can help to reduce the error in the numerical solution.

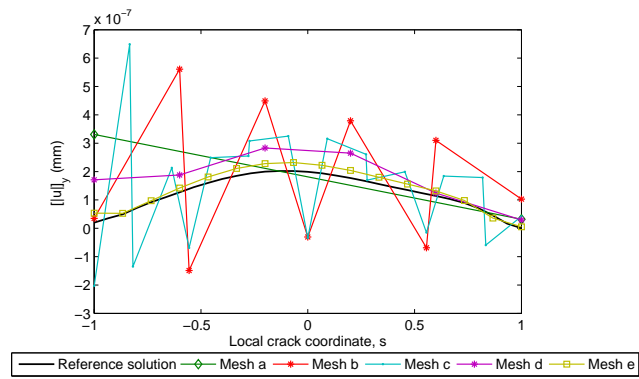


(a)

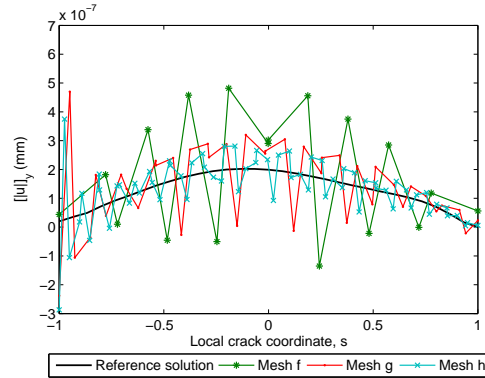


(b)

Figure A.21 Analysis results using Newton-Cotes/Lobatto integration scheme; horizontal displacement jump $[[u]]_x$

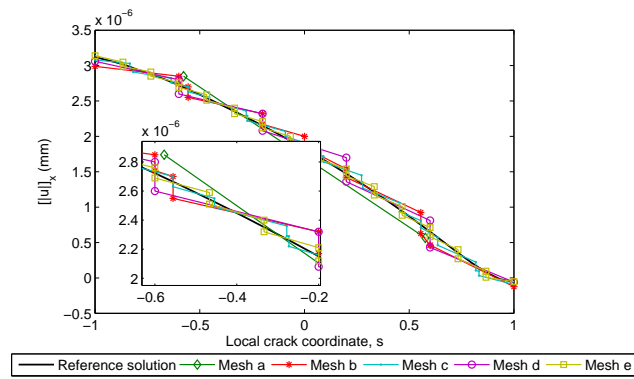


(a)

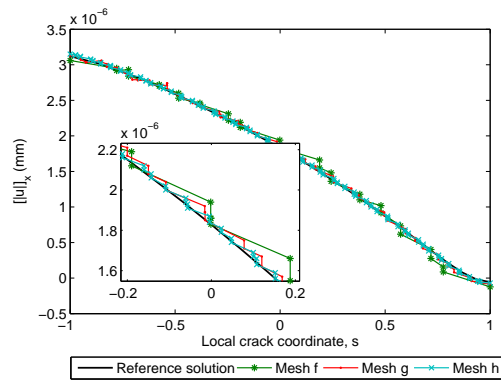


(b)

Figure A.22 Analysis results using Newton-Cotes/Lobatto integration scheme; vertical displacement jump $[[u]]_y$

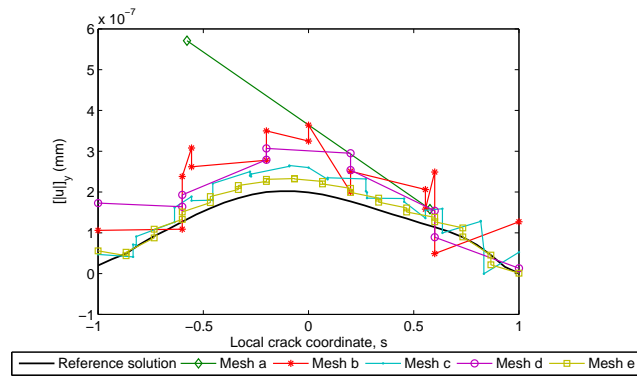


(a)

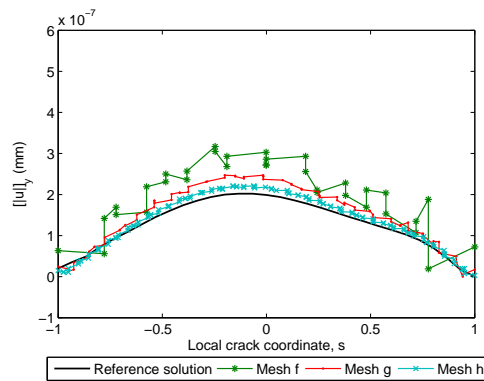


(b)

Figure A.23 Analysis results using Gauss integration scheme; horizontal displacement jump $[[u]]_x$



(a)



(b)

Figure A.24 Analysis results using Gauss integration scheme; vertical displacement jump $[[u]]_y$

Appendix B

Implementation aspects of DSLS

B.1 Transformation matrix

The transformation matrix \mathbb{T}^o is defined as

$$\mathbb{T}^o = \begin{bmatrix} (T_{11}^o)^2 & (T_{12}^o)^2 & (T_{13}^o)^2 & T_{11}^o T_{12}^o & T_{12}^o T_{13}^o & T_{11}^o T_{13}^o \\ (T_{21}^o)^2 & (T_{22}^o)^2 & (T_{23}^o)^2 & T_{21}^o T_{22}^o & T_{22}^o T_{23}^o & T_{21}^o T_{23}^o \\ (T_{31}^o)^2 & (T_{32}^o)^2 & (T_{33}^o)^2 & T_{31}^o T_{32}^o & T_{32}^o T_{33}^o & T_{31}^o T_{33}^o \\ 2T_{11}^o T_{21}^o & 2T_{12}^o T_{22}^o & 2T_{13}^o T_{23}^o & T_{11}^o T_{22}^o + T_{12}^o T_{21}^o & T_{12}^o T_{23}^o + T_{13}^o T_{22}^o & T_{11}^o T_{23}^o + T_{13}^o T_{21}^o \\ 2T_{21}^o T_{31}^o & 2T_{12}^o T_{32}^o & 2T_{23}^o T_{33}^o & T_{21}^o T_{32}^o + T_{22}^o T_{31}^o & T_{22}^o T_{33}^o + T_{23}^o T_{32}^o & T_{21}^o T_{33}^o + T_{23}^o T_{31}^o \\ 2T_{11}^o T_{31}^o & 2T_{12}^o T_{32}^o & 2T_{13}^o T_{33}^o & T_{11}^o T_{32}^o + T_{12}^o T_{31}^o & T_{12}^o T_{33}^o + T_{13}^o T_{32}^o & T_{11}^o T_{33}^o + T_{13}^o T_{31}^o \end{bmatrix} \quad (\text{B.1})$$

The transformation matrices \mathbb{T}^g and \mathbb{T}^{og} are obtained by replacing the components of \mathbb{T}^o in the above matrix with \mathbf{T}^g and $\mathbf{T}^{og} = \mathbf{T}^o \mathbf{T}^g$, respectively.

B.2 Computation of strains and B matrix

B.2.1 Displacement gradients

We arrange the vector of gradients of displacement field as

$$\Theta = \left[\frac{\partial \vartheta_1}{\partial \xi}, \frac{\partial \vartheta_1}{\partial \eta}, \frac{\partial \vartheta_1}{\partial \zeta}, \frac{\partial \vartheta_2}{\partial \xi}, \frac{\partial \vartheta_2}{\partial \eta}, \frac{\partial \vartheta_2}{\partial \zeta}, \frac{\partial \vartheta_3}{\partial \xi}, \frac{\partial \vartheta_3}{\partial \eta}, \frac{\partial \vartheta_3}{\partial \zeta} \right]^T \quad (\text{B.2})$$

The gradients of displacement field and their variations are obtained as

$$\Theta = \tilde{\mathbf{N}} \hat{\vartheta} \quad (\text{B.3})$$

$$\delta \Theta = \tilde{\mathbf{L}} \delta \hat{\vartheta} \quad (\text{B.4})$$

The matrix $\tilde{\mathbf{N}}$ can be split into parts related to regular and internal degrees of freedom according to

$$\tilde{\mathbf{N}} = \begin{bmatrix} \tilde{\mathbf{N}}_u & \tilde{\mathbf{N}}_w \end{bmatrix} \quad (\text{B.5})$$

where the matrices $\tilde{\mathbf{N}}_u$ and $\tilde{\mathbf{N}}_w$ for the node i are given as

$$\tilde{\mathbf{N}}_u^i = \begin{bmatrix} N_{,1}^o + N_{,1}^1 & 0 & 0 \\ N_{,2}^o + N_{,2}^1 & 0 & 0 \\ N^1 & 0 & 0 \\ 0 & N_{,1}^o + N_{,1}^1 & 0 \\ 0 & N_{,2}^o + N_{,2}^1 & 0 \\ 0 & N^1 & 0 \\ 0 & 0 & N_{,1}^o + N_{,1}^1 \\ 0 & 0 & N_{,2}^o + N_{,2}^1 \\ 0 & 0 & N^1 \end{bmatrix}_i, \quad \tilde{\mathbf{N}}_w^i = \begin{bmatrix} 0 \\ 0 \\ -2\zeta d(1)\phi_i \\ 0 \\ 0 \\ -2\zeta d(2)\phi_i \\ 0 \\ 0 \\ -2\zeta d(3)\phi_i \end{bmatrix}$$

The matrix $\tilde{\mathbf{L}}$ is given as

$$\tilde{\mathbf{L}} = \begin{bmatrix} \tilde{\mathbf{N}}_u + \tilde{\mathbf{N}}_{u\omega} & \tilde{\mathbf{N}}_w \end{bmatrix} \quad (\text{B.6})$$

with matrix $\tilde{\mathbf{N}}_{u\omega}$, for node i given as

$$\tilde{\mathbf{N}}_{u\omega}^i = \begin{bmatrix} 0 & 0 & 0 \\ 0 & 0 & 0 \\ -2\zeta\omega N^1 & 0 & 0 \\ 0 & 0 & 0 \\ 0 & 0 & 0 \\ 0 & -2\zeta\omega N^1 & 0 \\ 0 & 0 & 0 \\ 0 & 0 & 0 \\ 0 & 0 & -2\zeta\omega N^1 \end{bmatrix}_i$$

B.2.2 Computation of B matrix

The strain field and its variation are obtained as

$$\mathbf{E} = \left[\mathbf{H} + \frac{1}{2}\mathbf{A}(\Theta) \right] \Theta \quad (\text{B.7})$$

$$\delta\mathbf{E} = [\mathbf{H} + \mathbf{A}(\Theta)] \delta\Theta \quad (\text{B.8})$$

in which the matrices \mathbf{H} and \mathbf{A} are given as

$$\mathbf{H} = \begin{bmatrix} G_1(1) & 0 & 0 & G_1(2) & 0 & 0 & G_1(3) & 0 & 0 \\ 0 & G_2(1) & 0 & 0 & G_2(2) & 0 & 0 & G_2(3) & 0 \\ 0 & 0 & G_3(1) & 0 & 0 & G_3(2) & 0 & 0 & G_3(3) \\ G_2(1) & G_1(1) & 0 & G_2(3) & G_1(2) & 0 & G_2(3) & G_1(3) & 0 \\ 0 & G_3(1) & G_2(1) & 0 & G_3(2) & G_2(2) & 0 & G_3(3) & G_2(3) \\ G_3(1) & 0 & G_1(1) & G_3(2) & 0 & G_1(2) & G_3(3) & 0 & G_1(3) \end{bmatrix}$$

(B.9)

$$\mathbf{A}(\Theta) = \begin{bmatrix} \vartheta_{1,1} & 0 & 0 & \vartheta_{2,1} & 0 & 0 & \vartheta_{3,1} & 0 & 0 \\ 0 & \vartheta_{1,2} & 0 & 0 & \vartheta_{2,2} & 0 & 0 & \vartheta_{3,2} & 0 \\ 0 & 0 & \vartheta_{1,3} & 0 & 0 & \vartheta_{2,3} & 0 & 0 & \vartheta_{3,3} \\ \vartheta_{1,2} & \vartheta_{1,1} & 0 & \vartheta_{2,2} & \vartheta_{2,1} & 0 & \vartheta_{3,2} & \vartheta_{3,1} & 0 \\ 0 & \vartheta_{1,3} & \vartheta_{1,2} & 0 & \vartheta_{2,3} & \vartheta_{2,2} & 0 & \vartheta_{3,3} & \vartheta_{3,2} \\ \vartheta_{1,3} & 0 & \vartheta_{1,1} & \vartheta_{2,3} & 0 & \vartheta_{2,1} & \vartheta_{3,3} & 0 & \vartheta_{3,1} \end{bmatrix} \quad (\text{B.10})$$

substitution of equation (B.4) into equation (B.8) results in

$$\delta \mathbf{E} = (\mathbf{B}_L + \mathbf{B}_{NL}) \delta \hat{\boldsymbol{\vartheta}} = \mathbf{B} \delta \hat{\boldsymbol{\vartheta}} \quad (\text{B.11})$$

in which

$$\mathbf{B}_L = \mathbf{H} \tilde{\mathbf{L}} \quad (\text{B.12})$$

$$\mathbf{B}_{NL} = \mathbf{A} \tilde{\mathbf{L}} \quad (\text{B.13})$$

substitution of equation (B.4) into equation (B.7) results in

$$\mathbf{E} = \boldsymbol{\epsilon}_L + \boldsymbol{\epsilon}_{NL} \quad (\text{B.14})$$

$$\boldsymbol{\epsilon}_L = \mathbf{H} \tilde{\mathbf{N}} \hat{\boldsymbol{\vartheta}} \quad (\text{B.15})$$

$$\boldsymbol{\epsilon}_{NL} = \frac{1}{2} \mathbf{A}(\Theta) \tilde{\mathbf{N}} \hat{\boldsymbol{\vartheta}} \quad (\text{B.16})$$

B.3 Stiffness matrices

B.3.1 Geometric stiffness matrix for the bulk material

The stress tensor obtained from equation (2.70) represents the stress components in element's local coordinate system $\mathbf{l}(l_1, l_2, l_3)$, while the incremental change in virtual strain still refers to the covariant components in the iso-parametric frame of reference. The virtual work is expressed as

$$\mathbf{W} = \boldsymbol{\Sigma} : \delta \mathbf{E} = \Sigma_{ij}^g \delta E_{ij}^g = \Sigma^{ij} \delta E_{ij}$$

It is evident that the work term is the same, regardless of the frame of reference. Hence, we compute the contravariant components of stresses in an iso-parametric frame of reference as

$$\begin{aligned} \Sigma^{oj} &= (\mathbf{G}^{oi} \cdot \mathbf{i}_a)(\mathbf{G}^{oj} \cdot \mathbf{i}_b) \Sigma_{ab}^g \\ \Sigma^{ij} &= (\mathbf{G}^i \cdot \mathbf{G}_a^o)(\mathbf{G}^j \cdot \mathbf{G}_b^o) \Sigma^{oab} \end{aligned}$$

The same can be defined in compact form using the transformation matrix \mathbf{T}^{og} as

$$\boldsymbol{\Sigma} = \mathbf{T}^{ogT} \boldsymbol{\Sigma}^g \mathbf{T}^{og}$$

The geometric stiffness matrix can be written as

$$\mathbf{K}_{geo,int} = \begin{bmatrix} \mathbf{K}_{geo,int}^{uu} & \mathbf{K}_{geo,int}^{u\omega} \\ \mathbf{K}_{geo,int}^{\omega u} & \mathbf{K}_{geo,int}^{\omega\omega} \end{bmatrix} \quad (\text{B.17})$$

where the matrices $\mathbf{K}_{geo,int}^{uu}$, $\mathbf{K}_{geo,int}^{u\omega}$, $\mathbf{K}_{geo,int}^{\omega u}$ and $\mathbf{K}_{geo,int}^{\omega\omega}$ are defined as

$$\begin{aligned} \mathbf{K}_{geo,int}^{uu} &= \Sigma^{11} \left[\mathbf{N}_{,1}^o T \mathbf{N}_{,1}^o + \zeta \left(\mathbf{N}_{,1}^o T \mathbf{N}_{,1}^1 + \mathbf{N}_{,1}^1 T \mathbf{N}_{,1}^o \right) + \zeta^2 \left(\mathbf{N}_{,1}^1 T \mathbf{N}_{,1}^1 \right) \right] \\ &+ \Sigma^{22} \left[\mathbf{N}_{,2}^o T \mathbf{N}_{,2}^o + \zeta \left(\mathbf{N}_{,2}^o T \mathbf{N}_{,2}^1 + \mathbf{N}_{,2}^1 T \mathbf{N}_{,2}^o \right) + \zeta^2 \left(\mathbf{N}_{,2}^1 T \mathbf{N}_{,2}^1 \right) \right] \\ &+ \Sigma^{33} \left[\mathbf{N}^1 T \mathbf{N}^1 - 4\zeta\omega \mathbf{N}^1 T \mathbf{N}^1 + 4\zeta^2\omega^2 \mathbf{N}^1 T \mathbf{N}^1 \right] \\ &+ \Sigma^{12} \left[\mathbf{N}_{,1}^o T \mathbf{N}_{,2}^o + \mathbf{N}_{,2}^o T \mathbf{N}_{,1}^o + \zeta \left(\mathbf{N}_{,1}^o T \mathbf{N}_{,2}^1 + \mathbf{N}_{,2}^1 T \mathbf{N}_{,1}^o + \mathbf{N}_{,1}^1 T \mathbf{N}_{,2}^o + \mathbf{N}_{,2}^o T \mathbf{N}_{,1}^1 \right) + \right. \\ &\quad \left. \zeta^2 \left(\mathbf{N}_{,1}^1 T \mathbf{N}_{,2}^1 + \mathbf{N}_{,2}^1 T \mathbf{N}_{,1}^1 \right) \right] \\ &+ \Sigma^{13} \left[\mathbf{N}^1 T \mathbf{N}_{,1}^o + \mathbf{N}_{,1}^o T \mathbf{N}^1 + \zeta \left(\mathbf{N}_{,1}^1 T \mathbf{N}^1 + \mathbf{N}^1 T \mathbf{N}_{,1}^1 \right) - 2\zeta\omega \left(\mathbf{N}_{,1}^o T \mathbf{N}^1 + \mathbf{N}^1 T \mathbf{N}_{,1}^o \right) - \right. \\ &\quad \left. 2\zeta^2\omega \left(\mathbf{N}_{,1}^1 T \mathbf{N}^1 + \mathbf{N}^1 T \mathbf{N}_{,1}^1 \right) \right] \\ &+ \Sigma^{23} \left[\mathbf{N}^1 T \mathbf{N}_{,2}^o + \mathbf{N}_{,2}^o T \mathbf{N}^1 + \zeta \left(\mathbf{N}_{,2}^1 T \mathbf{N}^1 + \mathbf{N}^1 T \mathbf{N}_{,2}^1 \right) - 2\zeta\omega \left(\mathbf{N}_{,2}^o T \mathbf{N}^1 + \mathbf{N}^1 T \mathbf{N}_{,2}^o \right) - \right. \\ &\quad \left. 2\zeta^2\omega \left(\mathbf{N}_{,2}^1 T \mathbf{N}^1 + \mathbf{N}^1 T \mathbf{N}_{,2}^1 \right) \right] \\ \mathbf{K}_{geo,int}^{u\omega} &= \Sigma^{13} \left[2\zeta \mathbf{N}_{,1}^o T \mathbf{d} \mathbf{N}^\omega + 2\zeta^2 \mathbf{N}_{,1}^1 T \mathbf{d} \mathbf{N}^\omega - 2\zeta \left(\mathbf{G}_1 + \mathbf{u}_{,1}^o + \zeta \mathbf{u}_{,1}^1 \right) \mathbf{N}^1 T \mathbf{N}^\omega \right] \\ &+ \Sigma^{23} \left[2\zeta \mathbf{N}_{,2}^o T \mathbf{d} \mathbf{N}^\omega + 2\zeta^2 \mathbf{N}_{,2}^1 T \mathbf{d} \mathbf{N}^\omega - 2\zeta \left(\mathbf{G}_2 + \mathbf{u}_{,2}^o + \zeta \mathbf{u}_{,2}^1 \right) \mathbf{N}^1 T \mathbf{N}^\omega \right] \\ &+ \Sigma^{33} \left[-4\zeta \left(\mathbf{N}^1 T \mathbf{d} \mathbf{N}^\omega - 2\zeta \mathbf{N}^1 T \mathbf{u}^2 \mathbf{N}^\omega \right) \right] \\ \mathbf{K}_{geo,int}^{\omega u} &= \Sigma^{13} \left[2\zeta \mathbf{N}^\omega T \mathbf{d}^T \mathbf{N}_{,1}^o + 2\zeta^2 \mathbf{N}^\omega T \mathbf{d}^T \mathbf{N}_{,1}^1 - 2\zeta \left(\mathbf{G}_1 + \mathbf{u}_{,1}^o + \zeta \mathbf{u}_{,1}^1 \right) \mathbf{N}^\omega T \mathbf{N}^1 \right] \\ &+ \Sigma^{23} \left[2\zeta \mathbf{N}^\omega T \mathbf{d}^T \mathbf{N}_{,2}^o + 2\zeta^2 \mathbf{N}^\omega T \mathbf{d}^T \mathbf{N}_{,2}^1 - 2\zeta \left(\mathbf{G}_2 + \mathbf{u}_{,2}^o + \zeta \mathbf{u}_{,2}^1 \right) \mathbf{N}^\omega T \mathbf{N}^1 \right] \\ &+ \Sigma^{33} \left[-4\zeta \left(\mathbf{N}^\omega T \mathbf{d}^T \mathbf{N}^1 - 2\zeta \mathbf{N}^\omega T \mathbf{u}^2 T \mathbf{N}^1 \right) \right] \\ \mathbf{K}_{geo,int}^{\omega\omega} &= \Sigma^{33} \left[4\zeta^2 \left(\mathbf{d}^T \mathbf{d} \right) \mathbf{N}^\omega T \mathbf{N}^\omega \right] \end{aligned}$$

B.3.2 Cohesive stiffness matrix

In order to evaluate the stiffness contribution from the cohesive tractions, we follow [54]. In equation (2.75), the stiffness contribution is coming from two parts (a) $d\mathbf{t}_c \lambda_a$ and (b) $\mathbf{t}_c d\lambda_a$.

(i) Linearization of Part a

Using equation (2.77), we obtain the following two stiffness contributions

$$\mathbf{K}_{geo-1,coh}^{IJ} = \int_{\Omega_m} \mathbf{N}^I \mathbf{C}_n \mathbf{P}^J \lambda_a \quad (\text{B.18})$$

$$\mathbf{K}_{mat,coh}^{IJ} = \int_{\Omega_m} \mathbf{N}^I \mathbf{C}_{[\mathbf{u}]} \mathbf{N}^J \lambda_a \quad (\text{B.19})$$

in which

$$\mathbf{P}^J = \left(\mathbf{n}_i \frac{\partial \mathbf{N}^J}{\partial \bar{\mathbf{x}}_k} \mathbf{n}_k - \frac{\partial \mathbf{N}^J}{\partial \bar{\mathbf{x}}_i} \right) \mathbf{n}_j \quad (\text{B.20})$$

(ii) Linearization of Part b

Using equation (2.78), we obtain

$$\mathbf{K}_{geo-2,coh}^{IJ} = \int_{\Omega_m} \mathbf{N}^I \mathbf{t}(\mathbf{q}^J)^T \lambda_a \quad (\text{B.21})$$

in which

$$\mathbf{q}^J = - \left(\mathbf{n}_i \frac{\partial \mathbf{N}^J}{\partial \bar{\mathbf{x}}_k} \mathbf{n}_k - \frac{\partial \mathbf{N}^J}{\partial \bar{\mathbf{x}}_i} \right) \quad (\text{B.22})$$

The cohesive tangent matrix is now defined as

$$\mathbf{K}_{coh_{mn}} = \mathbf{K}_{mat,coh_{mn}} + \mathbf{K}_{geo,coh_{mn}} = \begin{bmatrix} \mathbf{K}_{coh_{AA}} & \mathbf{K}_{coh_{AB}} \\ \mathbf{K}_{coh_{BA}} & \mathbf{K}_{coh_{BB}} \end{bmatrix} \quad (\text{B.23})$$

where

$$\mathbf{K}_{geo-1,coh_{mn}}^{IJ} = \beta_m \int_{\Omega_m} \mathbf{N}_m^I \mathbf{C}_n \mathbf{P}_n^J \lambda_a \quad (\text{B.24a})$$

$$\mathbf{K}_{geo-2,coh_{mn}}^{IJ} = \beta_m \int_{\Omega_m} \mathbf{N}_m^I \mathbf{t}(\mathbf{q}_n^J)^T \lambda_a \quad (\text{B.24b})$$

$$\mathbf{K}_{geo,coh_{mn}}^{IJ} = \mathbf{K}_{geo-1,coh_{mn}}^{IJ} + \mathbf{K}_{geo-2,coh_{mn}}^{IJ} \quad (\text{B.24c})$$

$$\mathbf{K}_{mat,coh_{mn}}^{IJ} = \beta_m \int_{\Omega_m} \mathbf{N}_m^I \mathbf{C}_{[\mathbf{u}]} \mathbf{N}_n^J \lambda_a \quad (\text{B.24d})$$

with

$$m, n = A, B$$

and

$$\beta_m = \left\{ \begin{array}{ll} -1 & \text{for } m = A \\ +1 & \text{for } m = B \end{array} \right\}$$

Appendix C

Mass matrix for solid-like shell element

C.1 Discretized inertial virtual work

Inertial virtual work is given by

$$\mathcal{L}^{inert} = \int_{\Omega^o} \delta \boldsymbol{\vartheta} \cdot \rho \ddot{\boldsymbol{\vartheta}} \quad (\text{C.1})$$

Incorporating the discretizations of $\ddot{\boldsymbol{\vartheta}}$ and $\delta \boldsymbol{\vartheta}$ using equations (4.6), (4.11), (4.17) and (4.20), it yields

$$\begin{aligned} \mathcal{L}^{inert} &= \delta \hat{\boldsymbol{\vartheta}} \underbrace{\int_{\Omega^o} \mathbf{N}^T \rho \{ \mathbf{N}^{oT} \hat{\mathbf{U}} + \zeta \mathbf{N}^{1T} \hat{\mathbf{U}} + (1 - \zeta^2) (\mathbf{N}^{\omega T} \hat{\mathbf{W}} \mathbf{d} + \omega \mathbf{N}^{1T} \hat{\mathbf{U}}) \}}_{f_{inert}} \\ &+ \delta \hat{\boldsymbol{\vartheta}} \underbrace{\int_{\Omega^o} \mathbf{N}^T \rho \{ 2(1 - \zeta^2) \dot{\omega} \mathbf{d} \}}_{f_{conv}} \end{aligned} \quad (\text{C.2})$$

To obtain a discretized variational mass matrix, the term \mathbf{f}_{inert} of equation (C.2) will be used in further derivations and can be written in an extended form as

$$\begin{aligned} \mathbf{f}_{inert} &= \int_{\Omega^o} \mathbf{N}^T \rho \mathbf{N}^{oT} \hat{\mathbf{U}} + \int_{\Omega^o} \zeta \mathbf{N}^T \rho \mathbf{N}^{1T} \hat{\mathbf{U}} + \int_{\Omega^o} (1 - \zeta^2) \omega \mathbf{N}^T \rho \mathbf{N}^{1T} \hat{\mathbf{U}} \\ &+ \int_{\Omega^o} (1 - \zeta^2) \mathbf{d} \mathbf{N}^T \rho \mathbf{N}^{\omega T} \hat{\mathbf{W}} \end{aligned} \quad (\text{C.3})$$

Using the definition of matrix \mathbf{N} given in equation (4.21), the above equation (C.3) can be written in matrix form as

$$\begin{aligned} [\mathbf{f}_{inert}] &= \int_{\Omega^o} \begin{bmatrix} \mathbf{M}^o + \zeta \mathbf{M}^{1o} + (1 - \zeta^2) \omega \mathbf{M}^{1o} & (1 - \zeta^2) \mathbf{d} \mathbf{M}^{\omega o} \end{bmatrix}^T \begin{bmatrix} \hat{\mathbf{U}} \\ \hat{\mathbf{U}} \end{bmatrix} \\ &+ \int_{\Omega^o} \zeta \begin{bmatrix} \mathbf{M}^{o1} + \zeta \mathbf{M}^1 + (1 - \zeta^2) \omega \mathbf{M}^1 & (1 - \zeta^2) \mathbf{d} \mathbf{M}^{\omega 1} \end{bmatrix}^T \begin{bmatrix} \hat{\mathbf{U}} \\ \hat{\mathbf{U}} \end{bmatrix} \\ &+ \int_{\Omega^o} (1 - \zeta^2) \omega \begin{bmatrix} \mathbf{M}^{o1} + \zeta \mathbf{M}^1 + (1 - \zeta^2) \omega \mathbf{M}^1 & (1 - \zeta^2) \mathbf{d} \mathbf{M}^{\omega 1} \end{bmatrix}^T \begin{bmatrix} \hat{\mathbf{U}} \\ \hat{\mathbf{U}} \end{bmatrix} \\ &+ \int_{\Omega^o} (1 - \zeta^2) \mathbf{d} \begin{bmatrix} \mathbf{M}^{o\omega} + \zeta \mathbf{M}^{1\omega} + (1 - \zeta^2) \omega \mathbf{M}^{1\omega} & (1 - \zeta^2) \mathbf{d} \mathbf{M}^{\omega} \end{bmatrix}^T \begin{bmatrix} \hat{\mathbf{U}} \\ \hat{\mathbf{W}} \end{bmatrix} \end{aligned} \quad (\text{C.4})$$

in which

$$\begin{aligned} \mathbf{M}^o &= \mathbf{N}^{oT} \rho \mathbf{N}^o, & \mathbf{M}^{o1} &= \mathbf{N}^{oT} \rho \mathbf{N}^1, & \mathbf{M}^{o\omega} &= \mathbf{N}^{oT} \rho \mathbf{N}^\omega \\ \mathbf{M}^1 &= \mathbf{N}^{1T} \rho \mathbf{N}^1, & \mathbf{M}^{1o} &= \mathbf{M}^{o1T}, & \mathbf{M}^{1\omega} &= \mathbf{N}^{1T} \rho \mathbf{N}^\omega \\ \mathbf{M}^\omega &= \mathbf{N}^{\omega T} \rho \mathbf{N}^\omega, & \mathbf{M}^{\omega o} &= \mathbf{M}^{o\omega T}, & \mathbf{M}^{\omega 1} &= \mathbf{M}^{1\omega T} \end{aligned}$$

The consistent mass matrix can be obtained from equation (C.4) and is given as

$$\mathbf{M} = \begin{bmatrix} \mathbf{M}^{uu} & \mathbf{M}^{u\omega} \\ \mathbf{M}^{\omega u} & \mathbf{M}^{\omega\omega} \end{bmatrix} \quad (\text{C.5})$$

in which

$$\begin{aligned} \mathbf{M}^{uu} &= \int_{\Omega^o} \mathbf{M}^o + \zeta \mathbf{M}^{1o} + (1 - \zeta^2) \omega \mathbf{M}^{1o} \\ &+ \int_{\Omega^o} (\mathbf{M}^{o1} + \zeta \mathbf{M}^1 + (1 - \zeta^2) \omega \mathbf{M}^1) \zeta \\ &+ \int_{\Omega^o} (\mathbf{M}^{o1} + \zeta \mathbf{M}^1 + (1 - \zeta^2) \omega \mathbf{M}^1) (1 - \zeta^2) \omega \end{aligned} \quad (\text{C.6a})$$

$$\mathbf{M}^{u\omega} = \int_{\Omega^o} (\mathbf{M}^{o\omega} + \zeta \mathbf{M}^{1\omega} + (1 - \zeta^2) \omega \mathbf{M}^{1\omega}) (1 - \zeta^2) \mathbf{d} \quad (\text{C.6b})$$

$$\mathbf{M}^{\omega u} = \int_{\Omega^o} (\mathbf{M}^{\omega o} + \zeta \mathbf{M}^{\omega 1} + (1 - \zeta^2) \omega \mathbf{M}^{\omega 1}) (1 - \zeta^2) \mathbf{d} \quad (\text{C.6c})$$

$$\mathbf{M}^{\omega\omega} = \int_{\Omega^o} (1 - \zeta^2)^2 \mathbf{d}^2 \mathbf{M}^\omega \quad (\text{C.6d})$$

Appendix D

Properties of dirac-delta function

Consider a function $p(x, \epsilon)$ defined by

$$p(x, \epsilon) = \begin{cases} 0 & \text{for } |x| > \epsilon/2 \\ 1/\epsilon & \text{for } |x| < \epsilon/2 \end{cases} \quad (\text{D.1})$$

The function $p(x, \epsilon)$ can be considered as a Dirac delta function $\delta(x)$ in the limit $\epsilon \rightarrow 0$. Then the following property holds

$$\int_{-\infty}^{\infty} f(x)\delta_a(x)dx = \lim_{\epsilon \rightarrow 0} \int_{-\infty}^{\infty} f(x)p(x, \epsilon)dx = f(a) \quad (\text{D.2})$$

in which $\delta_a(x)$ is centered at $x = a$ and f is a continuous function. For three-dimensional case, we have

$$\int_{\Omega} f(x)\delta_{\Gamma_a}(x)d\Omega = \lim_{\epsilon \rightarrow 0} \int_{\Omega} f(x)p(x, \epsilon)d\Omega = \int_{\Gamma_a} f(a)d\Gamma \quad (\text{D.3})$$

References

- [1] S. Ahmad, B. M. Irons, and O. C. Zienkiewicz. Analysis of thick and thin shell structures by curved finite elements. *International Journal for Numerical Methods in Engineering*, 2:419–451, 1970.
- [2] A. Ahmed and L. J. Sluys. A computational model for prediction of progressive damage in laminated composites. In *Proceedings of 15th European Conference on Composite Materials (ECCM 2012)*, Venice, Italy. Pen drive, 2012.
- [3] A. Ahmed and L. J. Sluys. Anomalous behavior of bilinear quadrilateral finite elements for modeling cohesive cracks with xfem/gfem. *International Journal for Numerical Methods in Engineering*, 94:454–472, 2013.
- [4] A. Ahmed and L. J. Sluys. A numerical investigation on interacting damage mechanisms in frp laminated composite plates. *HERON*, 54:61–84, 2013.
- [5] A. Ahmed and L. J. Sluys. A three-dimensional progressive failure model for laminated composite plates subjected to transverse loading. *Engineering Fracture Mechanics*, 114:69–91, 2013.
- [6] A. Ahmed and L. J. Sluys. A computational model for the simulation of dynamic fracture in laminated composite plates. *Journal of Composite Materials*, 2014. DOI: 10.1177/0021998314539777.
- [7] A. Ahmed and L. J. Sluys. Computational modeling of impact damage in laminated composite plates. In *Proceedings of 16th European Conference on Composite Materials (ECCM 2014)*, Seville, Spain. Pen drive, 2014.
- [8] A. Ahmed and L. J. Sluys. Implicit/explicit elastodynamics of isotropic and anisotropic plates and shells using a solid-like shell element. *European Journal of Mechanics - A/Solids*, 43:118–132, 2014.
- [9] A. Ahmed and L. J. Sluys. A phantom node formulation for modeling coupled adiabatic-isothermal cracking in frp composites. *Computer Methods in Applied Mechanics and Engineering*, 278:291–313, 2014.
- [10] A. Ahmed, F. P. van der Meer, and L. J. Sluys. A geometrically nonlinear discontinuous solid-like shell element (dsls) for thin shell structures. *Computer Methods in Applied Mechanics and Engineering*, 201-204:191–207, 2012.
- [11] H. U. Akay. Dynamic large deflection analysis of plates using mixed finite element. *Computers & Structures*, 11:1–11, 1980.
- [12] G. Alfano and E. Sacco. Combining interface damage and friction in a cohesive-zone model. *International Journal for Numerical Methods in Engineering*, 68:542–582, 2006.
- [13] O. Allix and P. Ladeveze. Interlaminar interface modelling for the prediction of delamination. *Composite Structures*, 22:235–242, 1992.

-
- [14] U. Andelfinger and E. Ramm. EAS-elements for two dimensional, three dimensional, plate and shell structures and their equivalence to hr elements. *International Journal for Numerical Methods in Engineering*, 36:1311–1337, 1993.
- [15] R. A. Arciniega and J. N. Reddy. Tensor-based finite element formulation for geometrically nonlinear analysis of shell structures. *Computer Methods in Applied Mechanics and Engineering*, 196:1048–1073, 2007.
- [16] P. M. A. Areias, J. H. Song, and T. Belytschko. Analysis of fracture in thin shells by overlapping paired elements. *Computer Methods in Applied Mechanics and Engineering*, 194:2619–2640, 2005.
- [17] P. M. A. Areias, J. H. Song, and T. Belytschko. A finite-strain quadrilateral shell element based on discrete kirchhoff-love constraints. *International Journal for Numerical Methods in Engineering*, 64:1166–1206, 2005.
- [18] L. E. Asp, A. Sjogrem, and E. S. Greenhalgh. Delamination growth and thresholds in a carbon/epoxy composite under fatigue loading. *Journal of Composites Technology and Research*, 23:55–68, 2001.
- [19] C. Atkinson and J. D. Eshelby. The flow of energy into the tip of a moving crack. *International Journal of Fracture*, 4:3–8, 1968.
- [20] H. Baaser and D. Gross. Damage and strain localisation during crack propagation in thin-walled shells. *J. Phys. IV France*, 8:13–14, 1998.
- [21] H. Baaser and D. Gross. Crack analysis in ductile cylindrical shells using gurson’s model. *International Journal of Solids and Structures*, 37:7093–7104, 2000.
- [22] C. Balzani and W. Wagner. An interface element for the simulation of delamination in unidirectional fiber-reinforced laminates. *Engineering Fracture Mechanics*, 75:2597–2615, 2008.
- [23] K. J. Bathe, E. Ramm, and E. L. Wilson. Finite element formulation for large deformation dynamic analysis. *International Journal for Numerical Methods in Engineering*, 9:353–386, 1975.
- [24] T. Belytschko and T. Black. Elastic crack growth in finite elements with minimal remeshing. *International Journal for Numerical Methods in Engineering*, 45:601–620, 1999.
- [25] T. Belytschko, J. I. Lin, and C. Tsay. Explicit algorithms for the nonlinear dynamics of shells. *Computer Methods in Applied Mechanics and Engineering*, 42:225–251, 1984.
- [26] M. L. Benzeggagh and M. Kenane. Measurement of mixed-mode delamination fracture toughness of unidirectional glass/epoxy composites with mixed mode bending apparatus. *Composites Science and Technology*, 56:439–449, 1996.
- [27] M. Bischoff and E. Ramm. Shear deformable shell elements for large strains and rotations. *International Journal for Numerical Methods in Engineering*, 40:4427–4449, 1997.
- [28] T. W. Bjerke and J. Lambros. Theoretical development and experimental validation of a thermally dissipative cohesive zone model for dynamic fracture of amorphous polymers. *Journal of Mechanics and Physics of Solids*, 51:1147–1170, 2003.

-
- [29] B. R. K. Blackman, J. P. Dear, A. J. Kinloch, H. Macgillivray, Y. Wang, J. G. Williams, and P. Yayla. The failure of fibre composites and adhesively bonded fibre composites under high rates of test: Part-i: Mode I loading - experimental studies. *Journal of Materials Science*, 30:5885–5900, 1995.
- [30] C. Bouvet, B. Castanie, M. Bizeul, and J. J. Barrau. Low velocity impact modelling in laminate composite panels with discrete interface elements. *International Journal of Solids and Structures*, 46:2809–2821, 2009.
- [31] G. T. Camacho and M. Ortiz. Computational modelling of impact damage in brittle materials. *International Journal of Solids and Structures*, 33:2899–2938, 1996.
- [32] P. P. Camanho, C. G. Davila, and M. F. de Moura. Mixed-mode progressive delamination in composite materials. *Journal of Composite Materials*, 37:1415–1438, 2003.
- [33] W. J. Cantwell and J. Worton. Comparison of the low and high velocity impact responses of CFRP. 20:545–551, 1989.
- [34] R. P. R. Cardoso and J. W. Yoon. One point quadrature shell elements for sheet metal forming analysis. *Archives of Computational Methods in Engineering*, 12:3–66, 2005.
- [35] C. Y. Chia. *Nonlinear analysis of plates*. McGraw-Hill, NY, 1980.
- [36] H. Y. Choi and F. Chang. A model for predicting damage in graphite/epoxy laminated composites resulting from low velocity point impact. *Journal of Composite Materials*, 26:2134–2169, 1992.
- [37] H. Y. Choi, R. J. Downs, and F. Chang. A new approach toward understanding damage mechanisms and mechanics of laminated composite due to low velocity impact: Part I: Experiment. *Journal of Composite Materials*, 25:992–1011, 1991.
- [38] H. Y. Choi, H. T. Wu, and F. Chang. A new approach toward understanding damage mechanisms and mechanics of laminated composite due to low velocity impact: part II – analysis. *Journal of Composite Materials*, 25:1012–1038, 1991.
- [39] F. Cirak, M. Ortiz, and A. Pandolfi. A cohesive approach to thin shell fracture and fragmentation. *Computer Methods in Applied Mechanics and Engineering*, 194:2604–2618, 2005.
- [40] D. Coker and A. J. Rosakis. Experimental observations of intersonic crack growth in asymmetrically loaded unidirectional composite plates. *Philosophical Magazine A*, 81:571–595, 2001.
- [41] D. Coker, A. J. Rosakis, and A. Needleman. Dynamic crack growth along a polymer composite-homalite interface. *Journal of Mechanics and Physics of Solids*, 51:425–460, 2003.
- [42] F. Collombet, J. Bonni, and J. L. Lataillade. A three dimensional modelling of low velocity impact damage in composite laminates. *International Journal for Numerical Methods in Engineering*, 39:1491–1516, 1996.
- [43] A. D. Curson, D. C. Leach, and D. R. Moore. Impact failure mechanisms in carbon fibre/peek composites. *Journal of Thermoplastic Composite Materials*, 3:24–31, 1990.
- [44] D. Dias da Costa, J. Alfaiate, L. J. Sluys, and E. Julio. A comparative study on the modelling of discontinuous fracture by means of enriched nodal and element techniques and interface elements. *International Journal of Fracture*, 161:97–119, 2010.

-
- [45] I. M. Daniel and O. Ishai. *Engineering mechanics of composite materials*. Oxford University Press, Inc., 1994.
- [46] R. de Borst. Numerical aspects of cohesive-zone models. *Engineering Fracture Mechanics*, 70:17431757, 2003.
- [47] M. F. S. F. de Moura and J. P. M. Goncalves. Modelling the interaction between matrix cracking and delamination in carbon-epoxy laminates under low velocity impact. *Composites Science and Technology*, 64:1021–1027, 2004.
- [48] M. V. Donadon, L. Iannucci, B. G. Falzon, J. M. Hodgkinson, and S. F. M. de Almeida. A progressive failure model for composite laminates subjected to low velocity impact damage. *Composite Structures*, 86:1232–1252, 2008.
- [49] M. Dufloot. The extended finite element method in thermoelastic fracture mechanics. *International Journal for Numerical Methods in Engineering*, 74:827–847, 2008.
- [50] E. N. Dvorkin and K. J. Bathe. A continuum mechanics based four node shell elements for general nonlinear analysis. *Engineering Computations*, 1:77–88, 1984.
- [51] M. Fagerstrom and R. Larsson. A thermo-mechanical cohesive zone formulation for ductile fracture. *Journal of Mechanics and Physics of Solids*, 56:3037–3058, 2008.
- [52] L. B. Freund. Crack propagation in an elastic solid subjected to general loading: I: Constant rate of extension. *Journal of Mechanics and Physics of Solids*, 20:129–140, 1972.
- [53] L. B. Freund. Crack propagation in an elastic solid subjected to general loading: I: Stress wave loading. *Journal of Mechanics and Physics of Solids*, 21:47–61, 1973.
- [54] T. C. Gasser and G. A. Holzapfel. Geometrically non-linear and consistently linearized embedded strong discontinuity models for 3d problems with an application to the dissection analysis of soft biological tissues. *Computer Methods in Applied Mechanics and Engineering*, 192:5059–5098, 2003.
- [55] A. S. Gullerud, R. H. Dodds, R. W. Hampton, and D. S. Dawicke. Three-dimensional modeling of ductile crack growth in thin sheet metals: computational aspects and validation. *Engineering Fracture Mechanics*, 63:347–374, 1999.
- [56] A. L. Gurson. Continuum theory of ductile rupture by void nucleation and growth: Part I—yield criteria and flow rules for porous ductile media. *Journal of Engineering Materials and Technology*, 99:2–15, 1977.
- [57] M. E. Gurtin. Thermodynamics and the cohesive zone in fracture. *Zeitschrift für Angewandte Mathematik und Physik*, 30:991–1003, 1979.
- [58] A. Hansbo and P. Hansbo. A finite element method for the simulation of strong and weak discontinuities in solid mechanics. *Computer Methods in Applied Mechanics and Engineering*, 193:3523–3540, 2004.
- [59] P. W. Harper and S. R. Hallet. Cohesive zone length in numerical simulations of composite delamination. *Engineering Fracture Mechanics*, 75:4774–4792, 2008.
- [60] F. Hashagen, R. de Borst, and T. de Vries. Delamination behavior of spliced fiber metal laminates. part 2. numerical investigation. *Composite Structures*, 46:141–162, 1999.

-
- [61] F. Hashagen, J.C.J. Schellekens, R. de Borst, and H. Parisch. Finite element procedure for modelling fibre metal laminates. *Composite Structures*, 32:255–264, 1995.
- [62] A. Hattiangadi and T. Siegmund. A thermomechanical cohesive zone model for bridged delamination cracks. *Journal of Mechanics and Physics of Solids*, 52:533–566, 2004.
- [63] A. Hattiangadi and T. Siegmund. A numerical study on interface crack growth under heat flux loading. *International Journal of Solids and Structures*, 42:6335–6354, 2005.
- [64] R. Hauptmann and K. Schweizerhof. A systematic development of solid shell element formulations for linear and nonlinear analysis employing only displacement degrees of freedom. *International Journal for Numerical Methods in Engineering*, 42:49–69, 1998.
- [65] T. S. Hille, A. S. J. Suiker, and S. Turteltaub. Microcrack nucleation in thermal barrier coating systems. *Engineering Fracture Mechanics*, 76:813–825, 2009.
- [66] E. Hinton. The dynamic transient analysis of axisymmetric circular plates by the finite element method. *Journal of Sound and Vibration*, 46:465–472, 1976.
- [67] J. P. Hou, N. Petrinic, C. Ruiz, and S. R. Hallet. Prediction of impact damage in composite plates. *Composites Science and Technology*, 60:273–281, 2000.
- [68] T. J. R. Hughes, M. Cohen, and M. Haroun. Reduced and selective integration techniques in the finite element analysis of plates. *Nuclear Engineering and Design*, 46:203–222, 1978.
- [69] T. J. R. Hughes and W. K. Liu. Nonlinear finite element analysis of shells: Part i. three-dimensional shells. *Computer Methods in Applied Mechanics and Engineering*, 26:331–362, 1981.
- [70] T. J. R. Hughes, A. Masud, and I. Harari. Dynamic analysis and drilling degrees of freedom. *International Journal for Numerical Methods in Engineering*, 38:3193–3210, 1995.
- [71] T. J. R. Hughes and T. E. Tezduyar. Finite elements based upon mindlin plate theory with particular reference to the four node bilinear isoparametric element. *Journal of Applied Mechanics*, 48:587–596, 1981.
- [72] M. W. Hyer. *Stress analysis of fiber-reinforced composite materials*. McGraw-Hill, Boston, 1998.
- [73] L. Iannucci and J. Ankersen. An energy based damage model for thin laminated composites. *Composites Science and Technology*, 66:934–951, 2006.
- [74] E. V. Iarve. Mesh independent modelling of cracks by using higher order shape functions. *International Journal for Numerical Methods in Engineering*, 56:869–882, 2003.
- [75] Z. H. Jin and C. T. Sun. Cohesive fracture model based on necking. *International Journal of Fracture*, 134:91–108, 2005.
- [76] S. P. Joshi and C. T. Sun. Impact induced fracture in quasi-isotropic laminate. *Journal of Composites Technology and Research*, 9:40–45, 1987.
- [77] J. K. Kalthoff. Fracture behavior under high rates of loading. *Engineering Fracture Mechanics*, 23:289–298, 1986.

- [78] J. K. Kalthoff and S. Winkler. Failure mode transition at high rates of loading. In: *Chiem, C.Y., Kunze, H.D., Meyer, L.W. (Eds.), Proceedings of the International Conference on Impact Loading and Dynamic Behaviour of Materials. Deutsche Gesellschaft für Metallkunde*, pages 43–56, 1988.
- [79] S. Kamiya, H. Sekine, and Y. Yagishita. Computational simulation of interlaminar crack extension in angle-ply laminates due to transverse loading. *Journal of Composite Materials*, 32:744–765, 1998.
- [80] T. Kant and J. R. Kommineni. C^0 finite element geometrically nonlinear analysis of fiber reinforced composite and sandwich laminates based on a higher-order theory. *Computers & Structures*, 45:511–520, 1992.
- [81] J. Kim, V. V. Varadan, and V. K. Varadan. Finite element modeling of structures including piezoelectric active devices. *International Journal for Numerical Methods in Engineering*, 40:817–832, 1997.
- [82] K. D. Kim, S. C. Han, and S. Suthasupradit. Geometrically non-linear analysis of laminated composite structures using a 4 node rotational shell element with enhanced strains. *International Journal of Non-Linear Mechanics*, 42:864–881, 2007.
- [83] S. Klinkel, F. Gruttmann, and W. Wagner. A continuum based 3d-shell element for laminated structures. *Computers & Structures*, 71:43–62, 1999.
- [84] S. Klinkel and W. Wagner. A geometrical nonlinear brick element based on the eas-method. *International Journal for Numerical Methods in Engineering*, 40:4529–4545, 1997.
- [85] E. J. Kramer and L. L. Berger. Fundamental processes of craze growth and fracture. *Advances in Polymer Science*, 91/92:1–68, 1990.
- [86] P. Ladeveze and G. Lubineau. On a damage mesomodel for laminates: micro-meso relationships, possibilities and limits. *Composites Science and Technology*, 61:2149–2158, 2001.
- [87] P. Ladeveze, G. Lubineau, and D. Marsal. Towards a bridge between the micro- and the mesomechanics of delamination for laminated composites. *Composites Science and Technology*, 66:698–712, 2006.
- [88] P. Ladeveze, G. Lubineau, and D. Violeau. A computational damage micromodel of laminated composites. *International Journal of Fracture*, 137:139–150, 2006.
- [89] J. Lambros and A. J. Rosakis. Shear dominated transonic interfacial crack growth in a bimaterial: I: Experimental observations. *Journal of Mechanics and Physics of Solids*, 43:169–188, 1995.
- [90] J. Lambros and A. J. Rosakis. Dynamic crack initiation and growth in thick unidirectional graphite/epoxy plates. *Composites Science and Technology*, 57:55–65, 1997.
- [91] J. Lambros and A. J. Rosakis. An experimental study of dynamic delamination of thick fiber reinforced polymeric matrix composites. 37:360–366, 1997.
- [92] L. Lammerant and I. Verpoest. The interaction between matrix cracks and delaminations during quasi static impact of composites. *Composites Science and Technology*, 51:505–516, 1994.

-
- [93] R. Larsson. A discontinuous shell-interface element for delamination analysis of laminated composite structures. *Computer Methods in Applied Mechanics and Engineering*, 193:3173–3194, 2004.
- [94] R. Larsson, J. Mediavilla, and M. Fagerstrom. Dynamic fracture modeling in shell structures based on XFEM. *International Journal for Numerical Methods in Engineering*, 86:499–527, 2011.
- [95] W. Li and T. Siegmund. An analysis of crack growth in thin-sheet metal via a cohesive zone model. *Engineering Fracture Mechanics*, 69:2073–2093, 2002.
- [96] Z. Li and J. Lambros. Dynamic thermomechanical behavior of fiber reinforced composites. *Composites: Part A*, 31:537–547, 2000.
- [97] C. Liu, J. Lambros, and A. J. Rosakis. Highly transient elasto-dynamic crack growth in a bimaterial interface: higher order asymptotic analysis and optical experiment. *Journal of Mechanics and Physics of Solids*, 41:1887–1954, 1993.
- [98] D. Liu. Impact induced delamination—a view of bending stiffness mismatching. *Journal of Composite Materials*, 22:674–692, 1988.
- [99] S. Liu. Quasi impact damage initiation and growth of thick section and toughened composite materials. *International Journal of Solids and Structures*, 34:3079–3098, 1994.
- [100] S. Liu, Z. Kutlu, and F. Chang. Matrix cracking and delamination in laminated composite beams subjected to a transverse concentrated line load. *Journal of Composite Materials*, 27:436–470, 1993.
- [101] R. K. Luo, E. R. Green, and C. J. Morrison. Impact damage analysis of composite plates. *International Journal of Impact Engineering*, 22:435–447, 1999.
- [102] Mallikarjuna and T. Kant. Dynamics of laminated composite plates with a higher order theory and finite element discretization. *Journal of Sound and Vibration*, 126:463–475, 1988.
- [103] J. M. Melenk and I. Babuska. The partition of unity finite element method: basic theory and applications. *Computer Methods in Applied Mechanics and Engineering*, 139:289–314, 1996.
- [104] T. Menouillard and T. Belytschko. Smoothed nodal forces for improved dynamic crack propagation modeling in xfem. *International Journal for Numerical Methods in Engineering*, 84:47–72, 2010.
- [105] T. Menouillard, J. Rethore, A. Combescure, and H. Bung. Efficient explicit time stepping for the extended finite element method (xfem). *International Journal for Numerical Methods in Engineering*, 68:911–939, 2006.
- [106] J. Mergheim, E. Kuhl, and P. Steinmann. A finite element method for the computational modelling of cohesive cracks. *International Journal for Numerical Methods in Engineering*, 63:276–2889, 2005.
- [107] N. Moes, J. Dolbow, and T. Belytschko. A finite element method for crack growth without remeshing. *International Journal for Numerical Methods in Engineering*, 46:131–150, 1999.
- [108] N. Büttcher N., E. Ramm, and D. Roehl. hree-dimensional extension of non-linear shell formulation based on the enhanced assumed strain concept. *International Journal for Numerical Methods in Engineering*, 37:2551–2568, 1994.

-
- [109] P. M. Naghdi. *The theory of shells and plates*. Springer-Verlag, berlin/Heidelberg/New York, in encyclopedia of physics, s. flügge, eds., deel via/2. edition, 1972.
- [110] J. T. Oden, C. A. M. Duarte, and O. C. Zienkiewicz. A new cloud based hp finite element method. *Computer Methods in Applied Mechanics and Engineering*, 153:117–126, 1998.
- [111] L. Olovsson, K. Simonsson, and M. Unosson. Selective mass scaling for explicit finite element analyses. *International Journal for Numerical Methods in Engineering*, 63:1436–1445, 2005.
- [112] L. Olovsson, M. Unosson, and K. Simonsson. Selective mass scaling for thin walled structures modeled with tri-linear solid elements. *Computational Mechanics*, 34:134–136, 2004.
- [113] R. Olsson. Mass criterion for wave controlled impact response of composite plates. *Composites: Part A*, 31:879–887, 2000.
- [114] A. C. Orifici, I. Herszberg, and R. S. Thomson. Review of methodologies for composite amterial modelling incorporating failure. *Composite Structures*, 86:194–210, 2008.
- [115] K. D. Papoulia, C-H. Sam, and S. A. Vavasis. Time continuity in cohesive finite element modeling. *International Journal for Numerical Methods in Engineering*, 58:679–701, 2003.
- [116] H. Parisch. A continuum based shell theory for non-linear applications. *International Journal for Numerical Methods in Engineering*, 38:1855–1883, 1995.
- [117] T. Park, K. Kim, and S. Han. Linear static and dynamic analysis of laminated composite plates and shells using 4-node quasi-conforming shell element. *Composites: Part B*, 37:237–248, 2006.
- [118] A. Parvizi, K. W. Garrett, and J. E. Bailey. Constrained cracking in glass fibre-reinforced epoxy cross-ply laminates. *Journal of Materials Science*, 13:195201, 1978.
- [119] G. Prathap and B. P. Naganarayana. Consistent thermal stress evaluation in finite elements. *Computers & Structures*, 54:415–426, 1995.
- [120] A. Puck and H. Schurmann. Failure analysis of frp laminates by means of physically based phenomenological models. *Composites Science and Technology*, 58:1045–1067, 1998.
- [121] K. Ravi-Chandar. On the failure mode transition in polycarbonate under dynamic mixed-mode loading. *International Journal of Solids and Structures*, 32:925–938, 1995.
- [122] K. Ravi-Chandar and W. G. Knauss. An experimental investigation into dynamic fracture: I: Crack initiation and arrest. *International Journal of Fracture*, 25:247–262, 1984.
- [123] J. N. Reddy. Dynamic (transient) analysis of layered anisotropic composite plates. *International Journal for Numerical Methods in Engineering*, 19:237–255, 1983.
- [124] J.J.C. Remmers, R. de Borst, and A. Needleman. The simulation of dynamic crack propagation using the cohesive segments method. *Journal of Mechanics and Physics of Solids*, 56:70–92, 2008.
- [125] J.J.C. Remmers, G.N. Wells, and Rene de. Borst. A solid like shell element allowing for arbitrary delaminations. *International Journal for Numerical Methods in Engineering*, 58:2013–2040, 2003.

-
- [126] A. J. Rosakis. Intersonic shear cracks and fault ruptures. *Advances in Physics*, 51:1189–1257, 2002.
- [127] S. Roychowdhury, Y. D. A. Roy, and R. H. Dodds. Ductile tearing in thin aluminium panels: experiments and analysis using large displacement, 3-d surface cohesive elements. *Engineering Fracture Mechanics*, 69:983–1002, 2002.
- [128] C. Sansour. Large strain deformations of elastic shells; constitutive modelling and finite element analysis. *Computer Methods in Applied Mechanics and Engineering*, 161:1–18, 1998.
- [129] I. Scheider and W. Brocks. Cohesive elements for thin-walled structures. *Computational Material Science*, 37:101–109, 2006.
- [130] J. C. J. Schellekens and R. de Borst. On the numerical integration of interface elements. *International Journal for Numerical Methods in Engineering*, 36:43–66, 1993.
- [131] J.E. Schiermeier, R.K. Kansakar, J.B. Ransom, M.A. Aminpour, and W.J. Stroud. Interface elements in global-local analysis-part3:shell to solid transition. *The 1999 MSC worldwide aerospace conference, Long Beach, California*, 1999.
- [132] D. Shantaram, D. R. J. Owen, and O. C. Ziekiewicz. Dynamic transient behaviour of two- and three-dimensional structures including plasticity, large deformation effects and fluid interaction. *Earthquake Engineering and Structural Dynamics*, 4:561–578, 1976.
- [133] E. Sharon and J. Fineburg. The dynamics of fast fracture. 1:119–122, 1999.
- [134] C. F. Shih, B. Moran, and T. Nakamura. Energy release rate along a three-dimensional crack front in a thermally stressed body. *International Journal of Fracture*, 30:79–102, 1986.
- [135] J. C. Simo and D. D. Fox. On a stress resultant geometrically exact shell model. part I: formulation and optimal parametrization. *Computer Methods in Applied Mechanics and Engineering*, 72:267–304, 1989.
- [136] A. Simone. Partition of unity-based discontinuous elements for interface phenomena: computational issues. *Communications in Numerical Methods in Engineering*, 20:465–478, 2004.
- [137] R. P. Singh and A. Shukla. Subsonic and intersonic crack growth along bimaterial interface. *Journal of Applied Mechanics*, 63:919–924, 1996.
- [138] B. Skallerud, K. Holthe, and B. Haugen. Thin shell and surface crack finite elements for simulation of combined failure modes. *Computer Methods in Applied Mechanics and Engineering*, 194:2619–2640, 2005.
- [139] A. J. Smiley and R. B. Pipes. Rate effects on mode I interlaminar fracture toughness in composite. *Journal of Composite Materials*, 21:670–686, 1987.
- [140] J. H. Song, P. M. A. Areias, and T. Belytschko. A method for dynamic crack and shear band propagation with phantom nodes. *International Journal for Numerical Methods in Engineering*, 67:868–893, 2006.
- [141] J. H. Song and T. Belytschko. Dynamic fracture of shells subjected to impulsive load. *Journal of Applied Mechanics*, 76:1–9, 2009.

- [142] S. Srinivas, C. V. J. Rao, and A. K. Rao. An exact analysis for vibration of simply-supported homogeneous and laminated thick rectangular plates. *Journal of Sound and Vibration*, 12:187–199, 1970.
- [143] N. Stander, A. Matzenmiller, and E. Ramm. An assessment of assumed strain methods in finite rotation shell analysis. *Engineering Computations*, 6:58–66, 1989.
- [144] J. A. Stricklin, J. E. Martinez, J. R. Tillerson, J. H. Hong, and W. E. Haisler. Nonlinear dynamic analysis of shells of revolution by matrix displacement method. *AIAA*, 9:629–636, 1971.
- [145] T. Strouboulis, I. Babuska, and K. Copps. The design and analysis of the generalized finite element method. *Computer Methods in Applied Mechanics and Engineering*, 181:43–69, 2000.
- [146] G. I. Taylor and H. Quinney. The latent energy remaining in a metal after cold working. *Proceedings of the Royal Society of London. series A.*, 143:307–326, 1934.
- [147] S. Timoshenko and S. Woinowsky-Krieger. *Theory of plates and shells*. McGraw-Hill, NY, 1911.
- [148] A. Turon, P. P. Camanho, J. Costa, and C. G. Davila. A damage model for the simulation of delamination in advanced composites under variable-mode loading. *Mechanics of Materials*, 38:1072–1089, 2006.
- [149] V. Tvergaard. Material failure by void growth to coalescence. *Advances in Applied Mechanics*, 27:83–151, 1989.
- [150] M. J. van den Bosch, P. J. G. Schreurs, and M. G. D. Geers. An improved description of xu and needleman cohesive zone law for mixed-mode decohesion. *Engineering Fracture Mechanics*, 73:1220–1234, 2006.
- [151] F. P. van der Meer and L. J. Sluys. Continuum models for the analysis of progressive failure in composite laminates. *Journal of Composite Materials*, 43:2131–2156, 2009.
- [152] F. P. van der Meer and L. J. Sluys. A phantom node formulation with mixed mode cohesive law for splitting in laminates. *International Journal of Fracture*, 158:107–124, 2009.
- [153] F. P. van der Meer and L. J. Sluys. Mesh independent modeling of both distributed and discrete matrix cracking in interaction with delamination in composites. *Engineering Fracture Mechanics*, 77:719–735, 2010.
- [154] G. Ventura. On the elimination of quadrature subcells for discontinuous functions in the extended finite element method. *International Journal for Numerical Methods in Engineering*, 66:761–795, 2006.
- [155] C. V. Verhoosel, J. J. C. Remmers, and M. A. Gutiérrez. A dissipation-based arc-length method for robust simulation of brittle and ductile failure. *International Journal for Numerical Methods in Engineering*, 77:1290–1321, 2009.
- [156] D. Violeau, P. Ladeveze, and G. Lubineau. Micromodel-based simulations for laminated composites. *Composites Science and Technology*, 69:1364–1371, 2009.
- [157] L. Vu-Quoc and X. G. Tan. Optimal solid shells for non-linear analyses of multilayer composites. ii. dynamics. *Computer Methods in Applied Mechanics and Engineering*, 192:1017–1059, 2003.

-
- [158] G. N. Wells, R. de Borst, and L. J. Sluys. A consistent geometrically non-linear approach for delamination. *International Journal for Numerical Methods in Engineering*, 54:1333–1355, 2002.
- [159] G. N. Wells and L. J. Sluys. A new method for modeling cohesive cracks using finite elements. *International Journal for Numerical Methods in Engineering*, 50:2667–2682, 2001.
- [160] W. K. Wilson and I. W. Yu. The use of j-integral in thermal stress crack problem. *International Journal of Fracture*, 15:377–387, 1979.
- [161] M. R. Wisnom and F. Chang. Modelling of splitting and delamination in notched cross-ply laminates. *Composites Science and Technology*, 60:2849–2856, 2000.
- [162] Y. C. Wu, T. Y. Yang, and S. Saigal. Free and forced nonlinear dynamics of composite shell structures. *Journal of Composite Materials*, 21:898–909, 1987.
- [163] P. M. Wung. Laminated composite structures by continuum-based shell elements with transverse deformation. *Computers & Structures*, 62:1073–1090, 1997.
- [164] Q. Yang and B. Cox. Cohesive models for damage evolution in laminated composites. *International Journal of Fracture*, 133:107–137, 2005.
- [165] C. Yu, A. Pandolfi, M. Ortiz, D. Coker, and A. J. Rosakis. Three-dimensional modeling of intersonic crack growth in asymmetrically-loaded unidirectional composite plates. *International Journal of Solids and Structures*, 39:6135–6157, 2002.
- [166] G. Zavarise, P. Wriggers, E. Stein, and B.A. Schrefler. A numerical model for thermomechanical contact based on microscopic interface laws. *Mech. Res. Commun.*, 19:173–182, 1992.
- [167] P. D. Zavattieri. Modeling of crack propagation in thin-walled structures using a cohesive model for shell elements. *Transactions of the ASME*, 73:948–958, 2006.
- [168] G. Zhao and C. Cho. On impact damage of composite shells by a low velocity projectile. *Journal of Composite Materials*, 38:1231–1254, 2004.
- [169] M. Zhou, G. Ravichandran, and A. J. Rosakis. Dynamically propagating shear bands in impact-loaded prenotched plates–ii, numerical simulations. *Journal of Mechanics and Physics of Solids*, 44:1007–1032, 1996.

Publications

This thesis resulted in the following publications:

Journal papers

1. A. Ahmed, F.P. van der Meer, and L. J. Sluys. A geometrically nonlinear discontinuous solid-like shell element (DSL) for thin shell structures. *Computer Methods in Applied Mechanics and Engineering*, 201-204:191-207, 2012.
2. A. Ahmed and L.J. Sluys. Anomalous behavior of bilinear quadrilateral finite elements for modeling cohesive cracks with xfem/gfem. *International Journal for Numerical Methods in Engineering*, 94:454-472, 2013.
3. A. Ahmed and L.J. Sluys. A three-dimensional progressive failure model for laminated composite plates subjected to transverse loading. *Engineering Fracture Mechanics*, 114:69-91, 2013.
4. A. Ahmed and L.J. Sluys: A numerical investigation on interacting damage mechanisms in FRP laminated composite plates. *HERON*, 58:61-84, 2013.
5. A. Ahmed and L.J. Sluys. Implicit/explicit elastodynamics of isotropic and anisotropic plates and shells using a solid-like shell element. *European Journal of Mechanics - A/Solids*, 43:118-132, 2014.
6. A. Ahmed and L.J. Sluys. A phantom node method for modelling coupled adiabatic-isothermal cracking in FRP composites. *Computer Methods in Applied Mechanics and Engineering*, 278:291-313, 2014.
7. A. Ahmed and L.J. Sluys. A computational model for the simulation of dynamic fracture in laminated composite plates. *Journal of Composite Materials*, 2014, DOI: 10.1177/0021998314539777.

Conference proceedings

1. A. Ahmed, F.P. van der Meer, L.J. Sluys, A geometrically nonlinear, discontinuous solid-like shell element. In *Proceedings of the 2nd International Conference on Extended Finite Element Method (XFEM 2011)*, Cardiff, UK, July 2011. (available online)

2. A. Ahmed, F.P. van der Meer, L.J. Sluys, A geometrically exact, discontinuous shell model for transverse matrix cracking in composite laminates. *In Proceedings of 3rd ECCOMAS Thematic Conference on the Mechanical Response of Composites*, Hannover, Germany, R. Rolfes & E. Jansen (Eds.), pp. 371-378, 2011.
3. A. Ahmed and L. J. Sluys. A computational model for prediction of progressive damage in laminated composites. *In Proceedings of 15th European Conference on Composite Materials (ECCM 2012)*, Venice, Italy. Pen drive, 2012.
4. A. Ahmed, L.J. Sluys, A finite element procedure for modeling progressive damage in laminated composite shell structures. *Appeared as a chapter in the electronic book Computational Mechanics 2012, as part of the Congress Proceedings of 10th World Congress on Computational Mechanics (WCCM 2012)*, Sao Paolo, Brazil, 2012.
5. A. Ahmed and L.J. Sluys. A partition-of-unity method for modeling coupled thermo-mechanical problems in FRP laminates subjected to impact, *In Proceedings of 19th International Conference on Composite Materials, ICCM19*, Montreal, Canada, 2013.
6. A. Ahmed and L.J. Sluys. Dynamic modeling of interacting damage mechanisms in laminated composite plates using partition-of-unity, *In Proceedings of 3rd ECCOMAS Thematic Conference on XFEM, GFEM and fictitious domain methods: recent developments and applications (XFEM 2013)*, Lyon, France, 2013.

Propositions

- 1 The predictive value of computational models to determine laminate strength and stiffness heavily relies on accurate numerical representation of the micro-mechanically motivated failure modes.
- 2 The partition of unity approach of finite element shape functions, if exploited carefully, can be effectively used to model discontinuities in various physics and multi-physics problems.
- 3 A simplified mass lumping scheme (total mass equally distributed to all nodes) for a solid-like shell element can be used in transient analysis without loss of accuracy.
- 4 The role of matrix cracking is crucial for accurate numerical prediction of progressive damage in FRP laminates.
- 5 The dynamics of crack growth in FRP composites significantly differ from crack growth in isotropic materials.
- 6 The presence of a crack in an FRP composite laminate does not completely prevent heat flow across the crack.
- 7 “Absence of understanding does not warrant absence of existence.” (*Ibn-e-Sina*)
- 8 “Unfortunately, rigor and difficulty often travel in tandem.” (*Shellbey D. Hunt*)

These propositions are regarded as opposable and defensible, and have been approved as such by the promotor, Prof.dr.ir. L.J. Sluys.

Stellingen

- 1 De voorspellende waarde van numerieke modellen om de sterkte en stijfheid van een laminaat te voorspellen hangt in belangrijke mate af van de weergave van de micro-mechanisch bepaalde bezwijkmoden.
- 2 De 'partition of unity' benadering van de vormfuncties in eindige elementen kan, als zorgvuldig geformuleerd, effectief worden gebruikt om discontinuïteiten te modelleren in diverse fysica en multi-fysica problemen.
- 3 Een vereenvoudigde 'mass lumping' techniek (totale massa evenredig verdeeld over de knopen) voor een 'solid-like' schaalement kan in een tijdsafhankelijke analyse zonder verlies van nauwkeurigheid worden gebruikt.
- 4 De rol van matrix-scheurvorming is cruciaal voor een nauwkeurige numerieke voorspelling van zich voortplantende schade in vezelversterkte laminaten.
- 5 5. De dynamica van scheurgroei in vezelversterkte laminaten verschilt significant van scheurgroei in isotrope materialen.
- 6 De aanwezigheid van een scheur in een vezelversterkt laminaat voorkomt niet volledig dat warmte-uitwisseling in de scheur plaats vindt.
- 7 Afwezigheid van begrip garandeert geen afwezigheid van existentie. (*Ibn-e-Sina*)
- 8 Helaas, grondigheid en moeilijkheid gaan vaak hand in hand. (*Shellbey D. Hunt*)

Deze stellingen worden oponeerbaar en verdedigbaar geacht en zijn als zodanig goedgekeurd door de promotor, Prof.dr.ir. L.J. Sluys.

Curriculum vitae

December 16 th , 1982	born in Peshawar, Pakistan as Awais Ahmed
August, 2001	Intermediate Certificate (Pre-Engineering), Islamia college Peshawar, Pakistan
July, 2006	Bachelor of Science in Civil Engineering, N-W.F.P University of Engineering & Technology Peshawar, Pakistan
May, 2009	Master of Science in Earthquake Engineering, IUSS- Institute of Advanced Study and Università Degli Studi Di Pavia, Pavia, Italy
December, 2009 - 2013	Ph.D candidate in the Computational Mechanics group at the Faculty of Civil Engineering and Geosciences, Delft University of Technology
Since December. 2013	Postdoctoral researcher at Delft University of Technology

